# Analysis of flood hazard under consideration of dike breaches

**Dissertation**
zur Erlangung des akademischen Grades
"doctor rerum naturalium" (Dr. rer. nat.)
in der Wissenschaftsdisziplin "Geoökologie"
eingereicht an der
Mathematisch-Naturwissenschaftlichen Fakultät
der Universität Potsdam
von
Sergiy Vorogushyn

Potsdam, 2008

Online published at the
Institutional Repository of the Potsdam University:
http://opus.kobv.de/ubp/volltexte/2009/2764/
urn:nbn:de:kobv:517-opus-27646
[http://nbn-resolving.de/urn:nbn:de:kobv:517-opus-27646]

# Contents

# Abstract

River reaches protected by dikes exhibit high damage potential due to strong value accumulation in the hinterland areas. While providing an efficient protection against low magnitude flood events, dikes may fail under the load of extreme water levels and long flood durations. Losses arising from subsequent inundation may be dramatic not only because of the high value concentration in the hinterland, but additionally due to fast water level rise and high flow velocities caused by rapid breach outflow.

Hazard and risk assessments for river reaches protected by dikes have not adequately considered the fluvial inundation processes up to now. Particularly, the processes of dike failures and their influence on the hinterland inundation and flood wave propagation lack comprehensive consideration. Uncertainties in inundation characteristics related to the dike breach processes were not yet reported. To fill this gap and enable a more adequate flood hazard assessment for diked reaches, a new modelling approach is required.

This study focuses on the development and application of a new modelling system which allows a comprehensive flood hazard assessment along diked river reaches under consideration of dike failures. The proposed Inundation Hazard Assessment Model (IHAM) represents a hybrid probabilistic-deterministic model. It comprises three models interactively coupled at runtime. These are: (1) 1D unsteady hydrodynamic model of river channel and floodplain flow between dikes, (2) probabilistic dike breach model which determines possible dike breach locations, breach widths and breach outflow discharges, and (3) 2D raster-based diffusion wave storage cell model of the hinterland areas behind the dikes. Due to the unsteady nature of the 1D and 2D coupled models, the dependence between hydraulic load at various locations along the reach is explicitly considered.

The probabilistic dike breach model describes dike failures due to three failure mechanisms: overtopping, piping and slope instability caused by the seepage flow through the dike core (micro-instability). These mechanisms were identified as dominant failure modes of historically grown dikes. Dike failures for each mechanism are simulated based on fragility functions. These functions indicate the probability of failure of a dike section upon loading and were computed prior to the simulation for each spatially discretised dike section. The probability of breach is conditioned by the uncertainty in geometrical and geotechnical dike parameters. This uncertainty is explicitly taken into account during computation of the fragility functions in a Monte Carlo simulation.

The 2D storage cell model driven by the breach outflow boundary conditions computes an extended spectrum of flood intensity indicators such as water depth, flow velocity, impulse, inundation duration and rate of water rise. IHAM is embedded in a Monte Carlo simulation in order to account for the natural variability of the flood generation processes reflected in the form of input hydrographs and for the randomness of dike failures given by breach locations, times and widths.

The model was developed and tested on a ca. $91\ km$ heavily diked river reach on the German part of the Elbe River between gauges Torgau and Vockerode. The reach is characterised by low slope and fairly flat extended hinterland areas. These areas become readily inundated as consequence of dike failures as was experienced during the August 2002 flood event. The 1D hydrodynamic model was setup, manually calibrated in the steady-state by adjusting friction parameters and validated in the steady and unsteady

modes against high water marks and gauge records. Whereas performing reasonably well in the upstream part of the study reach with respect to the discharge and water stage simulations, the 1D model shows weaknesses and exhibits an underestimation of the water levels in the downstream part of the reach. This performance deterioration is explained by the inability of the 1D scheme to capture adequately the flow dynamics of the heavily meandering part of the reach with extremely wide floodplains exhibiting strong two-dimensional flow patterns during flood events. The developed fragility functions for the considered failure modes were exposed to the sensitivity analysis for an exemplary dike section. Due to large variation in hydraulic conductivity values for the dike core material and dike foundation, they exhibit a strong impact on fragility functions for piping and slope micro-instability. The piping failure probability is further sensitive to changes in thickness of the clay layer covering dike foundation and controlling the process of rupture. The 2D inundation model was parameterised using spatially distributed friction parameter values for various landuse types.

The scenario calculations for the developed synthetic input hydrographs for the main river and tributary were carried out for floods with return periods of $T = 100,\ 200,\ 500,\ 1000\ a$. 3000 Monte Carlo runs for each scenario were shown to deliver a reasonable convergence level in terms of the breach probability and mean and standard deviation of the maximum inundation depth. Based on the modelling results, probabilistic dike hazard maps could be generated that indicate the failure probability of each discretised dike section for every scenario magnitude. In the disaggregated display mode, the dike hazard maps indicate the failure probabilities for each considered breach mechanism. Thus, such maps can be effectively utilised for setting the priorities for dike maintenance and devising reinforcement measures during catastrophic flood events.

Besides the binary inundation patterns that indicate the probability of raster cells being inundated, IHAM generates probabilistic flood hazard maps. These maps display spatial patterns of the considered flood intensity indicators and their associated return periods. The probabilistic nature of IHAM allows for the generation of percentile flood hazard maps that indicate the median and uncertainty bounds of the flood intensity indicators. The uncertainty results from the natural variability of the flow hydrographs and randomness of dike breach processes. The same uncertainty sources determine the uncertainty in the flow hydrographs along the study reach. The simulations showed that the dike breach stochasticity has an increasing impact on hydrograph uncertainty in downstream direction. Whereas in the upstream part of the reach the hydrograph uncertainty is mainly stipulated by the variability of the flood wave form, the dike failures strongly shape the uncertainty boundaries in the downstream part of the reach.

Finally, scenarios of polder deployment for the extreme floods with $T = 200,\ 500,\ 1000$ were simulated with IHAM. The results indicate a rather weak reduction of the mean and median flow hydrographs in the river channel. However, the capping of the flow peaks resulted in a considerable reduction of the overtopping failures downstream of the polder with a simultaneous slight increase of the piping and slope micro-instability frequencies explained by a more durable average impoundment. Although a slight hazard reduction of inundation hazard for the hinterland areas downstream of the polder was simulated, a hazard increase upstream of the polder was detected. This increase is caused by the detention of hinterland flow by the polder surrounding dikes. This flow originated from breaches upstream of the polder opening. The polder overtopping during higher magnitude flood events additionally contributes to the hazard increase.

The developed IHAM simulation system represents a new scientific tool for studying fluvial inundation dynamics under extreme conditions incorporating effects of technical flood protection measures. With its major outputs in form of novel probabilistic inundation and dike hazard maps, the IHAM system has a high practical value for decision support in flood management.

# Zusammenfassung

Entlang eingedeichter Flussabschnitte kann das Hinterland ein hohes Schadenspotential, aufgrund der starken Akkumulation der Werte, aufweisen. Obwohl Deiche einen effizienten Schutz gegen kleinere häufiger auftretende Hochwässer bieten, können sie unter der Last hoher Wasserstände sowie langer Anstaudauer versagen. Aufgrund hoher Wasseranstiegsraten und Fliessgeschwindigkeiten, infolge schneller Breschenausflüsse, und der hohen Wertekonzentration in geschützten Bereichen können dabei auftretenden Schäden dramatische Ausmaße erreichen.

Gefährdungs- und Risikoabschätzungsmethoden für die eingedeichten Flussstrecken haben bisher die fluvialen Überflutungsprozesse nicht hinreichend berücksichtigt. Besonders, die Prozesse der Deichbrüche und deren Einfluss auf Überflutung im Hinterland und Fortschreiten der Hochwasserwelle verlangen eine umfassende Betrachtung. Die Unsicherheiten der Überflutungscharakteristika, die durch Deichbrüche bestimmt sind, wurden bisher nicht wissenschaftlich untersucht. Um diese Lücke zu schließen und eine adäquatere Abschätzung der Hochwassergefährdung entlang eingedeichter Flussstrecken zu ermöglichen, ist ein neuer Modellierungsansatz notwendig.

Die vorliegende Studie setzt ihren Fokus auf die Entwicklung und Anwendung eines neuen Modellierungssystems, das eine umfassende Hochwassergefährdungsanalyse entlang eingedeichter Flussstrecken unter Berücksichtigung von Deichbrüchen ermöglicht. Das vorgeschlagene Inundation Hazard Assessment Model (IHAM) stellt ein hybrides probabilistisch-deterministisches Modell dar. Es besteht aus drei laufzeitgekoppelten Modellen: (1) einem 1D instationären hydrodynamisch-numerischen Modell für den Flussschlauch und die Vorländer zwischen den Deichen, (2) einem probabilistischen Deichbruchmodell, welches die möglichen Bruchstellen, Breschenbreiten und Breschenausflüsse berechnet, und (3) einem 2D raster-basierten Überflutungsmodell für das Hinterland, das auf dem Speiherzellenansatz und der Diffusionswellengleichung basiert ist. Durch die Kopplung der instationären 1D und 2D hydraulischen Modelle, wird die Abhängigkeit zwischen den hydraulischen Lasten an verschiedenen Stellen entlang eines Flusses explizit berücksichtigt.

Das probabilistische Deichbruchmodell beschreibt Deichbrüche, die infolge von drei Bruchmechanismen auftreten: dem Überströmen, dem Piping im Deichuntergrund und dem Versagen der landseitigen Böschung als Folge des Sickerflusses und der Erosion im Deichkörper (Mikro-Instabilität). Diese drei Bruchmechanismen wurden als die wichtigsten Auslöser für Deichbrüche an historisch gewachsenen Deichen identifiziert. Für jeden Bruchmechanismus wurden Deichbrüche auf der Basis von Fragilitätsfunktionen simuliert. Diese Funktionen zeigen die Versagenswahrscheinlichkeit eines Deichsabschnittes unter bestimmter hydraulischer Last. Die Versagenswahrscheinlichkeit ist durch die Unsicherheiten der geometrischen und geotechnischen Deichparameter bedingt. Diese Unsicherheiten werden bei der Erstellung der Fragilitätsfunktionen in einer Monte Carlo Simulation explizit berücksichtigt. Die Fragilitätsfunktionen wurden für jeden räumlich diskretisierten Deichabschnitt vor der Simulation erstellt.

Das 2D Speicherzellenmodell, angetrieben durch den Breschenausfluss als Randbedingung, berechnet ein erweitertes Spektrum der Hochwasserintensitätsindikatoren wie: Überflutungstiefe, Fliessgeschwindigkeit, Impuls, Überflutungsdauer und Wasseranstiegsrate. IHAM wird im Rahmen einer Monte Carlo Simulation ausgeführt und berücksichtigt die natürliche Variabilität der Hochwasserentstehungs-

prozesse, die in der Form der Hydrographen und deren Häufigkeit abgebildet wird, und die Zufälligkeit des Deichversagens, gegeben durch die Lokationen der Bruchstellen, der Zeitpunkte der Brüche und der Breschenbreiten.

Das Modell wurde entwickelt und getestet an einem ca. $91\ km$ langen Flussabschnitt. Dieser Flussabschnitt ist durchgängig eingedeicht und befindet sich an der deutschen Elbe zwischen den Pegeln Torgau und Vockerode. Die Fliessstrecke zeichnet sich durch relativ geringe Gefälle und besonders breite flache Hinterländer aus. Infolge von Deichbrüchen werden diese Hinterlandflächen besonders großräumig überflutet, wie die Erfahrungen während des Hochwassers im August 2002 Hochwasser zeigten.

Das 1D hydrodynamische Modell wurde implementiert, manuell kalibriert im stationären Modus durch die Einstellung der Rauhigkeitsbeiwerte und validiert in stationären und instationären Modi anhand von Hochwassermarken und Pegelaufzeichnungen. Obwohl das 1D Modell relativ gut die Abfluss- und Wasserstandsdynamik im oberen Lauf der Flussstrecke abbildet, zeigt es Schwächen und unterschätzt die Wasserstände im unteren Teil des Untersuchungsgebietes, ab dem Pegel Wittenberg. Diese Verschlechterung der Modellierungsgüte kann dadurch erklärt werden, dass das 1D Modell nicht in der Lage ist, das Abflussgeschehen in einem stark mäandrierenden Flussabschnitt mit extrem breiten Vorländern, die ein zwei-dimensionalen Fliessmuster aufweisen, adäquat zu berücksichtigen. Die entwickelten Fragilitätsfunktionen für die betrachteten Bruchmechanismen wurden einer Sensitivitätsanalyse am Beispiel eines Deichabschnitts unterzogen. Aufgrund der extrem breiten Spannweite der Werte für die hydraulische Leitfähigkeit des Deichmaterials und des Deichuntergrundes, zeigen diese Parameter einen großen Einfluss auf die Bruchwahrscheinlichkeit durch Piping und Mikro-Instabilität. Die Versagenswahrscheinlichkeit durch Piping ist weiterhin sensitiv zu Variation der Mächtigkeit der Tonschicht, die den Deichuntergrund bedeckt, und den Auftriebsprozess bestimmt. Das 2D Überflutungsmodell wurde auf Basis räumlich verteilter Rauhigkeitsbeiwerte parametrisiert, die den entsprechenden Landnutzungstypen zugeordnet wurden.

Die Szenarioberechnungen wurden von synthetischen Hydrographen für den Hauptstrom und Nebenfluss angetrieben, die für Hochwässer mit Wiederkehrintervallen von $100,\ 200,\ 500,$ und $1000$ Jahren entwickelt wurden. Es konnte aufgezeigt werden, dass $3000$ Monte Carlo Läufe für jedes Szenario ausreichen, um eine angemessene Konvergenz der Bruchwahrscheinlichkeiten und der mittleren maximalen Überflutungstiefe und deren Standardabweichung zu erreichen. Basierend auf den Modellierungsergebnissen wurden probabilistische Deichgefährdungskarten generiert. Sie zeigen die Versagenswahrscheinlichkeiten der diskretisierten Deichabschnitte für jede modellierte Hochwassermagnitude. Die Deichgefährdungskarten im disaggregierten Darstellungsmodus zeigen die Bruchwahrscheinlichkeiten für jeden betrachteten Bruchmechanismus. Deshalb können solche Karten effizient für Planung der Deichaufbauarbeiten genutzt werden sowie Hinweise geben, welche Deichstrecken während extremer Hochwasserereignisse besonders geschützt bzw. verstärkt werden müssen.

Neben den binären Überflutungsmustern, die die Wahrscheinlichkeit der Überflutung jeder Rasterzelle im Hinterland zeigen, generiert IHAM probabilistische Hochwassergefährdungskarten. Diese Karten stellen räumliche Muster der in Betracht gezogenen Hochwasserintensitätsindikatoren und entsprechende Jährlichkeiten dar. Der probabilistische Charakter des IHAM ermöglicht die Berechnung von Perzentilkarten der Hochwassergefährdung, die den Median und die Unsicherheitsbänder der Hochwasserintensitätsindikatoren darstellen. Die Unsicherheiten resultieren aus der natürlichen Variabilität der Abflusshydrographen und Zufälligkeit der Deichbruchprozesse. Dieselben Unsicherheitsquellen bestimmen die Unsicherheit in den Abflusshydrographen entlang der Flussstrecke. Die Simulationsergebnisse zeigen, dass die Zufälligkeit der Deichbrüche einen zunehmenden Einfluss auf die Unsicherheit des Abflusshydrographen stromabwärts hat. Während im oberen Flussabschnitt die Unsicherheit des Abflusshydrographen maßgeblich durch die Variabilität der Hydrographform bestimmt wird, beeinflussen Deichbrüche die Unsicherheitsbänder im Unterlauf stark aus.

Schließlich, wurden mit IHAM Szenarien mit Aktivierung vom Polder bei extremen Hochwässern mit Jährlichkeiten von $200,\ 500,\ 1000$ Jahren simuliert. Die Ergebnisse zeigen einen leichten Rückgang der median und mittleren Abflüsse im Flussschlauch. Jedoch führt die Kappung des Abflussscheitels zu einem beträchtlichen Rückgang der Bruchwahrscheinlichkeiten durch Überströmen flussabwärts des Polders. Die Wahrscheinlichkeiten der Deichbrüche durch Piping und Mikro-Instabilität stiegen dagegen leicht an, was durch die länger andauernde mittlere Anstauung erklärt werden kann. Obwohl ein leichter Rückgang der Gefährdung für das Hinterland stromabwärts des Polders simuliert wurde, stieg dagegen die Gefährdung stromaufwärts des Polder an. Diese Zunahme ist im Wesentlichen die Folge einer Anstauung des Wassers im Hinterland an polderumgebenden Deichen. Dieses Wasser kommt aus den Deichbrüchen, die stromaufwärts des Polders auftraten. Zusätzlich kommt es zu einem Überlauf der Polderdeiche bei extremen Hochwässern aufgrund der Deichbrüche an der Polder/Fluss Grenze.

Das entwickelte IHAM Modellierungssystem stellt ein neues wissenschaftliches Werkzeug für die Untersuchung fluvialer Überflutungsdynamik in extremen Hochwassersituationen unter Berücksichtigung des Einflusses technischer Hochwasserschutzmaßnahmen dar. Das IHAM System hat eine hohe praktische Bedeutung für die Entscheidungsunterstützung im Hochwassermanagement aufgrund der neuartigen Deichbruch- und Hochwassergefährdungskarten, die das Hauptprodukt der Simulationen darstellen.

# Chapter 1

# Introduction

## 1.1 Identification of the research niche and thesis aims

Enormous flood damages in the recent years increased the sensitivity of the communities and stressed the necessity for comprehensive inundation risk assessment in flood-prone areas. Flood risk maps are one of the products of such assessments and aim at communicating inundation extent and expected damage. Flood risk mapping assists in developing flood risk management strategies that aim, among others, at raising public awareness, regulation of urban and rural development, maintenance of flood protection structures and planning of flood warning (Hall et al., 2003). The European Directive on the assessment and management of flood risks (EU, 2007) requires from all EU Member States the development of flood hazard and risk maps as well as the design of risk management plans by law. The investments in the country-wide flood danger and hazard maps in Germany are expected to payoff, taking into account the potential benefit in terms of avoided damages (Ludwig, 2005). For flood risk assessment, an accurate estimation of the inundation extent and flood intensity indicators, such as water depth, flow velocity, etc., is essential. Furthermore, the uncertainty associated with obtained results has to be analysed and communicated to the stakeholders.

In Germany, besides a number of studies on the local (Merz and Gocht, 2003; Herrmann et al., 2007) and river reach scale (Apel et al., 2004, 2006), several attempts were made to provide flood risk, hazard or danger assessment for large rivers, e.g. Rhein (IKSR, 2001). For the Saxonian part of the Elbe catchment, LfUG (2005) undertook a risk assessment for the $1^{st}$ and $2^{nd}$ order streams based on the 100-year and hypothetical extreme scenarios. In its turn, similar activities were undertaken in other European countries and overseas. Large-scale national flood risk assessment studies were reported from the United Kingdom in the RASP project (Sayers et al., 2002; Hall et al., 2003, 2005a) and in the more detailed national floodplain mapping project for England and Wales (Bradbrook et al., 2005). National flood hazard maps for more than 25000 river kilometres in Austria were developed in the HORA project in cooperation between the governmental authorities, research institutes, engineering and insurance companies (HORA, 2007). In the Netherlands, the long-term project FLORISK is underway that aims at providing a comprehensive flood risk assessment for all 53 land compartments surrounded by dike rings (TAW, 2004). In the United States, the hazard and risk estimation platform HAZUS-MH has been developed over the past decade and aims at providing a consistent methodology and nation-wide datasets for assessment of the natural hazards, in particular flood hazard, and estimation of losses (Scawthorn et al., 2006a,b).

Currently available methodologies for flood hazard assessment differ considerably in their complexity and underlying assumptions (Chapter 2). Detailed hydrodynamic simulations of flood processes are typically done for a few scenarios and restricted to reaches of several kilometres. For large-scale assessments, assumptions of the steady flow in the river network are often used accompanied with subsequent

simple inundation simulation schemes. The role of flood protection dikes and their possible failures found concideration in a scanty number of studies, primarily in the form of scenarios. Up to date, only a few works were reported which provided reach-scale hazard and risk estimations under consideration of dike failures in an unsteady analysis of flood propagation. Even fewer papers abstain from preselecting the dike failure scenarios based on hypothetical assumptions or historical evidence.

Yet hazard and damage, resulting from an inundation due to dike breaches, can be significantly higher compared to a gradual increase of the water level on a floodplain (Alkema and Middelkoop, 2005). This occurs partly due to physical factors, such as higher water velocity and rate of water rise caused by rapid dike breaches. The high rate of water rise can hinder the evacuation of residents and shorten the time available to undertake flood protection measures. Furthermore, the subjective safety sensation evoked by dikes results in an intensive settlement in the hinterland areas. The asset accumulation in the flood-prone areas due to the lack of awareness about inundation danger and due to socio-economic pressure results in a higher damage potential (Kron, 2006). While dikes can effectively protect the settlements during low magnitude events, more extreme floods bear a considerable threat. In case of dike breaches and failures of other technical flood protection measures, presumably safe regions may exhibit significant economic losses (IKSE, 2003). Hence, the estimation of hazard for high magnitude events in diked regions deserves special attention.

The assessments of reliability of flood protection structures was often carried out using the methods of system reliability research (Szidarovszky et al., 1975; Wood, 1977; CUR/TAW, 1990; Uno et al., 1994; Kortenhaus and Oumeraci, 2002; Lassing and Vrouwenvelder, 2003). Recently, a few studies additionally considered the consequences of dike failures in terms of subsequent inundation and flood risk in a steady (Hall et al., 2003, 2005a) and unsteady (Apel et al., 2004, 2006) flood analysis. However, these works remained limited to the consideration of one breach mechanism — overtopping. Dawson et al. (2005) extended the methodology of Hall et al. (2003) by a few more failure modes represented in a highly simplified form. Hence, there still remains a gap in a sound estimation of the flood hazard for fluvial systems considering all relevant dike failure mechanisms in an unsteady flood analysis.

The research project "Integration of Data and Models in Flood Information Systems" of the Young Investigators Group in the Helmholtz Association was initiated in 2004. It is aimed at investigation of extreme flood events exemplified for the Elbe and Mulde catchments in the eastern part of Germany. One of the aims was the development of a methodology for the river reach scale flood hazard assessment along diked reaches. Generation of flood hazard maps for the Elbe River was sought as one of the project outcomes. Flood hazard maps can be further combined with damage estimation models to generate flood risk maps.

In the context of the outlined project the presented thesis is particularly focused on the following aspects:

1. *Development of a methodology for flood hazard assessment on a river reach scale under consideration of dikes and their possible failures.* The methodology implies the coupling of models for flood scenario generation, flood wave routing, dike breach and inundation prediction. The distinctive features of the developed methodology should include an unsteady analysis of a flood wave that accounts for the dependence of the hydraulic load on dikes at various locations along the reach. The unsteady flood analysis would allow the consideration of the effects of flood control measures, e.g. activation of polders, on changes in dike breach propensity and inundation hazard.

2. *Identification of vulnerable dike sections and generation of dike hazard maps.* The analysis of dike stability along the river reach has to be carried out for a range of extreme flood events. To gain an added value, a wider range of relevant dike failure mechanisms should be considered in the modelling approach and embedded into the unsteady flood analysis. As a result, maps indicating vulnerable dike sections should be generated and analysed. Besides lumped dike hazard maps,

which indicate all the endangered sections, disaggregated maps for each failure mode are sought. These products can be of high interest to flood protection authorities responsible for maintenance planning and dike reinforcement during extreme floods.

3. *Computation of the flood intensity indicators and generation of flood hazard maps.* The application of an unsteady inundation simulation scheme should deliver an extended spectrum of flood intensity indicators, such as inundation depth, flow velocity, product of flow velocity and depth, inundation duration with water depth over a certain threshold and rate of water rise. These intensity indicators can be used as a background for the generation of the more sophisticated flood hazard maps, which are partly unattainable with the steady inundation modelling approaches.

4. *Quantification and visualisation of uncertainty in flood hazard maps.* Whereas many previous studies often focused on the uncertainties in inundation predictions originating from uncertain friction parameterisation of hydraulic models and their constraining observations (Chapter 2), the uncertainty in the dike breach processes description was rarely analysed. The challenge in quantification of this uncertainty in terms of the variation of flood intensity indicators is faced in this study. Properly visualised, it provides additional essential information to decision makers for devising and implementing flood protective measures.

The methodology and model should be implemented and tested on a typical river reach protected by dikes. While providing a methodology and background for hazard and risk assessment, the modelling approach is to be seen as a tool for studying the fluvial system dynamics under extreme conditions and consideration of flood defence measures, such as dikes and polders. Since extreme events are naturally rare and experimental setups on a large scale are not feasible, modelling represents an efficient way to gain the knowledge about system behaviour and investigate possible scenarios.

## 1.2 Structure of the thesis

After giving a short introduction into the problem of flood hazard assessment and defining the major aims of the thesis, Chapter 2 provides a detailed description of the methodologies available for flood inundation modelling. Special attention is paid to the analysis of predictive capability in comparison to the approach complexity. Sect. 2.4 is devoted to the description of data and methods for constraining the uncertainty in inundation model predictions. Integration of the inundation modelling approaches into the hazard assessment frameworks is discussed in Sect. 2.5 with the special focus on consideration of failures of fluvial defence structures. The advantages and deficits of the presented approaches are analysed, leading to a proposal for the innovative model development.

Chapter 3 details the structure, coupling approach and implementation specifics of the inundation hazard assessment model IHAM. A considerable part of the chapter is devoted to the description of dike breach mechanisms and evaluation of breach statistics. Identifying the relevant failure modes for fluvial dikes, Sect. 3.3 proceeds with the analysis of models, which describe selected breach mechanisms. The methodologies for the development of fragility functions are outlined for each failure mode. In the final section, the approaches for consideration of the breach width and development in flood hazard modelling are reviewed. An alternative way is proposed to account for an extreme uncertainty of ultimate breach width in a probabilistic framework.

Chapter 4 deals with an application of the developed IHAM model to a typical diked Elbe River reach. After giving a short introduction to the test site, the setup, calibration and validation of the 1D hydrodynamic model of a river channel are carried out. Parameterisation of the dike breach model describing the failure probabilities for the discretised dike sections is accompanied by a sensitivity analysis. The 2D raster-based inundation model for hinterlands was parameterised and evaluated using the observed

inundation extents from the extreme flood event. A methodology for development of synthetic flood scenarios for defined return periods based on past observations is applied to the main river and tributary in order to generate model boundary conditions.

The results of the probabilistic modelling for a range of extreme flood scenarios are converted into dike and inundation hazard maps and discussed in Sect. 4.7. Special emphasis is laid on the convergence analysis of Monte Carlo (MC) results with respect to the dike failure probability and inundation depth. Finally, scenarios of planned polder installation and control are evaluated in Sect. 4.8 in terms of polder capability to reduce the hazard for downstream parts of the reach.

The final Chapter 5 summarises the key findings and novel implementations presented in the thesis and draws final conclusions. Perspectives of further model development and application are highlighted in the closing section.

# Chapter 2

# Flood inundation modelling and hazard assessment

Numerous studies were carried out to assess inundation extent and/or depth for flood events. The applied methodology ranges from a simple planar water surface interpolation to complex simulations based on solving full two- or three-dimensional flow equations for river channel and floodplain flow. The following sections analyse the available methods for inundation prediction, focusing on the balance of model predictive capability and computational efforts required.

## 2.1 One-dimensional models for inundation prediction

### 2.1.1 Planar surface interpolation

The crude predictor of the inundation extent and depth is the planar water surface interpolation between gauge stations intersected with a digital elevation model (DEM), giving a first guess of inundation areas (Horritt and Bates, 2001b; Werner, 2004; Rodda, 2005). The resulting flood extent is usually significantly overestimated for lowland rivers (Mai and von Liebermann, 2001; Bradbrook et al., 2005), since the methodology does not take into account the available water volume in a river system and hydraulic conditions of a floodplain. An overestimation may also occur if the local depressions in DEM are not excluded from flood extent. Under local depressions, the DEM cells are meant, which lie below the water level, however, are not hydraulically connected to river channel. Following the algorithm of Werner (2001), it is possible to account for these raster cells. Nonetheless, the comparisons of planar surface approximations with results from a 2D hydrodynamic model show an apparent advantage of hydraulic techniques in terms of accuracy (Horritt and Bates, 2001b). The advantage can become even more pronounced for longer reaches, where the curvature of the water level between gauges might be poorly described by a straight line. Furthermore, the intersection of the water stage with a DEM does not explicitly consider dike failures and inundation areas associated with them. The risk associated with flow velocities and high rates of water rise cannot be assessed with the planar water surface approach.

### 2.1.2 1D hydrodynamic modelling approach

Inundation extent can be simulated using 1D hydraulic models of compound channel. This approach can explicitly include a floodplain described by extended cross-sections (Horritt and Bates, 2002; Pappenberger et al., 2005; Werner and Lambert, 2007). 1D hydrodynamic models solve a system of one-dimensional continuity (Eq. 2.1) and momentum (Eq. 2.2) equations and determine discharge, water

level, flow velocity and other hydraulic variables at every computational node.

$$\frac{\partial A}{\partial t} + \frac{\partial Q}{\partial x} = q \tag{2.1}$$

$$\underbrace{\frac{\partial (Q^2/A)}{\partial x}}_{\text{convective acceleration term}} + \underbrace{\frac{\partial Q}{\partial t}}_{\text{local acceleration term}} + gA \left( \underbrace{\frac{\partial d}{\partial x} + \underbrace{S_f - S_o}_{\text{kinematic wave}}}_{\text{diffusive wave}} \right) = 0 \tag{2.2}$$

where $A$ – flow cross-sectional area $[m^2]$, $t$ – time $[s]$, $Q$ – discharge $[m^3\ s^{-1}]$, $x$ – longitudinal distance along the channel $[m]$, $q$ – net lateral inflow per unit length $[m^2\ s^{-1}]$, $g$ - gravitational acceleration $9.81$ $[m\ s^{-2}]$, $d$ – water depth $[m]$, $S_f$ – friction slope [-], $S_o$ – bottom slope [-].

The planar water surface interpolation between the computational nodes can then be applied to generate inundation maps. An advantage of 1D hydrodynamic modells is a denser set of points used for the planar surface construction. Although in some cases 1D models can produce fairly good estimations of flood area, when calibrated against discharge or inundation extent (Horritt and Bates, 2002), the overland flow is considered to be not one-dimensional. Hence, the flow dynamics on a floodplain between the cross-sections lacks a sufficient consideration.

## 2.2 Two-dimensional models for inundation prediction

To overcome the limitation of the 1D models, residing in an insufficient discretisation of floodplain, two-dimensional hydraulic models have been developed and applied for flood simulations (Aronica et al., 1998b; Stelling et al., 1998; Hervouet, 2000; Bates et al., 1998a; Beffa and Connel, 2001). These models solve a two-dimensional version of shallow water equations using finite-difference, finite-element or finite-volume numerical schemes. Based on floodplain topography, two-dimensional inundation extent and flow characteristics can be directly computed. 2D hydrodynamic models deliver the estimates of the depth-averaged flow velocity field recognized as an important flood intensity indicator. The product of flow velocity and inundation depth is often used as an intensity indicator in flood risk mapping (Merz et al., 2007) and referred as specific discharge (LfUG, 2005) or as impulse (Alkema and Middelkoop, 2005). Strictly saying, this product represents specific momentum, i.e. momentum divided by water density and flow area.

The detailed processes description and numerical solutions that are involved, however, pose considerable requirements on the computational time for the 2D hydrodynamic models. It makes large scale applications extremely costly. The grid coarsening could somewhat relax the problem. However, in case of flow dominated in a main channel, the poor channel resolution may result in considerable model performance deterioration, as shown by Werner (2004) for the FLS 2D model (Stelling et al., 1998). Besides the computational constraints, detailed information about boundary conditions, depending on the critical or subcritical flow range, is required. These limitations led to the development of the simplified 2D models, which neglect the convective acceleration term in the momentum equations (Aronica et al., 1998b).

Nevertheless, the 2D approaches remain limited in application to the local-scale reaches of several kilometres in length. The limitation of the 2D models with regards to computation time still persists, thus hindering, currently, the performance of the large-scale simulations, probabilistic hazard assessment and uncertainty analysis within a Monte Carlo framework in reasonable time. These limitations led to further exploration of the raster-based storage cell inundation models and their applications to fluvial inundation problems.

### 2.2.1 Storage cell inundation models

The storage cell approach is based on the floodplain representation as a network of interlinked storage basins, described by stage-volume functions. This type of modelling approach was initially developed for irregular storage cells, with water flow between cells computed based on the Manning-Strickler equation or weir-type formula (Cunge, 1975; Estrela and Quintas, 1994; Romanowicz and Beven, 2003). Although initially developed for the gradually varied flow, the irregular storage cell approach was shown to deliver acceptable results for inundation dynamics in a particular topographic setup (Aureli et al., 2005). In combination with a 1D full dynamic channel flow model, it was able to reproduce the outflow hydrograph through a dike breach comparably to a full 2D finite-volume model, despite rapidly varied flow and presence of hydraulic jump. However, the implementation of the stage-volume or stage-area functions only emulates the dynamic behaviour of the system. The storage cell approach is founded on the assumption that the inflow water volume is spread over the whole area instantaneously, which may lead to gross errors for large or elongated storage basins. Furthermore, the delineation of the cells, calculation of the stage-volume functions, implementation of the links require additional preprocessing efforts.

To make use of the readily available topographic information in form of DEM, a regular storage cell approach to the fluvial flood propagation was developed and implemented as a raster-based code (Bates and De Roo, 2000; Horritt and Bates, 2001b; Bradbrook et al., 2004). In the surface hydrology research the same approach was used to simulate overland flow as part of the rainfall-runoff process (Merz, 1996; Wang and Hjelmfelt, 1998; Jain and Singh, 2005). Dutta et al. (2000) used the diffusion wave model component for both overland and overbank floodplain flow simulation within a complex distributed hydrologic model.

In a regular storage cell code each raster cell is treated as a storage basin with fluxes between cells computed according to the zero-inertia form of Eq. 2.2 (Hunter, 2005). The water flow is, thus, a function of water free surface height difference between neighbouring cells and governed by a continuity equation, relating change in water level to the net inflow (Eq. 2.3), and by a reduced momentum equation:

$$\frac{\partial h^{i,j}}{\partial t} = \frac{Q_x^{i-1,j} - Q_x^{i,j} + Q_y^{i,j-1} - Q_y^{i,j}}{\Delta x \Delta y} \tag{2.3}$$

where $h^{i,j}$ - water surface elevation at cell $(i,j)$ $[m]$, $t$ – time step $[s]$, $Q_x$, $Q_y$ – volumetric flow rates between cells in $x$ and $y$ directions $[m^3\ s^{-1}]$, $\Delta x$, $\Delta y$ - cell dimensions ($\Delta x = \Delta y$ for equidistant grid) $[m]$.
The momentum equation is given by the diffusive wave approximation of Eq. 2.2. Hence, the friction slope ($S_f$) can be expressed in $x$ direction as:

$$S_f = S_o - \frac{\partial d}{\partial x} \tag{2.4}$$

The $x$ and $y$ flow components are computed separately applying Manning's equation (Eq. 2.5).

$$Q = K S_f^{1/2} \tag{2.5}$$

where $K$ – conveyance $[m^3\ s^{-1}]$ given by Eq. 2.6.

$$K = \frac{1}{n} A R^{2/3} \tag{2.6}$$

with $n$ – Manning's roughness coefficient $[m^{1/3}\ s^{-1}]$, $R$ – wetted perimeter $[m]$.

Here the derivation of the $x$ flow component is presented. The flow in $y$ direction is derived analogously. Taking into account that

$$\frac{\Delta z}{\Delta x} = -S_o \tag{2.7}$$

with $z$ – datum or bottom elevation $[m]$,
and introducing Eq. 2.4 into Eq. 2.5 yields the following flow equation:

$$Q_x^{i,j} = \frac{1}{n} A R^{2/3} \left( -\frac{\Delta z}{\Delta x} - \frac{\Delta d}{\Delta x} \right)^{1/2} \tag{2.8}$$

Considering that

$$R = \frac{A}{\Delta y} \tag{2.9}$$

and expanding Eq. 2.8 delivers

$$Q_x^{i,j} = \frac{A^{5/3}}{n(\Delta y)^{2/3}} \left( \frac{(d^{i-1,j} + z^{i-1,j})}{\Delta x} - \frac{(d^{i,j} + z^{i,j})}{\Delta x} \right)^{1/2} \tag{2.10}$$

Let us define $h_{flow}$ as flow depth between adjacent cells, i.e. difference between the maximum water surface elevation and maximum ground elevation. Then considering $A = h_{flow} \cdot \Delta y.$ in Eq. 2.10 and applying $h = d + z$ yields:

$$Q_x^{i,j} = \frac{h_{flow}^{5/3}}{n} \left( \frac{h^{i-1,j} - h^{i,j}}{\Delta x} \right)^{1/2} \Delta y \tag{2.11}$$

Alternatively, a diffusive wave approximation of two-dimensional shallow water equations with coupled flow components results in the following momentum equation (here only flow in $x$ direction is given) (Horritt and Bates, 2001b; Yu and Lane, 2006a):

$$Q_x^{i,j} = \frac{\frac{h_{flow}^{5/3}}{n} \left( \frac{h^{i-1,j} - h^{i,j}}{\Delta x} \right) \Delta y}{\left[ \left( \frac{h^{i-1,j} - h^{i,j}}{\Delta x} \right)^{1/2} + \left( \frac{h^{i,j-1} - h^{i,j+1}}{2\Delta y} \right)^{1/2} \right]^{1/4}} \tag{2.12}$$

In the storage cell code the $x$ and $y$ flow components are decoupled contrary to the diffusive wave treatment given in Eq. 2.12. Hence, the storage cell model is expected to exhibit a larger error in water velocity estimations compared to the coupled treatment (CT) and full 2D hydrodynamic models. Nevertheless, flow velocity estimations with raster-based codes are used in practice for preliminary flood hazard assessment (LfUG, 2005; Assmann, 2005), (N. Hunter, University of Bristol, personal communication).

Werner and Lambert (2007) compared the depth averaged velocities from various modelling codes on a planar floodplain and reported marginal differences between 1D, 2D and storage cell models. The difference is expected to increase on a floodplain with steep slopes or at locations of rapidly varying flow, e.g. near dike breaches.

The storage cell code simulates larger flows compared to the CT approach that can be derived analytically (Horritt and Bates, 2001b). However, when calibrated and validated against the flood extent measurements, derived from the synthetic aperture radar (SAR), the solution of the diffusive wave equation with coupled $x$ and $y$ components does not lead to a better model performance. The theoretical

deficiencies are, thus, compensated for by calibration of the roughness value. Although the CT model exhibits a slightly higher sensitivity to the floodplain friction, which seems to be intuitively correct, the overall accuracy in inundation extent predictions is comparable to the storage cell model.

If the channel flow is not the main focus of a modelling study, a 2D storage cell modelling can directly be used for inundation predictions in a fluvial system. The bankfull discharge, which corresponds to a 2-year flood in natural streams, can be estimated and substracted from the inflow hydrograph prior the 2D overbank flow simulation. The JFLOW model (Bradbrook et al., 2004), which is based on the 2D CT diffusive wave, routes the excess overbank discharge over a floodplain to produce an inundation pattern. This approach avoids explicit channel flow computations and, hence, is suitable for a first flood extent approximations over large areas as applied in England and Wales (Bradbrook et al., 2005). The approach is particularly focused on derivation of a flood outline and neither explicitly considers the flood protection structures nor their possible failures during an extreme event.

Despite the extended research on two-dimensional treatments of inundation flow, the computational constraints dictate further progress in computational efficiency. Assuming a 1D nature of inbank channel flow, recent research studies link the two-dimensional floodplain inundation codes to the 1D channel simulation schemes in 1D-2D hybrid models. These models are further discussed in Sect. 2.3.

## 2.3 Hybrid models for inundation prediction

Recent developments in the field of computer models for inundation prediction propose a coupled full 1D-2D approach, such as SOBEK-Overland Flow (SOBEK, 2007) or MIKE FLOOD (DHI, 2007). Following this approach water flow in a river channel is modelled using a one-dimensional hydrodynamic model. In case of bank overflow the overland flow is simulated using a full 2D code. The coupled 1D-2D model has been successfully applied in several studies for inundation prediction including dike breach scenarios (Frank et al., 2001; Werner, 2004).

Another simplified hybrid approach is implemented in the raster-based LISFLOOD-FP model (Bates and De Roo, 2000; Horritt and Bates, 2001b) separately simulates the channel flow in a river network using either kinematic or diffusive wave treatment, and two-dimensional flow on a floodplain based on the decoupled treatment of diffusive wave (Eq. 2.11). The coupled diffusive wave treatment of overbank flow is implemented as an option, however, not considered in practical applications because of no superiority with regards to inundation extent prediction accuracy and twice as high computational effort (Horritt and Bates, 2001b). A set of open questions, however, remains with reagrds to the performance of both treatments in terms of inundation depth, flow velocity and wetting/drying front propagation that are relevant for advanced hazard and risk assessment. The performance measured solely in terms of inundation extent predictions may mask the model deficiencies in terms of other prediction quantities, especially on topographically constrained floodplains. Although, detailed records of flood dynamics are too scarce currently to evaluate the model dynamics, a benchmark testing against other codes remains a promissible option. The first tests of a storage cell model against the more detailed approaches described by Werner (2004) and Hunter et al. (2005a) indicate an inferior performance of the LISFLOOD-FP model. The predictive capability, however, improves when the model is properly calibrated.

The 1D channel flow equations are solved in the LISFLOOD-FP using an implicit numerical scheme, whereas the 2D floodplain flow equations are treated explicitly for the purpose of simplicity. However, the explicit numerical schemes are conditionally stable and demand a restriction on the time step. Practically, it would be rather difficult to find an optimum trade-off between the stable solution and computational time step. Therefore two approaches to stabilise the numerical schemes were developed.

The first classical approach applies the flow limiter (Eq. 2.13) at cells with small free surface gradi-

ents in the areas of deep flow to prevent parasitic oscillations of the water level (Hunter et al., 2005a).

$$Q_x^{i,j} = min\left(Q_x^{i,j}, \frac{\Delta x \Delta y (h^{i,j} - h^{i-1,j})}{4\Delta t}\right) \tag{2.13}$$

The flow limiter (Eq. 2.13) is independent of the Manning's n value and is influenced by the mesh size and time step. Therefore, when flow limiter is invoked, the flood extent and flood wave travel time were found to be insensitive to the floodplain roughness (Horritt and Bates, 2001b, 2002; Hunter et al., 2005b). However, the overall model sensitivity to Manning's n depends on how often the fluxes through the cell boundaries are controlled by the flow limiter during a simulation course. Furthermore, the insensitivity reported by Horritt and Bates (2002) may be the impact of the constraining topography of a reach that is mentioned by the authors. Moreover, it is a complex interaction between the channel and floodplain flow that contributes to the model sensitivity. Indeed, Horritt and Bates (2001b) indicate that at higher friction values in a channel, the 2D storage cell model becomes more sensitive to the floodplain roughness values. This can be explained by the fact that a higher channel roughness results in a higher water stage with more water forced onto a floodplain. As soon as the floodplain flow becomes more important comapred to the channel flow, the sensitivity to friction values with respect to the inundation extent increases. Similar effect was reported for the full 2D shallow water model on a wider floodplain (Horritt, 2000). An impact of the channel flow description onto the floodplain model response is further undelined by implementing the diffusive wave approximation in a channel (Horritt and Bates, 2001b). This immediately changed the calibration surface towards a higher sensitivity to floodplain friction. Consequently, it seems to be not a generally valid assumption that a storage cell model shows insensitivity to roughness parameterisation. But it is obviously the case, when flow limiter is in use. Especially, for wide floodplains, where the impact of a channel flow diminishes, the storage cell code is expected to show a higher sensitivity to friction values.

A second approach applies the theoretical criterion of model stability to find an optimum time step. The adaptive time step approach developed by Hunter et al. (2005c) for a storage cell code determines the time step small enough to prevent numerical instabilities at each model iteration. The comparison agaist the analytical solutions for flood wave propagation on a horizontal plane and planar beach revealed a more realistic development of wetting and drying fronts in an adaptive time step solution compared to the flood limiter approach (Hunter et al., 2005c). The sensitivity of the flood wave travel time to the floodplain friction increased markedly. This indicates that the floodplain acts no longer only as a storage but also has an impact on flood wave routing. The accuracy of the classical formulation depends on the initially selected time step and flow conditions, whereas an adaptive time step scheme insures an optimum solution any time during simulation. However, the increase in accuracy is achieved at approximately $6$ times higher computational costs on a $50\ m$ grid (Hunter et al., 2005b).

Comparison against the observed flood extent on a real river reach revealed only a modest performance improvement and marginal increase in sensitivity to the floodplain roughness in case of adaptive time step solution (Hunter et al., 2005b). This suggests that in a real world case for a complex floodplain topography the scheme using the flow limiter may deliver comparable results of inundation extent predictions, when properly calibrated. To further discriminate the alternative model formulations, a comparison is required against spatially distributed records of flood dynamics e.g. multiple images of inundation extent or time-dependent records of water stage on a floodplain. The first attempt to assess the dynamic model performace against the multiple remote sensing observations of inundated area was recently reported by Bates et al. (2006), indicating some deficiencies in floodplain dewatering dynamics. The shortcomings probably resulted due to the effect of small-scale channelized flow uncaptured in the model, or simplifications of the governing shallow water equations.

## 2.4 Constraining inundation model uncertainty

### 2.4.1 In-situ measurements

The uncertainty in inundation predictions is constrained by the calibration of roughness values given observed flood events. Various information sources about the flood dynamics can be utilised for model calibration. Until recently the observational data sources included discharge and water stage time series at gauging stations along a river reach. These measurements represented the aggregated hydrologic and hydraulic responce of the entire catchment and its subcatchments. Spatially distributed measurements of maximum water stages are often limited to the river course, whereas the wide floodplains behind the dikes remain unconsidered. Although these measurements represent a valuable source of very precise data with an accuracy of $0.05 - 0.2\ m$ RMSE, data collection and processing are time- and cost-intensive (Oberstadtler et al., 1997). Based on wrack records, the accuracy of high water marks may be $\pm 0.3\ m$ as reported by Schumann et al. (2007b).

The bulky discharge and water stage data are not sufficient for efficient constraining of spatially distributed inundation model parameters. The inundation models thus suffer from the lack of calibration and validation data, which is a cause of equifinality of model parameters (Bates, 2004). Remote sensing appears to be a vast source of spatially distributed information and offers an alternative to in-situ measurements of hydraulic quantities.

### 2.4.2 Inundation extent observations

Inundation extent can be derived from airborne imagery, visible range satellite images (e.g. Landsat 7 ETM+) and synthetic aperture radar (SAR). Comparably to the visible range sensors SAR exhibits all-weather capability, i.e. ability in penetrating the cloud cover. Therefore, it has been extensively used for calibration and validation of various inundation models (Horritt and Bates, 2001b, 2002; Aronica et al., 2002; Bates et al., 2004; Hunter et al., 2005a). The primary disadvatange of the spaceborne imagery, as yet, is relatively low spatial resolution compared to airborne data (Lane et al., 2003). This may result in considerable uncertainties in the flood extent delineation. Pappenberger et al. (2007) explicitly acknowledged this uncertainty of the remotely sensed data by implementing a fuzzy evaluation methodology for an inundation model.

### 2.4.3 Water levels extracted from inundation extent observations

Several studies were aimed at extraction of spatially distributed water level data based on airborne and satellite SAR imagery of the inundation extent (Oberstadtler et al., 1997; Brakenridge et al., 1998; Raclot, 2006; Schumann et al., 2007a). A 2-dimensional representation of inundation extent is converted into a 3-dimensional characterisation of the water levels using ancillary data, amongst others, topography. The accuracy of the derived water depth is in the range of $1 - 2\ m$ and appears to be inferior compared to the stage measurements or steady-state modelling results (Brakenridge et al., 1998). The error mainly stems from the imprecise DEM, coarse SAR image resolution delivered by the ERS-1 satellite, inherent speckle effects impeding the flood boundary identification, and shift in phase between the in-situ and remote sensing observations. Data of such accuracy can hardly be used for inundation model calibration and validation.

With recent developments in the field of photogrammetric image processing an accuracy of the extracted water levels could be raised to the level of in-situ water stage measuremets of $\sim 0.15\ m$ (Lane et al., 2003). Furthermore, the methods of the water/land boundary delineation from SAR imagery using the statistical contour model (Horritt, 1999; Horritt et al., 2001), and applying a correction methods based

on identification of submerged vegetation and canopy height maps (Horritt et al., 2003) have a potential to significantly improve the water boundary estimations and, consequently, the accuracy of spatially distributed water levels. Further improvements in the water elevation calculations may be possible by considering the hydraulic compartments with horizontal water level and boundaries determined by linear structures, such as dikes, roads and walls. Raclot (2006) interpreted the hydraulic connections between the compartments and considered them in the evaluation scheme. The author achieved a mean absolute error of $0.23\ m$ compared to the in-situ measurements of water level.

### 2.4.4 Satelite radar altimetry and interferometric synthetic aperture radar

Satelite radar altimetry technology emerged in the eighties and is capable of providing water stage elevation profiles. The technique has significantly improved over the past two decades. The first applications to fluvial systems showed an accuracy with an RMSE of $0.7 - 1.2\ m$ (Koblinsky et al., 1993). At present it delivers water stages with the best accuracy of up to $0.11 - 0.14\ m$ RMSE when applied to fluvial systems, which is comparable to the average accuracy of high water marks. The average accuracy of satellite radar altimetry is $\sim 0.25 - 0.3\ m$ RMSE with along-track ground resolution of up to $300\ m$ (Birkett, 1998; Frappart et al., 2006; Alsdorf et al., 2007). However, this technique, previously applied in the large-scale ocean, land and ice-cover observation research, is limited to river-floodplain systems of $1 - 1.5\ km$ minimum width. With a time resolution of about $10 - 35$ days satelite altimetry was readily used for the long-term observation of seasonal and inter-annual dynamics of large river and lake systems (Birkett, 1998; Frappart et al., 2006). In case of fluvial inundation, it would provide a snapshot of water stages at limited number of points. Thus, the satellite radar altimetry can practically be regarded as zero-dimensional in time with respect to the flood events typical for Central Europe. Water stage elevation data delivered by satelite radar altimetry have not been used for calibration and validation of flood inundation models due the gross temporal and spatial resolution (Raclot, 2006), although some authors advocate the high potential of this technology (Smith, 1997; Alsdorf et al., 2007).

Recent developments in the field of remote sensing allow direct area-wide measurements of water stage dynamics. Based on interferometric synthetic aperture radar (InSAR) measurements, Alsdorf et al. (2000) detected centimetre-scale water level changes over tens of kilometers on the Amazon floodplain. This promissing technique, delivering high information content data, is, however, limited to floodplains with submerged vegetation. The near surface submerged vegetation is required to return the radar pulse echo back to the sensor. The technique does not currently work over open water, i.e. typical river channels, lakes and reservoirs (Alsdorf et al., 2007). InSAR has not been used for inundation model calibration up to now. The first attempt or proof-of-concept study in assimilating the water surface elevation and inundation area, as obtained from InSAR, into the LISFLOOD-FP hydrodynamic model was carried out by Andreadis et al. (2007). The authors used synthetically derived observations to update the model predictions at various hypothetical satellite overpass frequencies. The synthetic observations emulated the remote sensing data that would be obtained from the proposed joint European-U.S. satellite mission, WATER (Water Elevation Recovery). The altimetry imagery ('swath altimetry') that uses two interferometric SARs proposed in the WATER initiative is expected to deliver water elevation data accuracy of $\sim 0.5\ m$ for 10-$m$-sized pixels. Applying correction techniques, it can be possible to improve the accuracy to better than $0.05\ m$ for river widths of greater than $30\ m$ (Alsdorf et al., 2007).

The review of the available data used for constraining the inundation model uncertainty revealed the following:

- Relatively precise measurements of catchement discharge and water level dynamics at gauge station are one-dimensional in time and zero-dimensional in space. It means that the measurements are carried out over time, but only at one location. Therefore, they have a low potential in constraining uncertainty of spatially distributed model output.

- Increasing the spatial density of observation points by conventional in-situ measurements is costly, however, effective for uncertainty reduction and should be used if possible. In particular, high water marks along the river channels are readily available for calibration and validation of hydraulic models (Sec. 4.3.1).

- Synoptic imagery is currently efficiently used for calibration and validation of the spatially distributed inundation models due to its two-dimensional nature. However, its zero-dimensionality in time limits the dynamic model evaluation. Nevertheless, an available visible range satelite image was used to assess the inundation model performance in this work (Sec. 4.5).

- Direct distributed water stage measurements from space are currently limited in terms of temporal and spatial resolution as well as by technical constraints of the remote sensors.

## 2.5 Flood hazard assessment under defence failure

The majority of flood impact assessment studies considering dike failures rely on predefined breach location(s) and breach width(s), either based on historical information (Han et al., 1998; Hesselink et al., 2003; Alkema and Middelkoop, 2005) or hypothetical assumptions (Decker et al., 2002; Aureli and Mignosa, 2004; Niemeyer et al., 2005) in form of scenarios. The resulting modelling outcome does not represent the flood hazard since the probability of each particular scenario is not known. The resulting inundation maps rather indicate the flood danger according to the terminology proposed by Merz et al. (2007).

Recently, a number of studies acknowledged in their modelling approaches the considerable impact of flood defence structures on flood hazard statements. Hall et al. (2003, 2005a) subdivided the flood defence structures into discrete sections and considered flood impact zones attributed to these sections.

Assuming the probability of hydraulic load corresponding to a certain return period, the authors computed the probability of any system state conditional upon loading. This probability results from combining the probabilities of individual defence sections states, which may fail or not, under this load. The probability of failure for individual sections is characterised by fragility curves, whose concept is discussed in Sect. 3.3 in more details. Originally applied to overtopping, breaching without overtopping and breaching as a consequence of overtopping (Hall et al., 2003), the methodology was further extended to consider wall instability and piping mechanism in a simplified manner for fluvial structures (Dawson et al., 2005) and shingle beach erosion, rockarmour damage and dune erosion for maritime structures (Dawson and Hall, 2006). In case of a defence failure, the inundation extent and depth are computed either in a simplified form based on statistical depth distribution for events of various magnitude or using a raster-based storage cell model (Sect. 2.2.1). The analysis described above enabled a preliminary large-scale flood risk assessment on whole England and Wales aiming at setting the priorities for resources allocation on political level (Hall et al., 2005a). The methodology was also used to assess possible scenarios in terms of climate change and economical development. However, the methodology is based on a series of assumptions, which simplify the computational procedure, such as:

1. The loading of all defence structures is assumed to be of the same magnitude at the same time. Thus, in case of a dike section failure, the load reduction for other sections due to capping effect is not considered. This assumption allows for an application of a steady-state hydraulic model to represent the load.

2. The response of different defence sections is independent from each other. This allows for an independent consecutive assessment of defense sections.

3. Finally, the resistance within a section is homogeneous, hence, the section responds to the load uniformly.

The first assumption, used by Hall et al. (2003); Dawson et al. (2005), might be suitable for maritime defence structures. However, for fluvial systems, which may have a considerable water retention potential, the capping effect on a flow hydrograph may be significant. Indeed, Apel et al. (2004, 2006) waived this assumption by implementing a dynamic-probabilistic flood risk assessment model with an unsteady hydraulic routing. In this modelling system the probabilistic modules for synthetic hydrograph generation and dike breach are combined with deterministic models for flood routing, stage discharge curves and irregular storage cell inundation in a Monte Carlo simulation. The authors showed for a couple of Rhine dikes a remarkable reduction of failure probability for a downstream dike, when a breach upstream was simulated. Further implications of this retention effect can be observed for an extreme value statistics at the downstream gauges (Apel et al., in press). Whereas the traditional statistically-based flood frequency curves do not account for the retention effect in their extrapolation range, the flood frequency curve, resulting from the dynamic-probabilistic model, shows an intuitively correct asymptotical behaviour.

The approach of Apel et al. (2004, 2006) is, however, limited to only one breach mechanism due to overtopping. Merz (2006) argues that this may be justifiable for modern well-kept dikes, which are less likely to breach due to other mechanisms (Sect.3.2). But for the older historically-grown dikes without drainage the consideration of other breach mechanisms is required. Otherwise the hazard may be underestimated when solely overtopping is considered.

Comprehensive flood risk analysis requires the investigation of uncertainties associated with flood hazard and vulnerability resulting in an uncertainty range for expected damage (Apel et al., 2004). Moreover, Merz et al. (2007) suggest to indicate and map the uncertainties, as far as possible, in order to prevent the unfounded confidence in flood risk maps among the users.

Two types of uncertainty are distinguished: aleatory or natural and epistemic uncertainty. Natural uncertainty is identified by the variability of quantities in space, time or over the population of objects and is inherent to the system. Thus it cannot be reduced. Epistemic uncertainty results from the lack of knowledge about the processes and parameters and can be represented by a range of possible system states given a confidence interval (Merz and Thieken, 2005; Apel et al., 2004; Hall, 2003). The models seek to capture the natural variability of the phenomena. The degree of descriptive power of the model can be characterised by the epistemic uncertainty range, which is reduced by gaining more process knowledge and achieving better parameter estimation. In flood hazard statements it can be difficult to distinguish between natural and epistemic uncertainty. However, the result is worth the attempt, since it would give an insight into uncertainty structure and suggest measures for uncertainty reduction.

For flood hazard maps this implies an indication of the confidence interval for inundation extent and flood intensity indicators. Especially, for extremely rare events the representation of uncertainty is important. Firstly, it represents the potential degree of system variability and the ability of model to capture this range of variation in a mathematical formulation and parameterisation. Secondly, the narrowing of uncertainty bounds can be used as an indicator of model improvement if more data and/or process knowledge are integrated.

The uncertainty can be quantified, for example, using the GLUE framework (Beven and Binley, 1992), which is based on Monte Carlo simulation. At first step the GLUE identifies 'behavioural' parameter sets based on a likelihood measure and constraining observations. The likelihood measure determines the quality of fit between simulated and observed quantities. The 'behavioural' parameter sets, which provide a satisfactory model performance, are then identified based on the subjectively selected threshold value for the likelihood. In the second step, the model realisations with 'behavioural' parameter sets are used in the predictive mode. They provide a set of model outputs weighted by the likelihood values associated with the parameter set and comprise the uncertainty range. This methodology explicitly

acknowledges the fact that the model uncertainty originates not solely from the parameter uncertainty but paramter/model structure combination. It further tries to reduce the uncertainty range by deploying the constraining power of observation data.

However, measurements are rare, particularly for extreme events. Hall and Anderson (2002) recognize this limitation and advocate the use of models clearly describing the cause-effect relationship in a straightforward Monte Carlo analysis, including the expert judgments for parameter probability distribution. The derived band of possible system states directly represents the uncertainty range. Especially for unrepeatable events, like dike failures, the probability or better propensity to failure can be assessed with the help of causal models (Hall, 2003). The credibility of the modelling outcome can be assured by the transparent and utmost comprehensive description of the causal relationships between various modelled processes.

## 2.6 Framing of modelling approach

The development of the modelling approach faces a main methodical challenge in providing the solution to the discussed questions under limited computational resources. Summarising the discussion on flood hazard studies, it seems that for fluvial systems protected by dikes the hydraulic load should be dynamically modelled in order to approach plausible hazard assessment results. Especially for lowland rivers with high retention potential, the impact of upstream breaches on hazard downstream may be considerable. An adaptation of a 1D full dynamic model for the river channel and floodplain between dikes seems to deliver sound prediction of water stages in reasonable CPU times. In a fully one-dimensional representation of the channel flow the inertial terms that become more important for deeper flows (Bradbrook et al., 2005) are included (Eq. 2.2) contrary to the kinematic and diffusive wave equations.

To provide dynamic predictions of flood intensity indicators, such as flow velocity, the product of flow velocity and depth as well as the rate of water rise, the dynamic model was selected to simulate the water spread in the hinterland. This approach directly delivers the flood hazard indicators, contrary to the basic volume filling algorithm based on stage-volume functions. To compute the primarily two dimensional flow on a flat hinterland area in case of dike breach outflow, a regular storage cell approach seems to suffice in terms of accuracy and performance. For the floodplain flow, the 2D storage cell model with decoupled treatment of flow components and flow limiter formulation seems to offer an appropriate compromise between the compuational costs and predictive accuracy, when using the moderate time step of $2 - 5$ seconds.

An approach of connecting a 1D channel representation with a 2D raster-based floodplain model using weir-type links is proposed in this study. Although the combined full 1D-storage cell modelling solution seems to offer an acceptable compromise between the degree of process representation and computational effort, it has been explored only in a limited number of studies (Bechteler et al., 1994; Bláde et al., 1994; Han et al., 1998). Especially for dike stability consideration, where precise estimations of water level in a river channel are crucial, a combined one- and two-dimensional modelling approach is required.

The proposed coupled approach is adapted to a diked river reach and enhanced by probabilistic dike breach modelling. The significance of breach mechanisms for dikes under consideration is analysed. The relevant mechanisms are taken into account by formulating and parameterising corresponding reliability models. Imbedding the sketched model in a Monte Carlo framework enables the analysis of uncertainties claimed in the flood hazard and risk assessment. This philosophy was adopted for the development of the inundation hazard assessment model (IHAM) described in more details in the following Chapter 3.

# Chapter 3

# Inundation hazard assessment model (IHAM)

## 3.1 Model structure

The inundation hazard assessment model (IHAM) is comprised of three main modules representing the core of the system. These modules are an unsteady 1D hydrodynamic model for river channel flood routing, probabilistic dike breach model and 2D raster-based inundation model. The modules are coupled at runtime that ensures a continuous data exchange between modules during the simulation course. The mechanisms of coupling are discussed in Sect. 3.1.4 in more details. The core of the modelling system is run in a Monte Carlo framework, referred here as the core Monte Carlo simulation, to address the uncertainty, resulting from the stochastic processes of dike breaches and natural variability of flood generation processes expressed in various flood wave forms. The IHAM structure is schematically illustrated in Figure 3.1 and consists, besides the modelling system core, of pre- and post-processing blocks.

### 3.1.1 1D hydrodynamic module

For the hydrodynamic simulation of the flood wave propagation in a river channel and floodplain between dikes, an unsteady 1D hydrodynamic model based on the full St.-Venant equation was used. The EPDRiv1h hydrodynamic code (USACE, 1995; Clayton Eng., 2003), which uses the four-point implicit numerical solution scheme, was integrated into the IHAM system. The model is run in unsteady simulation mode and delivers predictions of discharge and water stages at every discretised river node, based on the conveyance description. The conveyance is given by the measured cross-sections and estimated or calibrated Manning's roughness values. The model is driven by the inflow hydrograph at the upstream end of the river reach and uses a rating curve as outflow boundary condition. The available FORTRAN source code of the EPDRiv1h model was coupled to the dike breach and 2D hydrodynamic modules to supply hydraulic state variable at runtime, as discussed in Sect. 3.1.4.

### 3.1.2 Dike breach module

The dike breach module represents a probabilistic model aimed at the simulation of dike failures along the river course. It models breach locations, breach development and outflow discharge for three breach mechanisms: overtopping, piping and micro-instability reviewed in Sect. 3.3. The stability of dike sections is assessed in probabilistic terms based on fragility functions which are discussed later in this section.

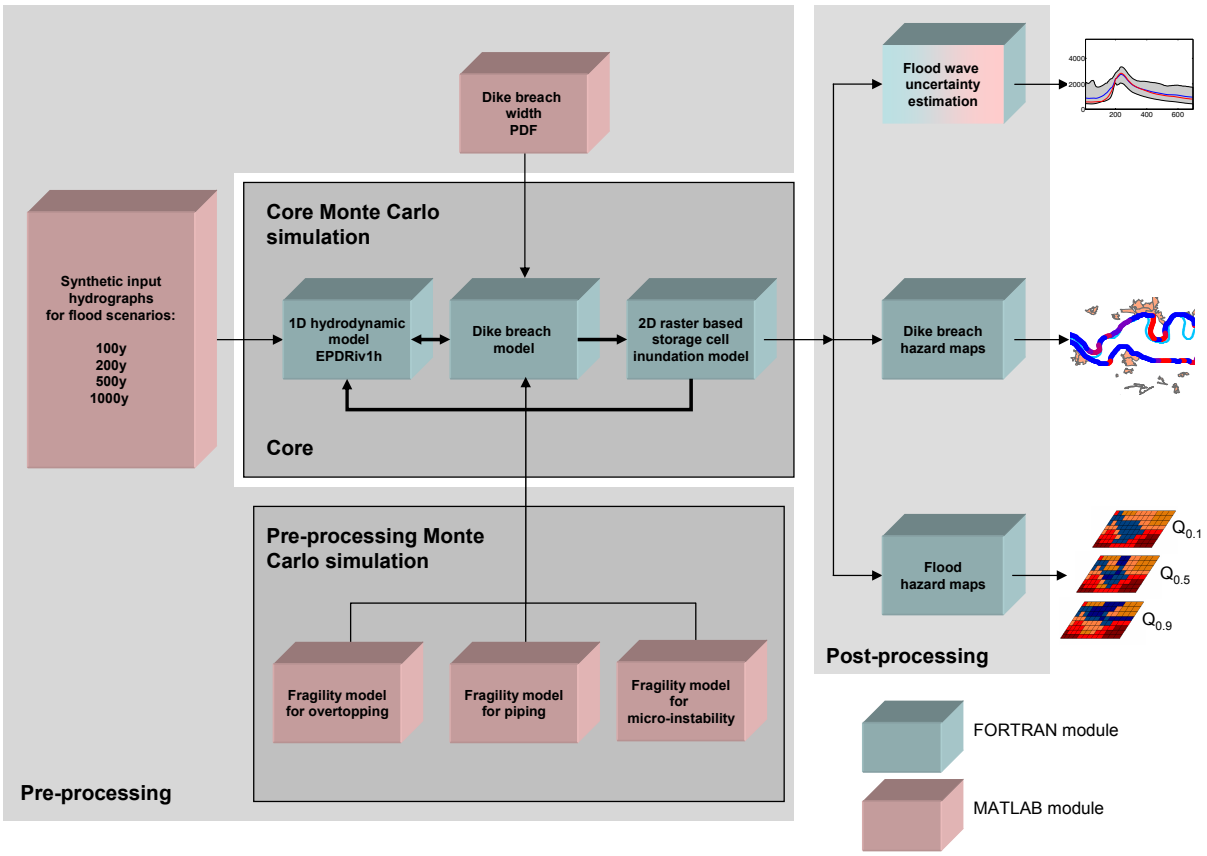


**Figure 3.1:** *Schematic representation of the IHAM structure.*

Dike stretches should be discretised into sections of a certain length. The length is selected in a way that the dike sections are independent in terms of their response to hydraulic load, i.e. they react differently upon loading and breach as a consequence of different mechanisms. Dependence is characterised by the correlation of dike properties which determine the resistance to failure. The correlation tends to zero for samples at a certain distance referred as correlation length. CUR/TAW (1990) suggests that the correlation length for dikes is about $300 - 500\ m$, so the dike sections of this length can be regarded as independent. This assumption has been adopted by Hall et al. (2003) for dikes in England and Wales. Vrijling and van Gelder (1998) suggest that correlation length may be in the order of 30 to 100 $m$. However, this cannot be proved so far, since soil properties of dikes are sampled with a step of about $500\ m$. A more intensive dike structure investigation may deliver a spatially dense dataset, which could elucidate the true correlations of dike properties. Such a measurement campaign is being currently carried out for all Saxonian dikes (U. Müller, Saxonian Dam Authority, personal communication).

The failure probability of each dike section due to overtopping, piping and slope micro-instability (Sect. 3.2) is described by fragility functions. They represent the probability of section failure given the hydraulic load simulated by the 1D hydrodynamic module. For each particular failure mode, a separate fragility function should be developed. For complex failure mechanisms, such as piping and micro-instability, which are comprised of several failure modes, the separate fragility functions are combined in a probabilistic framework describing dependent events.

Traditionally applied in system reliability research, particularly in earthquake research to describe the failure probability of engineering structures as a function of peak ground acceleration (e.g. Shinozuka et al., 2000; Bhargava et al., 2002; Kim and Shinozuka, 2004), fragility functions were recently adopted

for flood hazard and risk assessment. However, the number of applications is limited to a few studies, briefly outlined here. Apel et al. (2004, 2006) developed 2D fragility surfaces for dike overtopping based on the reliability function (Eq. 3.1) and applied them in a dynamic unsteady flood risk analysis. Sayers et al. (2002) introduced the fragility curve concept for a steady large scale risk assessment based on the classification of flood defence structures and expert judgements about their failure probability. Fragility functions for fluvial dikes were developed by Hall et al. (2003) and Dawson et al. (2005) for a number of failure modes described by simplified reliability functions. Further, Dawson and Hall (2006) extended the approach for maritime structures and their major failure mechanisms.

Fragility functions can generally be n-dimensional depending on the number of load variables. They are defined on the interval $[0; 1]$. For development of fragility functions, each load variable is discretised within a range of feasible values. Each tuple of load variables represents a point in the n-dimensional space, for which the probability of dike section failure is computed. The failure probability at each point in a load space is assessed by performing a Monte Carlo simulation with the so-called limit state function or reliability function formulated for each particular failure type. This function represents a critical relation between the load and resistance variables and can be expressed in a general form in Eq. 3.1:

$$Z = R - L \tag{3.1}$$

where $R$ - resistance and $L$ - load.
For a combination of $R_i$ and $L_i$ yielding $Z_i > 0$ no failure occurs. Failure is considered for $Z_i \leq 0$. Uncertain dike state variables $r_1, r_2, ...r_n$, representing geometrical and physical properties that contribute to dike resistance are randomised in Monte Carlo simulation. The resulting probability of failure is defined at each point of the load space as a ratio between the number of negative limit state function outcomes and total number of Monte Carlo runs:

$$P_{failure} = N(Z(r_1, r_2, ... r_n) \leq 0)/N(MC\ runs) \tag{3.2}$$

The result of the Monte Carlo simulation is a fragility function defined at every discretised point of the load space. In the IHAM structure, the MC simulation for development of the fragility functions is referred as the pre-processing Monte Carlo simulation (Figure 3.1). IHAM utilises fragility functions for overtopping, piping and micro-instability, which are developed in the pre-processing step by formulating, parameterising and applying respective reliability models (Sect. 3.3.1-3.3.3).

Since failure probabilities are defined at discrete points of the load space, linear interpolation procedures for 2D, 3D and 4D spaces were developed based on Press et al. (1992), in order to provide the probability values at any point other than discretised. These algorithms are also used for extrapolation, in case the load exceeds the range, for which the fragility function was computed.

In case failure of a dike section occurs, the ultimate breach width is stochastically simulated based on the defined probability distribution function (Sect. 4.4.5).

The outflow discharge through the breach is computed using the broad-crested weir formula (Chow, 1959). The model switches automatically between the free and drowned weir overfall depending on the water level in the river channel and hinterland.

### 3.1.3 2D hydrodynamic module

The flood propagation over a flat hinterland area in case of a dike breach is simulated using the 2D raster-based diffusive wave model originally developed by Merz (1996) and further enhanced by H. Apel (GeoForschungsZentrum Potsdam, personal communication). The model is driven by the discharge input calculated in the dike breach module for all breach locations. The wetting and drying front propagation is simulated over the topography described by the digital elevation model. It should be noted, that the

2D inundation simulation is carried out exclusively in the hinterland areas in case of dike breaches. The floodplain between dikes is assumed to be completely flooded, which is justified for events of high magnitudes with the return period exceeding 100 years ($T \geq 100$).

The available FORTRAN storage cell code was enhanced by implementing the free outflow boundary condition on the borders of the modelling domain. At any time step, water depth in the cell beyond the boundary is assumed to be equal to the depth at the neighbouring cell inside the domain. Hence, the water flux across the boundary is computed assuming the free water surface slope is equal to the bed slope. The same boundary formulation is used in comparable storage cell codes such as LISFLOOD-FP and JFLOW (Bradbrook et al., 2004).

Because of considerable simplifications of the governing equations, it was restrained, so far, from computing the flow velocities with the storage cell codes. Furthermore, for the course grid, the average velocity estimations may deviate vastly from those determined by local terrain features. Nevertheless, the model was extended to calculate the preliminary average velocity fields from the uncoupled fluxes in $x$ and $y$ directions according to Eq. 3.3:

$$v^{i,j} = \sqrt{\left(\frac{Q_x^{i,j}}{h_{flow,x}^{i,j} \cdot \Delta x}\right)^2 + \left(\frac{Q_y^{i,j}}{h_{flow,y}^{i,j} \cdot \Delta y}\right)^2} \tag{3.3}$$

where $v^{i,j}$ - flow velocity for the $i, j$ cell $[m\ s^{-1}]$; $Q_x^{i,j}$ and $Q_y^{i,j}$ are the fluxes over the cell boundaries in $x$ and $y$ directions computed in Eq. 2.11.

Errors in the velocity estimations can be assessed by means of comparison with results of a full 2D hydrodynamic model that uses the same discretisation.

For each storage or raster cell in the modelling domain the product of the water depth and flow velocity can be computed. The resulting value, referred as impulse (Alkema and Middelkoop, 2005), is considered to be an important flood intensity indicator, especially for human instability in flood situations (Merz et al., 2007). This intensity indicator gains significance in recent flood hazard and risk assessment studies on a state scale (LfUG, 2005).

The model was further enabled to compute the inundation duration for water levels over depth thresholds of $0.2$ and $0.5\ m$. Inundation duration is an important damage factor for ecosystems and farmland (Merz et al., 2007). Moreover, in industrially used areas it determines, among others, the interruption time in the production process and services and, hence, leads to indirect economic losses. The selected threshold values are relevant for the determination of agricultural damages and were suggested for use with the agricultural damage model being developed in the MEDIS project (MEDIS, 2007).

The average rate of water rise is acknowledged as the relevant flood intensity indicator for estimating the time left for flood protection and evacuation measures. The rate of water rise in a storage cell may vary dramatically for different points in time over the duration of a flood event. For instance, directly after the dike breach it can be very high, while after a certain topographically constrained volume is filled, it may drop significantly. Therefore, computation of an average rate of water rise over a large time period may not be meaningful and may represent a rather optimistic estimate. On the other hand, the average rate of water rise determined over a short time period may not be representative for the whole inundation event. For preliminary computation, a time step of one hour was selected. The resulting hazard maps thus indicate the maximum rate of water rise within one hour over the whole simulated event.

### 3.1.4 Coupling of core modelling components

The 1D hydrodynamic, dike breach and inundation modules are interactively coupled at runtime in order to correctly reflect the process chain of reach scale inundation. Besides the schematic representation

of the coupled approach in Figure 3.1, an explanation of the data flow as well as spatial and temporal iteration procedures is illustrated in Figure 3.2.

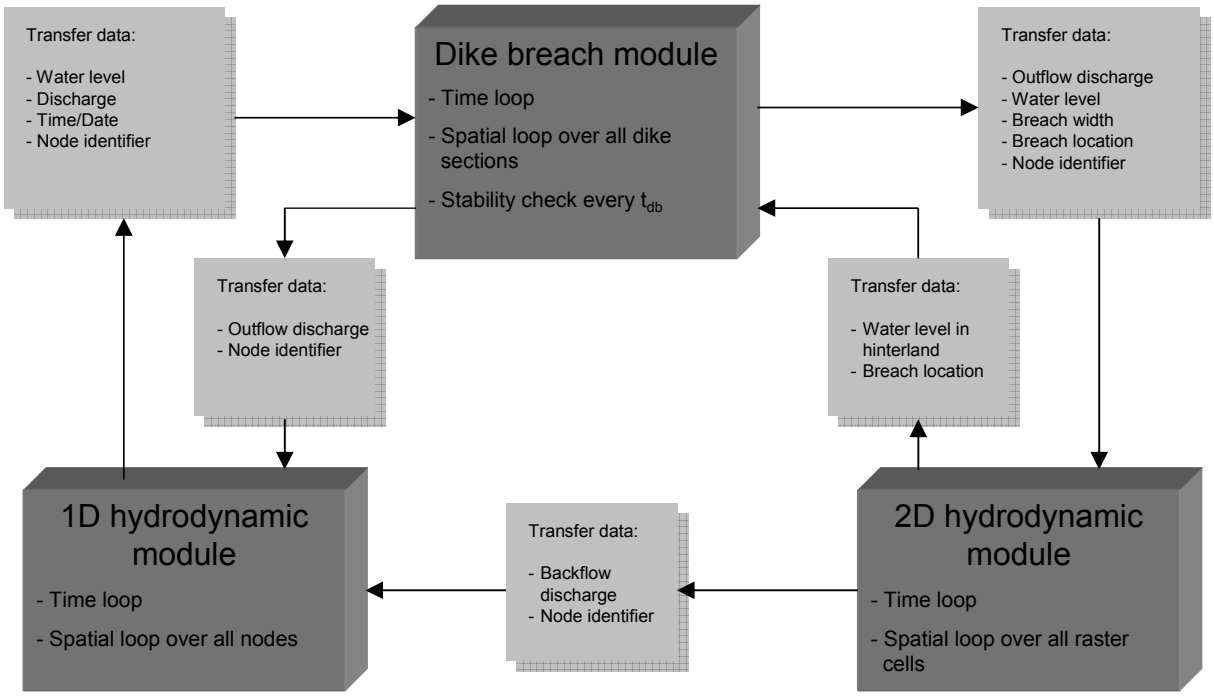


**Figure 3.2:** *Schematic representation of the coupling approach in IHAM: data flow chart and transfer packages.*

An efficient data transfer between models at runtime was realised with help of the Typed Data Transfer (TDT) Library (Linstead, 2005), which provides a series of interfaces for platform and language independent transfer of typed data. Other available methods for model coupling, such as CORBA, MpCCI (MpCCI, 2007) and OpenMI (Gregersen et al., 2007) provide comprehensive solutions for handling data transfer, spatial and temporal interpolation but appear to be complex and require significant investments of time for their implementation. Contrary, TDT provides a sufficiently simple and flexible solution, which was found to be appropriate for the coupling task in this work. However, TDT has one limiting feature, which is a need for an intervention into the source code in order to integrate the data transfer interfaces. This requires that the modelling code is available and implies the code understanding by the modeller. The other mentioned coupling approaches are capable of utilising the open APIs (Application Programming Interface), and therefore can couple also the proprietary modelling codes.

All three constituting models are run with the same time step $t$ at which the data exchange takes place. The modelling time step is specified by the user in the setup file. Time steps not greater than several seconds are recommended in order not to jeopardise simulation accuracy of the 2D inundation model (Sect. 2.2.1). Additionally, a nested time loop in the dike breach module is initiated that checks dike section stability every time step $t_{db}$. The time step selection is subjective. $t_{db}$ should be large enough to keep the computation tractable. On the other side, it must be small enough to represent the process dynamics correctly. This implies that the $t_{db}$ is selected in a way that the change in failure probability between two stability checks is not too large. Otherwise, the dike failures would be simulated with a considerable time lag, introducing a distortion into modelling results. Tentatively $t_{db}$ was set to $1\ h$ and can be changed by the modeller. The sensitivity analysis for the time step $t_{db}$ would elucidate an effect on modelling results and should be carried out in the future.

Water levels computed by the channel model on all spatial nodes at each time iteration are commu-

nicated to the dike breach module. All the transferred values are identified by the corresponding 1D model node identifier (Figure 3.2). The spatial loop over all discretised dike sections is executed every temporal iteration $t$ in order to update the boundary conditions at already simulated breach locations and conduct dike stability checks every $t_{db}$ time step. Stability of each discretised dike section is successively checked for three considered breach mechanisms. Contrary to Dawson et al. (2005), who identified a primary breach mechanism for each dike section and used respective fragility curve in the analysis, several breach mechanisms are considered here for each dike section independently from each other. Depending on the dynamically changing load, one or another mechanism may trigger the failure for the same dike section. Complex interactions between failure modes were not considered in the IHAM on the river reach scale, such as, for example, intensified phreatic line development inside a dike core as a consequence of water percolation due to overtopping.

Probability of dike breach is read from the developed fragility functions depending on the currently simulated load in terms of water level and duration of overtopping and impoundment. This probability is compared to a randomly generated number in the range $[0; 1]$. If the random number exceeds the sampled probability, the failure is simulated. The breach growth is initiated and gradually progresses within a defined time period till the full breach development is accomplished. Discharge through the breach computed with the weir-type equation is, firstly, subtracted from the channel discharge at the corresponding node as lateral outflow. Secondly, it is supplied as boundary condition for the inundation model and distributed over the interface raster cells in the hinterland.

The interface cells are defined on the DEM at runtime for each simulated breach location. The number of interface cells ($N_{ic}$) is defined at each time iteration, based on the current breach width and pixel size, according to the rule given in Eq. 3.4.

$$N_{ic} = \begin{cases} 1 & \text{if } B_w(t) < \Delta x; \\ int(B_w(t)/\Delta x) & \text{if } B_w(t) \geq \Delta x \quad \text{and} \quad mod(B_w(t), \Delta x) < \Delta x/2; \\ int(B_w(t)/\Delta x) + 1 & \text{if } B_w(t) \geq \Delta x \quad \text{and} \quad mod(B_w(t), \Delta x) \geq \Delta x/2. \end{cases} \tag{3.4}$$

where $B_w(t)$ – breach width $[m]$ at time $t$.

The water spread in the hinterland is computed with the 2D storage cell model. The 1D-2D model coupling using the weir-type links, obviously, neglects the momentum transfer into the hinterland. Only mass transfer is accounted for in this case. The momentum transfer is expected to play an important role for inundation dynamics in the first hours after the breach. Later, the water volume becomes more decisive in shaping the inundation extent and depth, as a case study of Aureli et al. (2005) also demonstrates.

As soon as the water level in the hinterland (average water level in the interface cells) overshoots the water level in the corresponding 1D model node, the backwater discharge through the developed breach is calculated and supplied as lateral inflow to the 1D channel model. The back coupling between the inundation and channel flow models (Figure 3.2) insures the true representation of system dynamics in case of filled hinterland areas.

Here it should be noted that the IHAM neither simulates the water flow over dikes in direction of the hinterland, nor backward in direction of the river channel. Thus, the overtopping discharge over non-breached dikes remains unconsidered. It is expected that dikes fail already after several hours of overtopping. This is suggested by a high sensitivity of the overtopping failure probability to the overtopping duration as indicated by steep fragility surfaces (Sect. 4.4.2). Therefore unconsidered overtopping discharge is assumed to be negligible. The cases of durably overtopped but stable dikes known to occur in reality are poorly understood and can hardly be considered on the reach scale.

The IHAM core components (Figure 3.1) implemented in FORTRAN were coupled and compiled on a Linux cluster comprised of more than $500$ processors. The Portland FORTRAN compiler was used to compile the code. The cluster environment provides the capacity to run the core Monte Carlo simulation,

with each Monte Carlo run initiated on a separate node processor. This facilitates the execution of a relatively large number of runs with the computationally intensive IHAM model.

### 3.1.5 Input data and pre-processing

Each module of the IHAM is supplied with input data provided as plain ASCII files. This section dwells upon some issues concerning the input data preparation, particularly, dike data.

#### Input hydrographs

IHAM is driven by a set of hydrograph scenarios corresponding to defined return periods (Figure 3.1). The model can be provided either with historical or synthetic hydrographs at the upstream 1D model node and tributaries. Development of the scenario sets is accomplished prior to the event modelling. In this thesis, synthetic input hydrographs for return periods of $T = 100, 200, 500, 1000$ years were derived according to the methodology presented in Sect. 4.6.

#### Dike breach model input

The dike breach model requires a series of input data for successful model initialisation.

- Two lists, containing dike kilometre values, are supplied for each dike side. Dike kilometre corresponds to the kilometre value of the nearest node in the river channel. Every dike section is assigned such a value, whereas several sections may have the same concordance.

  In civil engineering, the river kilometre is traditionally assigned to the dike points by constructing an orthogonal line to the flow direction in the river node. The intersection point of this line and dike stretch obtains the river node chainage (Jankiewicz et al., 2005). This methodology has, however, a significant drawback, when considered for modelling with IHAM. It becomes pronounced for the reaches which exhibit strong meandering behaviour. The orthogonal line to the flow direction might intersect the dike stretch, in this case, several kilometres upstream or downstream of the river node. Thus, the true hydraulic load in terms of water level could be significantly over- or underestimated, when compared to the dike crest height. Therefore, an alternative approach to dike chainage is suggested in this work. The dike points are assigned the kilometre value of the nearest node in the river channel. The correspondence is established using the developed DikeTOPO software tool. DikeTOPO is a VisualBasic program embedded in the ArcGIS environment that processes ESRI point shape files of dike locations and river channel. DikeTOPO is used for splitting the dike point shape file into sections of predefined length, computing mean and variance of the dike properties for each section stored in the attribute table and, finally, determining the chainage for each section.

- Two ESRI ASCII raster data sets should be provided for left- and right-side dikes containing dike kilometre. The dike kilometre rasters are used for the localisation of breached dike sections in the geographical space. At these locations the boundary condition in terms of outflow discharge is provided to the 2D inundation model.

- Fragility functions for each breach mechanism are provided in ASCII format for every discretised dike section. The implemented fragility models are discussed in Sect. 3.3 in more details. The software modules were developed in MATLAB (Figure 3.1). The environment was selected because it provides efficient tools to process vector/matrix-type variables and to handle probability

distribution functions. The provided graphical output of fragility functions was found to be essential in checking the plausibility of the obtained results. The fragility input files contain the average height of dike section in $[m\ asl]$ used for computation of dike overtopping and outflow discharge.

- Parameters of the probability density function, which is used for stochastic generation of the ultimate breach width during the core Monte Carlo simulation. The approach is framed in Sect. 3.3.4. In the application study, the probability density function for Elbe dikes was derived based on the observed breach widths in the Elbe catchment during the August 2002 flood (Sect. 4.4.5).

#### Inundation model input

The inundation model requires two ESRI ASCII raster data sets as input data. The first one is the DEM of modelling domain used for raster-based flow computation. Additionally, either an uniform roughness value or raster of the spatially distributed friction coefficients is required for the hinterland.

### 3.1.6 Post-processing

The IHAM modules produce ASCII output files that can be evaluated using the developed post-processing routines (Figure 3.1). The post-processing routines were implemented in FORTRAN and face a challenge in processing considerable amount of output data in the tenth of gigabytes range. The final visualisation is accomplished in the MATLAB environment for the 1D model output. To display the spatially referenced output of the dike breach and inundation models, a GIS environment can be used.

#### Flood wave uncertainty estimation

The output file of the 1D hydrodynamic module represents a table, which contains water level, discharge, flow velocity and water depth at every model node and output time. The output time is specified by the modeller in the hydrodynamic input file. Each Monte Carlo run produces a separate output file. The post-processing routine for the flood wave uncertainty estimation computes mean, median and uncertainty bounds, corresponding to the modeller-defined quantiles, for output quantities at any specified cross-section.

#### Dike breach hazard maps

The output ASCII files from the dike breach module contain the list of breached dike sections, failure time and responsible breach mechanisms for each Monte Carlo run. The files are evaluated by the post-processing routine in order to compute an average failure probability of any dike section due to all considered breach mechanisms. The final output table contains relative failure frequencies for every dike section. It can be easily joined with the spatially referenced point shape files representing geographical locations of dikes. The failure probabilities are finally visualised in a GIS environment to produce the dike breach hazard map indicated schematically in Figure 3.1.

#### Flood hazard maps

The 2D inundation model produces output ASCII rasters of maximum water depth, flow velocity, impulse, inundation duration with water level over defined threshold values and rate of water rise for each Monte Carlo run. The post-processing routine evaluates the output rasters for all flood intensity indicators. Derived probabilistic flood hazard maps display the median of intensity indicators corresponding to $0.5$-quantile map $Q_{0.5}$ (Figure 3.1) and associated uncertainty bounds for each pixel. The latter are illustrated by the quantile maps, which indicate the values of intensity indicators corresponding to the

modeller-defined quantiles, e.g. $0.1$ ($Q_{0.1}$) and $0.9$ ($Q_{0.9}$). Additionally, a raster indicating the standard deviation is computed for each intensity indicator. It represents a measure for spread of values for every pixel. Finally, a binary pattern map, which shows the probability of every pixel being inundated, is computed.

## 3.2 Overview of dike breach mechanisms

Dikes may fail as a consequence of various breach mechanisms and their combinations. Kortenhaus and Oumeraci (2002) provide a detailed description of about twenty breach triggering processes. Distinction between these processes is often difficult in practice. Modelling of many breach mechanisms may easily end up in a computationally intractable problem with high number of uncertain parameters. Therefore, for the purpose of a reach-scale modelling, a clustering of breach mechanisms is required. Armbruster-Veneti (1999) distinguishes, for instance, between the following groups of failure mechanisms:

- **Hydraulic failure**
  Under hydraulic failure, dike collapse as a result of overtopping and wave scour is understood. Overtopping occurs as a consequence of water level exceeding the crest height or wave swashing. The surface erosion of the landward slope can then be initiated if the shear stress induced by the overtopping flow exceeds the critical shear stress of the dike material. The progressive erosion may lead to a breach development and total dike collapse. The wave scouring induces erosion of the dike material on water side that may result in an outer slope failure.

- **Geohydraulic failure**
  Seepage flow through a dike core or dike foundation may initiate erosion processes and transport of material. Progressing material relocation from the slope leads to the inner slope failure. CUR/TAW (1990) and Vrijling (2001) denote the geohydraulic failure of inner slope as micro-instability. In the dike foundation, the erosion processes result in a formation of pipes that lead to a sagging of the dike core with subsequent overtopping, slope failure and collapse. This particular failure mode is referred as piping (CUR/TAW, 1990; Vrijling, 2001).

- **Global static failure**
  In this case, dike collapse is triggered by the pressure forces of water and ice, wind and waves as well as own weight that exceed dike resistance. Additionally, the progress of a phreatic surface in a dike core and dike foundation as well as the increase of moisture content due to precipitation dynamically influence the shearing resistance of dike material. The collapse usually occurs in the form of core sliding, slope failure (inner or outer) following a slip circle with or without foundation sagging. The static slope failure as a consequence of gravity and pressure forces is denoted as macro-instability (CUR/TAW, 1990; Vrijling, 2001).

The hydraulic, geohydraulic and static failure mechanisms are presented in a simplified fault tree and further discussed in Sect. 3.2.2.

There is a number of further possible breach mechanisms such as:

- deliberate destruction also referred as man-induced failure,
- destruction of a dike by debris flow,
- failure at dike crossing hydraulic structures, e.g. gated sluice, culverts etc.

These failure mechanisms occur seldom as indicated by the breach statistics in Sect. 3.2.1. Nevertheless, they are discussed in the fault tree analysis in Sect. 3.2.2.

### 3.2.1 Dike breach statistics

Records of extreme events such as dike breaches are very rare. During flood events the resources are rather allocated in favour of damage mitigation than for monitoring and analysis of breaches. Thus the reconstruction of breaching processes based on the post-event field observations and witness interview is often difficult. For historical events, only the archive records represent a source of information. Nevertheless, the analysis of 1266 historical dike breaches in Hungary was carried out in the EU-IMPACT Project (Nagy and Tóth, 2005). An overview of the distribution of responsible breach mechanisms is given in Figure 3.3.

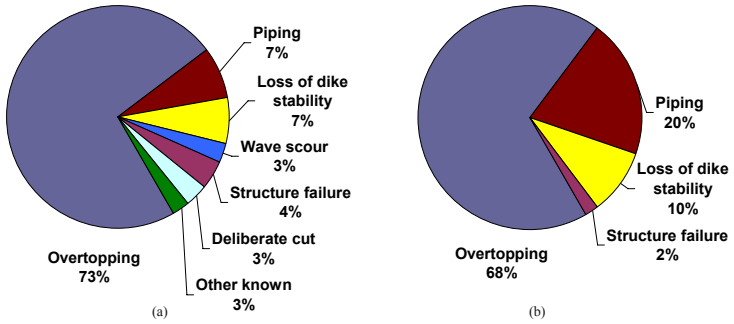


**Figure 3.3:** *(a) Distribution of identified failure mechanisms for dike breaches in Hungary in the period 1802-2004. The analysis is based on the* 506 *dike breaches out of* 1266 *for which the breach mechanism could be identified. (b) Distribution of failure mechanisms for dike breaches in Hungary in the period 1954-2004. The analysis is based on* 105 *identified mechanisms out of* 117 *recorded breaches. Source: Nagy and Tóth (2005).*

It can be concluded from this analysis that from the identified breach mechanisms, $87\%$ are attributed to overtopping, piping and loss of dike slope stability (Figure 3.3(a)). Remarkably, the proportion of breaches due to overtopping has reduced in favour of piping and slope instability over the last fifty years (Figure 3.3(b)). This effect is likely due to the continuous increase of dike crest height. These three breach mechanisms are responsible for $98\%$ of all identified breaches in Hungary in the last 50 years. Although the statistics is based on rather old and uncertain data (T. Heyer, TU Dresden, personal communication), it can be used as an indicator of prevailing failure modes. The results of the analysis of Hungarian dikes are further supported by recent observations in the Elbe catchment.

The analysis of responsible breach mechanisms in Saxony during the August 2002 flood by Horlacher et al. (2005) is based on $84$ identified dike failures (Figure 3.4). Although the definition of breach mechanisms included in the statistics of Horlacher et al. (2005) is slightly different from Nagy and Tóth (2005), one can expect that for the Elbe catchment dike overtopping, piping as well as slope stability are the primary failure modes. Gui et al. (1998) also indicates that overtopping and piping are major failure mechanisms based on the study of Cheng (1993), which summarises dam failure statistics. The pathways of dike failure due to these mechanisms are further elucidated in a fault tree analysis (Sect. 3.2.2).

### 3.2.2 Fault tree

A fault tree is a particular case of a logical tree. It represents the pathways leading to a final negative consequence (e.g. dike failure) (Merz, 2006; Pohl, 2000b). This consequence can be initiated by either of the failure modes which is reflected by the 'OR' operator or gate. The vertical linkage corresponds to the 'AND' operator and implies a consecutive occurrence of the events leading to a negative consequence.

Dike failure can be a result of various triggering mechanisms (Sect. 3.2), which are presented in

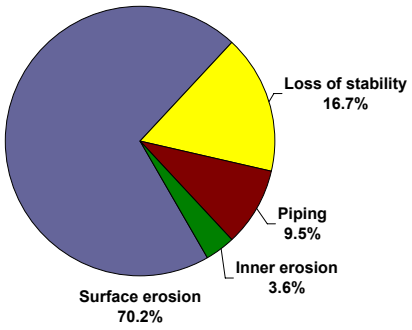


**Figure 3.4:** *Distribution of identified failure mechanisms for dike breaches in Saxony during the August 2002 flood event. The analysis is based on* 84 *observed breach locations. Source: Horlacher et al. (2005).*

Figure 3.5 as a fault tree based on the definitions of breach mechanisms according to Armbruster-Veneti (1999) and CUR/TAW (1990), and adopting the analysis of Zesch et al. (2007).

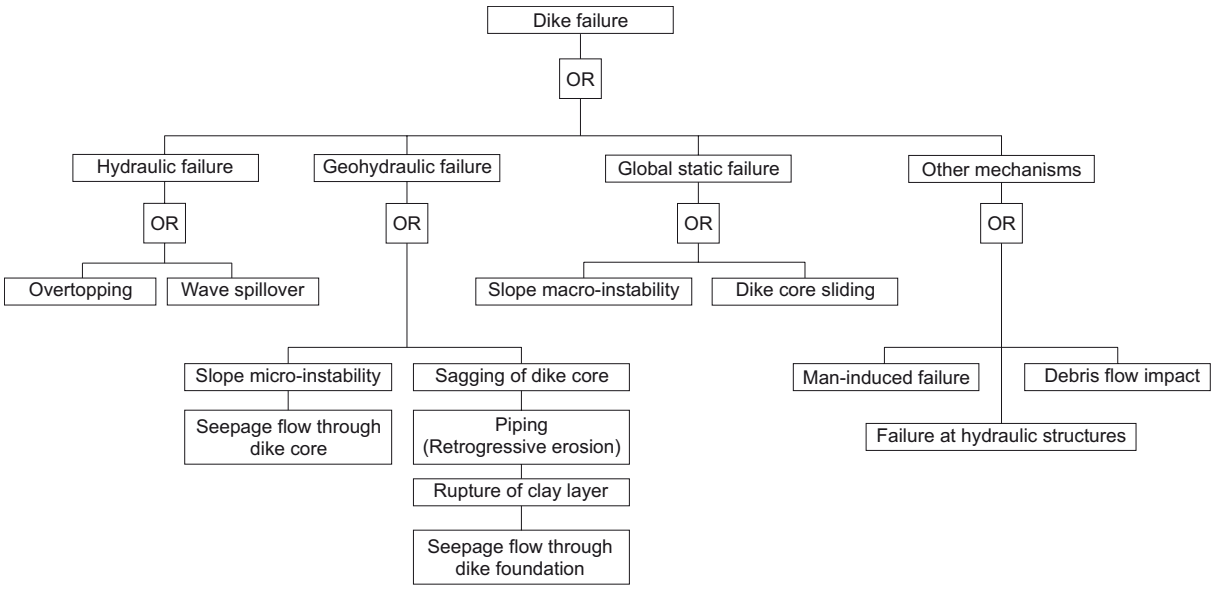


**Figure 3.5:** *Fault tree for a dike failure based on analysis of Armbruster-Veneti (1999); CUR/TAW (1990); Zesch et al. (2007).*

The fault tree is aimed at representing the utmost comprehensive set of pathways leading to a failure. However, for modelling it is required to keep balance between the degree of process description and efficient model handling (Merz, 2006). Therefore only the relevant breach mechanisms have to be selected, focusing on the trade-off between process complexity and computational effort.

Based on the dike breach statistics (Sect. 3.2.1), overtopping seems to be the most prevalent breach mechanism and obviously deserves detailed consideration. It seems that in the fluvial environment the wave spillover is not that significant as at the sea coast. Taking into account the uncertainties in water stage modelling (Sect. 4.3.1), it seems that the wave spillover does not merit a special consideration.

Rupture of a low-permeability layer induces a continuous water flux through a sandy dike foundation resulting in piping described in details in Sect. 3.3.2. This mechanism is responsible for a considerable portion of dike failures in Germany (Figure 3.4) and Hungary (Figure 3.3) with increasing frequency

over time. In some parts of the Netherlands this mechanism appears to be dominant for the majority of dikes (Van et al., 2005).

As shown in the fault tree (Figure 3.5), the erosion of dike foundation results in sagging of the dike core. Yet, this does not necessarily imply immediate dike collapse. The core sagging can further lead to the overtopping or global static failure. These complex interactions, however, are poorly understood and lack sufficient observational and experimental evidence. Nevertheless, recent research attemted to formalise such interactions in a complex model proposed by Van et al. (2005) to describe the global static slope failure induced by rupture.

In case of dike sagging, Zesch et al. (2007) assumed, for example, a complete freeboard loss of $1\ m$. This freeboard is prescribed by legislation for river dikes in Germany. However, the reviewed literature provided no experimental evidence or theoretical derivation for the depth range of pipes and resulting subsidence.

Therefore a rather conservative approach adopted in this work assumes a complete dike failure in case the piping has progressed to a critical length (Sect. 3.3.2). This approach neglects the core subsidence or slope failure and seems to be appropriate in the absence of sufficient reliable information. It has been used by Kortenhaus and Oumeraci (2002) and Dawson and Hall (2006) for assessment of the stability of sea dikes as well as implemented in the PC-Ring Software (Steenbergen and Vrouwenvelder, 2003; Lassing and Vrouwenvelder, 2003) developed for the reliability assessment of river dikes in the Netherlands.

Inner slope failure can occur either due to micro-instability or macro-instability. Both mechanisms together may be responsible for about $17\%$ of all dike breaches (Figure 3.4). This figure can naturally vary depending on the dike structure and type of load. The share of slope failure between both mechanisms is largely unknown. The presence of seepage flow on a landward slope can, for instance, be used as possible indicator in favour of micro-instability, although without any assurance. Whereas the seepage flow can be efficiently controlled by drains or isolation materials in modern dikes, for historically grown dikes it remains an issue. Thus micro-instability deserves attention in the context of modelling Elbe dike breaches (Sect. 3.3.3), despite the fact that this is a much more local phenomenon compared to macro-instability.

Slope macro-instability occurs along a large failure surface if the overturning moment induced by gravity and pressure forces acting upon a mass of soil exceeds the resisting moment striving to prevent sliding. The resisting moment is induced by the shearing resistance forces acting along the potential failure surface (CUR/TAW, 1990). Investigations of slope macro-instability are usually carried out by looking for a slip circle with the lowest stability factor by trial and error procedure, using e.g. the method of Bishop (1955). A number of commercial software packages are available, e.g. MPROSTAB, GGU-STABILITY, etc., for stability factor calculation. This factor is determined by a large number of uncertain variables, among others, by pore water pressure and soil cohesion, which contribute at most to the variance of the stability factor (CUR/TAW, 1990). Particularly, pore water pressure is a dynamic quantity, which depends on the seepage front propagation and net rainfall input.

For river dikes, the impact of the phreatic surface on slope stability is of utmost importance. The pore water pressure directly depends on the soil moisture content in a dike core, which is influenced by wetting front propagation. Macro-instability investigations are usually carried out for individual selected dike sections (e.g. Pohl, 1999, 2000a). On a reach scale such investigations require considerable effort in terms of data acquisition, model discretisation and computation. Therefore macro-instability was, at least currently, not considered in the framework of the Monte Carlo based IHAM model. It certainly merits consideration in the future, especially for cohesive clay dikes.

Breach mechanisms listed in the fourth category 'Other breach mechanisms' are partly difficult to formalise. The assignment of a probability of occurrence may also be complicated because of a small number of evidences. Moreover, evidence statistics (Sect. 3.2.1) indicate that these mechanisms contribute marginally to the total number of observed breaches and therefore are not further discussed here.

Hence, overtopping, piping and slope micro-instability are further considered in the IHAM modelling system. These mechanisms are described in detail in Sect. 3.3 along with the implementation of the respective reliability functions.

## 3.3 Probabilistic dike failure assessment

### 3.3.1 Dike failure due to overtopping

In case of dike overtopping, the flow over a dike crest induces shear stress on the inner slope cover. With increasing overtopping discharge, the critical shear stress can be exceeded resulting in progressing slope erosion and breach formation.

Applying a deterministic full 2D hydrodynamic model, it may be possible to allocate the dike zones of high shear stress. Such zones during the 1999-flood on the river Iller in Germany corresponded well with the observed breach locations due to overtopping with a couple of exceptions (UniBwM, 2004). Remarkably, the exceptions are partly due to the load relaxation induced by upstream breaches. This effect was not considered by UniBwM (2004) and led to an overestimation of the number of breaches. Further fault predictions are explained by the destructive impact of tree vegetation on a dike core that may lead to failure even at low shear stress. The presence of large vegetation on the crest and slopes adversely affects the dike stability. The rooting forms preferential flow paths inside a dike core. These enhance the inner erosion, which may lead to the dike collapse. Notably, $64\%$ of failed dikes in Saxony in August 2002 exhibited timber vegetation (Horlacher et al., 2005).

Based on seven correctly identified breach locations, the shear stress at the dike crest of $\tau = 50\ N\ m^{-2}$ and at the dike foot of $\tau = 20\ N\ m^{-2}$ were proposed as threshold values for overtopping failure (UniBwM, 2004). The rule is based, however, on a small sample of breaches constrained geographically. Thus the dikes in the sample are likely to exhibit strong similarity in material properties and geometry. The validity of this threshold is, therefore, has to be further investigated at other fluvial dikes. Moreover, an empirical threshold derived from a deterministic model does not take into account the uncertainties of dike parameters. In this respect, the fragility function approach based on a Monte Carlo simulation of limit state functions offers an alternative to deterministic thresholds.

For overtopping, the limit state function can be formulated as (Apel et al., 2004; Merz, 2006):

$$Z_o = Q_a(t) - Q_{crit}(t), \tag{3.5}$$

where $Q_a(t)$ – overtopping discharge, $[m^3\ s^{-1}]$ and $Q_{crit}(t)$ – critical discharge as a function of time, $[m^3\ s^{-1}]$. Steenbergen and Vrouwenvelder (2003) and Vrijling and van Gelder (2000) propose the following equation for $Q_{crit}$:

$$Q_{crit}(t) = \frac{v_{crit}^{5/2}(t) \cdot k^{1/4}}{125(\tan\alpha)^{3/4}} \tag{3.6}$$

with $t_e$ – overtopping duration $[h]$, $f_g$ – turf quality parameter $[-]$, $f_g \in [0.7; 1.4]$, $\alpha$ – inner slope angle $[deg]$.
$k$ is the absolute roughness of the inner slope $[m]$, which can be related to the Manning's n value based on experiments as:

$$n = \frac{k^{1/6}}{c} \tag{3.7}$$

where the coefficient $c = 26$ according to Bollrich (2000), whereas Steenbergen and Vrouwenvelder (2003) and Vrijling and van Gelder (2000) give a slightly different value of $c = 25$, which was adopted

hereafter. The equation for the critical flow velocity ($v_{crit}$), originally proposed by Steenbergen and Vrouwenvelder (2003) and Vrijling and van Gelder (2000):

$$v_{crit}(t) = f_g \frac{3.8}{1 + 0.8 \log_{10}(t_e)}, \tag{3.8}$$

was further refined by Apel et al. (in press), based on experiments of Hewlett (1987) for turf covered slopes:

$$v_{crit}(t) = \frac{3.9177 + 1.5(f_g - 1)}{1 + (0.8575 - 0.45(f_g - 1)) \log_{10}(t_e)} \tag{3.9}$$

with $f_g \in [0.5; 1.5]$.

The overtopping discharge $Q_a(t)$ over the dike crest can be computed according to Kortenhaus and Oumeraci (2002) for a broad-crested weir ($h_e/b_c \in (0.1; 0.35)$):

$$Q_a(t) = A h_e^{3/2}(t) \tag{3.10}$$

where $h_e$ - overtopping height $[m]$, $b_c$ - dike crest width $[m]$ and

$$A = 1.444(1 + C_W) \cdot C_L \cdot C_R \cdot C_N \cdot C_M \tag{3.11}$$

$$C_L = 1.286 \left(1 - \frac{2/9}{1 + (h_e/b_c)^4}\right) \tag{3.12}$$

$$C_R = 1 + 0.1\sqrt{3R_c/h_c \cdot e^{(1-3R_c/h_c)}} \tag{3.13}$$

$$C_W = \frac{1}{3}\left(\frac{h_e}{h_e + h_c} - 1.3\right)^{3/4}, \qquad \text{for} \quad \frac{h_e}{h_e + h_c} \in (\frac{1}{3}; \frac{2}{3}), \tag{3.14}$$

$$\text{otherwise } C_W = 0 \tag{3.15}$$

$$C_N = N \cdot \frac{1 + 0.45/N \cdot (h_e/b_c)}{1 + (h_e/b_c)^4} \tag{3.16}$$

$$N = 0.9 + \frac{\sqrt{n}}{8} \tag{3.17}$$

$$C_M = 0.326 \cdot \frac{1 + M(h_e/b_c)^4}{1 + (h_e/b_c)^4} \tag{3.18}$$

$$M = 1 + 0.5\sqrt{\sin\frac{\pi}{2m}} \tag{3.19}$$

where $1/n$ – outer slope $[-]$, $1/m$ – inner slope $[-]$, $R_c$ – crest rounding $[-]$.

The application of the overtopping limit state function to derive fragility functions for the Elbe reach dikes is further discussed in Sect. 4.4.2.

### 3.3.2 Dike failure due to rupture and piping

#### 3.3.2.1 Process of rupture and piping

During a flood, the seepage of a high permeability sandy layer, typically confined between low permeability clayey layers (Figure 3.6), progresses with increasing hydraulic gradient towards a downstream dike toe. In case the seepage pressure of the water percolating upwards exceeds the effective weight of the soil, rupture of the clayey layer occurs. This process is also referred as heave (Terzaghi et al., 1996) or uplifting (van Noortwijk et al., 1999; Van et al., 2005). The rupture enhances the seepage flow through the dike foundation, which may initiate material transport towards the downstream dike foot if the critical

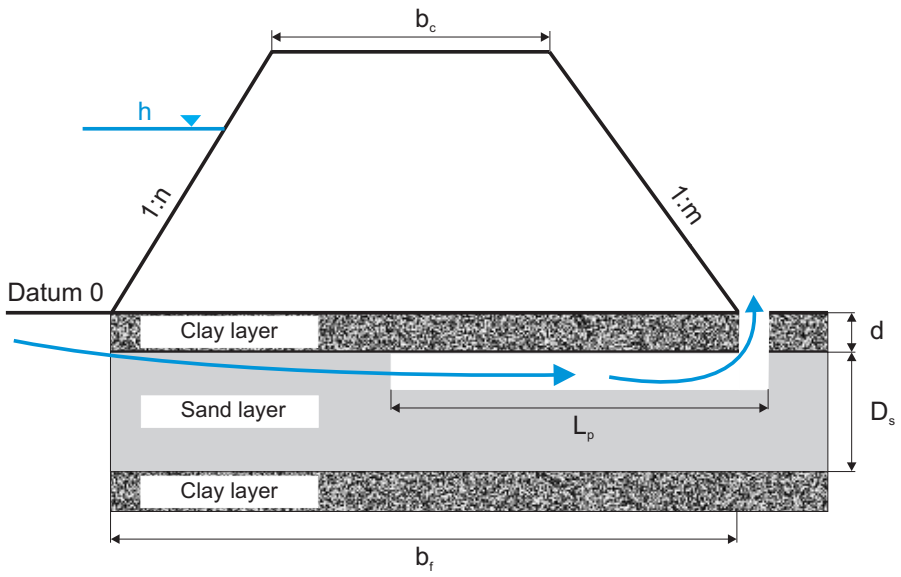


**Figure 3.6:** *Schematic representation of the piping failure mechanism.*

shear stress in the sand material is exceeded. This results in the formation of a sandboil behind a dike core — a typical indicator of progressive erosion.

As a consequence of the retrogressive erosion, initiated at the downstream dike toe, the channels or tunnels (also called pipes) develope in the sandy dike foundation. The pipes progress towards the outer dike toe until an equilibrium is attained expressed in the halted erosion. Evidences prove that after increase of the water level at the dike to a certain level a new equilibrium state is reached (Sellmeijer, 1989; Hanses et al., 1985). The development of erosion pipes progresses till the critical pressure difference $H_{crit}$ is reached. $H_{crit}$ is defined as the difference between the water levels at outer and inner dike slopes. Further increase in pressure difference beyond $H_{crit}$ results in progressive erosion, for which no equilibrium state is possible (Sellmeijer, 1989). This leads to the development of extended pipes under the dike core, which progress to the upstream dike toe causing a subsequent dike collapse.

In clayey foundations under high dispersed clay soil particle concentrations, plugging of pipes may occur, ceasing erosion processes. Khilar et al. (1985) developed a piping model for clay soils, which predicts particle detachment based on critical shear stress criterion and particle migration through a porous medium. A boundary between piping and plugging is delineated based on critical dispersed particle concentration. However, it remains unclear, how decisive the plugging process is. Its relevance is not emphasised for sandy dike foundations that are assumed here, making further consideration of this process superfluous in this study.

#### 3.3.2.2 Failure probability due to piping

The probabilistic description of dike failure due to piping can be given by a combination of four fragility functions. A dike failure occurs if the following conditions are fulfilled:

- The seepage front has progressed through a sandy dike foundation till the downstream dike toe.
- The rupture of an upper clay layer occurred in the hinterland. The rupture is assumed to happen directly behind the dike toe, so the seepage length equals the dike foot length.
- The critical head difference is achieved resulting in a progressive erosion towards the upstream dike toe.

- Finally, the pipes have developed to a critical length at which core subsidence takes place.

Each of the above listed failure modes can be described by a reliability function. Randomisation of the uncertain function arguments in a Monte Carlo framework delivers fragility functions analogously to the case of overtopping (Sect. 3.3.1).

The final dike failure probability $P_{pfailure}$ can be expressed as a probability for dependent events according to the multiplication rule of probability theory:

$$P(pfailure) = P(piping) \cdot P(cl|piping) \tag{3.20}$$

$$P(piping) = P(rs) \cdot P(Hcrit|rs) \tag{3.21}$$

$$P(rs) = P(seepage) \cdot P(r|seepage) \tag{3.22}$$

where $P(pfailure)$ – probability of dike failure when the critical pipe length is reached, $P(cl|piping)$ – probability of pipes reaching the critical length after erosion progressed beyond the critical state, $P(piping)$ – probability of progressive piping and rupture, $P(Hcrit|rs)$ – probability of reaching the critical state for piping after rupture has occurred, $P(rs)$ – probability of rupture and seepage, $P(seepage)$ – probability of foundation seepage, $P(r|seepage)$ – probability of rupture given the seepage.

This rule for the determination of probabilities of dependent events is embedded in the sampling procedure of failure probabilities in the core Monte Carlo simulation. It means that the probability of one dependent failure process is sampled only if failure due to the preceding process has been simulated.

#### Seepage probability

The probability of seepage through a dike foundation can be computed based on the reliability function relating the seepage length and foundation width:

$$Z_s = b_f - x(t) \tag{3.23}$$

where $b_f$ – foundation width $[m]$ and $x(t)$ – time-dependent seepage length through dike foundation $[m]$.

For the time-dependent hydraulic load, such as the water level at the dike, the seepage length can be determined using 2D models of flow in porous media (Fenton and Griffiths, 1996; Diersch, 2000; Scheuermann, 2005). These codes are, however, prohibitive in terms of CPU time requirements and thus can only be used on a local scale, for instance, for a particular dike or dam design purpose. For reliability assessment of a large number of dike sections, a simple approach for seepage length calculation has to be developed.

Scheuermann (2005) provides a comprehensive overview of analytical methods for unsteady seepage length computation inside a dike core. Some of these methods were developed for the case of sudden dike impoundment. The flood wave or impoundment water level exhibits, however, an unsteady behaviour. In such a case Scheuermann (2005) suggests an iterative use of the proposed methods for gradual water level rise.

The method of Brauns (1999), originally developed for a rectangular soil sample, is based on the assumption of mainly horizontal seepage flow along an impervious floor. Hence, it can be applied to seepage calculation in a confined dike foundation. With hydraulic gradient expressed as

$$i = h_p(t)/x(t) \tag{3.24}$$

where $h_p(t) = h(t) + d + D_s/2$ according to Figure 3.6, with $d$ – thickness of clay layer $[m]$, $D_s$ – thickness of sandy layer $[m]$ and $x(t)$ – seepage length $[m]$ (Figure 3.7), the pore water velocity $(v_p)$ can be computed according to Eq. 3.25:

$$v_p = \frac{K_f \cdot i}{n_a} \tag{3.25}$$

where $K_f$ – saturated hydraulic conductivity $[m\ s^{-1}]$, $n_a$ – air-filled porosity $[-]$.

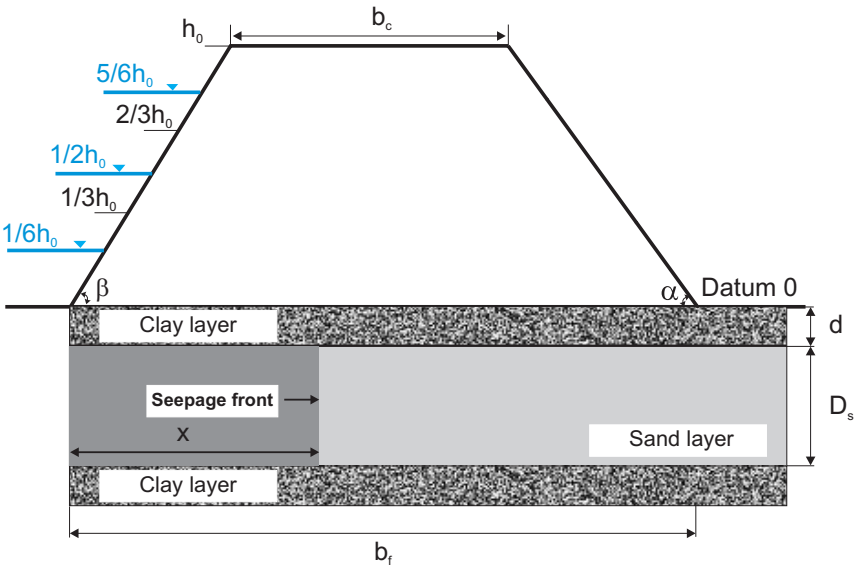


**Figure 3.7:** *Solution for the seepage length through a dike foundation for gradual impoundment.*

The velocity of the seepage front (Figure 3.7) can be expressed as:

$$v_a = \frac{dx}{dt} \tag{3.26}$$

Equating the pore water velocity to the velocity of the seepage front, i.e. combining Eq. 3.25 with Eq. 3.26 and Eq. 3.24, yields:

$$x(t)\ dx = \frac{K_f}{n_a} h_p(t)\ dt \tag{3.27}$$

Scheuermann (2005) provides an integration of Eq. 3.27 considering a sudden impoundment, i.e. $h_p$ is independent of time. Here the hydraulic potential resulting from a gradual impoundment is taken into account. This leads to Eq. 3.28 for the time dependent seepage length along a rectangular dike foundation (Figure 3.7):

$$x(t) = \sqrt{2\frac{K_f}{n_a} \int_0^T h_p(t)dt} \tag{3.28}$$

with $T$ – total impoundment duration $[s]$.

Eq. 3.28 is developed assuming the gravity as the only driving force of seepage flow. Additionally one can include the matric potential as an additional driving force of the phreatic line:

$$x(t) = \sqrt{2\frac{K_f}{n_a} \left( \psi \cdot T + \int_0^T h(t)dt \right)} \tag{3.29}$$

where $\psi$ – specific matric potential $[m]$.
However, the influence of the matric potential on the phreatic line is considered to be negligible compared to the effect of the gravitational force and therefore not further considered here.

The integral $\int_0^T h(t)dt$ in Eq. 3.28 is solved numerically by the trapezium rule for the continuous function $h(t)$. For this purpose, the dike crest height $h_0$ is discretised into three equidistant intervals

$(1/3h_0, 2/3h_0, h_0)$, as demonstrated in Figure 3.7. Water levels within these intervals is approximated by the average stages $(1/6h_0, 1/2h_0, 5/6h_0)$, respectively. Thus the fragility function, resulting from Monte Carlo randomisation of Eq. 3.23, can be represented by the probability volume in a 3D-space: $(D(0 - 1/3h_0), D(1/3h_0 - 2/3h_0), D(2/3h_0 - h_0))$, where $D(h)$ is the duration of load for a given water level interval. Development of the fragility functions for foundation seepage is demonstrated in Sect. 4.4.3 for the Elbe dikes.

### Probability of rupture

Fragility functions for rupture can be derived by randomising the reliability function in Eq. 3.30, which is based on the definition given in Sect. 3.3.2.1. After the seepage front has reached the downstream dike toe, rupture may occur. Assuming zero water depth in the hinterland results in zero buoyancy acting on clayey layer particles. Thus the reliability function can be expressed in a simplified form (Vrijling and van Gelder, 2000; Steenbergen and Vrouwenvelder, 2003) as:

$$Z_r = \frac{\gamma_k}{\gamma_w} d - h(t) \tag{3.30}$$

where $\gamma_k$ – weight per volume of clay soil $[kN\ m^{-3}]$, $\gamma_w$ – weight per volume of water $[kN\ m^{-3}]$, d – thickness of clay layer $[m]$.

### Probability of piping

The reliability function for piping given in Eq. 3.31 represents a limit state of progressive erosion, beyond which no equilibrium is possible (Sect. 3.3.2.1). It is represented by the difference in actual water head and critical head that is a function of foundation properties.

$$Z_p = H_{crit} - h(t) \tag{3.31}$$

Empirical reliability functions for piping were traditionally based on the approaches of Bligh (1912) and Lane (1935) and are still being extensively used in practice as design criteria (Weijers and Sellmeijer, 1993; Calle and Weijers, 1995). In the approach of Bligh, the critical pressure head is calculated according to the following equation:

$$H_{crit} = \frac{L}{C_{B,creep}} \tag{3.32}$$

with $C_{B,creep}$ – Bligh creep coefficient $[-]$, $L$ – seepage length $[m]$.
The approach of Lane extends the formulation of Bligh by incorporating the vertical component of the seepage length. The reliability function is given in Eq. 3.33:

$$H_{crit} = \frac{L_v + \frac{1}{3}L_h}{C_{L,creep}} \tag{3.33}$$

$C_{L,creep}$ – Lane creep coefficient $[-]$, $L_v$ – vertical component of seepage length $[m]$, $L_h$ – horizontal component of seepage length $[m]$.
The empirically derived values for $C_{B,creep}$ and $C_{L,creep}$ depend on soil characteristics and are given in Table 3.1. The characteristics of soils for the corresponding creep coefficients are rather of descriptive nature, which complicates the selection of proper values in practical analysis.

Consideration of the vertical seepage length component in the Lane formula makes this approach attractive for application to hydraulic structures. Along hydraulic structures the flow can induce erosion of soil material, resulting in failure of flood protection. The simplicity of the Lane formula makes it

**Table 3.1:** *Creep coefficients for piping reliability functions according to Bligh (1912) and Lane (1935)*

| Soil type | $C_{B,creep}$ | $C_{L,creep}$ |
|---|---|---|
| Very fine sand or silt | – | 8.5 |
| Fine sand | 15 | 7 |
| Medium-grained sand | – | 6 |
| Coarse sand | 12 | 5 |
| Medium-grained gravel | – | 3.5 |
| Coarse gravel | – | 3 |
| Boulders and gravel | – | 2.5 |
| Boulders, gravel and sand | $4-6$ | – |
| Soft clay | – | 3 |
| Medium-firm clay | – | 2 |
| Hard clay | – | 1.8 |
| Very hard clay | – | 1.6 |

practical and fast for applications to the analysis of dike stability and piping along hydraulic structures, where detailed information about soil properties in not available. For instance, it has been used by Dawson et al. (2005) and Dawson and Hall (2006) to derive fragility functions for piping in case of fluvial and maritime flood defences. However, the necessity to account for the influence of various soil parameters led to the development of a more complicated physically based approach.

The approach of Sellmeijer (1989) represents a physically based treatment of three main processes leading to progressive piping. These processes include:

- groundwater flow through the sand layer beneath the dike core
- flow through the erosion channels developing in the sand layer
- limit state stability of the sand grains in the erosion channels

The solution of the system of differential equations describing these processes delivers an expression for the critical water height difference, for which sand grains are in equilibrium state. Originally developed by Sellmeijer (1989); Sellmeijer and Koenders (1991) and Koenders and Sellmeijer (1992), the equation for critical water height difference did not consider thickness of the sand layer ($D_s$):

$$H_{crit} = c \left( \frac{\gamma_p}{\gamma_w} - 1 \right) \tan(\theta) \left(1 - 0.65 c^{0.42}\right) L \tag{3.34}$$

$\gamma_p$ – weight per unit of volume of sand particles [$kN\ m^{-3}$], $\theta$ – friction angle of soil particles [$deg$], with

$$c = 0.25\ \pi\ \eta\ d_{70} \left( \frac{1}{0.5 \kappa L} \right)^{\frac{1}{3}} \tag{3.35}$$

$\eta$ – White's drag coefficient [$-$], $d_{70}$ – sand particle diameter of 70%-weight grain size distribution [$m$], $\kappa$ – intrinsic permeability [$m^2$].
$\kappa$ is calculated according to Eq. 3.36:

$$\kappa = \frac{\nu}{g} \cdot k \tag{3.36}$$

$\nu$ – kinematic viscosity $[m^2\ s^{-1}]$, $g$ – gravitational acceleration $9.81\ [m\ s^{-2}]$, $k$ – permeability coefficient of sand $[m\ s^{-1}]$.

Further, the formula presented in Eq. 3.34 was refined based on the experiments of Weijers and Sellmeijer (1993) and incorporated the influence of the sand layer thickness ($D_s$) on the critical head difference:

$$H_{crit} = \alpha c \left( \frac{\gamma_p}{\gamma_w} - 1 \right) \tan(\theta)(0.68 - 0.1 \ln(c))L \tag{3.37}$$

where

$$\alpha = \left( \frac{D_s}{L} \right)^{\frac{0.28}{\left(\frac{D_s}{L}\right)^{2.8}-1}} \tag{3.38}$$

The $\alpha$ term explicitly considers the thickness of a water conducting layer and

$$c = \eta \left( \frac{d_{70}^2}{\kappa} \cdot \frac{d_{70}}{L} \right)^{\frac{1}{3}} \tag{3.39}$$

Comparison of the proposed model with experimental results revealed a good agreement for very fine sands and river sands over a range of porosity values from ca. $34\%$ till $40\%$. Poor predictions of the critical head difference for coarse sands is probably due to the assumption of laminar flow through the sand core, whereas in case of coarse sands flow becomes turbulent (Weijers and Sellmeijer, 1993). At turbulent flow conditions through a slit, a lower critical head is required for progressing piping, compared to that derived analytically.

Strictly saying, development of pipes is a 3-dimensional process with pipes forming a net in sandy foundation. The pipes develop towards pathways of the weakest erosion resistance. Weijers and Sellmeijer (1993) argue, however, that a pipe can be represented by one-dimensional slit without invalidating modelling results.

#### Probability of critical pipe development

The probabaility of critical pipe development is computed based on the reliability function in Eq. 3.40. As soon as the erosion pipes reach the upstream dike toe, direct water flow between the upstream and downstream ends takes place, which generally leads to a dike collapse (Hanses et al., 1985; Terzaghi et al., 1996). Therefore the critical length is assumed to be equal to the dike foundation width.

$$Z_{cl} = b_f - L_p \tag{3.40}$$

where pipe length $L_p$ is calculated in Eq. 3.41 according to the experiments of Weijers and Sellmeijer (1993).

$$L_p = 6/38 \cdot t_d \tag{3.41}$$

with $t_d$ – time $[days]$.

Unfortunately, very few experiments of piping dynamics are reported in the literature. This hinders the derivation of the variability range for the pipe development velocity. Therefore, only the dike foot width is considered as random variable in the pre-processing Monte Carlo simulation. The presented relationship is purely empirical and does not take into account the characteristics of dike foundation. It can be expected that material geotechnical properties influence the transport velocity of particles. Further experimental investigation of slit formation velocity and studies on the effect of material properties would refine the model and allow the uncertainty investigation.

Furthermore, the pipe development rate was derived from an experiment with constant dike impoundment. The variation of the pipe growth rate can be expected to depend on the impoundment water level fluctuations. The effect of variable impoundment height on a slit progress was not sufficiently investigated and reported in the reviewed literature. The pipe development velocity was therefore assumed constant in this study.

### 3.3.3 Dike failure due to seepage and micro-instability

Micro-instability is a particular mode of slope instability, which occurs when the slope material particles are detached and relocated by the seepage flow. The material transport occurs if the effective weight and force exerted by the flow exceed the resisting shear stress.

For micro-instability to occur, the phreatic surface has to reach the inner slope and seepage flow has to develop. The exit point of the phreatic line determines the height at which the slope failure starts. If the failure profile (Figure 3.8) is high enough to damage the dike crest, a substantial material relocation leads to the dike failure. Micro-instability is more likely to occur in materials with low cohesion, although it can also happen in cohesive soils (CUR/TAW, 1990).

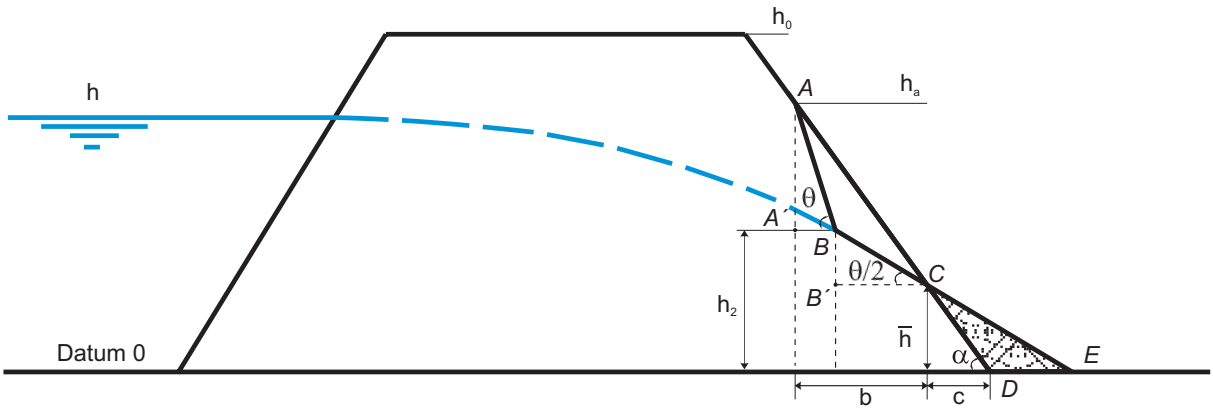


**Figure 3.8:** *Schematic representation of slope failure due to micro-instability. Adopted from Vrouwenvelder and Wubs (1985) for the special case of a dike without ditch.*

The probability of dike failure can be expressed in terms of the probability of two dependent processes: seepage and slope failure as given in Eq. 3.42.

$$P(mifailure) = P(seepage) \cdot P(micro - instability|seepage) \tag{3.42}$$

where $P(mifailure)$ – probability of dike failure due to micro-instability, $P(seepage)$ – probability of seepage through the dike core, $P(micro - instability|seepage)$ – probability of slope failure affecting the dike crest after seepage flow has developed.

These probabilities can be computed for a range of possible loads based on the reliability functions discussed in Sect. 3.3.3.1 and 3.3.3.2.

#### 3.3.3.1 Probability of seepage

The probability of seepage flow development can be derived from the reliability function (Eq. 3.43), which relates the foot width to the seepage length along the dike foot.

$$Z_{sm} = b_f - x(t) \tag{3.43}$$

where $b_f$ - dike foot width $[m]$, $x(t)$ - seepage length along a dike foot as function of time and hydraulic load $[m]$.

The method presented in Sect. 3.3.2.2 is taken as a basis for seepage calculation in a dike core. However, it does not consider the inclination of a dike slope that may result in an underestimation of the seepage length. The flater the slope is, the greater the percolation area becomes, the more water can penetrate into the dike core yielding a larger seepage length in a given time.

In order to account for the slope effect, Brauns (1999) proposed to use the average seepage length $x^*$ in Eq. 3.28 instead of $x$, where $x^*$ can be derived from the geometrical relations shown in Figure 3.9 for the a steady impoundment:

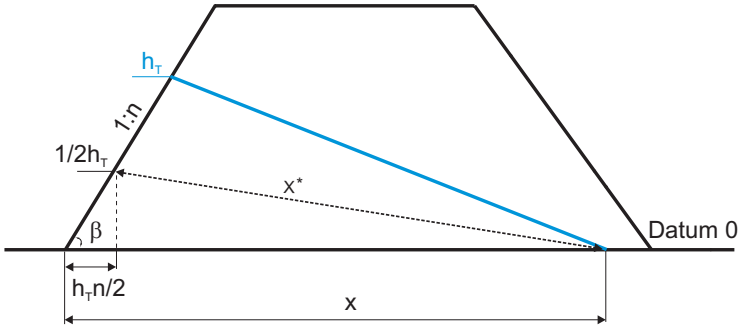


**Figure 3.9:** *Definition of the average seepage length after Brauns (1999) for a dike on impervious floor. Taken from Scheuermann (2005).*

$$x^* = \sqrt{\left(x - \frac{h_T}{2}n\right)^2 + \frac{h_T^2}{4}} \tag{3.44}$$

where $h_T$ - height of the phreatic line starting point $[m]$, $n$ - outer slope $[-]$.

For the case of gradual impoundment, the water height $h_T$ is substituted with $\frac{1}{T}\int_0^T h(t)dt$.

Hence, combining Eq. 3.28 and Eq. 3.44 considering gradual impoundment yields the horizontal projection of the average seepage length:

$$x(t) = \sqrt{\frac{2K_f}{n_a}\int_0^T h(t)dt - \frac{(\frac{1}{T}\int_0^T h(t)dt)^2}{4}} + \frac{\frac{n}{T}\int_0^T h(t)dt}{2} \tag{3.45}$$

Eq. 3.45 is applied to unsteady seepage flow calculation for gradual impoundment. The resulting horizontal projection of a seepage length is used in the reliability function (Eq. 3.43). Analogously to the seepage through a dike foundation (Sect. 3.3.2.2), the integral over impoundment time at a dike core is computed by discretising the crest height into three intervals (Figure 3.10).

By randomising the stochastic variables in Eq. 3.43 in the Monte Carlo simulation, the probability space can be computed. An example of the resulting fragility function is demonstrated for a selected Elbe dike section in Sect. 4.4.4.

#### 3.3.3.2 Probability of slope micro-instability

Under action of seepage flow the slope failure profile develops, as shown in Figure 3.8 for a schematized case. Implying no material compression, the volume of the slipped material equals the volume of the relocated material. Thus, the height of slide ($h_a$) can be derived from a simplified geometrical

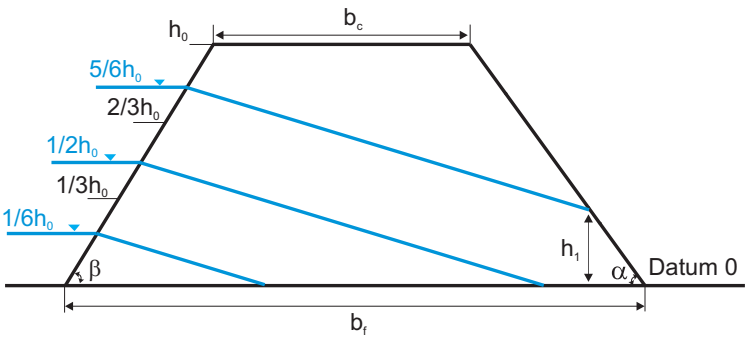


**Figure 3.10:** *Solution for the seepage length in a dike for gradual impoundment.*

representation given in Figure 3.8, where $S_{\triangle ABC} = S_{\triangle CDE}$ with $S_{\triangle}$ denoting the area of respective traingle.

A failure is assumed for $h_a > h_0$, yielding a reliability function for slope micro-instability:

$$Z_{mi} = h_0 - h_a \tag{3.46}$$

The inner slope is assumed to fail up to a state when it equals the friction angle of the dike material ($\angle ABA' = \theta$), whereas the relocated material forms $\theta/2$ angle with the ground ($\angle BCB' = \theta/2$) (Vrouwenvelder and Wubs, 1985; CUR/TAW, 1990).

For the case of a non-submerged slope, which is further assumed here, the material transport occurs for slopes with (CUR/TAW, 1990):

$$\tan\theta < \tan 2\alpha \iff \alpha > \theta/2 \tag{3.47}$$

with $\theta$ – friction angle of dike material [$deg$], $\alpha$ – outer slope angle [$deg$].
Slopes with $\alpha \geq \theta$ are unstable, whereas those with $\alpha \leq \theta/2$ are unconditionally stable against micro-instability (CUR/TAW, 1990).

Adopting the analysis of Vrouwenvelder and Wubs (1985) for a dike without ditch, $h_a$ can be computed according to Eq. 3.48:

$$h_a = h_2 \frac{\sin\alpha}{\sin(\theta-\alpha)} + \overline{h}\left(1 - \frac{\sin\alpha}{\sin(\theta-\alpha)}\right) \tag{3.48}$$

where

$$\overline{h} = \frac{1}{2}h_2, \qquad \text{for} \quad h_2 < \frac{\sin(\theta-\alpha)}{\sin\alpha - \sin(\theta-\alpha)}, \tag{3.49}$$

In this case $h_a$ becomes:

$$h_a = \frac{h_2}{2}\left(1 + \frac{\sin\alpha}{\sin(\theta-\alpha)}\right) \tag{3.50}$$

Otherwise

$$\overline{h} = h_2 \frac{1 - \sqrt{\frac{\sin(\theta-\alpha)}{\sin\alpha}}}{1 - \frac{\sin(\theta-\alpha)}{\sin\alpha}}, \qquad \text{for} \quad h_2 \geq \frac{\sin(\theta-\alpha)}{\sin\alpha - \sin(\theta-\alpha)} \tag{3.51}$$

A detailed derivation of Eq. 3.48 as well as of $h_2$ is given in Appendix A.

### 3.3.4 Breach development and width

Breach growth appears to be non-linear. One distinguishes between the rate of headcut migration in case of overtopping, breach deepening and widening rates. In small-scale experiments with the dam of $0.9\ m$ height and $1\ m^3\ s^{-1}$ overtopping discharge, Hahn et al. (2000) observed a 5-fold increase in the headcut migration rate over time. The authors measured the rates ranging between $0.47\ m/h$ to about $2.1\ m/h$. The headcut migration rate depends on the erosion stage starting with the surface erosion due to overtopping sheetflow, progressing into the cascading overfalls and ending up with a single headcut. When the breach is completely developed in the vertical direction, the widening process can further progress triggered by water flow through the breach. The rate of breach growth varies dramatically, according to the experiments of Hahn et al. (2000) as much as 60-fold, depending on the dike material ranging from sandy and silty to clayey soils.

In the large-scale embankment failure tests, accomplished in the IMPACT project (IMPACT, 2001), typical durations for development of the approximately $30\ m$ wide breaches range between $5 - 10$ minutes for rockfill dams to 1 hour for clayey dams. For the silty moraine core dams about 20 minutes were required for breach development (Vaskinn et al., 2004). On the other hand, there exist evidences of non-gradual breach development, e.g. when the whole clayey dike section of $190\ m$ was flushed away in a few seconds (Hesselink et al., 2003).

While there was a progress in understanding the breaching process for non-cohesive dikes, the erosion of cohesive dikes remains poorly understood (Broich, 2003). Ironically, the majority of breached dikes ($95\%$) during the Elbe 2002-flood in Saxony were constructed out of cohesive material (Horlacher et al., 2005).

The reviewed experimental studies indicate a strong variation of breach development rates, which makes the modelling of breach growth a highly complex task. Over the past four decades only moderate progress has been achieved concerning sound simulation of breach development in fluvial dikes and embankment dams. Singh (1996) provides a comprehensive overview of the currently available empirical and analytical models of dam breaching that vary considerably in terms of data requirements and complexity. However, the predictions of breach development remain highly uncertain (Wahl, 1998, 2001).

In flood hazard assessment studies of fluvial dikes, several approaches were adopted to handle the breach morphology. Rather often breach width was considered in a form of scenarios, derived from past observations (Alkema and Middelkoop, 2005; Hesselink et al., 2003). In the absence of observation evidence, assumptions from a physically plausible range were made. Apel et al. (2004, 2006) investigated 5 scenarios with $B_w = 0,\ 100,\ 200,\ 300,\ 400\ m$ and determined the impact in terms of breach probability reduction for a downstream dike using a dynamic-probabilistic model.

In several studies simple empirical models were used. Hall et al. (2003) employed a simple linear relationship between the ultimate breach width and dimensionless load (load related to a standard of protection in terms of a return period) multiplied by the defence length (Eq. 3.52).

$$B_w = 0.05 x L_d, B_w \leq L_d \tag{3.52}$$

where $B_w$ – ultimate breach width $[m]$, $x$ – dimensionless load $[-]$, $L_d$ – length of a defence structure/section $[m]$.

Eq. 3.52 relates the breach width not directly to the load expressed as a water level but rather to the dimensionless load. The dimensionless load is given by the relationship between the return period of the actual load and design return period of a structure. Such relationship implies the knowledge of a return period for the load at any dike section, if water level is explicitly simulated. The fact that the water level and corresponding return period are not linearly related, further impedes the direct use of Eq. 3.52 in a dynamic model.

Further empirical rule employed by Dawson et al. (2005); Dawson and Hall (2006) is based on the cohesion property of the dike material. Eq. 3.53 relates the dike overtopping height in absolute terms to the ultimate breach width:

$$B_w = min[10h_o a, L_d] \tag{3.53}$$

where $h_o$ – overtopping height $[m]$, $a$ – empirical coefficient ranging between 3 and 15 for cohesive and non-cohesive materials, respectively.
The value of $a = 6$ was adopted for fluvial dikes and $a = 12$ for sea dikes. It seems that this rule is not applicable to breach mechanisms other than overtopping. Moreover, it would considerably underestimate the breach width on the Elbe river during August 2002 flood, when compared to the data of Gocht (2002). There is even an evidence of $1.5\ m$ overtopping on the Elbe without dike breaching. This suggests that there exist other processes influencing dike stability, which are not accounted for by overtopping height and cohesion.

The correlation between the final breach width and other influencing factors, such as the area of hinterland polders and width of a downstream outflow polder opening, was investigated by Horlacher et al. (2005) for Saxonian dikes. The results indicate no correlation between the analysed data. The knowledge about the factors influencing the breach width remains limited. The problem is further aggravated by the small number of breach evidences and their often poor documentation. Recent fluvial dike breach events, however, become systematically documented (Horlacher et al., 2005).

Therefore, there is a need for a new approach to account for the breach width in a modelling process. The quantification of the impact of breach width on flood intensity indicators also remains an open question. In this work, a probabilistic treatment of final dike breach width is proposed and integrated in the IHAM modelling approach.

A theoretical probability distribution function can be fitted to the empirical distribution of breach width observed during flood events. In a Monte Carlo simulation, the breach width is treated as a random variable following the fitted distribution. Provided a sufficient number of MC samples, the uncertainty of flood hazard statements can be determined as a function of breach width. As new findings about breach development and width correlation with other state variables such as discharge, flow velocity etc. become available, they can be integrated into the modelling framework either as deterministic or as probabilistic variables.

Breach development rate is considered as a deterministic variable in IHAM. It is assumed here that uncertainty in ultimate breach width has comparably larger impact on the uncertainty of flood hazard statements than the breach development rate. The development rate of a full breach width within one hour was adopted for modelling, as also used by Apel et al. (2004, 2006). This value, however, can be changed by the modeller depending on the dikes under consideration. The adopted rate corresponds to the experiments of Vaskinn et al. (2004) for comparable soil types as found in Elbe dikes. A similar approach was adopted by Alkema and Middelkoop (2005), who allowed the breach development within 3 hours in their modelling study on the Rhein and Meuse Rivers. However, they simulated relatively large breach widths of $525\ m$ and $300\ m$. Han et al. (1998) also assumed a linear increase of the breach width up to $200\ m$ within 3 hours for a dike in Korea. The time lag adopted here prevents sharp water outflow from the river channel, hence, encouraging numerical stability of the 1D hydrodynamic model.

# Chapter 4

# Application of IHAM to the Middle Elbe reach

## 4.1 Modelling objectives

The modelling exercise discussed in this chapter aims at testing of the developed modelling approach to deliver hazard statements for a typical river reach protected by dikes. The performed simulations should identify the dike sections vulnerable to a particular failure mode. The inundation hazard resulting from dike breaches must be characterised in terms of various flood intensity indicators. Changes in failure probability and flood hazard with increasing flood magnitude should be analysed. The ultimate objective of the modelling study is the development of advanced flood hazard maps based on the extended range of intensity indicators. The generated flood hazard maps must include uncertainty bounds and indicate a likely range of possible system states and their associated probability of occurrence. The IHAM was setup and applied to a typical diked river reach on the Middle Elbe.

## 4.2 Description of the study reach

A study reach of ca. $91\ km$ length was selected on the German part of the Elbe River for setup of the IHAM model. The reach is located between the gauges Torgau (Elbe-Km $154.6$) and Vockerode (Elbe-Km $245.5$) as shown in Figure 4.1. The only large tributary entering the study reach approximately in the middle (Elbe-Km $199$) is Schwarze Elster, whose catchment comprises about $5541\ km^2$.

The study reach belongs to the Middle Elbe that is the Elbe River part between kilometres $96$ and $585.9$. On the stretch between the Elbe-Km $96$ and $437.9$ the average slope amounts to $0.2‰$ (BfG, 1998). Based on the morphometry, the study reach can be subdivided into two parts according to Nestmann and Büchele (2002):

- Elbe-Km $154.2-199$: this part of the reach till the confluence with Schwarze Elster is charactrized by a larger slope and comparably narrow and deep cross-sections developed as a consequence of bed erosion;
- Elbe-Km $199-245.5$: in the second half, the average slope becomes smaller and the cross-sections are flater. Especially, between the Elbe-Km ca. $220-245.5$ the channel exhibits a very strong meandering behaviour on a wide (up to $5\ km$) floodplain.

In the period between the $12^{th}$ and $17^{th}$ century, straightening of the Middle Elbe channel and erection of dikes resulted in a reduction of natural flood retention capacity up to $2.3\ billion\ m^3$ at a 100-year

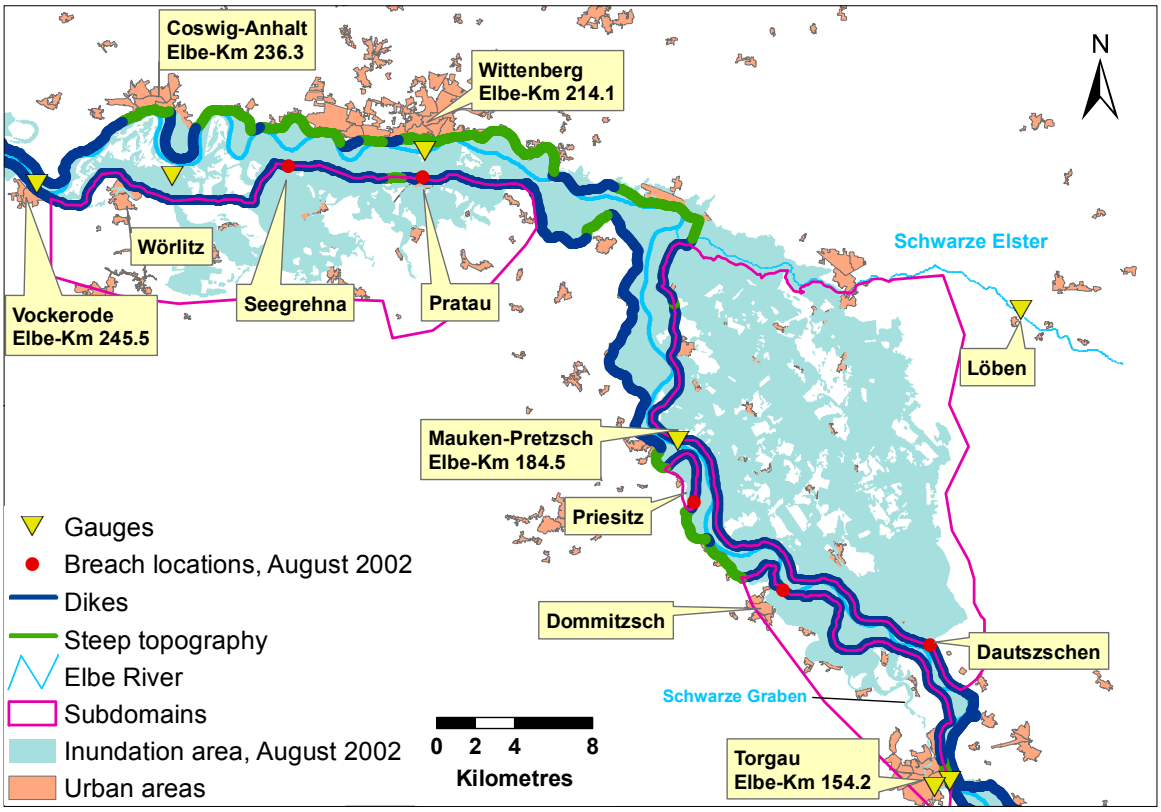


**Figure 4.1:** *Study reach between gauges Torgau (Elbe-Km* 154.6*) and Vockerode (Elbe-Km* 245.5*). Subdomains of inundated areas outlined in pink are used for evaluation of the 2D inundation model performance.*

flood (IKSE, 2003). These measures lead to an acceleration of the flood wave and increase of the peak water level. The process of anthropogenic channel manipulation was continued also in the $20^{th}$ century. Due to further straightening of the channel, the Elbe lost 128 $km$ of its length with approximately 71 $km$ on the German side. The retention capacity of the lower Middle Elbe was further reduced during the last century. The retention area comprises currently only $13.8\%$ of the original one (BfG, 2002). Simultaneously, a considerable retention capacity of 3.94 $billion\ m^3$ was gained by constructing flood retention ponds and reservoirs, however, primarily in the upstream parts of the river basin. Moreover, the studies indicate that the retention effectiveness of reservoirs drops with increasing flood magnitude (see Nestmann and Büchele, 2002, for review).

The Middle Elbe, including the study reach, is nowadays heavily protected by dikes on the most of its length. The exceptions are given by a few stretches characterised by steep banks as indicated in Figure 4.1. The dikes start at the Elbe-Km 97.7 downstream of Dresden and span till the North Sea. The dikes provide, however, extremely different levels of protection, ranging from $T = 10$ to $T = 100$ (Table 4.1). In total 365000 residents living in 249 towns and communities are protected by dikes on the Middle Elbe and its tributaries. In case of dike failures, the area potentially susceptible to flooding amounts to 3400 $km^2$.

An extreme flood event caused by the Vb-weather pattern struck the Elbe catchment in August 2002. Intensive rainfall of long duration over wide areas coincided with the saturated soil conditions in many parts of the catchment. The measured rainfall amounts exceeded at some stations (e.g. Dresden and

**Table 4.1:** *Protection level of Elbe dikes between the German-Czech border (Elbe-Km 0.0) and weir Geesthacht ($Elbe - Km\ 585.9$). The numbers represent the percentage of dike length corresponding to the protection level expressed in terms of return period. Source: IKSE (2003).*

| **Return period** $[a]$ | **Left bank** $[\%]$ | **Right bank** $[\%]$ |
|---|---|---|
| $100$ | $68$ | $55$ |
| $50 - 100$ | $4$ | $14$ |
| $25 - 50$ | $18$ | $27$ |
| $10 - 25$ | $10$ | $4$ |

Zinnwald-Georgenfeld) all-time records. This resulted in an extraordinary runoff. Whereas the average flow in the German part of the Elbe ranges between $300$ and $800\ m^3\ s^{-1}$, during this event the peak discharge of $4680\ m^3\ s^{-1}$ was measured in Dresden (BfG, 2002). Although, the recorded discharge was not the highest observed (somewhat above 200-years flood), the resulted water level of $9.4\ m$ at gauge Dresden was the all-time record. The reduction of channel capacity as well as increase of roughness are considered to be the reasons of the extreme water levels (BfG, 2002; DKKV, 2003). For some, predominantly upstream reaches of the Elbe tributaries, the discharge return period exceeded $500$ years (Petrow et al., 2007). In the main river at gauge Torgau the return period was calculated at $T = 242$ using Generalised Extreme Value (GEV) distribution and the L-moment parameter estimation method. A more detailed description of the meteorological and hydrological characteristics of the event is given in BfG (2002).

During this flood, $104$ dike breaches occured in the german part of the Elbe catchment, most of them on the Mulde River (Table 4.7). Along the study reach, five breaches (Figure 4.1) caused an inundation of $277.7\ km^2$ (IKSE, 2004), which comprises about $87\%$ of the whole inundated area caused by dike failures on the Middle Elbe. The regions, characterised by flat topography that adjoin to the study reach on the right side between Torgau and Schwarze Elster confluence and on the left side between Wittenberg and Vockerode, were readily inundated as a consequence of dike failure causing considerable threat to the population, assets and infrastructure.

After the catastrophic flood event a number of technical flood protection measures, such as dike strengthening and relocation as well as construction of polders, were intensively brought into limelight. Although between the years 1991 and 2002 $197\ km$ of Elbe dikes were restored and strengthened, still $60.7\%$ of the dike length did not meet the protection standards as of 01.01.2003. Along the study reach almost all dike stretches are categorized as inadequate (IKSE, 2003). However, in the last years $241.4$ dike kilometres, urgently requiring reconstruction after the 2002 flood event, were strengthened. This reduced the restoration need to $547.4$ $(42.1\%)$ dike kilometres (IKSE, 2006). Especially, in the States of Saxony and Saxony-Anhalt there is still a considerable demand for a higher protection level of about $363.7$ dike kilometres. Besides the improvement of protection level, dike relocations are planned at some parts of the Middle Elbe. However, the recent study indicates a marginal reduction potential of the water level due to these measures for a 100-year flood. At the gauge Wittenberge (Elbe-Km $454.8$) the water level is expected to drop by just $1\ cm$ with a simultaneous peak delay of 12 hours (IKSE, 2003).

A stronger peak reduction effect is expected from the $16$ planned polders in Saxony and Saxony-Anhalt with a total retention capacity of $177.3\ million\ m^3$. Assuming no dike relocation, a water level reduction of about $22\ cm$ is expected at gauge Wittenberge with the operated polders during a 100-year flood. Half of the polders with a total retention volume of $70.9\ million\ m^3$ are planned along the study reach between Elbe-Km $155.5 - 233.5$. Currently, there is a need for studies assessing the effect of

polders on the flood wave transformation (peak reduction and delay) on the Middle Elbe (IKSE, 2003).

The presented thesis provides a methodology and shows a case study for the evaluation of polder effects in terms of dike breach probability and inundation hazard reduction during extreme flood events (Sec. 4.8).

## 4.3 1D hydrodynamic model setup

Application of the IHAM model was originally intended for the Elbe reach between gauges Dresden (Elbe-Km 55.6) and Vockerode (Elbe-Km 245.5) (Figure 4.2). Therefore, the 1D hydrodynamic model EPDRiv1h was setup, calibrated and validated for this reach. In the course of the work, the study reach between gauges Torgau (Elbe-Km 154.6) and Vockerode, as described in Sect. 4.2, was selected for flood hazard assessment. The reason for that were the limitations in terms of precise absolute dike height data for the reach usptream of Torgau and computational burden associated with the significantly enlarged modelling domain.

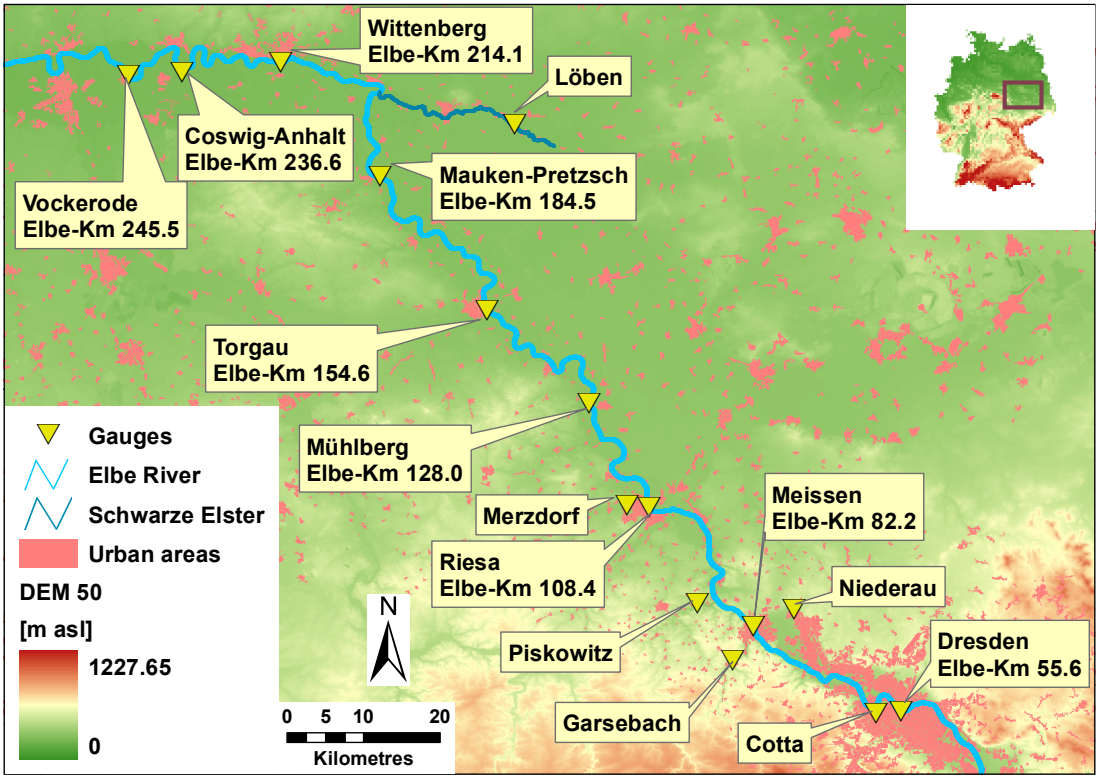


**Figure 4.2:** *Elbe reach between gauges Dresden (Elbe-Km 55.6) and Vockerode (Elbe-Km 245.5), for which the EPDRiv1h model was setup, calibrated and validated.*

The EPDRiv1h model was setup for the Elbe channel and adjacent floodplain between the river dikes. Cross-section profiles were provided by the Helmholtz Centre for Environmental Research (UFZ) every $400 - 600\ m$ for the whole German Elbe part. The majority of surveyed cross-sections covered the floodplain topography. However, in the regions with extremely wide floodplains, e.g. between Seegrehna and Wörlitz (Figure 4.1), approx. between Elbe-Km 221.6 and Elbe-Km 241.0 , the measured cross-

section did not completely cover the floodplain area between the left- and right-side dikes and had to be extended.

At locations of strongly meandering channels, the cross-sections can be bent as often practised in hydrodynamic modelling (Bloß, 2005; Werner, 2001). The part of a cross-section describing the main river channel remains orthogonal to the channel flow direction and the tails capture the floodplain topography.

Preferential flow on the floodplain is expected to develop during extreme events in this part of the reach. The computations of the Institute of Water and River Basin Management, University of Karlsruhe with a 2D calibrated hydrodynamic model indicate that approximately $60\%$ of the specific discharge is carried through the floodplain at $Q = 2070\ m^3\ s^{-1}$ at the reference cross-section at Elbe-Km $241.0$ (Figure 4.3a). This proportion increases with increasing event magnitude, e.g. up to $70\%$ for the August 2002 flood event with $4000\ m^3\ s^{-1}$ (Figure 4.3b).

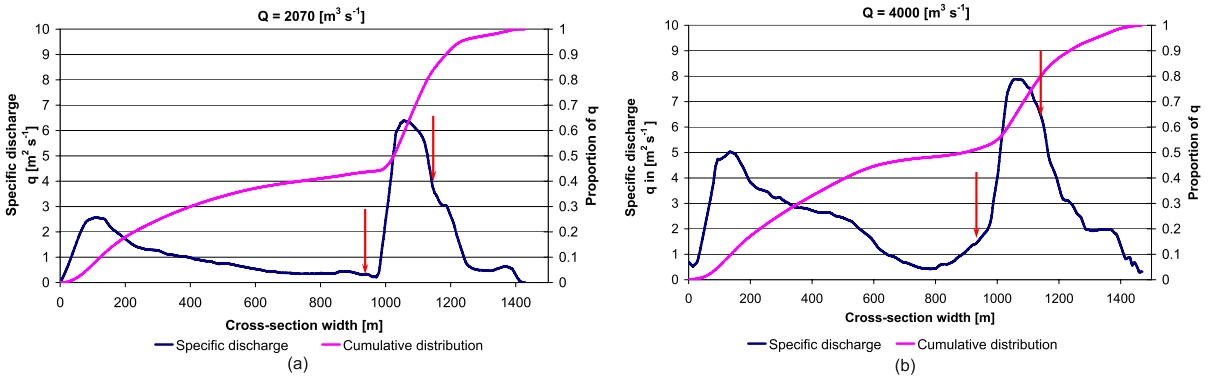


**Figure 4.3:** *Distribution of the specific discharge along the reference cross-section at Elbe-Km* $241.0$ *for maximum discharges during the 01.2003 (a) and 08.2002 (b) flood events. The arrows indicate the location of the river bed. (Source: Institute of Water and River Basin Management, University of Karlsruhe)*

Therefore, it seems that, especially for extreme events, the assumption of preferential flow over the floodplain may be justified. In order to grasp the area between the dikes, the manually generated cross-sections were drawn over the whole floodplain between Elbe-Km $221.6$ and $241.0$ using EasyProfiler extension to ArcGIS Software. The surface elevation values were assigned to the profile points based on the digital terrain model of $2 \times 2\ m$ resolution. The extended cross-section tails were kept orthogonal to the assumed preferential flow direction. It should be noted that the errors are introduced into the model by using the manually derived profiles. These result from the errors in the DEM and uncertainty in preferential flow path. These errors are compensated by roughness parameterisation during calibration (Sect. 4.3.1). However, it may result in extreme roughness values and thus reduce the predictive accuracy of the hydrodynamic model.

### 4.3.1 Calibration and validation

Water flow in a river channel is influenced by the river bed surface features. The effect of hindering the flow is described by the surface roughness. Physical measurements of roughness are very difficult and cannot be accomplished on a reach scale. Therefore empirical approaches are often used to establish the roughness values corresponding to the surface feature types. These friction values can then be adopted in hydrodynamic models. However, the roughness coefficients used in the computer codes represent effective rather than actual roughness coefficients. The effective roughness compensates for all model

errors, such as model structure error, errors in numerical solution, errors in boundary conditions (Lane, 2005). It also compensates for heterogeneity in land cover, variation in cross-section geometry and slope, which is captured by discretisation only to a certain extent. Therefore a need for calibration arises from the uncertainty in model parameterisation.

1D hydrodynamic models are traditionally being calibrated by adjusting the roughness parameter given the upstream and downstream boundary conditions. In the EPDRiv1h model, the Manning's roughness coefficient can be assigned to every cross-section. Several cross-sections can be lumped into stretches, which are assigned the same roughness value. The question about the optimal number of distributed roughness values used in hydrodynamic modelling is a topic of ongoing debate. It seems that the number of degrees of freedom depends on the reach characteristics and constraining observations (Hall et al., 2005b; Schumann et al., 2007b).

The roughness values can be manually or automatically calibrated using lumped or distributed observations of discharge and water levels. In automatic calibration various objective functions can be optimized to approach the suitable friction parameter values. On the other hand, typical values for different river bed types can be assigned based on the literature (e.g. Chow, 1959; Bollrich, 2000). These values are then manually altered within the physically plausible range to achieve the targeted model performance. The latter procedure was adopted in this work.

Another approach to the model calibration explicitly acknowledges the fact that there exists no single optimal parameter set, with which the model reproduces observations. Taking into account the potential degrees of freedom, i.e. the possibility of assigning different friction parameter values to different cross-sections and distributed floodplain parameterisation, and given the inherent errors in model structure, i.e. in the way the model describes natural processes, there exists a number of parameter sets, which are equally satisfactory. This is referred to as equifinality (Beven and Binley, 1992; Aronica et al., 1998a; Beven, 2001, 2006). The parameter space can be explored using the generalised uncertainty estimation (GLUE) framework (Beven and Binley, 1992) discussed in Sect. 2.5. The appropriate parameter sets are obtained by comparison of modelling results with observed data. They can be derived conditioned on flood extent (Aronica et al., 2002; Bates et al., 2004), discharge records (Werner, 2004; Pappenberger et al., 2005) and/or maximum water level observations (Werner et al., 2005a; Hunter et al., 2005a). The cited works have already extensively explored the uncertainty in roughness parameterisation and its effect on inundation predictions with 1D and 2D hydrodynamic models. Furthermore, the GLUE procedure, which is based on Monte Carlo simulation, is computationally costly for complex models, large model domains and relatively fine discretisation. Therefore, the impact of roughness parameterisation on the flood hazard is not investigated in this work. The study rather focuses on the influence of dike failures and inflow hydrograph variability on the inundation intensity indicators, which, to the knowledge of author, has not been explored in detail up to now.

One distinguishes between external and internal hydrodynamic model validation. In external model validation, hydraulic predictions are compared to the measurements at reach outflow and prove the model's routing capabilities. Although the observations at the reach outflow are not sufficient in constraining friction parameters, the external validation is an important benchmark test of model performance (Bates et al., 1998b). To gain trust in distributed model predictions, e.g. predictions of water stages at every cross-section, the model has to be validated on spatially distributed measurements. In case of a 1D model these are the records along the river channel. This comparison is referred to as internal validation since the measurements involved are collected within a model domain (Bates et al., 1998b). This type of validation includes the comparison between the steady-state predictions of maximum water level versus the high water marks (Sect. 4.3.1.1). Furthermore, the unsteady predictions of discharge and stage hydrographs can be compared to the records of internal gauging stations (Sect. 4.3.1.2) and evaluate the dynamic model performance over a range of flow conditions.

#### 4.3.1.1 Steady-state calibration and validation

Manual calibration was employed to sanely constrain friction parameters and provide a spatially distributed roughness data set. Using solely lumped catchment response for model calibration, e.g. discharge series at the downstream gauge, may be insufficient in constraining the roughness coefficients. It may result in a variety of parameter combinations meeting the observations, whereas the model performance along the reach is unsatisfactory. Since the precise water level predictions are crucial for dike breach modelling, the calibration against the distributed observations is preferred over the lumped model fit.

High water marks along the Elbe River between Elbe-Km $55.6 - 245.5$ were provided by the Saxonian State Agency for Environment and Geology (LfUG) for five flood events. The spatial resolution of the provided data varies along the reach and ranges between $200 - 600\ m$. The maximum water levels recorded in the field have typical an accuracy of about $0.05 - 0.2\ m$ RMSE (Oberstadtler et al., 1997). The measurements of water stage were provided for a series of gauges and are summarised in Table 4.2. Additionally, the maximum event discharges were available from LfUG for gauges Dresden, Torgau and Wittenberg.

**Table 4.2:** *Water stage elevation ($H$ in $[m]$) and corresponding discharge ($Q$ in $[m^3\ s^{-1}]$) for flood events used for calibration and validation of the EPDRiv1h model. Maximum event discharge values for gauges Dresden, Torgau and Wittenberg were provided by LfUG. Discharges at other locations were estimated using the rating curves developed by Nestmann and Büchele (2002).*

| **Gauge records** | **Flood events** | | | | |
|---|---|---|---|---|---|
| | **01.1995** | **11.1998** | **03.1999** | **02.2002** | **01.2003** |
| $H_{Dresden}$ | 4.96 | 5.89 | 5.9 | 5.8 | 6.65 |
| $Q_{Dresden}$ | 1227 | 1640 | 1644 | 1598 | 2078 |
| $H_{Meissen}$ | 5.57 | 6.33 | 6.47 | 6.33 | 7.31 |
| $Q_{Meissen}$ | 1197 | 1599 | 1667 | 1599 | 2145 |
| $H_{Riesa}$ | 5.57 | 6.47 | 6.51 | 6.33 | 7.31 |
| $Q_{Riesa}$ | 1101 | 1447 | 1465 | 1383 | 1867 |
| $H_{Mühlberg}$ | 6.07 | 6.88 | 7.1 | 6.84 | 7.69 |
| $Q_{Mühlberg}$ | 1227 | 1605 | 1717 | 1585 | 2116 |
| $Q_{Torgau}$ | 1160 | 1580 | 1620 | 1520 | 2060 |
| $H_{Pretzsch-Mauken}$ | 5.45 | 5.97 | 6.01 | 5.89 | 6.47 |
| $Q_{Pretzsch-Mauken}$ | 1368 | 1729 | 1762 | 1673 | 2189 |
| $H_{Elster}$ | 5.05 | 5.34 | 5.31 | 5.31 | 5.61 |
| $Q_{Elster}$ | 1304 | 1645 | 1598 | 1598 | 2029 |
| $Q_{Wittenberg}$ | 1290 | 1730 | 1630 | 1730 | 2120 |
| $H_{Coswig-Anhalt}$ | 5.53 | 5.95 | 5.96 | 5.92 | 6.17 |
| $Q_{Coswig-Anhalt}$ | 1324 | 1784 | 1796 | 1746 | 2010 |
| $H_{Vockerode}$ | 5.03 | 5.72 | 5.89 | 5.42 | 6.3 |
| $Q_{Vockerode}$ | 1278 | 1865 | 2050 | 1587 | 2503 |

In order to be used for steady-state model calibration, the water stage records have to be converted into discharge using H-Q-relationships at the respective gauges. Using the H-Q-curves developed for the whole German part of the Elbe River by Nestmann and Büchele (2002), discharge values were estimated

using linear interpolation (Table 4.2). In case no rating curve was available directly at the gauge location, the values were linearly interpolated between the neighbouring curves available every $400 - 600\ m$. The recorded and derived maximum event discharge values were used as boundary conditions of the steady-state hydrodynamic model.

In order to determine the return periods of the events, the recorded discharge at gauges Dresden, Torgau and Wittenberg was compared to the flood frequency distribution at these locations. Extreme value statistics was applied to the annual maximum discharge series (AMS) at gauges Dresden, Torgau and Wittenberg. A number of distribution functions were fitted to the respective AMS using the L-moment (Robson and Reed, 1999) and maximum likelihood parameter estimation methods. None of the distribution functions was used with the method of moments, which is regarded to be inferior when applied to strongly skewed peak discharge series (Robson and Reed, 1999). The Kolmogorov-Smirnov test was implemented to test the goodness of fit at considered gauges. The GEV distribution with the L-moment method appears to give the best fit to the observed annual maximum discharge series compared to the other tested distribution functions (Table 4.3). It seems to provide the best fit to the observed data in many studies, when used in combination with L-moment method (for review see e.g. Petrow et al., 2007). The GEV is therefore subsequently used for flood frequency analysis throughout this work.

**Table 4.3:** *Goodness of fit between annual maximum discharge series and theoretical probability distribution functions tested with the Kolmogorov-Smirnov test. The numbers represent the maximum difference between empirical cdf and theoretical probability. GEV = Generalised Extreme Value distribution, GL = Generalised Logistics distribution, Log-Normal2 = 2-parameter Log-Normal distribution, Log-Normal3 = 3-parameter Log-Normal distribution, LM = L-moments method, ML = maximum-likelihood method.*

| Distribution function | Dresden | Torgau | Wittenberg |
|---|---|---|---|
| GEV (LM) | 0.41 | 0.44 | 0.39 |
| GL (LM) | 0.52 | 0.37 | 0.47 |
| Gumbel (LM) | 0.73 | 0.55 | 0.46 |
| Log-Normal3 (LM) | – | 0.47 | 0.38 |
| Pearson3 (LM) | 0.42 | 0.55 | 0.37 |
| Gumbel (ML) | 0.72 | 0.6 | 0.47 |
| Log-Normal2 (ML) | 0.42 | 0.49 | 0.62 |
| Weibull (ML) | 1.08 | 0.9 | 0.52 |

The return periods of the flood events used for calibration and validation were estimated based on the GEV distribution and summarised in Table 4.4.

Effective friction parameters tend to vary remarkably for events of different magnitude. Several authors observed variations in roughness coefficients obtained for the same river reaches during calibration (Hunter et al., 2005a; Romanowicz and Beven, 2003). The reason for that is the change of average cross-sectional roughness, when additional floodplain areas become inundated at higher water stages. The problem can be tackled by introducing the friction parameter as a function of water level or adopting a spatially distributed roughness along the cross-section axis. In the latter approach zones of different roughness are distinguished, which finally form a composite roughness value. In both cases, the number of degrees of freedom increases dramatically, making the calibration task extremely complex and ambiguous. Although the floodplain roughness may exhibit remarkable spatial variation due to inhomogeneous vegetation patterns, a unique roughness value per cross-section was assigned. A distinction of

**Table 4.4:** *Discharge ($Q$ in $[m^3\ s^{-1}]$) and corresponding return periods ($T$ in $[a]$) for flood events used for calibration and validation of the EPDRiv1h model. The return period is determined from the GEV distribution fit to the discharge time series using the L-moment method.*

| **Discharge/Return period** | **Flood events** | | | | |
|---|---|---|---|---|---|
| | **01.1995** | **11.1998** | **03.1999** | **02.2002** | **01.2003** |
| $Q_{Dresden}$ | 1227 | 1640 | 1645 | 1598 | 2078 |
| $T_{Dresden}$ | 1.62 | 2.65 | 2.67 | 2.52 | 4.79 |
| $Q_{Torgau}$ | 1160 | 1580 | 1620 | 1520 | 2060 |
| $T_{Torgau}$ | 1.71 | 3.2 | 3.41 | 2.9 | 7.15 |
| $Q_{Wittenberg}$ | 1290 | 1730 | 1630 | 1730 | 2120 |
| $T_{Wittenberg}$ | 2.03 | 3.83 | 3.28 | 3.83 | 7.42 |

different roughness intervals along the cross-section profile would further complicate the calibration procedure. It would, presumably, aggravate the equifinality problem, without providing a robust parameter set, when taking into account the available constraining observations.

The event in January 1995 slightly exceeds the $T = 2$ threshold only at gauge Wittenberg. At the 2-year discharge the flow in natural streams stays predominantly in the river bed filling the bankfull channel cross-section (Leopold et al., 1964). Naturally, this relationship exhibits certain variability. Since the model is aimed at simulation of high magnitude events with considerable over-bank flow, it was calibrated on higher magnitude events in the years 1998, 1999 and 2002. The simulated water stages for the event in 1995 were additionally compared to the high water marks. The return periods of events listed in Table 4.4 do not exceed $T = 10$. It should be noted that the events considered for calibration are too small to provide a robust model parameterisation intended for high flow predictions. However, it was not feasible to calibrate the Manning's roughness over a large spectrum of flood magnitudes because of the absence of reliable high water stage records. The uncertainty of parameterisation can be reduced subject to available constraining observations for high magnitude events. The only high water marks provided for an extreme event were recorded during the August flood in 2002. However, the constraining power of this data is severely limited by the processes of dike overtopping and failure accompanied by significant water outflow into the hinterland. Therefore these measurements cannot be used for model calibration and/or evaluation.

The roughness coefficients were varied in the range between $0.017$ and $0.2\ m^{-1/3}\ s^{-1}$ corresponding to the physically possible values for natural channels and floodplains. Similar intervals were used for roughness value calibration in the works of Aronica et al. (1998a) and Werner et al. (2005b). The friction coefficients were manually adjusted in order to achieve the best possible fit between the simulated and observed water stages. Comparison between the calibrated and observed water stages along the Elbe reach is depicted in Figures B.1 and B.2. The steady-state model was validated on the January 2003 event. The fit was characterised by four performance statistics: $BIAS$, mean absolute error ($MAE$), root mean square error ($RMSE$) and maximum difference ($MD$). The latter is defined according to Eq. 4.1.

$$MD = \begin{cases} max(P-O), & \text{if } abs(max(P-O)) > abs(min(P-O)); \\ min(P-O), & \text{if } abs(max(P-O)) < abs(min(P-O)). \end{cases} \tag{4.1}$$

where $P$ – vector of predicted water levels or discharges, $O$ – vector of observed water levels or discharges.

Table 4.5 provides the summary of model performance statistics achieved during steady-state calibration and validation. Calibration results exhibit a rather low bias of few centimetres at maximum. The bias for the validation run is less than $0.01\ m$, which indicates almost no systematic under- and over-prediction. The mean absolute error is very similar to the root mean square error. This indicates a low variance in the individual errors. The $RMSE$ will always be larger or equal to the $MAE$. For the low magnitude event in 01.1995 the difference between $MAE$ and $RMSE$ increases. This corresponds to the high individual errors, which are pennalized by the $RMSE$. The calibration results are considered to be acceptable, since for the larger magnitude events as well as for the validation event, the $RMSE$ lies within the uncertainty range of the water stage measurements. The maximum difference between the simulated and observed water stages ranges between $-0.72$ and $0.566\ m$ (Table 4.5) with low value for low magnitude event. The maximum difference for the validation event is $0.531\ m$. This value occured in a strongly meandering part of the reach, where the 1D approach has a pronounced weakness.

**Table 4.5:** *Calibration and validation statistics for steady-state EPDRiv1h model runs for the reach between gauges Dresden and Vockerode. The flood events in 1995, 1998, 1999 and 2000 were used for calibration. The model was validated on data for the flood event in 2003.*

| **Performance statistics** | **Flood events** | | | | |
|---|---|---|---|---|---|
| | **01.1995** | **11.1998** | **03.1999** | **02.2002** | **01.2003** |
| $BIAS$ | $-0.048$ | $-0.004$ | $-0.003$ | $0.032$ | $0.003$ |
| $MAE$ | $0.16$ | $0.121$ | $0.118$ | $0.101$ | $0.136$ |
| $RMSE$ | $0.218$ | $0.156$ | $0.161$ | $0.134$ | $0.169$ |
| $MD$ | $-0.719$ | $0.467$ | $0.566$ | $0.5$ | $0.531$ |

The variation of differences in water level for the validation event is comparable to the calibration runs and somewhat higher. The median difference is about zero (Figure 4.4). The difference in water stage for $80\%$ of locations does not exceed $\pm 0.23\ m$ for the high magnitude calibration events and for the validation event. It seems to be reasonably accurate taking into account the reach length of about $90\ km$ and the negligence of the distributed lateral inflow. The maximum difference of $0.531\ m$ is observed in downstream part of the reach (Elbe-Km $221 - 240$), where the performance is generally poorer (Figure B.2).

The resulting distribution of the effective roughness coefficients along the reach is shown in Figure 4.5. The roughness coefficient exhibits a sharp change at Elbe-Km 221.6, which is caused by a widening of the floodplain from about $2000\ m$ to more than $5000\ m$ at several cross-sections between Elbe-Km $221.6 - 241$. The widely extended cross-sections incorporate a densely vegetated floodplain that may contribute to an extremely high calibrated Manning's value of up to $0.2\ m^{-1/3}\ s^{-1}$.

Furthermore, the channel meandering, that is strongly pronounced in this part of the reach (Figure 4.1), may increase the n-values by $30\%$ and greater depending on the meander curvature and the ratio of meander length to the straight length of the reach, as reported by Chow (1959) and Greenhill and Sellin (1993) from experimental evidence and confirmed by Werner and Lambert (2007) based on numerical investigations. With respect to 1D hydrodynamic models of compound channels, Werner and Lambert (2007) argue that additional reduction of discharge capacity results from momentum loss due to secondary currents, crossing flows and complex momentum interchange between channel and floodplain. The relative discharge error may reach up to $35\%$, comparing approaches with and without momentum interactions resolved depending on the flow depth and floodplain roughness. This additionally contributes to the increase in the calibrated roughness of the reach, where these processes are believed to play a role

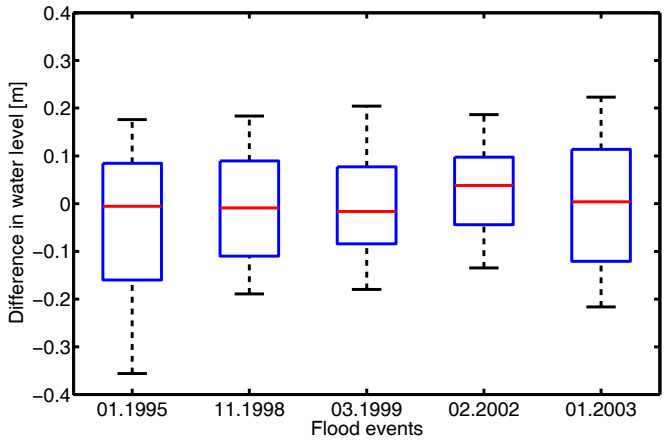


**Figure 4.4:** *Box-whisker plots of the absolute difference in predicted and observed water levels along the Elbe reach between gauges Dresden and Vockerode. Flood events in 1995, 1998, 1999 and 2000 were used for calibration. The steady-state model was validated on data of the flood event in 2003. Red line indicates the location of median, blue boxes correspond to the interquartile range and whiskers to the* $10^{th}$ *and* $90^{th}$ *percentiles.*

for the larger events with over-bank flow. Furthermore, the roughness parameterisation compensates for

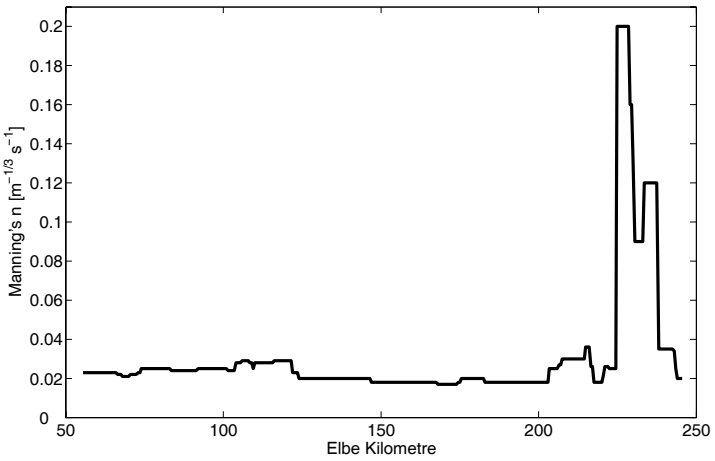


**Figure 4.5:** *Distribution of the calibrated Manning's roughness coefficient along the study reach.*

errors in topography representation by manually derived cross-sections as discussed in Sect. 4.3.

The calibrated high roughness values indicate a poor representation of the meandering part of the model domain by the 1D approach. It challenges the pertinence of the one-dimensional flow description for the case of a meandering channel on a wide floodplain. Aronica et al. (1998b) and Wilson et al. (2002) suggest that a full 2D modelling approach would be more suitable in cases when the overland flow "cuts" the meander as it accounts for turbulent momentum losses. However, the 2D approach seems to be nonviable for the scale of the presented study. The preferential flow on the floodplain, indicated by the numerical experiments in Figure 4.3, can possibly be represented by a branched 1D approach to

better capture the reach hydrodynamics.

#### 4.3.1.2 Unsteady model validation

The unsteady hydrodynamic model was set up for the reach Dresden-Vockerode and driven by the mean daily discharge provided by the LfUG at the Dresden gauging station for the validation event in 2003. At the downstream end of the reach, the stage-discharge relationship was used as boundary condition. Based on data provided by Nestmann and Büchele (2002), the depth-discharge relationship in Eq. 4.2 was derived for the gauge Vockerode, whereas a correlation coefficient of $R^2 = 0.99$ was achieved.

$$d = 0.5089 \cdot Q^{0.3532} \tag{4.2}$$

The discharge records at gauges Cotta, Garsebach, Niederau, Piskowitz, Merzdorf and Löben located at Elbe tributaries (Figure 4.2) were considered as lateral inflow boundary conditions. For the gauge Löben, a correction factor of $1.224$ was applied, since it is located $\sim 20\ km$ away from the confluence. The factor was computed using the drainage-area ratio method (Stedinger et al., 1992), which assumes that the discharge at the site of interest can be estimated by multiplying the discharge of a nearby gauge with the ratio of the drainage area of the site of interest and the drainage area of the gauge. The drainage basin was delineated on $25 \times 25\ m$ DEM using the ArcHydro software package (Maidment, 2002).

Unsteady validation run was performed for the period between 29.12.2002 and 28.01.2003. The hydrographs were compared to the mean daily discharge and hourly water stage records at gauging stations (Figure B.3). The performance statistics, including $BIAS$, $MAE$, $RMSE$, difference of peak values ($PD$), and Nash-Sutcliffe efficiency ($NSE$) (Nash and Sutcliffe, 1970), is summarised in Table 4.6.

**Table 4.6:** *Performance statistics for unsteady EPDRiv1h validation run between gauges Dresden and Vockerode for the 2003 flood event. Simulated discharge (Q) values are compared to the daily mean observed discharge. Simulated water levels (H) are compared to the mean hourly records.*

| **Gauges** | **Performance statistics** | | | | |
|---|---|---|---|---|---|
| | $BIAS$ | $MAE$ | $RMSE$ | $PD$ | $NSE$ |
| $H_{Meissen}$ | $-0.23$ | $0.23$ | $0.26$ | $-0.31$ | $0.96$ |
| $H_{Riesa}$ | $0.15$ | $0.15$ | $0.17$ | $0.097$ | $0.98$ |
| $H_{Mühlberg}$ | $-0.34$ | $0.36$ | $0.41$ | $0.004$ | $0.9$ |
| $H_{Torgau}$ | $-0.6$ | $0.61$ | $0.68$ | $-0.14$ | $0.75$ |
| $Q_{Torgau}$ | $-83.19$ | $85.53$ | $98.25$ | $-89.8$ | $0.96$ |
| $H_{Pretzsch-Mauken}$ | $-0.09$ | $0.2$ | $0.23$ | $-0.3$ | $0.95$ |
| $H_{Wittenberg}$ | $-0.46$ | $0.49$ | $0.67$ | $-0.03$ | $0.24$ |
| $Q_{Wittenberg}$ | $-81.11$ | $133.08$ | $171.46$ | $-16.6$ | $0.89$ |
| $H_{Coswig-Anhalt}$ | $-0.16$ | $0.4$ | $0.44$ | $-0.53$ | $0.8$ |
| $H_{Vockerode}$ | $-0.39$ | $0.39$ | $0.43$ | $-0.33$ | $0.83$ |

The simulated water stages show consistent underprediction characterised by the negative bias ranging between $-0.09$ and $-0.6\ m$. Only at gauge Riesa a slight tendency to overprediction is detected. The performance is spatially heterogeneous with poorer statistics at gauges Torgau and Wittenberg. However, the $NSE$ varies in the acceptable range between $0.75$ and $0.98$, except for the gauge Wittenberg with $NSE = 0.24$. Water stage predictions at this gauge indicate a striking discrepancy at lower water stages, despite acceptable predictions of the peak water level ($PD = -0.03$). This divergence significantly degrades the performance statistics at this location (Table 4.6). The error results, most probably, from the

poor surveyed topography of the river bed or from local cross-section transformation due to construction activities in the period between survey and water stage records. The difference in water level diminishes sharply at discharges above $1200 - 1300\ m^3\ s^{-1}$ that correspond to the bankfull discharge (Table 4.4). A thorough examination of the neighbouring cross-sections suggests that this discrepancy is a local effect at this particular cross-section. It becomes insignificant as soon as the water level is largely controlled by over-bank flow, as it is the case for extreme flood events.

The water stages at gauges Coswig-Anhalt and Vockerode, downstream of Wittenberg, are underpredicted with $RMSE$ of $0.43 - 0.44\ m$ and $NSE$ of $0.8 - 0.83$. This undeprediction can be related to the error in channel and floodplain representation by manually derived cross-sections. In the generated cross-section profiles the conveyance (Eq. 2.6) seems to be overestimated, although the calibrated roughness reaches the maximum physically plausible value for some profiles (Figure 4.5) and partially compensates for errors in geometry. The peak water stages are underestimated by up to $0.53\ m$. This can result in an underestimation of dike breach probability and flood hazard in this part of the reach.

The variation in performance over time exhibits different patterns. While the rising limb and peak stage are acceptably predicted for a number of hydrographs, the performance deteriorates for the falling limb. This can be explained by the unconsidered diffused lateral inflows that become increasingly important over a long river stretch. Although matching the peak flow satisfactorily, the discharge hydrograph at Wittenberg indicates an increased frictional resistance causing the time shift in peak flow and falling hydrograph limb. The apparent volume error in the recession hydrograph limb is likely due to unconsidered diffused lateral inflow. The volume error, however, remains almost invariable on the reach between Torgau and Wittenberg with $7.95\%$ and $7.28\%$, respectively. Consideration of the diffused lateral inflow requires a distributed input from a rainfall runoff model and is not considered in the scope of this work.

The validation run, performed with the unsteady hydrodynamic model, indicates an acceptable model performance in the upstream part of the reach till gauge Torgau and for the gauge Pretzsch-Mauken with respect to discharge dynamics and peak prediction. Performance deteriorates at gauge Wittenberg and further downstream. Underprediction of the water level peak is to be expected for the reach downstream of Elbe-Km 221.

## 4.4 Dike breach model setup and sensitivity analysis

### 4.4.1 Dike input data and pre-processing

Dike data for the German part of the Elbe reach were compiled by Jankiewicz et al. (2005) in the ElbeDSS project. The data were provided in form of a georeferenced ESRI point shape file, with points located on the crest of the dikes in intervals between 50 and 250 $m$. Elevated banks were also represented by shape points and distinguished from the dike points by the respective attribute value. The shape file was supplied with an attribute table, which contains information on dike height and geometrical properties such as

- crest height $[m]$
- crest width $[m]$
- inner or downstream slope $[-]$
- outer or upstream slope $[-]$
- absolute dike height $[m\ asl]$
- absolute height of upstream toe $[m\ asl]$

- absolute height of downstream toe [$m\ asl$].

The provided information was complemented by dike survey data from Saxony-Anhalt (Macke, 2001) and Saxony (LTV, 2006). It should be noted that the dikes were surveyed at different times. The dike data from Saxony-Anhalt correspond to the old non-strengthened dikes, whereas data from Saxony partly reflect the new reconstructed dikes after the August 2002 flood. At the moment of data acquisition, only a part of the dikes in Saxony was reinforced. Hence, the dike properties comprise an inconsistent data set. Unfortunately, no up-to-date data for the dikes in Saxony-Anhalt was available.

An additional attribute describing the dike turf quality ($f_g$) was introduced as required for the overtopping reliability model (Sect. 3.3.1). It was assumed to be $1.05$ for recently reinforced dikes and $0.5$ for old dikes and dikes of unknown state.

For the modelling purpose, the dike shape was interpolated using the DikeTOPO software tool (Sect. 3.1.5) to the grid size of $50\ m$. This ensures a continuous course of dike/elevated bank data (Fig. 4.1) when the dike raster is constructed from the point shape file as required for the input (Sect. 3.1.5). Further, DikeTOPO was applied to discretise the dike shape into sections of about $500\ m$ length as suggested in Sect. 3.1.5. Each section was assigned a unique identifier used throughout the modelling.

Chainage of the dike sections, i.e. setting up the correspondence between the sections and 1D river nodes, was carried out in the next step. The appropriate kilometre value, as discussed in Sect. 3.1.5, was assigned to the central point of each section. Finally, mean and standard deviation of dike geometry characteristics were determined for each discretised dike section and also attributed to the central section point. The resulting attribute table was further used for computing fragility functions (Sect. 4.4.2-4.4.4).

While measured dike geometry data were available for most of the dike sections in the study area, information on the geotechnical properties of dike core and foundation material is scarce. Therefore, respective model parameters had to be adopted from literature review and derived from scarce indications available for the site or from comparable dikes. The range of parameter variation can be restricted to the physically possible interval, whereas the mean value is uncertain for the dike under study. Therefore the sensitivity analysis was carried out and aimed at investigating the impact of mean location within the variation range onto the fragility functions. The analysis should highlight for each breach mechanism sensitive geotechnical parameters, which require a special attention during measurement campaigns and model setup. Propagation of parameter uncertainty through the IHAM would provide an estimate of the sensitivity of hazard statements. However, this, currently, represents an unfeasible computational task. Hence, the analysis was restricted to the sensitivity of fragility functions for a particular exemplary right-side dike section at Elbe-Km $162.45$. Since no spatially distributed geotechnical parameter values were available, the sensitivity analysis for a single dike section seems to be appropriate.

### 4.4.2 Fragility curves for overtopping

The reliability function for overtopping (Eq. 3.5) was randomised in a Monte Carlo simulation to derive fragility functions. Dike properties, treated as stochastic variables, were sampled from the distribution functions using the mean and standard deviation provided in Table A.1. Observed dike properties were used where available. In the other case, an estimation based on literature review was adopted (Table A.1). The employed probability distribution functions for each dike property were taken from Vrijling and van Gelder (2000) and Kortenhaus and Oumeraci (2002) as used in dike reliability analyses. However, the unconstrained nature of the normal and log-normal distribution would necesserily result in the generation of values beyond the physically possible range. Therefore a physically plausible range of variation was introduced to confine the randomly generated parameter values resulting in a trancated probability distribution function.

The overtopping failure is conditioned by two load variables: overtopping height ($h_e$) and overtopping duration ($t_e$). Hence, the fragility function is a surface indicating the failure probability in the

$(h_e, t_e)$ space. For each $(h_e, t_e)$-point in space, $10^4$ random samples of the stochastic variables were generated. The evaluation of the reliability function provides a fragility surface for each discretised dike section. A fragility surface for overtopping failure is demonstrated in Figure 4.6 for an exemplary dike section.

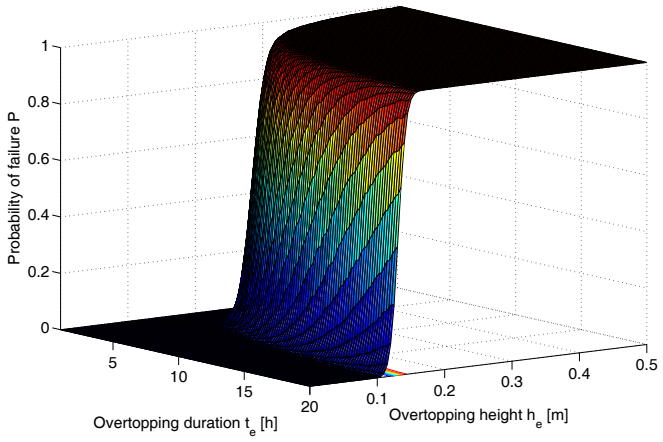


**Figure 4.6:** *Fragility surface for overtopping failure for the right dike section at the Elbe-Km* 162.45.

The number of random samples was selected by a trail and error procedure in order to obtain a smooth fragility surface. Finally, it was weighted against the computational time requirements in order to keep the procedure tractable.

For a range of loading conditions with very small overtopping height, below $0.1\ m$, the failure probability is $0$, even for long duration. The surface is further characterised by a very strong sensitivity to the overtopping height between $0.1$ and $0.2\ m$ and overtopping durations of several hours. For overtopping heights above $0.5\ m$ nearly immediate failure occurs, which is characterised by the probability of $1$.

### 4.4.3 Fragility curves for piping

Fragility functions for the mechanism of piping were developed according to the algorithms described in Sect. 3.3.2. Distributions of stochastic parameters, as well as selected mean, standard deviation and variation range of the reference model version are summarised in Table A.1.

#### 4.4.3.1 Seepage through dike foundation

Probability of dike foundation seepage was derived taking the duration of impoundment as a load variable. The duration was discretised into 3 intervals for water levels up to $1/3$, $1/3 - 2/3$ and $2/3 - 1$ of a dike height in order to account for gradual impoundment. Applying the reliability function for seepage (Eq. 3.23) the probability of seepage is derived as a function of 3 variables $(D(0 - 1/3h_0), D(1/3h_0 - 2/3h_0), D(2/3h_0 - h_0))$, whereas impoundment duration for each level was ranged between 0 and 10 days in 1 day steps. The projections of the resulting probability volume into the $(D(0 - 1/3h_0), D(1/3h_0 - 2/3h_0), P)$ space represent the probability surfaces for $D(2/3h_0 - h_0) = 0\ days$ and $D(2/3h_0 - h_0) = 9\ days$ (Figure 4.7).

The hydraulic conductivity of the foundation material was treated as a stochastic variable with the mean $\mu(K_f) = 3{\cdot}10^{-5}\ m\ s^{-1}$, which corresponds to fine/medium sands (Berry and Reid, 1987; Bollrich, 2000). The standard deviation was taken as $\sigma(K_f) = 25 \cdot \mu(K_f)$ as suggested by USACE (1999). The

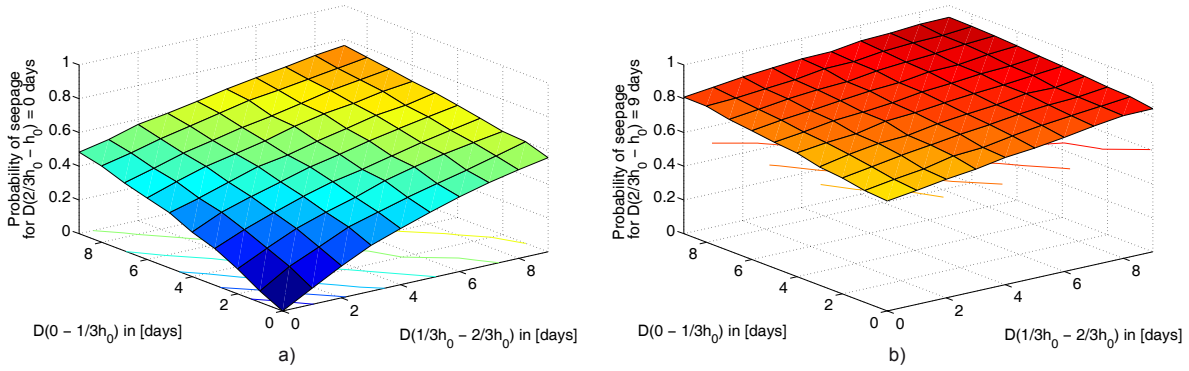


**Figure 4.7:** *Fragility surfaces for seepage through the foundation for the right-side dike section at the Elbe-Km* 162.45 *(*$\mu(K_f) = 3 \cdot 10^{-5}\ m\ s^{-1}$*). Projection of the fragility volume into the* $(D(0 - 1/3h_0), D(1/3h_0 - 2/3h_0), P)$ *space for (a)* $D(2/3h_0 - h_0) = 0\ days$ *and (b)* $D(2/3h_0 - h_0) = 9\ days$.

$K_f$ values were constrained by two orders of magnitude around the mean value. $K_f$ was assumed to follow the lognormal distribution. Fenton and Griffiths (1996) provides a literature review supporting this assumption, which was also adopted by Pohl (1999).

The parameters of the lognormal distribution (mean and standard deviation of $ln\ x$) were derived from adopted sample mean and standard deviation using Eq. 4.3 and 4.4.

$$\sigma_{ln\ x} = \sqrt{ln(1 + \frac{\sigma_x^2}{\mu_x^2})} \tag{4.3}$$

$$\mu_{ln\ x} = ln(\mu_x) - \frac{1}{2}\sigma_{ln\ x}^2 \tag{4.4}$$

The probability surface was found to be rather sensitive to the selected mean value. This becomes apparent from the comparison of Figures 4.7 and 4.8, where the mean $K_f$ value was decreased by an order of magnitude.

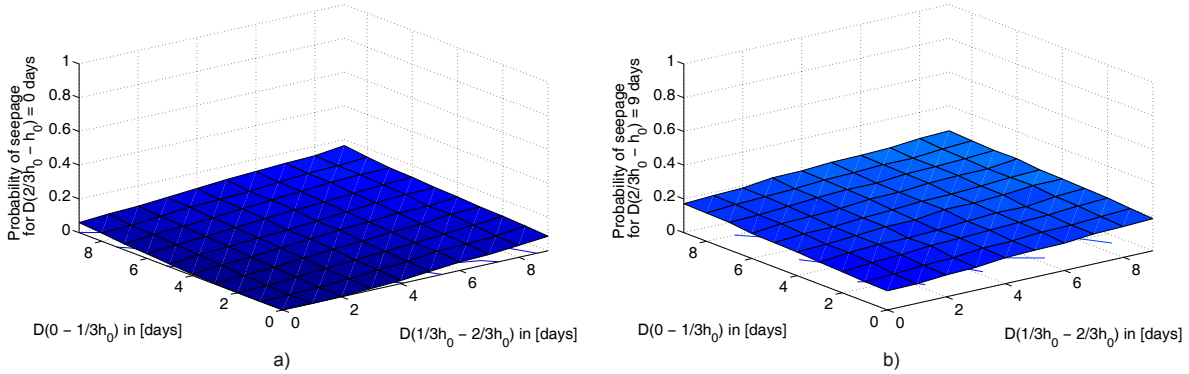


**Figure 4.8:** *Fragility surface for seepage through the foundation for the right-side dike section at the Elbe-Km* 162.45 *(*$\mu(K_f) = 3 \cdot 10^{-6}\ m\ s^{-1}$*). Projection of the fragility volume into the* $(D(0 - 1/3h_0), D(1/3h_0 - 2/3h_0), P)$ *space for (a)* $D(2/3h_0 - h_0) = 0\ days$ *and (b)* $D(2/3h_0 - h_0) = 9\ days$.

Air-filled porosity was adopted based on data of Kanowski (1977) for Elbe dikes (Table A.1) with $\mu(n_a) = 0.188$, $\sigma(n_a) = 0.15\mu(n_a)$.

The local sensitivity analysis was performed based on the approach of Güntner and Bronstert (2004). The sensitivity of fragility function to the changes in the mean hydraulic conductivity and mean air-filled porosity was explored. The mean $K_f$ and $n_a$ values were varied in their likely ranges by using the multiplicator to the reference mean parameter value. The standard deviation was kept constant. The range of variation for air-filled porosity was set to $n_a \in [0.095; 0.288]$ (Kanowski, 1977).

The range of variation for hydraulic conductivity values spans over several orders of magnitude. The composition of the foundation sand may exhibit a strong variability with $K_f$ values from about $10^{-8}\ m\ s^{-1}$ for silty sands to $10^{-3}\ m\ s^{-1}$ for coarse sands (Berry and Reid, 1987; Bollrich, 2000). However, within a single dike section such a strong variabily might be unlikely. Therefore the range of variation for the $K_f$ values of one order of magnitude around the mean was adopted, as also implemented by Pohl (1999). The mean was than varied between $3 \cdot 10^{-7}\ m\ s^{-1}$ and $3 \cdot 10^{-4}\ m\ s^{-1}$. The resulting percentage change of seepage probability is indicated over the complete load space in a form of box-whisker plots (Figure 4.9).

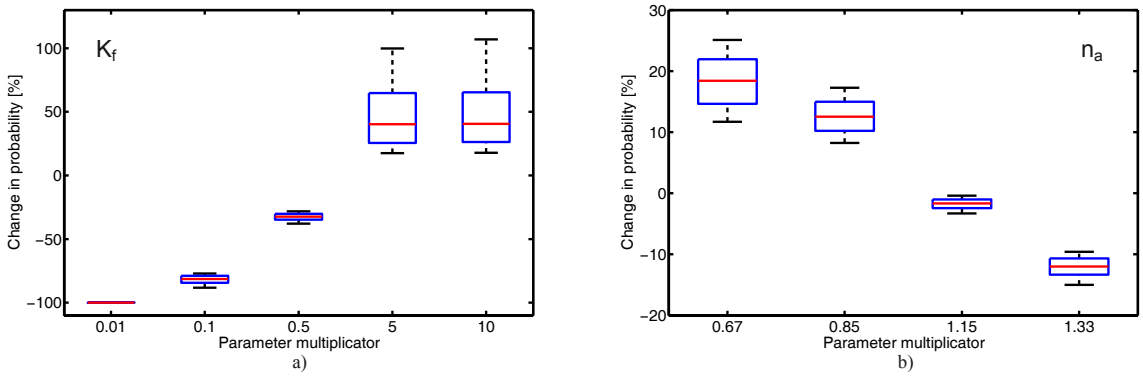


**Figure 4.9:** *Sensitivity analysis of seepage probability to the mean (a) hydraulic conductivity and (b) air-filled porosity of the dike foundation material for the dike at Elbe-Km* 162.45*. Box-whisker plots for $K_f$ and $n_a$ indicate the percentage change in seepage probability over the complete load space as a function of parameter multiplicator (in this case* 1000 *load combinations). Boxes indicate the interquartile range, red line corresponds to the median and whiskers to the $10^{th}$ and $90^{th}$ percentiles.*

The change of mean hydraulic conductivity by one order of magnitude with respect to the reference value may result in up to $100\%$ change in probability for some loading conditions (Figure 4.9a). The median values range between approx. $-100\%$ for decreased and $40\%$ for increased mean hydraulic conductivity. The reduction of the variability of probability change for multiplicator $0.01$ is stipulated by the nature of the probability quantity, which is constrained in the $[0; 1]$ interval. For this reduction of $K_f$, 0 seepage probability is expected for the majority of loading conditions. On the other side, the almost constant variability of probability change for increased mean $K_f$ indicates that for the majority of loading conditions the maximum seepage probability of 1 is expected.

Relating the sensitivity to the range of $K_f$ values encourages special attention to measuring and selecting the hydraulic conductivity value for fragility curve development.

Although the seepage probability exhibits a high sensitivity to the selected mean antecedent air-filled porosity (Figure 4.9b), the range of variation of $n_a$ is well-restricted by observations. So, the overall variation of probability change $(-20; +30\%)$ is smaller compared to the variation due to uncertainty of $K_f$.

The variation of mean value within a likely parameter range produces uncertainty bounds for fragility functions. Consideration of these bounds in flood risk analysis was proposed by Sayers et al. (2002). This uncertainty, propagated through the proposed IHAM model structure, could be reflected in flood hazard statements. However, currently, this appears to be an overwhelming computational task.

#### 4.4.3.2 Rupture

The rupture model (Sec. 3.3.2.2) was parameterised based on the data provided by Vrijling and van Gelder (2000); Gocht (2002); Kortenhaus and Oumeraci (2002) and summarised in Table A.1. The mean weight per volume of clay soil was adopted at $\mu(\gamma_k) = 19\ kN\ m^{-3}$ and standard deviation $\sigma(\gamma_k) = 0.05\mu(\gamma_k)$. The range of variation was restricted to $\gamma_k \in [17; 21]$.

No information was available about the mean clay layer depth for the study reach. Therefore the range of variation $d \in [0; 3]$ was assumed for the whole study reach based on indications of Gocht (2002) and assumptions of Vrijling and van Gelder (2000). The mean depth of a clay layer was taken in the reference model version at $\mu(d) = 1\ m$ with $\sigma(d) = 0.3\mu(d)$ (Vrijling and van Gelder, 2000).

The subsequent sensitivity analysis (Figure 4.10) indicates the impact of the selected mean values of $d$ and $\gamma_k$ on the rupture probability for an examplary dike section. $10^5$ Monte Carlo runs were performed for each of the 100 load steps ranging from foot height till foot height plus 5 metres. The fragility function thus indicates the failure probability up to a hypothetical load with a water column of $5\ m$ above the dike foot. The failure probability is then calculated in the core Monte Carlo simulation based on the actual load.

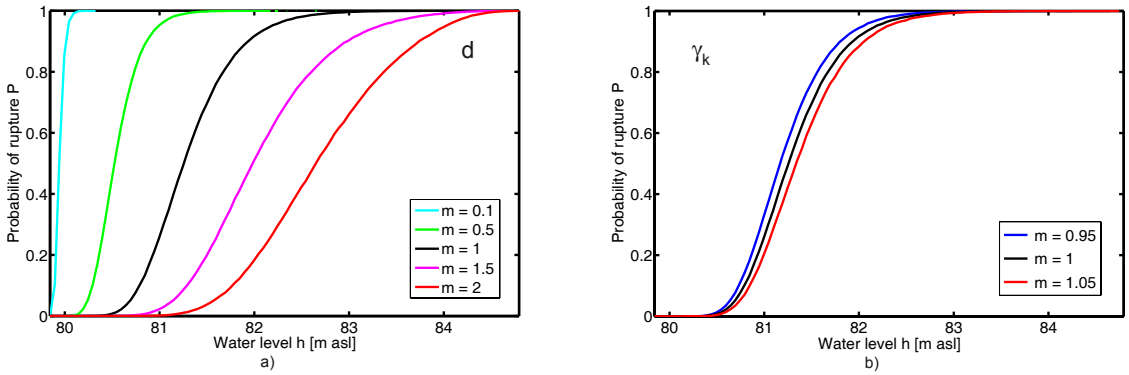


**Figure 4.10:** *Sensitivity of rupture probability to the mean value of(a) clay layer thickness and (b) weight per volume of clayey soil for the dike section at Elbe-Km* 162.45. *$m$ represents a multiplicator applied to the parameter value in the reference model version (Table A.1).*

Figures 4.10a,b indicate a much greater model sensitivity to the location of the mean clay layer thickness within the variation range compared to the weight per volume of clay soil, which is rigorously constrained in a narrow interval. The high sensitivity indicates a necessity for exploring the clay layer thickness along the fluvial dikes.

#### 4.4.3.3 Piping

The hydraulic load in terms of impoundment water level determines the progress of piping in a sandy dike foundation. The fragility functions for piping were computed based on Eq. 3.31, which employs the model of Weijers and Sellmeijer (1993) (Eqs. 3.37-3.39). They indicate the probability of reaching

the critical state of pipe development, beyond which no equilibrium is possible, resulting in continuous retrogressive erosion. The seepage path $L$ was assumed to be the length of the dike foundation $b_f$. This conservatively implies a rupture directly behind the downstream dike toe. The reference critical head model was parameterised based on measured indicative values and literature data summarised in Table A.1. For several stochastically treated variables, such as the thickness of the sand layer, weight per volume of sand particles, hydraulic conductivity, friction angle and particle diameter of $70\%$-weight fraction, the sensitivity of the piping probability to the selected mean was analysed for an examplary dike section.

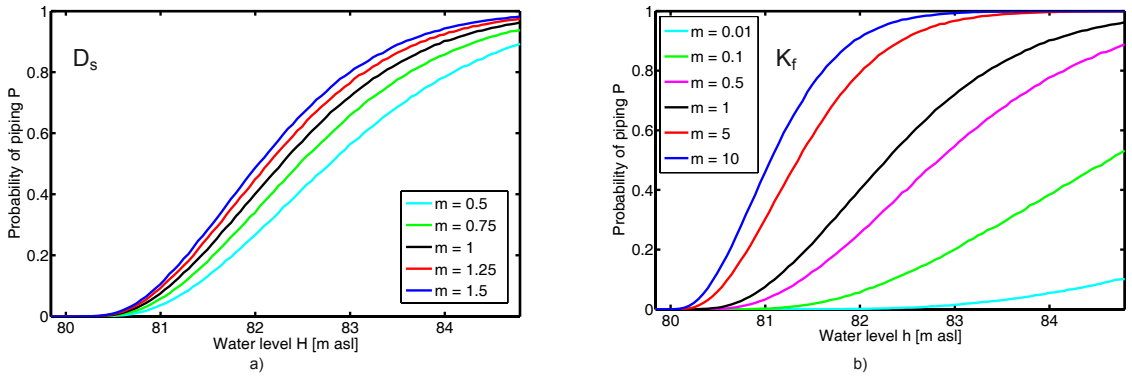


**Figure 4.11:** *Sensitivity of piping probability to the mean value of (a) sand layer thickness and (b) hydraulic conductivity of the sand layer for the dike section at Elbe-Km* 162.45. $m$ *represents a multiplicator applied to the parameter value in the reference model version (Table A.1).*

Figure 4.11a demonstrates the sensitivity of piping probability to the thickness of the sand layer. Interestingly, the increase of thickness does not result in an increase of probability at the same rate. The model reflects intuitively correct the process of piping: although the thicker aquifer can conduct more water, the upward flow path length becomes larger, which reduces the probability of piping. The range of probability variation due to changes in the sand layer thickness is comparably smaller than due to changes in thickness of the clay layer and hydraulic conductivity within the range of possible values. The mean selected $K_f$ value shows a very pronounced impact on the piping probability, similarly to the effect on seepage fragility functions.

The piping probability exibits a relatively high sensitivity to the change in mean weight per volume of foundation material (Figure 4.12b). It appears to be stronger than the sensitivity to the mean friction angle $\theta$ altered by comparable parameter multiplicator values (Figure 4.12a).

The uncertainty in the mean particle diameter $d_{70}$ may also considerably influence the piping probability (Figure 4.13). Comparing the fragility curves for $m = 0.5, 1$ and $1.5$ reveals that for lower loads, piping is stronger favoured for material with finer $70\%$-weight fraction, whereas the coarser mean $d_{70}$ does not decrease the piping probability at the same rate. However, opposite holds at high water levels, where the fragility function for $m = 0.5$ reaches its maximum of 1.

#### 4.4.3.4 Pipe development

As soon as the critical impoundment height is reached continuous erosion takes place, which leads to the formation of a slit in the dike foundation. The reliability function for pipe development (Eq. 3.40) was evaluated in $10^4$ Monte Carlo realisation at each time discretisation point between $0 - 200$ $h$ for each dike section. A resulting fragility curve indicates the probability of a slit reaching a critical length. The

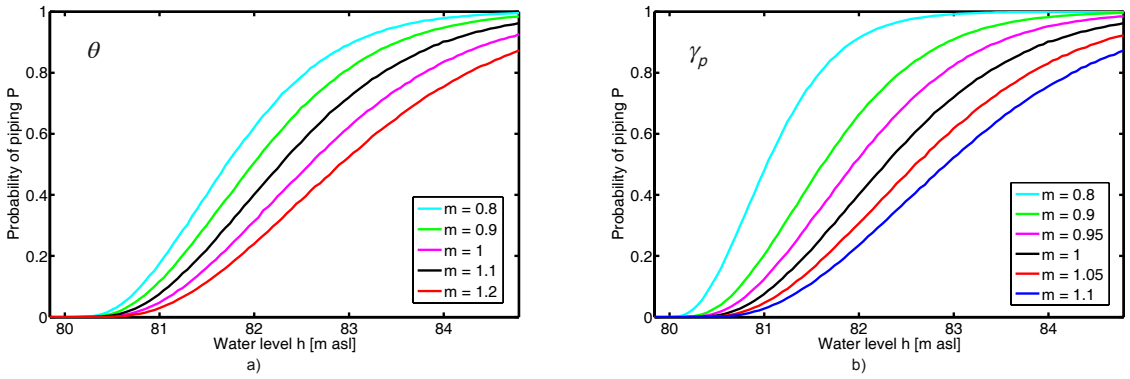


**Figure 4.12:** *Sensitivity of piping probability to the mean value of (a) friction angle and (b) weight per volume of the sandy material for the dike section at Elbe-Km* 162.45. $m$ *represents a multiplicator applied to the parameter value in the reference model version (Table A.1).*

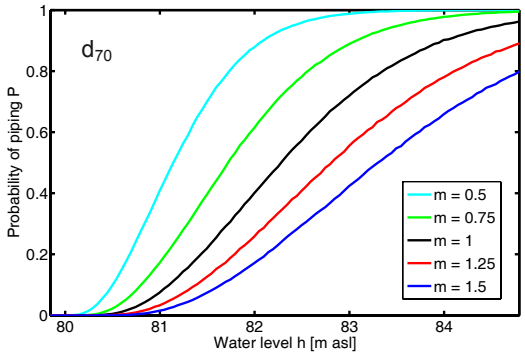


**Figure 4.13:** *Sensitivity of piping probability to the mean value of particle diameter corresponding to* 70%*-weight fraction of foundation material for the dike section at Elbe-Km* 162.45. $m$ *represents a multiplicator applied to the parameter value in the reference model version (Table A.1).*

pipe devlopment rate was treated deterministically as discussed in Sect. 3.3.2.2. The stochastisity of the exceedance of critical length results from the variable dike geometrical parameters, such as inner and outer slopes, crest width and core height. These parameters finally determine the width of a dike foot. The supplementary sensitivity analysis explored the response of the fragility curve at Elbe-Km 162.45 to the pipe development velocity Figure 4.14. The changes in velocity by a factor of two revealed a dramatic variation in fragility for pipe development. It is currently unclear how strong the piping velocity may vary. The scarcity of experimental evidences and high sensitivity of fragility curves demand further investigations aimed on quantification of pipe development rates for different material types. A variation range of development rate could then be used as a stochastic parameter in development of fragility functions.

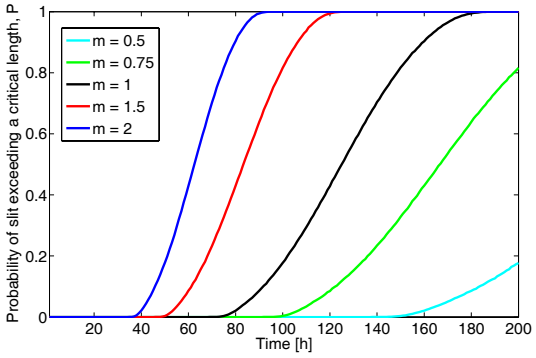


**Figure 4.14:** *Sensitivity of fragility curve for pipe development to changes in pipe development rate for the dike section at Elbe-Km* 162.45. $m$ *represents a multiplicator applied to the parameter value in the reference model version.*

### 4.4.4 Fragility curves for micro-instability

#### 4.4.4.1 Seepage through the dike core

The fragility functions for seepage through a dike core were computed in a Monte Carlo simulation applying the limit state function given in Eq. 3.43. Besides the dike geometry parameters, hydraulic conductivity and air-filled porosity of the dike core material were treated probabilistically.

Saturated hydraulic conductivity of the dike material can vary over several orders of magnitude. For the dikes on Elbe and Mulde breached during the August 2002 flood, Gocht (2002) provides indications of $K_f$ values ranging from $3 \cdot 10^{-4}$ to $10^{-8}$ $m\ s^{-1}$. Since detailed spatial information about the material properties was not available, an appropriate assumption had to be made.

The Elbe dikes were built over the past eight hundred years (IKSE, 2003). However, due to continuous change of the river course and settlement patterns, dikes were successively relocated and partially rebuilt. Present dikes were erected over the past 150 years and possess a historical core (BfG, 2002). Historical dikes are typically built from the locally available materials and exhibit, therefore, large inhomogeneity of material properties (Pohl, 2000a). Whereas the material properties of newer dikes are documented, the older dikes remain largely unexplored. Assuming a homogeneous dike structure within a single section, and adopting the hydraulic conductivities in historical dikes given by Pohl (1999) for the Oder River, a mean value of $\mu(K_f) = 10^{-5}\ m\ s^{-1}$ was assumed in the reference model version. $\sigma(K_f) = 25\mu(K_f)$ was taken based on USACE (1999). The range of variation was assumed to two orders of magnitude around the mean value with $K_f \in [10^{-6}; 10^{-4}]$. This range is comparable to that of the Oder River dikes with historical dike cores (Pohl, 1999). Air-filled porosity values were adopted from Kanowski (1977) and summarised in Table A.1.

Applying the model described in Sect. 3.3.3.1 in the pre-processing Monte Carlo simulation, a fragility volume for seepage probability was derived for every dike section. The fragility volume was computed in $2 \cdot 10^4$ Monte Carlo iterations for each load vector. Each load axis was discretised in 1 $day$ steps between $0 - 14$ days. Projection of the fragility volume into the $(D(0 - 1/3h_0), D(1/3h_0 - 2/3h_0), P)$ space results in fragility surfaces demonstrated in Figure 4.15 for $D(2/3h_0 - h_0) = 0\ days$ and $D(2/3h_0 - h_0) = 14\ days$.

The sensitivity analysis of seepage probability to the selected mean hydraulic conductivity indicates a considerable variation of the change in probability between $-100$ and $500\%$ (Figure 4.16a). Small variation of probability change at low values of mean $K_f$ (parameter multiplicators equal $0.1$ and $0.01$)

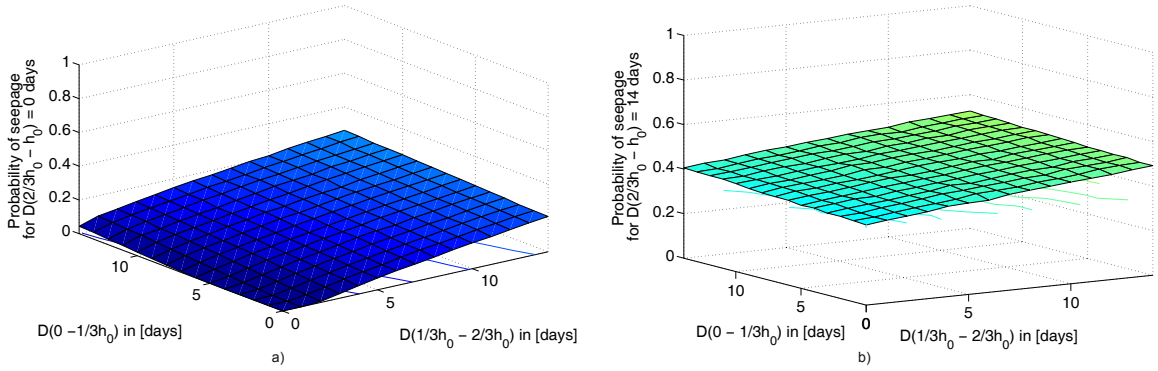


**Figure 4.15:** *Fragility surfaces for seepage through a dike core of the right-side dike section at Elbe-Km* 162.45. *Projection of the fragility volume into the* $(D(0-1/3h_0), D(1/3h_0-2/3h_0), P)$ *space for (a)* $D(2/3h_0-h_0)=0$ *days and (b)* $D(2/3h_0-h_0)=14$ *days.*

reflects the constrained nature of probability defined between $[0;1]$. For low mean $K_f$, the seepage probability tends to 0 even for larger load values. An increase of the mean hydraulic conductivity compared to the reference model (parameter multiplicator of 5 and 10) results in a sharp response of the fragility function towards higher seepage probability values.

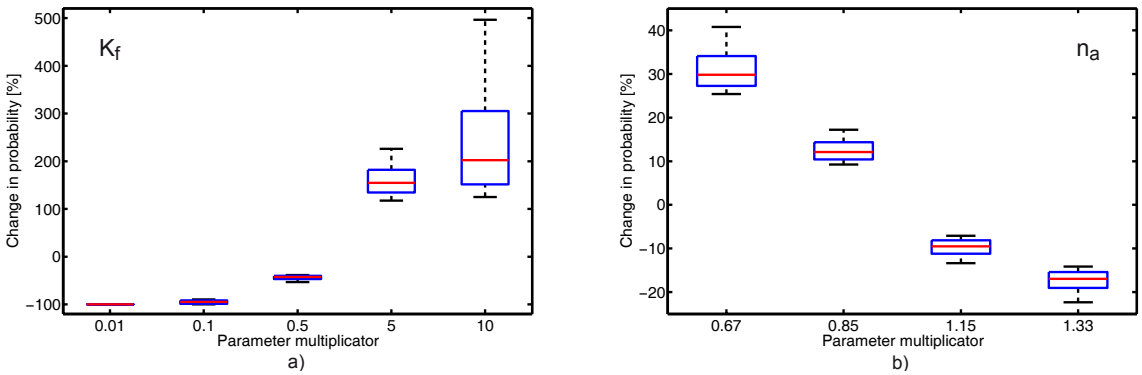


**Figure 4.16:** *Sensitivity analysis of seepage probability to the mean (a) hydraulic conductivity and (b) air-filled porosity of dike material for the right-side dike section at Elbe-Km* 162.45. *Box-whisker plots for* $K_f$ *and* $n_a$ *indicate the percentage change in seepage probability over the complete load space as a function of parameter multiplicator (in this case* 3375 *load combinations). Boxes indicate the interquartile range, red line corresponds to the median and whiskers to the* $10^{th}$ *and* $90^{th}$ *percentiles.*

The seepage probability reacts stronger to changes in mean air-filled porosity compared to hydraulic conductivity. However, the absolute variation of change in probability is smaller due to the relatively narrow $n_a$ parameter range (Table A.1). Nevertheless, a change of the average antecedent moisture content of a dike core directly related to the air-filled porosity may have a considerable impact on seepage probability.

The performed sensitivity analysis suggests that further efforts should, first of all, concentrate on reducing the uncertainty in hydraulic conductivity values, either by conducting field measurements or exploring available documentary records on dike construction materials.

#### 4.4.4.2 Slope micro-instability

The failure probability due to micro-instability is computed as a function of water level height at the dike outer slope (Eq. 3.46). $2 \cdot 10^4$ Monte Carlo realisations at each discretisation point of the load axis were found sufficient to obtain a smooth fragility curve. The $h$-axis was discretised in $0.05\ m$ steps between $0 - 5\ m$ related to the absolute dike foot height.

An example of a resulting fragility curve and its sensitivity to the mean value of the friction angle is shown for a selected dike section in Figure 4.17. The fragility curve for micro-instability reacts strongly

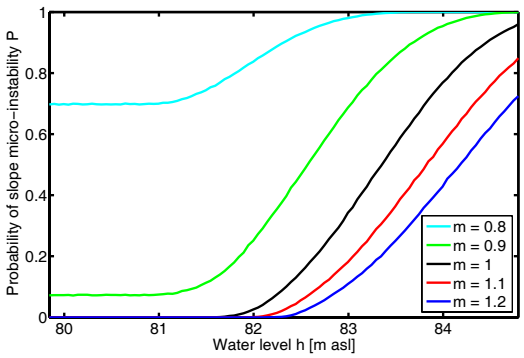


**Figure 4.17:** *Sensitivity of probability for slope micro-instability to the selected mean value of friction angle of the dike material for the right-side dike section at Elbe-Km* 162.45.

to changes in $\theta$. At lower mean values of friction angle ($m = 0.8$ and $0.9$), the non-zero probability of slope failure is observed even for low impoundment water levels. The frequency of the randomly sampled slope and friction angle pairs, which do not fullfil the static stability criterion given in Eq. 3.47, is increased in the Monte Carlo simulation with lower mean friction angle.

The fragility curve reacts sharply to a reduction of the mean friction angle. However, an increase of the mean $\theta$ by the same amount ($m = 1.1$ and $1.2$) does not lead to drastic reduction of failure probability. Firstly, it may be the constraining effect of the upper boundary set by the range of friction slope variation (Table A.1). Despite the increased mean parameter value, the randomly sampled friction angle values do not exceed the upper parameter bound and restrain probability reduction.

Secondly, with incresed mean the randomly generated pairs of friction angle and inner slope meet the static stability criterion (Eq. 3.47) more often. Thus, the impact of the friction angle on the slide height ($h_a$) becomes more pronounced (Eq. 3.48). This influence on the reduction of slope failure probability appears to be not strong.

### 4.4.5 Stochastic breach width modelling

As discussed in Sect. 3.3.4, deterministic predictions of breach width and development are highly uncertain. Therefore, an approach to stochastic breach width modelling in a Monte Carlo simulation was proposed and implemented in the IHAM (Sect. 3.3.4).

Dike breach records during the August 2002 flood in the Elbe catchment were used to construct an empirical breach width distribution (Figure 4.18). The data compiled by Horlacher et al. (2005) for the Saxonian part of the catchment was extended by data of Gocht (2002) for Saxony-Anhalt.

Table 4.7 summarises the ranges, mean and median for breach widths from different streams in the Elbe catchment. Table 4.7 indicates no great difference neither in the range nor in the mean value of breach widths observed on Mulde and Elbe. The breach widths on the Elbe reach tend to lower values

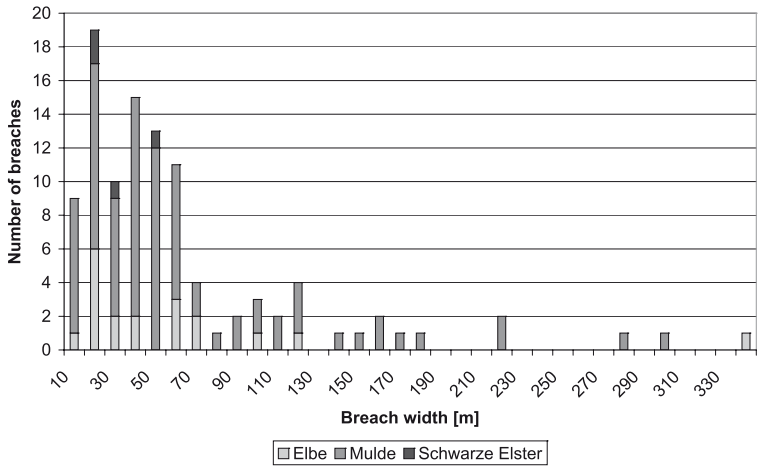


**Figure 4.18:** *Empirical frequency distribution of breach width for Elbe, Mulde and Schwarze Elster reaches during the August 2002 flood.*

**Table 4.7:** *Dike breach statistics from the August 2002 flood in the Elbe catchment based on data from Horlacher et al. (2005) and Gocht (2002)*

| River | Whole catchment | Elbe | Mulde | Schwarze Elster |
|---|---|---|---|---|
| Number of breaches | 104 | 19 | 81 | 4 |
| Mean $B_w$ | 62.88 | 60.53 | 65.06 | 29.5 |
| Median $B_w$ | 44 | 40 | 50 | 30 |
| Min $B_w$ | 5 | 10 | 5 | 18 |
| Max $B_w$ | 340 | 340 | 300 | 50 |

compared to Mulde that is indicated by a smaller median. This is probably due to the higher flood return period observed on the Mulde River compared to Elbe. The patterns of breach width distribution in the Elbe and Mulde reaches are similar (Figure 4.18). Hence, the whole observed sample was used to derive a theoretical probability density function of breach width. Additionally, four observed breaches from the Schwarze Elster stream were involved in the analysis.

Normal, log-normal, Weibull, beta and Pearson III distributions were examined and fitted to the observed sample. $\chi^2$ and Kolmogorov-Smirnov tests were employed to test the goodness of fit of the selected distribution functions. Both tests indicated that only in case of the log-normal distribution the null-hypothesis cannot be rejected with $1\%$ level of significance. The log-normal distribution with $\mu_{ln} = 3.77$ and $\sigma_{ln} = 0.86$ is fitted in Figure 4.19 to the observed breach width sample.

Breach width is sampled from the fitted distribution during the core Monte Carlo simulation. Thus, the uncertainty associated with the breach width can be accounted for in a probabilistic framework. Contrary to the limited range distributions, e.g. beta-distribution, the log-normal distribution is defined for values in the range $[0; +\infty)$. Hence, during the sampling procedure very small and very large values of $B_w$ can be generated. In such a case the truncation is applied by skipping values of $B_w < 3\ m$ and $B_w > 500\ m$. This eliminates implausibly small and large breach widths and sustains consistency with the discretisation step of ca. $500\ m$ for dike sections.

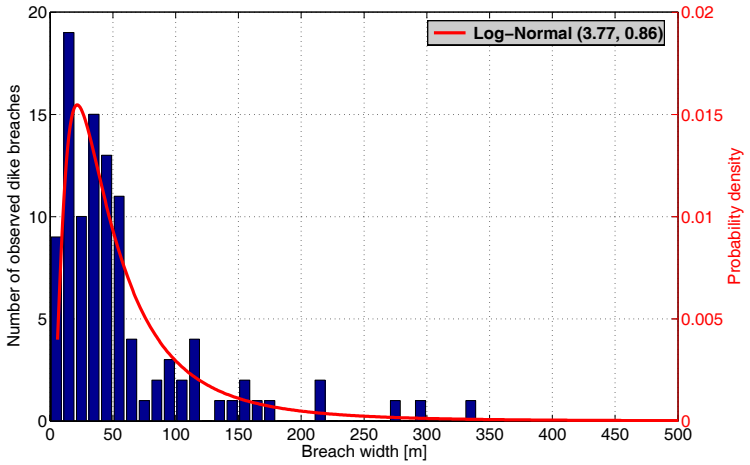


**Figure 4.19:** *Empirical frequency distribution of breach width in the Elbe catchment during the August 2002 flood and fitted log-normal probability density function* $(3.77,\ 0.86)$

## 4.5 Storage cell inundation model setup

### 4.5.1 Model parameterisation

The 2D storage cell inundation model described in Sect. 2.2.1 was setup for the study area between gauges Torgau and Vockerode (Fig. 4.1). The basis of the topographic terrain representation formed a $50 \times 50\ m$ digital elevation model with vertical accuracy of $\pm 1 - 5\ m$, comprised of heterogeneous data sources, such as digitised topographic maps, photogrammetric and laser scanned data (BKG, 2007). The digital elevation model was supplied into the IHAM model for the hinterland areas behind the dikes, where the 2D inundation modelling was intended.

Floodplain roughness parameterisation was accomplished by assigning literature values (Chow, 1959; Bollrich, 2000) to landuse classes (Table 4.8) based on ATKIS (Amtliches Topographisch-Kartographisches Informationssystem) and CORINE (COoRdinated INformation on the Environment) landuse data. For the areas of non-identified landuse the average roughness coefficient of $0.06$ was assigned as also applied in other studies for typical floodplain surfaces (Horritt and Bates, 2001a; Yu and Lane, 2006a).

With regards to the roughness parameterisation in urban areas, there exist two different approaches. Water flow can be seen to occur primarily in the streets that form a channel network. The streets are largely covered by asphalt and concrete, exhibiting relatively low roughness values adopted by some authors (Dutta et al., 2000; Neelz and Pender, 2007). Others consider urban areas as relatively rough in their modelling studies. Typical Manning's n assigned in this case range between $0.1$ and $0.12$ (Alkema and Middelkoop, 2005; Bradbrook et al., 2005). Sometimes even more extreme values of up to $0.2$ are used (Niemeyer et al., 2005). It seems that the first approach is applicable to the small scale urban modelling, where the model grid resolution can resolve dwellings and gaps between them. The latter one is suitable for less detailed reach-scale inundation models using coarse grid-resolution, typically coarser than $10 \times 10\ m$ (Neelz and Pender, 2007). At such grid sizes the model is unable to resolve single housings and other bulky objects and explicitly account for their inhibitive effect on flood propagation. This effect can be compensated by higher selected effective roughness values as indicated by the case studies in certain urban environments (Neelz and Pender, 2007). The value of $0.11$ was adopted here for the $50 \times 50\ m$ grid resolution. Another approach to account for sub-grid scale effects was recently

**Table 4.8:** *Manning's n roughness coefficients assigned to ATKIS and CORINE landuse classes*

| ATKIS Landuse classes | Manning's n | CORINE Landuse classes | Manning's n |
|---|---|---|---|
| Agricultural area | 0.035 | Agricultural areas | 0.035 |
| Pastures | 0.033 | Pastures | 0.033 |
| Gardens | 0.06 | Fruit trees plantations | 0.11 |
| Swamps | 0.05 | Peat, bogs | 0.05 |
| Forests | 0.11 | Forests | 0.11 |
| Sparsely vegetated areas | 0.03 | Sparsely vegetated areas | 0.03 |
| Urban areas | 0.11 | Urban areas | 0.11 |
| Recreation areas | 0.06 | Recreation areas | 0.06 |
| Water bodies | 0.03 | Water bodies | 0.03 |
| Roads | 0.013 | Roads | 0.013 |
| Forest aisle | 0.035 | Sands, Dunes, Beaches | 0.033 |
| Fallow | 0.05 | | |
| Other areas | 0.06 | | |

proposed by Yu and Lane (2006b). It applies a scheme based on water volume adjustment and porosity concept in order to account for changes in flux and flow blockage effects caused by sub-grid features. The approach, however, requires high-resolution topographic data in order to explicitly parameterise the sub-grid-scale topographic variability in the course model.

### 4.5.2 Model evaluation

In order to test the inundation model performance and explore the sensitivity to the roughness parameterisation, runs with the IHAM were performed to simulate the August 2002 flood event. The calibrated 1D hydrodynamic model for the Elbe channel was driven by the mean hourly discharge values at gauge Torgau. Inundation areas resulting from 5 dike breaches, which occurred at the study reach, were simulated using the storage cell code. Breach locations, breach time and ultimate width were predefined in the dike breach model based on the information provided by Gocht (2002); IKSE (2004); Horlacher et al. (2005). Unfortunately, only rough information about the breach development dynamics was available in a descriptive form. Therefore, the breach development to the maximum width was assumed to be gradual within one hour. The storage cell code was run for a series of roughness parameterisation, aiming at testing the sensitivity of the inundation extent and depth. Two distributed roughness datasets based on landuse characteristics (Table 4.8) as well as uniform Manning's roughness values in a range between $0.04$ and $0.2$ were explored.

The resulting inundation extents were assessed against the available inundation shape derived from the Landsat 7, ETM+ visible range sensor with $30\,m$ horizontal resolution and overpass on the 20.08.2002, 9:50 UTC (processed by the German Aerospace Centre (DLR) and Federal Agency for Cartography and Geodesy (BKG)). Despite the disadvantages of visible sensors compared to radar techniques (Sect. 2.4.2), the Landsat imagery seems to be suitable for integration with hydraulic modelling for large scale inundation (Bates et al., 1997).

The observed flooded area was subdivided into four subdomains (Figure 4.1), for which the comparison was carried out. Considering the modelled raster data set as $M$ and observed as $D$, we denote flooded cells with 1 and non-flooded with 0. Hence, four possible cell states can be distinguished: $M_1D_1$ - modelled and observed as flooded, $M_0D_1$ - modelled as dry, observed as flooded, $M_1D_0$ - modelled

as flooded, observed as dry and, finally, $M_0D_0$ - modelled and observed as dry. The model performance has been quantified using statistics (Eq. 4.5- 4.8) based on the cell-by-cell comparison of the modelled and observed inundation extents.

$$BIAS = \frac{M_1D_1 + M_1D_0}{M_1D_1 + M_0D_1} \in [0, \infty) \tag{4.5}$$

$$F^{<1>} = \frac{M_1D_1}{M_1D_1 + M_0D_1 + M_1D_0} \in [0, 1] \tag{4.6}$$

$$F^{<2>} = \frac{M_1D_1 - M_1D_0}{M_1D_1 + M_0D_1 + M_1D_0} \in [-1, 1] \tag{4.7}$$

$$F^{<3>} = \frac{M_1D_1 - M_0D_1}{M_1D_1 + M_0D_1 + M_1D_0} \in [-1, 1] \tag{4.8}$$

Hunter (2005) gives a comprehensive overview of these performance measures for binary spatial pattern predictions, concluding that $F^{<1,2,3>}$-statistics are efficient in characterising inundation model performance. While $F^{<1>}$ equitably assesses prediction capability by disregarding a larger proportion of correctly simulated dry cells in non-inundated regions, $F^{<2>}$ and $F^{<3>}$ explicitly penalise over- and underprediction, respectively. The latter two statistics provide a more rigorous performance characteristic to distinguish between over- and underprediction. $BIAS$ is additionally used and is useful for summarising model performance in terms of overall over- or underprediction.

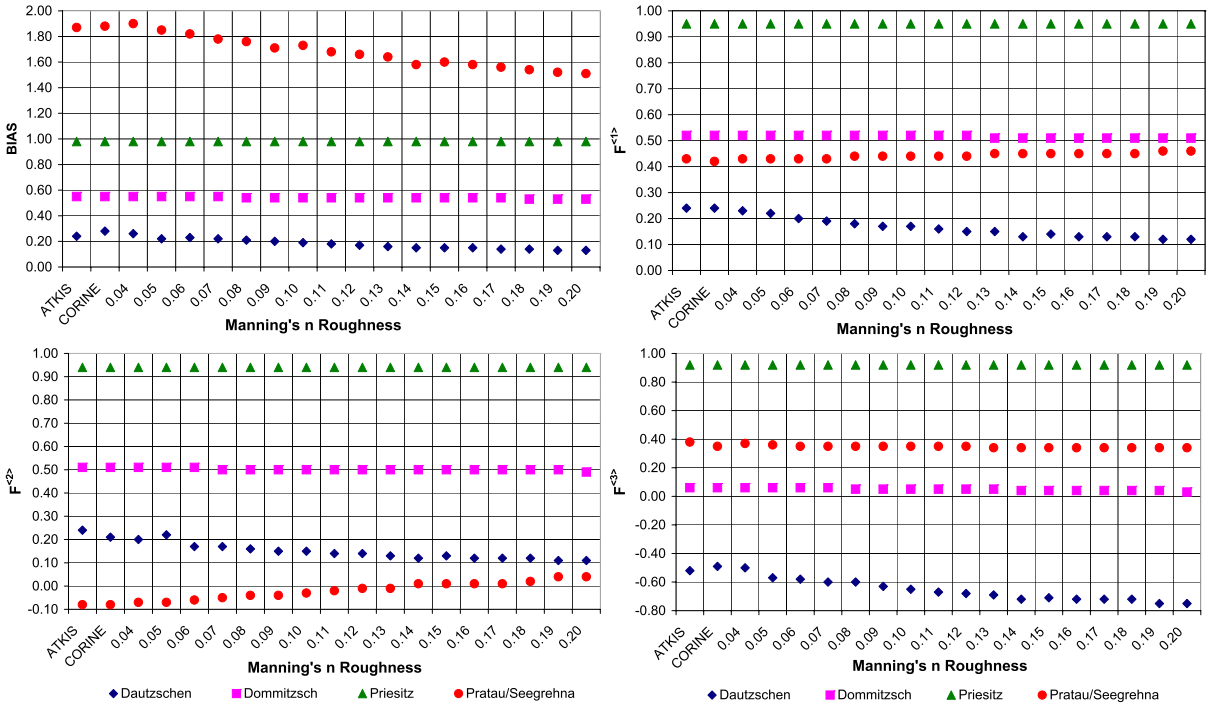


**Figure 4.20:** *Performance statistics for the 2D storage cell model as function of different roughness parameterisation schemes.*

The resulting performance statistics summarised in Figure 4.20 indicates a relatively low sensitivity of the performance measures to the variations in roughness coefficient. This can partly be attributed to

the relative insensitivity of the inundation extent predictions to the Manning's n values reported for this type of storage cell code with flow limiter used (Sect. 2.3) (Horritt and Bates, 2002; Hunter et al., 2005a).

In overall, the inundation model performs very differently at various parts of the modelling domain. An attempt to fit the modelled inundation areas to the observed flood extents proves highly problematic. The following reasons can explain the poor fit in some areas and low sensitivity of the performance statistics to the floodplain roughness:

- At Dautzschen subdomain (Figure 4.1), the striking underestimation of the inundation area results most probably from the significant overtopping volume over the right-side dike and backwater flow from the Schwarze Elster river in the northern part of domain (Gocht, 2002).

- At Dommitzsch and Priesitz subdomains, the topography seems to be a major controlling factor of inundation extent. Additionally the inundation of the Schwarze Graben tributary is not considered in the model, however, present on the flood extent image.

- At Pratau/Seegrehna, inundation extent is grossly overestimated which is indicated by the $F^{<2>}$ statistics (Figure 4.20). Overprediction is likely due to the overestimated outflow volume through the breach and cannot be compensated by varying the Manning's roughness value. The outflow volume might have been considerably affected by dike reinforcement and breach closure during the August 2002 flood as reported by AH (2002).

The calibration procedure requires the knowledge of dike breach development and closure dynamics, overtopping flow, possible backwater flow and contribution from tributaries. The high number of degrees of freedom could not be compensated by manipulating Manning's roughness. Nevertheless, a plausible roughness parameterisation is required to place confidence in the model predictions. Since any uniform roughness parameterisation could be identified as superior with respect to inundation extent simulations (Figure 4.20), distributed roughness was favoured over an uniform friction coefficient. Compared to the CORINE landuse, ATKIS data (as summarised in Table 4.8) possess a higher degree of detail and therefore were adopted hereafter. Although Werner et al. (2005b) found no improvement of flood extent predictions using distributed roughness values, the response of maximum inundation depth to the roughness parameterisation may be significant. Hence, it is explored here by comparing the maximum depth patterns simulated with uniform friction parameters and spatially distributed ATKIS-based roughness. Water depth differences between CORINE- and ATKIS-based model runs were additionally computed.

Figure B.4 demonstrates the spatial variations of the difference in maximum inundation depth using various roughness parameterisation schemes. The difference in maximum water depth is predominantly in the $\pm 0.1\ m$ range. However, the differences of up to four metres are simulated at some locations. On a complex topography, high friction values restrain the propagation of the wetting front. This may prevent flooding of the depressions resulting in considerable variation of water depth. This are inundated at lower roughness values due to wider spread of flood waters.

This example demonstrates an extremely high complexity of the calibration task, when dike breach processes heavily control flood dynamics. Breach development dynamics, including breach closure by the flood protection forces during the event, as well as dike overflow and inundation of tributaries, which are not accounted for in the model, seem to have a considerable impact on flood extent during the August 2002 flood. An attempt to compensate for these processes by varying the roughness coefficient may lead to erroneous and physically unrealistic values. Even though a suitable parameter could be found, the parameterisation might not be robust and applicable for predictive purposes. In the absence of sufficient constraining observations the model parameterisation based on distributed ATKIS landuse data and literature roughness values was preferred over an uniform friction parameter.

## 4.6 Generation of synthetic flood scenarios

Merz (2006) distinguishes between static and dynamic flood scenarios. Static scenarios are generated for the whole catchment and indicate a certain discharge magnitude, e.g. corresponding to the return period of $T = 100y$. They can be derived based on the statistical analysis of the observed flood discharges combined with an regionalisation technique in order to transfer the estimates to ungauged locations. Static scenarios, however, have two striking weaknesses. Firstly, they can be used only in a steady-state flood hazard analysis since the scenarios do not provide consistent discharge time series. Secondly, especially for the large catchments, the probability of simulataneous occurence of such area-wide discharge values is expected to depart from an assigned return period. In other words, the 100-year discharges at every gauge may occur over an entire catchment, however, the return period of such large-scale flood would be greater than $T = 100$. The variation of discharge within a catchment is expected to increase with increasing return period (Merz, 2006).

For a dynamic unsteady flood hazard assessment model, employed in this study, a set of dynamic flood scenarios has to be developed. Whereas numerous studies used historical or hypothetical scenarios for flood danger assessment (Sec. 2.5), flood hazard analysis requires probability or return period statements be adhered to a scenario set. Therefore, an approach delivering dynamic event-based hydrographs at gauge of interest should be adopted.

Methods based on the transformation of measured or statistically generated rainfall fields, such as design storm method and continuous long-term rainfall-runoff simulation (for a review see e.g. Merz, 2006), require the setup of a catchment-wide hydrologic model. This goes beyond the scope of the presented thesis. Hence, an approach based on extreme value statistics of the observed flood events was adopted from Apel et al. (2004, 2006). In this method, the statistical analysis of annual maximum discharge series is combined with a cluster analysis of the event hydrographs, in order to account for the hydrograph shape and, consequently, for the flood volume. The method and its application to the discharge series at gauge Torgau is discussed in Sect. 4.6.1.

### 4.6.1 Synthetic input hydrographs for the main river

Synthetic input hydrographs for a range of extreme events, $T = 100, 200, 500, 1000$, were generated at gauge Torgau based on the method of Apel et al. (2004, 2006). Flood frequency analysis was applied to the annual maximum discharge series (AMS) from 1936 to 2003 at gauge Torgau. The GEV distribution was fitted to the AMS series using the L-moments method for parameter estimation. The derived flood frequency distribution was used to determine the maximum discharge corresponding to a selected return period (Figure 4.21a).

For continuous event simulation, a flood hydrograph with the defined peak discharge has to be generated. For this purpose, events of 30 days duration were extracted around the annual maximum, with 10 days prior to the maximum discharge and 20 days after. A linear baseflow hydrograph was assumed between the hydrograph ends and subtracted from the total observed runoff. The direct runoff ($QD$) hydrographs were normalised by

$$QD_{norm} = QD/QD_{max} \tag{4.9}$$

where $QD_{norm}$ - normalised direct runoff $[-]$ and $QD_{max}$ - maximum direct runoff $[m^3\ s^{-1}]$.

The normalised hydrographs were clustered using the "ward" algorithm and squared Euclidian distances as a measure of affinity between cluster members. The "ward" method computes the total variance inside the cluster by summing up the squared Euclidian distances between the cluster members and its centroid. The clusters are built in a way that the total variance, i.e. heterogeneity, is minimised. The resulting dendrogram is shown in Figure 4.21b.

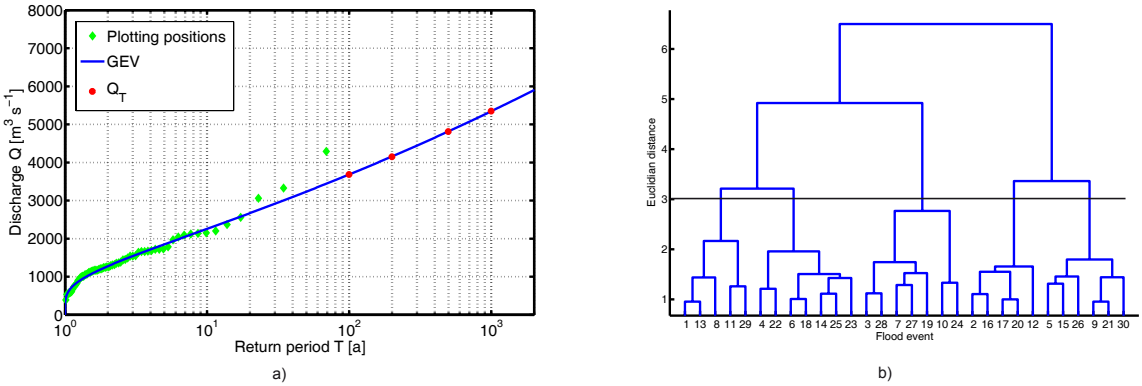


**Figure 4.21:** *(a) Flood frequency analysis of the discharge time series at gauge Torgau for the period 1936-2003. The GEV distribution function was fitted to the AMS series with the L-moment method. $Q_T$ indicates the peak discharges corresponding to the return periods selected for the construction of the synthetic hydrographs. (b) Cluster analysis of the extracted event hydrographs. Dendogram indicates the clustering of hydrographs using the "ward" method. The selected clusters are highlighted by the horizontal bar.*

For the generation of synthetic hydrographs, five clusters were selected in order to account for the natural variability of the flood wave form and flood volume. A greater number of selected hydrographs may require a higher number of the core Monte Carlo runs to achieve comparable convergence of simulation results. For each hydrograph cluster the mean normalised discharge was computed and assigned a probability value. The probability of cluster occurence is based on the proportion of the hydrographs within a cluster to the total number of events (Figure 4.22). Finally, mean normalised cluster hydrographs were rescaled using the flood frequency statistics (Figure 4.21a) to produce synthetic hydrographs for $T = 100, 200, 500, 1000$ return periods.

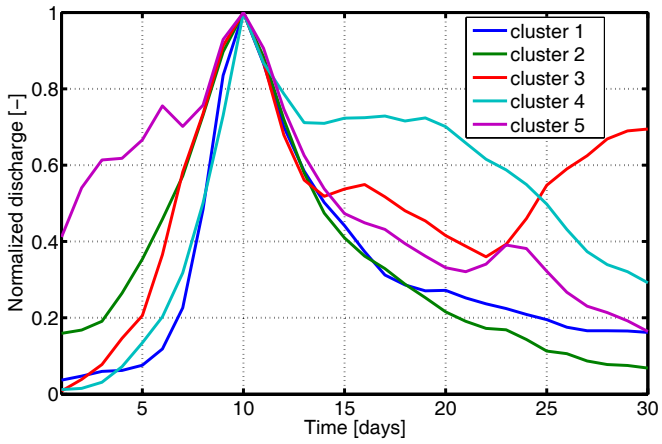


**Figure 4.22:** *Normalised mean hydrographs corresponding to the five selected hydrograph clusters with the following assigned probabilities: cluster 1* - 36.77%, *cluster 2* - 23.52% , *cluster 3* - 11.77% , *cluster 4* - 14.71%, *cluster 5* - 13.23%.

The probability of hydrograph occurrence listed in the caption of Figure 4.22 was taken into account

in the Monte Carlo sampling (Sec. 3.1). A randomly selected hydrograph cluster is used as boundary condition each Monte Carlo run. Given a sufficient amount of samples, the frequency of cluster occurrence approaches computed probabilities.

### 4.6.2 Tributary input hydrographs

To account for the discharge contribution from the tributary, Schwarze Elster, the correlation analysis for the maximum discharge values at gauge Löben and corresponding AMS events at gauge Torgau was carried out. The daily average discharge series for the period 01.11.1973 - 31.10.2003 at gauge Löben was used in the analysis. Peak discharges in the tributary corresponding to those in the main river can be generated using a regression equation (Apel et al., 2004). Apel et al. (2004, 2006) used a linear regression to explain the correlation between the maximum discharge in the Rhine River and Ruhr and Lippe tributaries. Figure 4.23a shows a correlation analysis between peak discharges at the gauge Torgau and Löben indicating no linear correlation between both series ($R^2_{linear} = 0.31$). Interestingly, the regression

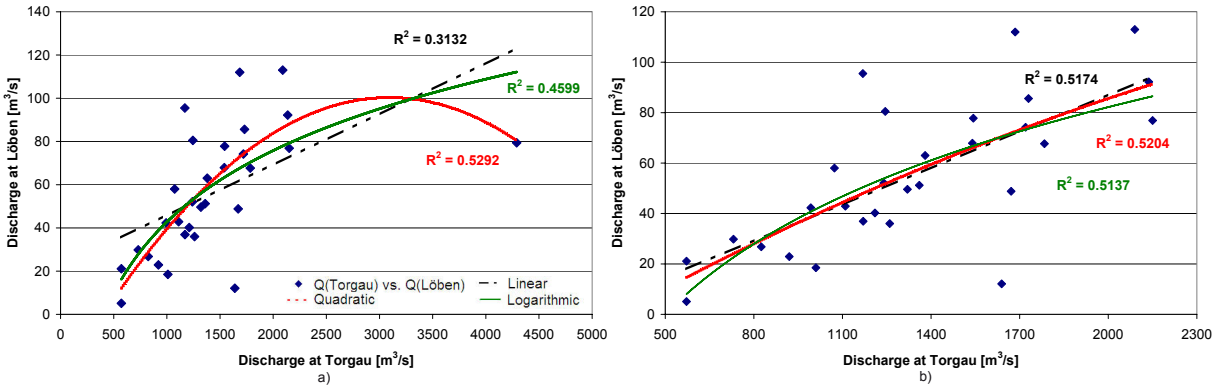


**Figure 4.23:** *(a) Regression analysis of peak discharge at gauge Torgau and corresponding maximum event discharges at gauge Löben for the period 01.11.1973 - 31.10.2003. (b) Same analysis with excluded maximum discharge for the August 2002 flood.*

analysis for the data with excluded maximum discharge for the August 2002 flood indicate a weak linear correlation (Figure 4.23b). A relatively low tributary discharge corresponding to the high flow in the main river may be an indication of different flood generation pathways for extreme events. Floods of moderate return periods in the Elbe, corresponding to high tributary discharges, may result from precipitation patterns also strongly covering the Schwarze Elster catchment. The Vb-weather system, which triggered the August 2002 extreme flow in Elbe and Mulde, generated a high rainfall input in the headwater catchments (Petrow et al., 2007). Thus, it may be expected that extreme discharges in the main river can be conjugated with a moderate flow in the Schwarze Elster, which might be proved with longer time series. Therefore, the extreme discharge of 2002 was not treated as an outlier.

Additionaly, logarithmic and quadratic regression functions were employed to explore the data dependency. The quadratic regression was also rejected, although the regression coefficient indicates a weak correlation ($R^2_{quadratic} = 0.53$) as shown in Figure 4.23a. Extrapolation of the quadratic regression function for the high main river discharges would result in unrealistically low values for the tributary flow tending towards zero. Instead, the logarithmic regression was adopted as an approximation to determine the maximum tributary discharge, despite the low regression coefficient ($R^2_{log} = 0.46$).

The correlation method to determine the maximum tributary discharge reveals to be not robust in case of the Elbe and Schwarze Elster series under the current data limited conditions, with only one

record at Löben corresponding to the extreme event in the Elbe reach. In such cases the long-term continuous rainfall-runoff simulations based on synthetic continuous rainfall time series may represent a viable alternative to the correlation analysis.

The tributary hydrographs were extracted, normalised and clustered correspondingly to the Elbe reach events. Mean shapes of tributary hydrographs were computed for each cluster. Employing the logarithmic regression, the normalised tributary hydrographs were rescaled to the defined return periods. Hence, for each hydrograph cluster of the main river, a corresponding mean tributary hydrograph was constructed. The time lags between the peak discharges were kept constant for each cluster.

The resulting scenario sets, comprised of the main river and tributary hydrograph pairs, are further referred as $100y$, $200y$, $500y$ and $1000y$, corresponding to the respective return periods.

## 4.7 Flood hazard analysis for the reach Torgau-Vockerode

The IHAM model, setup for the Elbe reach Torgau-Vockerode, was driven by the synthetic hydrographs and run in the core Monte Carlo simulation. In a complex modelling system such as IHAM, it might be difficult to estimate the number of MC runs, necessary to achieve a predefined level of convergence. Moreover, different output quantities may require an unequal number of simulations to meet the targeted convergence level. Therefore, the number of runs was constrained by the available computational resources. For each of the four extreme scenarios, 3000 simulations for a period of 30 days were performed. The convergence level, achieved for some output variables such as dike breach probability and maximum inundation depth, was further analysed. In a decision-making process the targeted level of convergence should be discussed with the stakeholders prior to simulation.

Scenario simulations were based on the presently available dike information including location, absolute crest height and other geometrical parameters. As discussed in Sect. 4.4.1, the dike data set was compiled from various data sources and may not represent the current protection level, especially, taking into account the ongoing dike relocation and reinforcement measures after the August 2002 flood. The dike information, however, suffices for the purpose of methodology testing and can readily be updated for a real case application.

One should be aware of the limitations posed by the used methodology and particular model setup prior to the interpretation of the results. The IHAM is currently not capable to incorporate dike heightening and strengthening schemes at runtime, which is often carried out during an event by stakeholders, such as firemen, army and ordinary residents. Neither breach closure, nor man-made blasting of dikes for the purpose of inundation relief in the hinterland is considered in the current model setup. However, such scenarios can be integrated into the modelling through modest code modifications. Thus, the obtained modelling results represent a conservative estimation of the flood hazard without consideration of human intervention.

### 4.7.1 Dike breach hazard

One of the output variables of the Monte Carlo simulation with IHAM is the breach probability associated to each discretised dike section. The spatial representation of breach probabilities, which correspond to a certain flood return period, is referred here to dike breach hazard. The dike breach hazard map for the $100y$ scenario is demonstrated in Figure 4.24a. The map can be particularly useful for identification of the dike sections prone to failure for events of a given magnitude.

The high failure probability for several dike sections corresponds well with the dike stretches identified as weak by IKSE (2001) for the left- and right-side Elbe dikes between Wittenberg and Coswig-Anhalt as well as for the stretches between gauge Pretzsch-Mauken and Schwarze Elster confluence. Although the direct comparison between simulation results and dike survey provided by IKSE (2001) is

not reliable because of possible difference in the basis dike data used for simulation and survey analysis, the results may indicate a model plausibility.

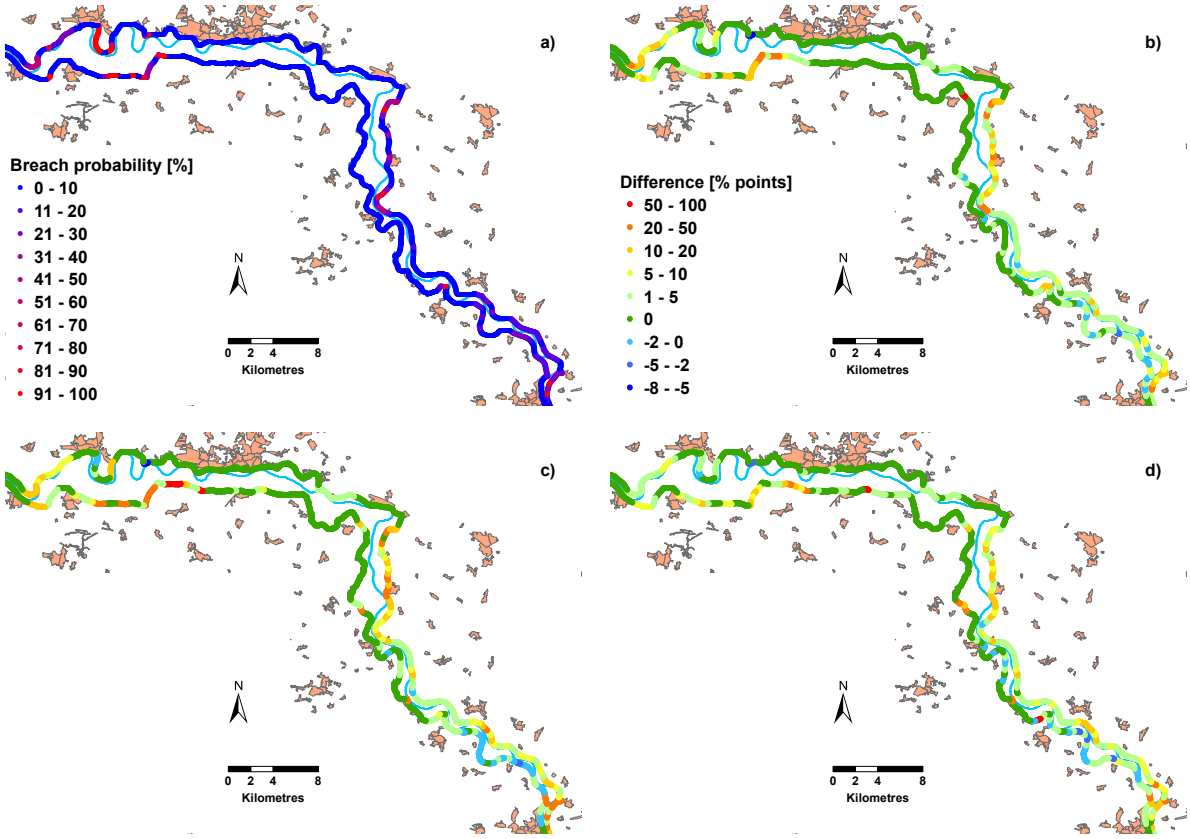


**Figure 4.24:** *(a) Probability of dike breaches for the flood scenario* $100y$*. Difference in dike breach probability between scenarios (b)* $200y$ *and* $100y$*, (c)* $500y$ *and* $200y$*, and (d)* $1000y$ *and* $500y$*.*

Figures 4.24b-d show the differences in dike breach probability between the simulated scenarios. The effect of breach probability reduction for downstream dikes as a consequence of increased failure frequency of upstream dikes for higher magnitude scenarios cannot be observed. With increasing flood magnitude the dike breach probability is mainly rising. Exceptionally, a slight reduction of breach frequency can be observed for several left-side dike sections between Torgau and Pretzsch-Mauken, likely due to load relief because of the increased failure frequency of the right-side sections. Either an insufficient flood retention capacity of the hinterland or comparably slow breach outflow dynamics seem to ineffectively cap the flood waves and drop the failure probability downstream.

Breach probability maps can be disaggregated according to the considered breach mechanisms: overtopping, piping and slope micro-instability. As a result, the dike breach sections can be identified, whose stability is perilled by a particular failure mode. The dike hazard for the $100y$ scenario (Figures 4.25a, c, e) exhibits a different spatial pattern for the various failure modes. Whereas the dike sections downstream of Wittenberg appear to be prone to overtopping and micro-instability failure, the sections upstream of the Schwarze Elster confluence exhibit a weakness against piping. With increasing flood magnitude, the spatial pattern of breaches due to overtopping changes moderately (Figures 4.25b, and 4.26a, b). The overtopping mainly intensifies for sections downstream of Wittenberg on both dike sides. Upstream of Wittenberg only a few sections are vulnerable to overtopping, with increasing breach probability for the

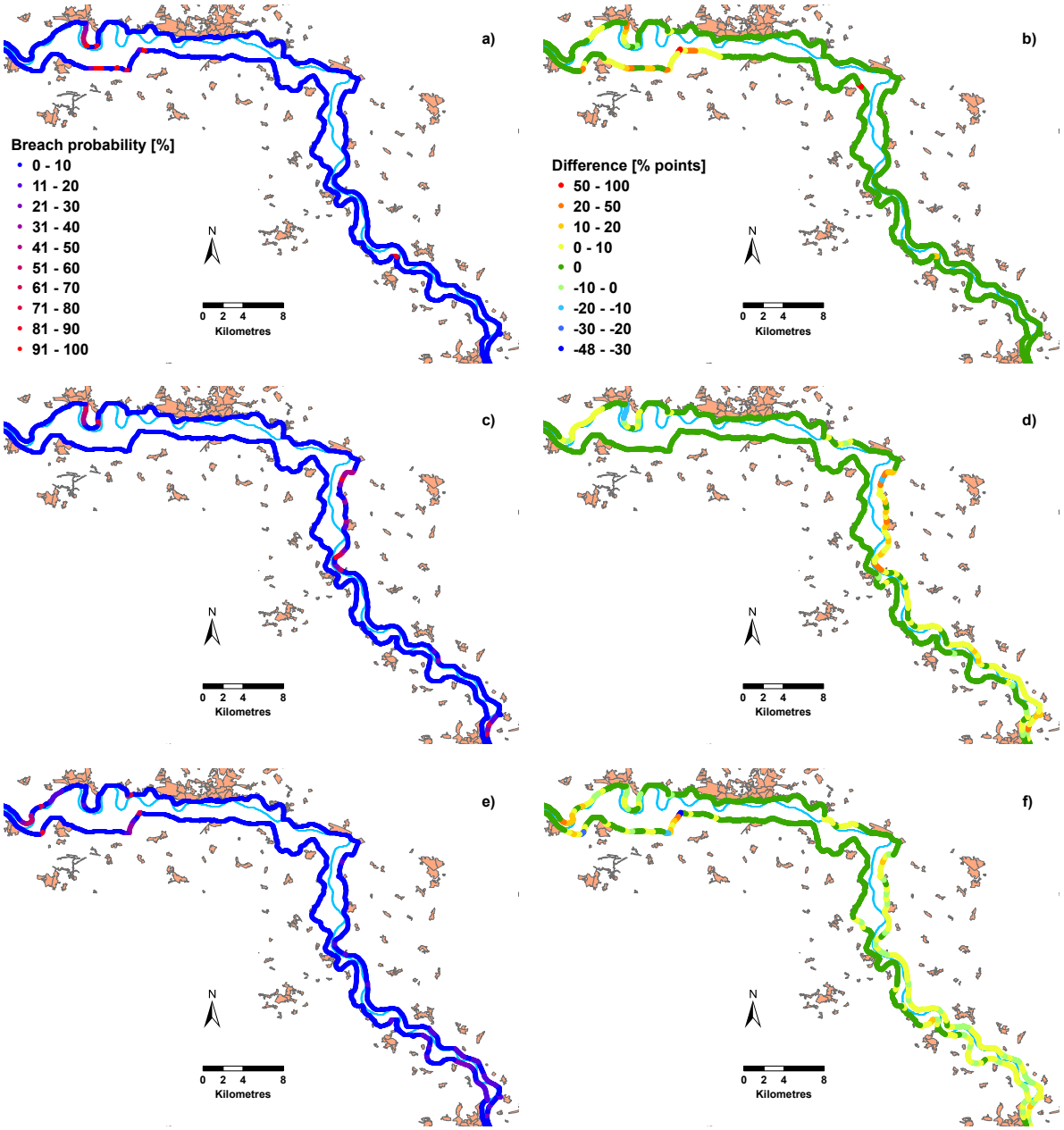


**Figure 4.25:** *Probability of dike breaches disaggregated into* 3 *breach mechanisms (a) overtopping, (c) piping, (e) micro-instability for the flood scenario* $100y$*. Difference in dike breach probability between flood scenarios* $200y$ *and* $100y$ *disaggregated into breach mechanisms (b) overtopping, (d) piping, (f) micro-instability. Legend in (b) applies to (c) and (d).*

high magnitude scenarios $500y$ and $1000y$.

The failure probability due to piping shows an increasing trend for the majority of dike sections with exception of several right-side dikes at Coswig-Anhalt (Figures 4.25d and 4.26c, d). Comparison with Figures 4.25b and 4.26a, b suggests that at higher magnitude events these dikes are rather prone to overtopping than to piping or micro-instability. Similarly, the increase of piping failure frequency for

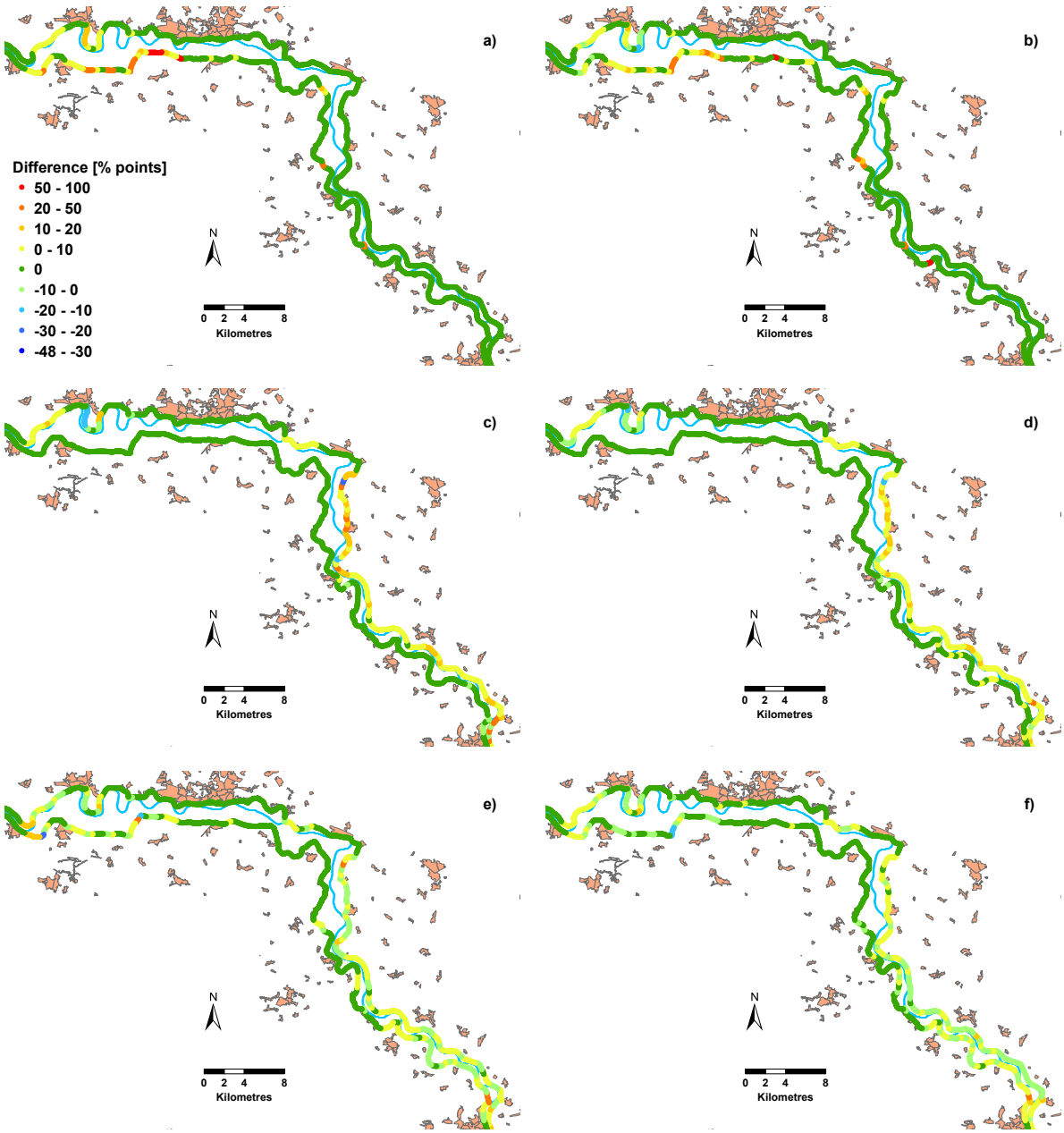


**Figure 4.26:** *Difference in dike breach probability between flood scenarios* $500y$ *and* $200y$*, disaggregated into breach mechanisms (a) overtopping, (c) piping, (e) micro-instability. Difference in dike breach probability between flood scenarios* $1000y$ *and* $500y$*, disaggregated into breach mechanisms (b) overtopping, (d) piping, (f) micro-instability. Legend in (a) applies to (c) and (e), legend in (b) applies to (d) and (f).*

dikes upstream of the Schwarze Elster confluence leads to a moderate decline of breach probability due to micro-instability for some of these stretches, whereas others exhibit a slight increase.

Disaggregation of dike breach hazard according to the breach mechanisms allows the generation of spatially distributed failure probability maps for each failure mode. Identification of a primary failure

mode for each particular dike section may help for efficient planning of dike reinforcement measures prior and during extreme flood events. The results may also be used as a preliminary indicator for more detailed geotechnical measurements and investigations of dike stability.

The proportion of breach mechanisms responsible for dike failures in the simulated scenarios is analysed in Figure 4.27. Overtopping and piping appear to be increasingly dominant failure mechanisms with higher magnitude floods. The proportion of micro-instability induced failures decreases gradually. This indicates a stronger sensitivity of overtopping and piping failures to an increase in peak load and load duration.

Although a direct comparison between the simulated proportion and dike breach statistics presented in Sec. 3.2.1 is not legitimate, since the statistics for Hungarian dikes was derived from the whole spectrum of flood events — from small return period floods to the maximum event — this comparison indicates too frequently simulated breaches due to piping and micro-instability. In the simulated results the proportioning of breach mechanisms is far from the observed statistics, based on breaches observed in multiple events (Figure 3.3) and breaches from a single event in Saxony (Figure 3.4). It can be expected that at high return periods, failure due to overtopping becomes much more pronounced. The result can

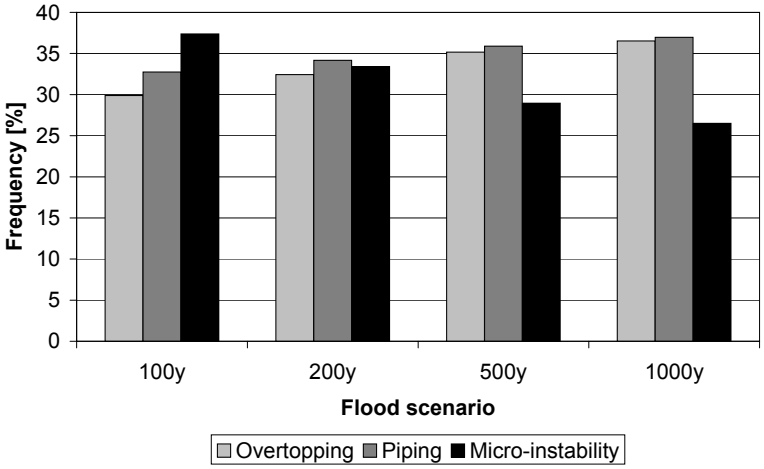


**Figure 4.27:** *Relative frequency of considered dike breach mechanisms responsible for dike failures in simulated scenarios* $100y, 200y, 500y$ *and* $1000y$*.*

be stipulated by the too conservative parameter assumptions, used for developing the fragility functions for piping (Sec. 4.4.3) and micro-instability (Sec. 4.4.4), especially, taking into account a high sensitivity to hydraulic conductivity values, which are largely unknown.

A detailed review of the dike breach model revealed an erroneous sampling procedure of breach probabilities from fragility curves. The procedure was inherited by the IHAM model from Apel et al. (2004, 2006). At each Monte Carlo sampling, the probability of breaching was directly read from the fragility functions based on the current load. A sampling frequency of $1\ h$ was adopted from Apel et al. (2004) and Apel et al. (2006). If the failure probability at the sampling time step $t_s$ was, for instance, $10\%$ and no breach was simulated, the model proceeded to the next sampling time step $t_s + 1\ h$. At the next step, the failure probability of, e.g. $20\%$ given by the fragility function, was directly compared to a randomly generated number. Hence, accounting two samplings within two time steps, the total breach probability appears to be $10\% + 20\% = 30\%$ and not $20\%$ as given for the current load!

De facto, the failure probability at the second sampling step is smaller than that given by the fragility function. It is calculated from the difference between the failure probability at the current and previous sampling step, i.e. $20\% - 10\% = 10\%$. Hence, comparing the random number against the increment

in probability would result in the correct total failure probability after $n$ sampling steps, as given by the fragility function for the load at this step (Eq. 4.10).

$$P_n = \underbrace{(P_1 - 0)}_{1^{st}\text{ sampling}} + \underbrace{(P_2 - P_1)}_{2^{nd}\text{ sampling}} + ... + \underbrace{(P_n - P_{n-1})}_{n^{th}\text{ sampling}} \tag{4.10}$$

The implication of the erroneous sampling is likely an overestimation of failure probabilities. Moreover, the error may result in too early failures. However, the impact is expected to be different for various breach mechanisms. Fragility functions for seepage through dike foundation and dike core are by far less sensitive to changes in water level (Figure 4.7 and Figure 4.15) compared to the sensitivity of the overtopping fragility surface in the region above the crest height (Figure 4.6). It means, that the erroneous sampling would rather overestimate the failure probabilities for piping and micro-instability than for overtopping. This appears to be consistent with the results presented in Figure 4.27.

The correction of the probability sampling procedure will be implemented in the next IHAM version. Future Monte Carlo experiments should reveal the error magnitude in terms of breach probability and inundation areas. A shift in failure partitioning towards more frequent overtopping is expected.

#### 4.7.1.1 Convergence analysis of breach probability

Results obtained from Monte Carlo simulations should be tested for convergence prior to interpretation. Convergence is typically assessed by analysing the sample moments of output variables that are computed as functions of the number of Monte Carlo runs (Ballio and Guadagnini, 2004). Convergence can than be assessed qualitatively by analysing the graphical representation of the moments. Convergence is assumed, when the moment functions, typically mean and variance, reach a stable region and hardly fluctuate with additional number of runs.

The quantitative analysis of convergence can be also applied using an empirical convergence criterion. Dawson and Hall (2006), for instance, considered the simulation to be converged if the difference between the minimum and maximum estimate of the last $10\%$ of samples was less than $0.1\%$ of the estimate after total number of samples. In other words, the convergence was considered if the additional $10\%$ of samples contribute less than $0.1\%$ to the change in output quantity.

Dike breach probability represents a discrete spatial quantity. Therefore, it would not be sufficient to prove the convergence of the breach probability for several selected dike sections. Instead a graphical comparison of breach probability maps is employed hereafter to assess the variation of the MC output in space.

The convergence of dike breach probability is analysed for two flood scenarios $100y$ (Figure 4.28) and $1000y$ (Figure 4.28) by depicting the breach probability changes as a function of the number of Monte Carlo runs. It is assumed that convergence for these two extreme scenarios would also imply convergence for the $200y$ and $500y$ simulations. Breach probability actually represents the mean of a binary quantity (failed/not failed). From the $3000$ performed simulations, arbitrary subsets of $500$, $1000$, $1500$, $2000$ and $2500$ runs were assembled retaining the frequency of the hydrograph clusters (Sec. 4.6).

A pairwise comparison of assembled subsets for the $100y$ scenario indicates that after $1000$ simulations the difference in breach probability exhibit a considerable variation of up to $100\%$ $points$ (Figure 4.28a) compared to the first $500$ runs. However, already after $2000$ runs, further $500$ simulations contribute to the change of breach probability only up to $\pm 1.5\%$ $points$ for the majority of the dike sections. A few sections exhibit a variation of maximum $\pm 3\%$ $points$ (Figure 4.28c). The pattern of variation in probability changes does not differ significantly with a further increase of the number of MC runs (Figure 4.28d), suggesting a convergence of breach probability in the $\pm 3\%$ $points$ range.

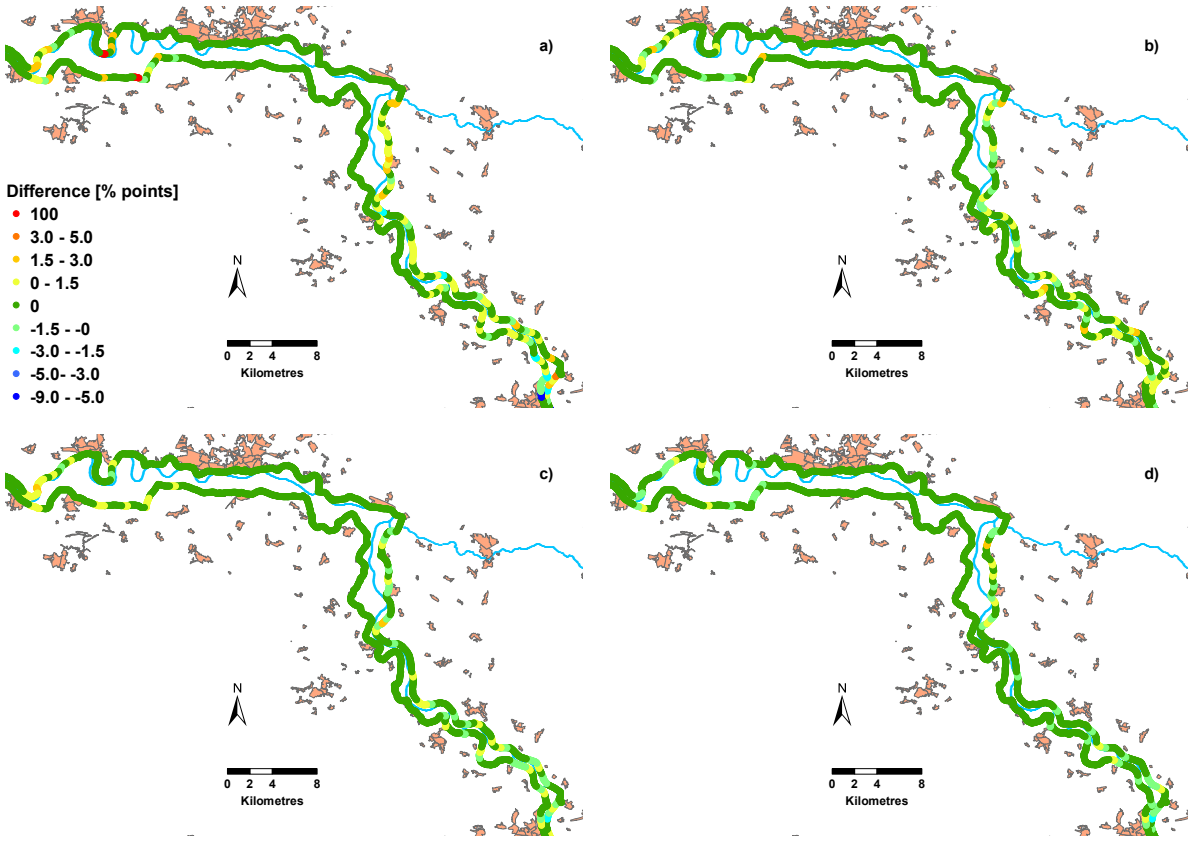


**Figure 4.28:** *Convergence assessment of the Monte Carlo simulations in terms of dike breach probability for the scenario* $100y$*. Difference in [*$\%$ *points] between (a)* $1000$ *and* $500$*, (b)* $1500$ *and* $1000$*, (c)* $2500$ *and* $2000$*, (d)* $3000$ *and* $2500$ *runs. The frequency of* $5$ *hydrograph clusters was retained in the assembled simulation subsets.*

A comparable convergence of the breach probability for the higher magnitude scenario $1000y$ is achieved much faster than for the $100y$ scenario. Already the probability difference between $1000$ and $500$ runs does not exceed $\pm 3\%$ *points* (Figure 4.29). A further increase of the simulation number reduces the range of variation to $[-2; 1]$ (Figures 4.29c, d). The reason for a slower convergence of the breach probability for the lower magnitude scenario can be the stochasticity of dike breaches and their mutual interactions. The breach outflow for upstream failures has a comparably stronger reduction effect on discharge and water stage hydrographs in case of the lower magnitude $100y$ scenario than for the $1000y$ scenario. Hence, the randomness of breach locations, time and breach widths becomes more pronounced in terms of breach probability variation for the $100y$ scenario. It is expected that the dike breach failure probability for the $200y$ and $500y$ scenarios at least converges to a range comparable to the $100y$ scenario.

### 4.7.2 Inundation hazard and associated uncertainty

Inundation hazard is given by the spatial distribution of flood intensity indicators associated with a certain return period. The resulting flood hazard maps and respective uncertainty maps are discussed in this section. Additionally, binary pattern maps are derived for the study reach which indicate the probability

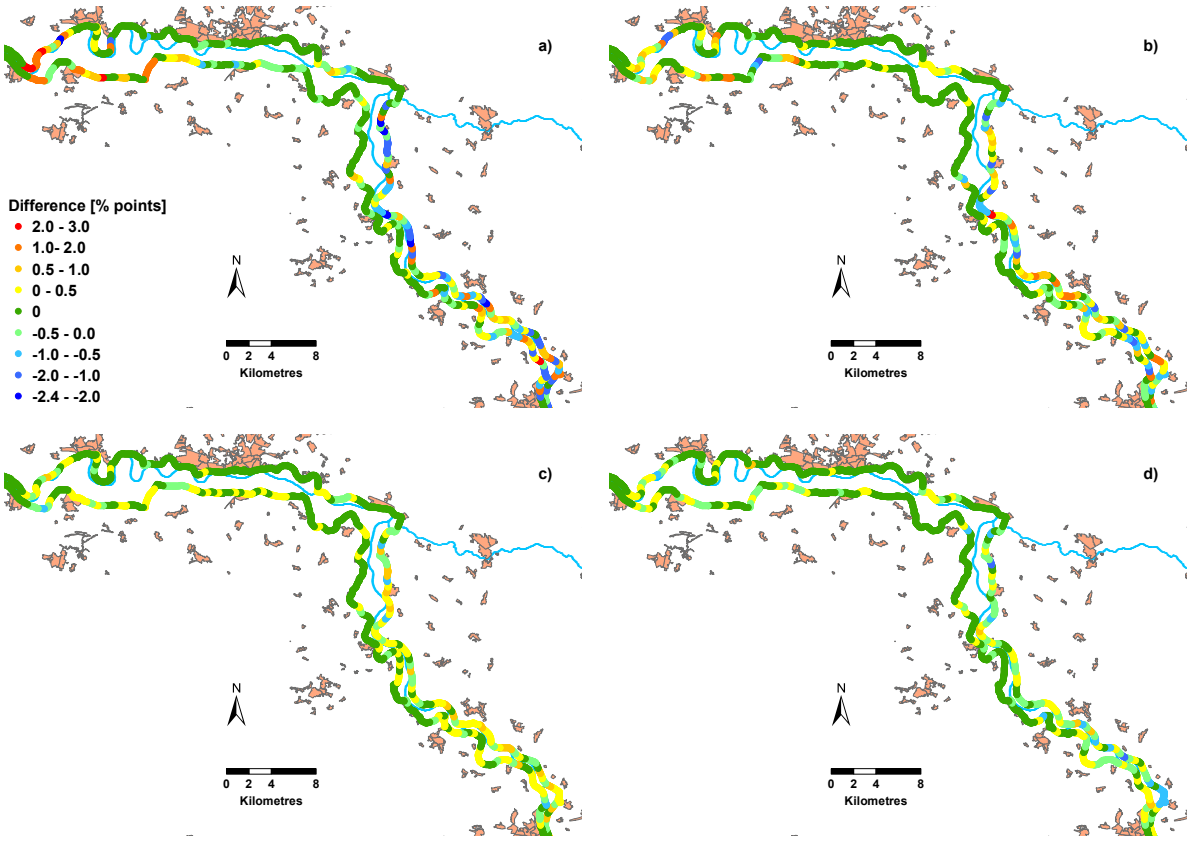


**Figure 4.29:** *Convergence assessment of the Monte Carlo simulations in terms of dike breach probability for the scenario* $1000y$*. Difference in [*$\%$ *points] between (a)* $1000$ *and* $500$*, (b)* $1500$ *and* $1000$*, (c)* $2500$ *and* $2000$*, (d)* $3000$ *and* $2500$ *runs. The frequency of* $5$ *hydrograph clusters was retained in the assembled simulation subsets.*

of inundation for each raster cell.

Obviously, considering solely the flow dynamics, as a primary factor influencing inundation intensity indicators, one neglects the impact of infiltration, evapotranspiration and direct rainfall input onto the flooded area. It is anticipated that not all intensity indicators are affected to the same extent by the net loss. For instance, flow velocity is expected to be much more strongly influenced by the pressure head, frictional and gravitational forces than by net water loss, whereas an impact on inundation duration may be considerable. Bates et al. (2006) assessed the influence of infiltration losses for the range of $K_f = 0.5 - 2.0 \cdot 10^{-6}\ m\ s^{-1}$, detecting a minor impact on the inundation extent. Variation of the $F^{<1>}$-statistics within a range of $\pm 1\%$ was observed. This, however, can be the result of constraining topography. Therefore, water depth predictions should be additionally used to quantify the impact along with the inundation extent. In topographically constricted areas, water depth fields possess by far stronger discriminative power of model performance.

The results presented here should provide a first guess on inundation characteristics for a typical expected event. Estimation of the impact of the net loss on the flood hazard is expected to be insignificant and can be a subject of future research.

#### 4.7.2.1 Binary pattern maps

A binary inundation pattern indicates the probability of flooding of each raster cell in a modelled domain. A cell is considered flooded if a non-zero water depth is computed inside. Binary pattern maps were previously developed within the GLUE framework and reported for an irregular storage cell inundation model (Romanowicz and Beven, 2003) and for a raster-based model (Aronica et al., 2002; Bates et al., 2004) conditioned on the observed maximum inundation extent. Probability of inundation for each cell was determined by weighting the model outcome (wet/dry) by the measure of global model performance for each parameter set used.

In this study, the concept of binary pattern maps is adopted to reflect the probability of a pixel being wet as a result of the flood wave form and dike breach uncertainty. Since no global likelihood measure is deployed in this study, in difference to the GLUE methodology, no weighting of the model outcome is required. The probability of pixel flooding directly results from the core Monte Carlo analysis by calculating a ratio between the number of MC runs with pixel flooded to the total number of MC realisations.

Depending on the modelling objective, it might make no sense to consider pixel wetting if the water depth does not exceed a few centimetres. In such a case, a depth threshold value can be introduced, so a pixel is considered as flooded if the threshold depth is exceeded. A threshold would generally lead to smaller probabilities of flooding. The results presented hereafter did not apply a depth threshold, although it can easily be implemented.

Figure 4.30a demonstrates the binary inundation pattern map for the $100y$ scenario. A high inundation probability for the $100y$ scenario is identified in the right-side hinterland between Mauken-Pretzsch gauge and Schwarze Elster confluence and in the left-side hinterland downstream of Pratau and Seegrehna. Besides these two large, often inundated areas, the topographically constricted area at Coswig-Anhalt and the hinterland at Dommitzsch are endangered with high probability. Interestingly, these areas have been considerably inundated during the August flood 2002 due to dike overflow and/or failure.

However, when compared to the observed ones, the simulated patterns are naturally different, since the modelling results represent an average inundation pattern for a range of flood wave forms. Moreover, the flood protection measures, such as breach closure and load relief due to man-made dike blasting during the August flood (AH, 2002), are not considered in the modelled scenario.

The inundation probability for $200y$ increases drastically by $0.8 - 0.9$ for the left-side hinterland upstream of Wittenberg, when compared to the $100y$ scenario (Figure 4.30b). This corresponds well with the sharply increased dike breach probability in this region as shown in Figure 4.24b. Additionally, intensified back flow from downstream breaches at Wörlitz might contribute to high probability values. Besides an increase of inundation probability between Dommitzsch and Torgau by up to $0.4 - 0.8$, a moderate positive change in the rest of the study area can be observed with exception of the relatively small areas, for which a marginal decrease in inundation probability is indicated.

Strong changes in inundation probability can be expected for the $200y$ scenario compared to $100y$, since the dikes are supposed to be designed for a 100-year flood event. Nevertheless, already for the $100y$ scenario set, large inundation areas are likely. This may indicate the consequences of the lower protection standard and poor dike state as discussed in Sec. 4.7.1. On the other hand, erroneous breach probability sampling (Sect. 4.7.1) may result in an overestimation of breach probabilities.

With increasing flood magnitude (Figures 4.30c,d), the inundation probability exhibits a continuous increase for the majority of the pixels. A few small areas in the modelling domain indicate a slight decrease, which, however, amounts at maximum to $7\%$. The analysis indicates no reduction of inundation probability for downstream hinterland areas at increasing flood magnitude. The reduction may be expected as a consequence of water retention in the hinterland areas due to dike breaches in the upstream part of the reach.

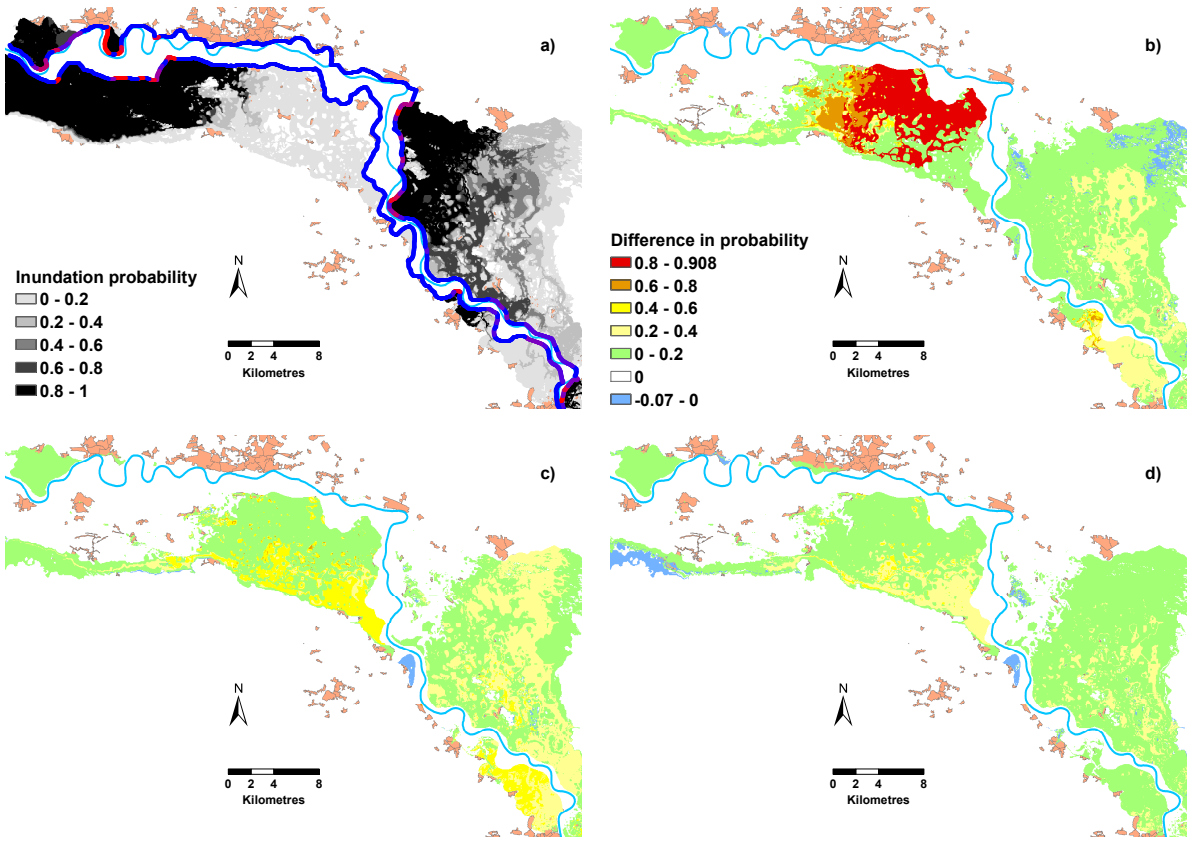


**Figure 4.30:** *(a) The binary inundation pattern map for the scenario* $100y$ *indicates the probability of inundation in the study area. Additionally, the dike breach probability for the same scenario is depicted as shown in Figure 4.24a. Difference in inundation probability between scenarios (b)* $200y$ *and* $100y$*, (c)* $500y$ *and* $200y$ *and (d)* $1000y$ *and* $500y$*.*

#### 4.7.2.2 Inundation depth

Probabilistic flood hazard maps were developed with inundation depth as intensity indicator computed by IHAM. Inundation depth is regarded as the most influential flood intensity indicator for flood losses and is widely used as a basis for depth-damage functions in contemporary flood damage models (Merz and Thieken, 2004). Hazard maps, displayed in Figures 4.31a, b, c, indicate the maximum simulated inundation depths in the study region and are assigned an exceedance probability. This is a key difference between deterministic and probabilistic flood hazard maps.

For example, the median simulated water depth in each pixel (Figure 4.31a) indicates the water depth that would be exceeded with $50\%$ probability at a 100-year flood event. Analogously, the uncertainty bounds of the water depth, given by the $10^{th}$ and $90^{th}$ percentile maps (Figure 4.31b and 4.31c), report the expected water depth, which will be exceeded with $90\%$ and $10\%$ probability, respectively.

Water depth in the $10 - 90$ interpercentile range varies between a couple of centimetres and $7.4$ metres. Regions of deep water above $4\ m$ are simulated in the locations of lakes and ponds originated from the historical Elbe course. The difference between two percentile maps is remarkable. It is not only that the $90^{th}$ percentile map shows generally deeper flows, also additional areas at the right-side of the Elbe appear inundated downstream of Coswig-Anhalt and Mauken-Pretzsch.

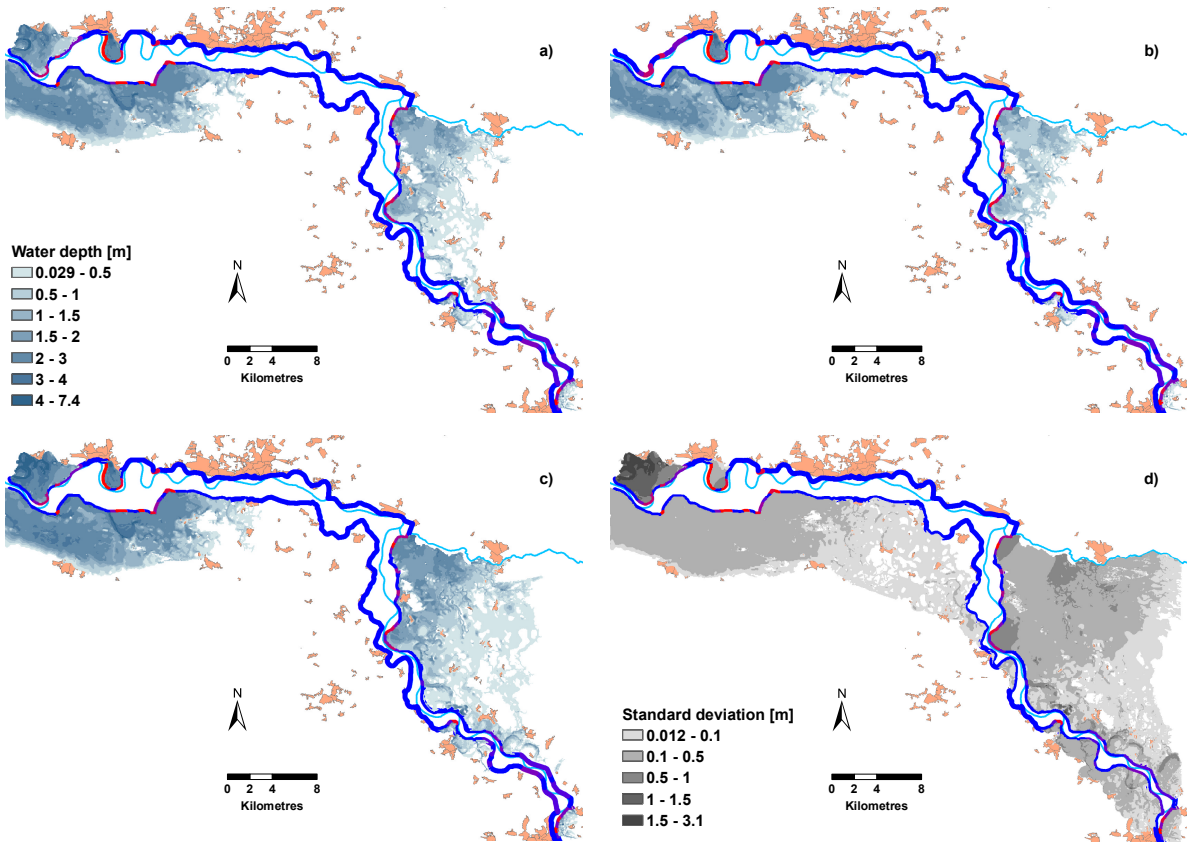


**Figure 4.31:** *Hazard maps for the scenario* $100y$*. (a) Median, (b)* $10^{th}$ *and (c)* $90^{th}$ *percentiles and (d) standard deviation of the maximum inundation depth. Legend in (a) applies to (b) and (c).*

It is abstained here from presenting the hazard maps which indicate the mean inundation depth. Such maps may create a misimpression that all the pixels, for which the average water depth is computed, would be flooded during a 100-year flood event. In reality, some pixels would be inundated in not all the cases, as the binary pattern map (Figure 4.30a) and percentile maps (Figure 4.31b and 4.31c) show. Maps, indicating mean inundation depth, are deployed later for the convergence analysis of MC results together with the standard deviation maps. The latter indicate the quantity spreading around the mean value (e.g. Figure 4.31d). Thus, the areas are highlighted, in which the variability of the intensity indicator is strongly influenced by the flood wave form and dike breach stochasticity.

Figures C.1-C.3 depict the difference in maximum inundation depth and its variation between the computed scenarios. For the vast majority of the cells, an increase of the maximum inundation depth can be expected with increasing flood magnitude. This holds for the median as well as for the $10^{th}$ and $90^{th}$ percentiles. Again, no retention effect can be observed for the downstream part of the reach with increasing scenario magnitude.

The increase in frequency of higher water stages with increasing flood severity varies spatially. While in some regions the variation changes moderately, others exhibit a more frequent occurrence of deeper flows, which is indicated by the difference in standard deviation (Figures C.1d, C.2d, C.3d). Particularly, the area on the left side upstream of Torgau tends to be more severely inundated with increasing flood magnitude. The same holds for the area opposite to Wittenberg behind the left Elbe dike. The effect is especially pronounced for the increase from $100y$ to $200y$ (Figure C.1) and from $200y$ to $500y$ (Fig-

ure C.2) flood magnitudes. The higher values of the standard deviation suggest a stronger spread around the mean. Taking into account the strongly increasing maximum depth, corresponding to the $90^{th}$ percentiles (Figures C.1c and C.2c), the spread tends towards greater maximum depths. Deeper flows are expected in those regions that become inundated with higher probability (Figures 4.30b and 4.30c).

#### Convergence analysis for maximum inundation depth

In Sect. 4.7.1.1, convergence of dike failure probability was analysed. Similarly, convergence of the 2D inundation model results in terms of spatially distributed predictions of maximum inundation depth is assessed for the $100y$ and $1000y$ scenarios. As in the case of dike breach probability, inundation map subsets were extracted randomly from 3000 output files. Pairwise differences between the mean and standard deviations of the generated subsets were computed. They provide an indication for the degree of convergence.

Similarly to the dike breach probability convergence, the mean of the maximum depth for the $1000y$ scenario converges faster to comparable values as one for the $100y$ scenario (Figure 4.32 and Figure 4.34) for the majority of the model domain. The difference in mean depth, contributed by the last $500$ runs for the $100y$ scenario(Figure 4.32e), ranges at maximum between $-0.01$ and $0.05\ m$, whereas for the $1000y$ scenario, a similar level of convergence ($[-0.02; 0.02]$) was achieved after $2000$ runs (Figure 4.34c). After $3000$ simulations, it is even reduced to $[-0.01; 0.02]$ for most of the pixels (Figure 4.34e). The reason for a faster convergence of the $1000y$ results compared to $100y$ is presumably the same as for the difference in dike breach probability convergence. The stochasticity of dike breaches (location, time, breach width) in combination with the hydrograph form has a higher potential in distributing relatively smaller water volume for $100y$ in space. Thus, more MC runs are required to account for significant variations in maximum inundation depth. With the higher water volume and peak discharge in the $1000y$ scenario, the constraining topography and friction gain importance compared to the stochasticity of dike breaches.

While convergence of the mean value expresses the degree of stability in the central tendency of model outcome, convergence of the variance or standard deviation is an indicator for the stability of distribution tails. An occurrence of values at the same distance right- and left-side of the mean value would not be reflected in its change. Contrary, the standard deviation captures the occurrence of those values and reacts stronger, the more extreme the values are. Hence, standard deviation is used as a complementary convergence criterion to the mean value.

A faster convergence of the standard deviation for $1000y$ compared to $100y$ is even more pronounced than in the case with the mean value (Figures 4.33 and 4.35). It signifies that the probability of occurrence of extreme maximum depth (either small or great) farther away from the mean in the additional simulation subset is higher for $100y$ than for $1000y$. The last $500$ runs for $1000y$ contribute the difference of $[-0.02; 0.02\ m]$ (Figures 4.35e) for the majority of the pixels, with exception of a few cells near the breaches. For the $100y$ scenario set, the difference in standard deviation reaches up to $0.05\ m$ in the upstream half of the reach. Remarkably, the difference in standard deviation for pixels located close to the dikes and breach locations is higher than in the rest of the domain. It suggests that the stochasticity of the breach width influences strongly the variation of maximum water depth at these locations. The impact, however, diminishes fast towards the hinterland.

In summary, it can be stated that for a comparable convergence level, a higher number of MC runs is required for the low magnitude scenario $100y$ in contrast to $1000y$. This difference is stipulated by a complex interaction of flood magnitude (peak discharge and volume), dike breach stochasticity, constraining topography and friction in the hinterland. Since the latter three factors remain unchanged in all scenarios, the convergence of the MC results for $200y$ and $500y$ is influenced by flood magnitude. Therefore, the difference in mean and standard deviation is expected to be in the range between those for

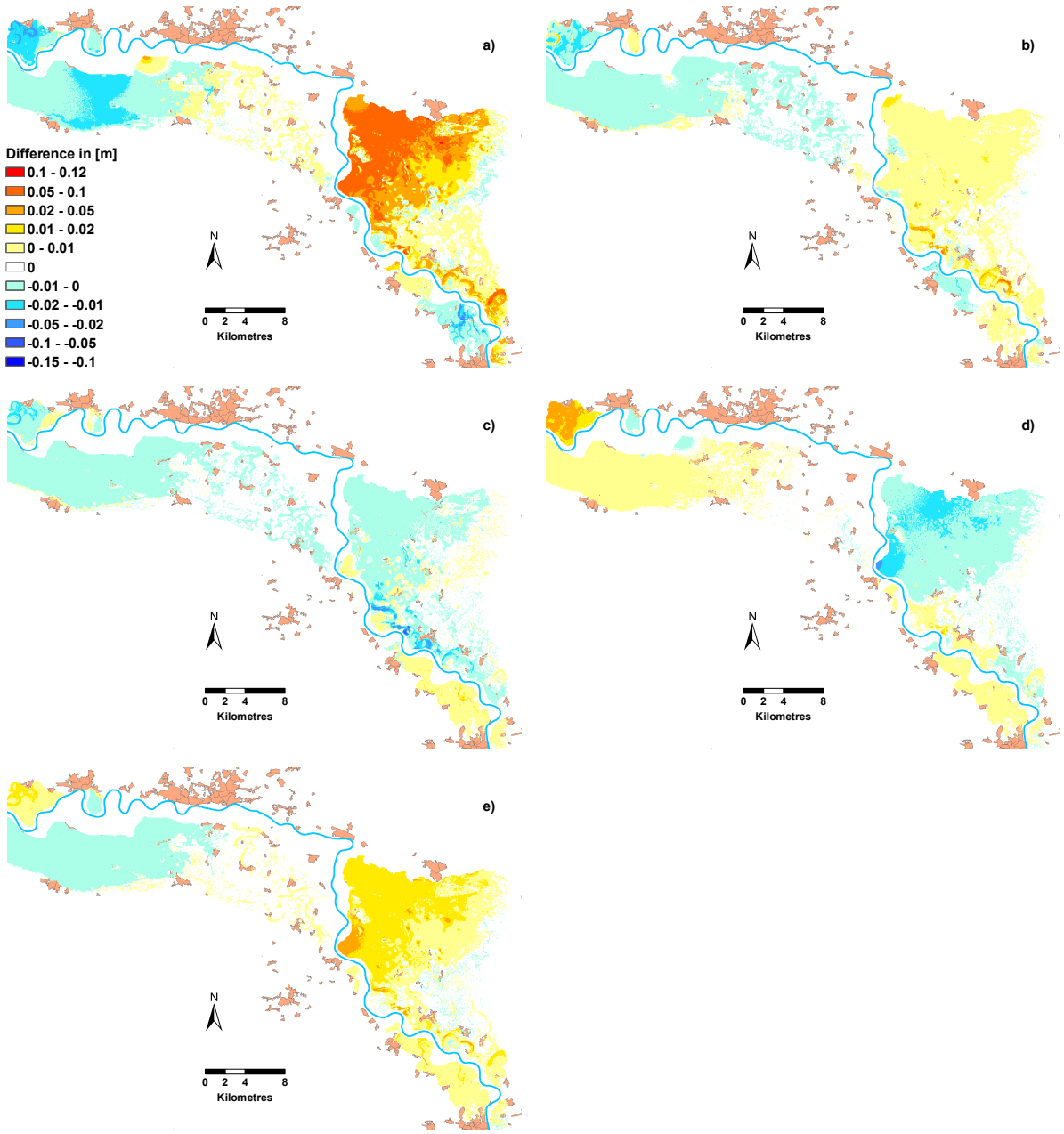


**Figure 4.32:** *Convergence assessment of the MC simulation in terms of maximum inundation depth for the* $100y$ *scenario. Difference in mean maximum inundation depth* $[m]$ *between (a)* 1000 *and* 500*, (b)* 1500 *and* 1000*, (c)* 2000 *and* 1500*, (d)* 2500 *and* 2000*, (e)* 3000 *and* 2500 *runs. The frequency of* 5 *hydrograph clusters was retained in the assembled simulation subsets.*

$100y$ and $1000y$ for the identical number of runs.

#### 4.7.2.3 Flow velocity and impulse

The spatial distribution of the maximum flow velocity and its standard deviation is depicted in Figure 4.36 for the $100y$ scenario. The results are indicative and should be interpreted with care, since the

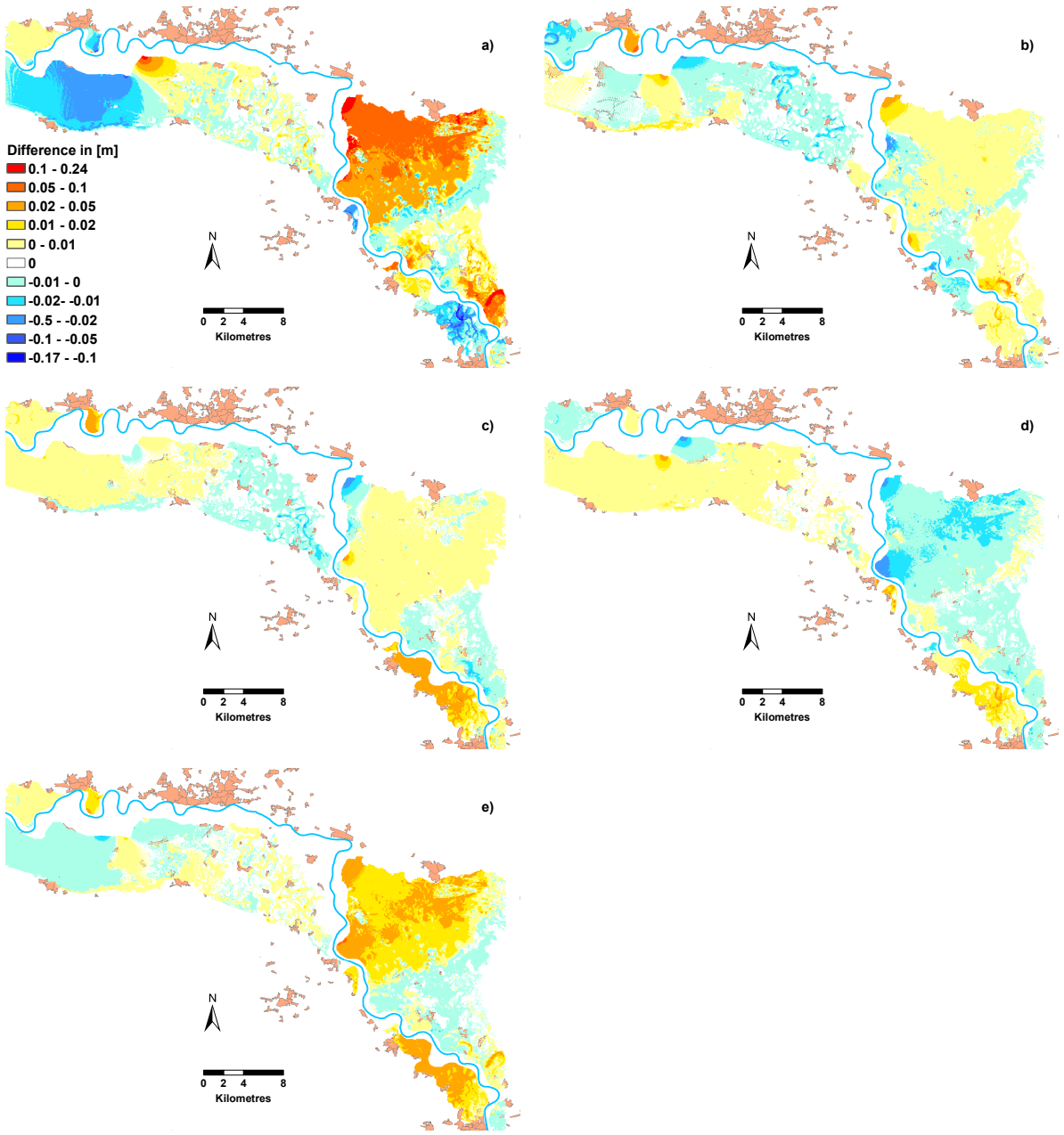


**Figure 4.33:** *Convergence assessment of the MC simulation in terms of maximum inundation depth for the* $100y$ *scenario. Difference in standard deviation of maximum inundation depth* $[m]$ *between (a)* 1000 *and* 500*, (b)* 1500 *and* 1000*, (c)* 2000 *and* 1500*, (d)* 2500 *and* 2000*, (e)* 3000 *and* 2500 *runs. The frequency of* 5 *hydrograph clusters was retained in the assembled simulation subsets.*

methodology used for computation includes several considerable simplifications discussed in Sect. 3.1. It should be remembered that the impulse transfer from the channel into the hinterland is not considered in the IHAM. Water velocity is controlled by pressure and slope gradients, as the diffusion wave approach implies. The initial water level behind the breaches is additionally determined by the interface cell rule (Eq. 3.4). The latter depends on the grid cell size. Moreover, as other indicators, flow velocity

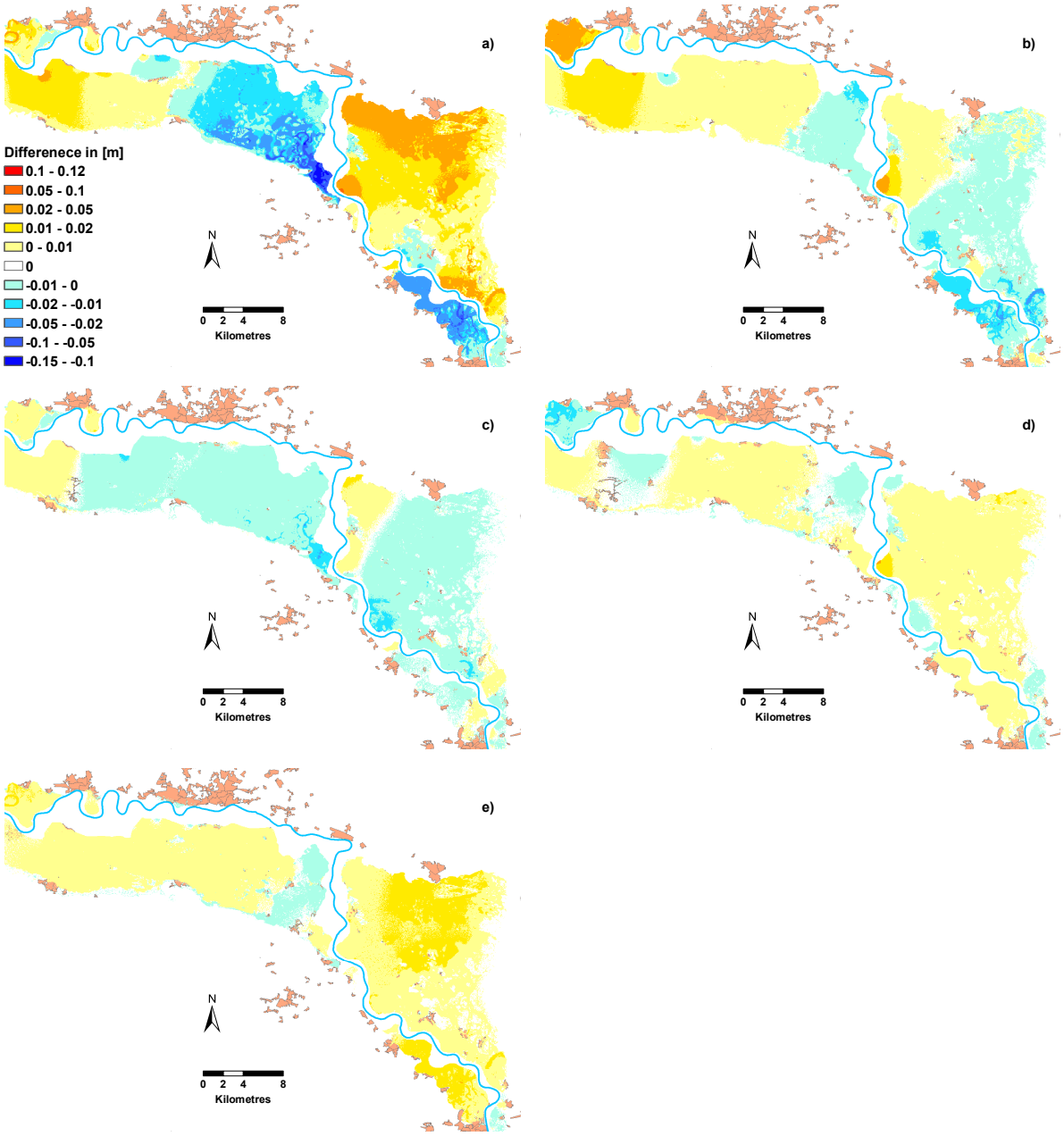


**Figure 4.34:** *Convergence assessment of the MC simulation in terms of maximum inundation depth for the* $100y$ *scenario . Difference in mean maximum inundation depth* $[m]$ *between (a)* 1000 *and* 500*, (b)* 1500 *and* 1000*, (c)* 2000 *and* 1500*, (d)* 2500 *and* 2000*, (e)* 3000 *and* 2500 *runs. The frequency of* 5 *hydrograph clusters was retained in the assembled simulation subsets.*

is averaged over a grid cell. In a real situation, it can vary significantly, determined by subgrid-scale features, e.g. narrowing of streets, where the flow can be accelerated.

Higher maximum velocities are generally simulated closer to the breaches. The variation at these location is also high (Figure 4.36d). The maximum flow velocity increases for the majority of the cells with increasing flood magnitude for the presented percentiles (Figures C.4-C.6). The increase is marginal

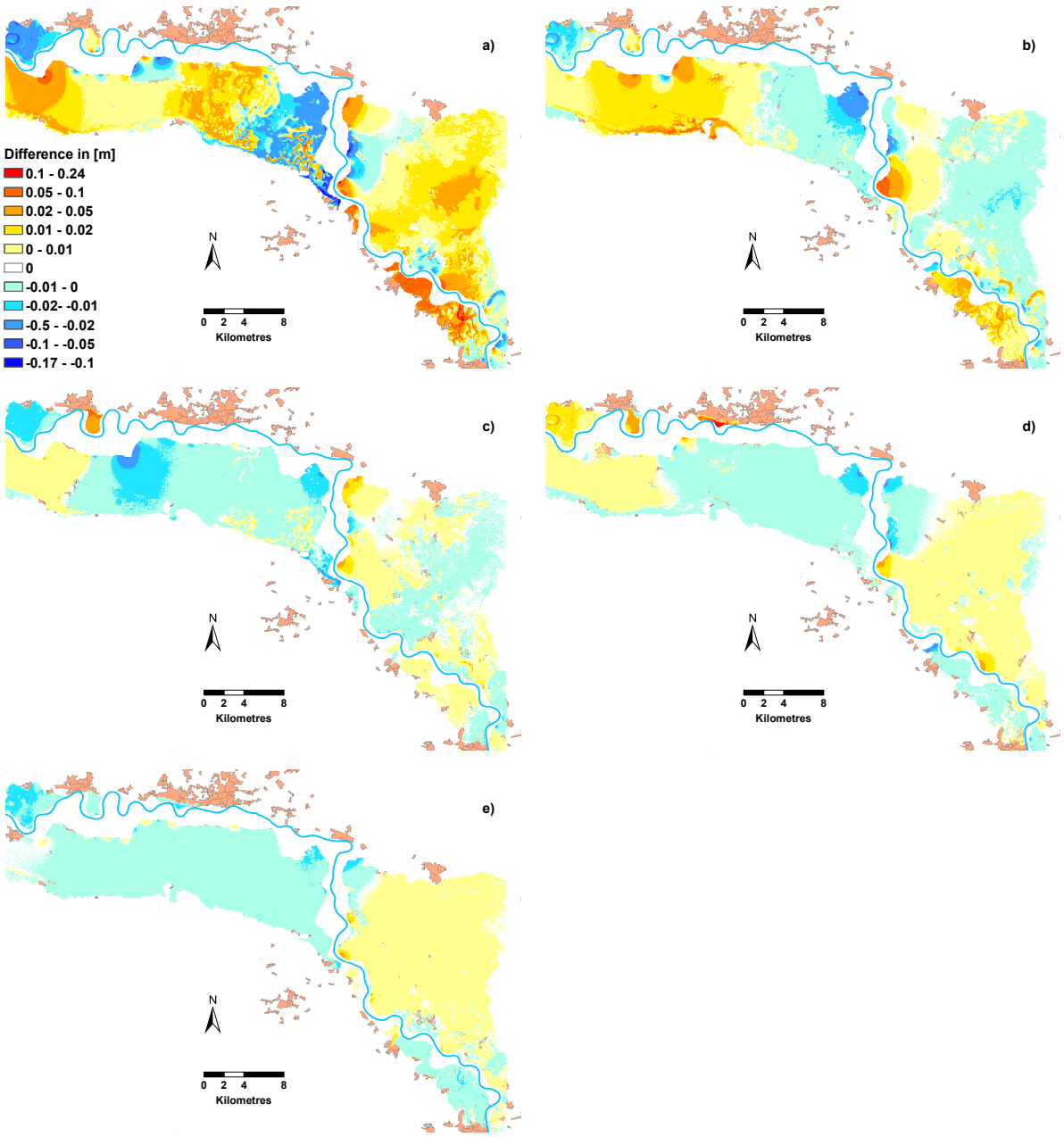


**Figure 4.35:** *Convergence assessment of the MC simulation in terms of maximum inundation depth for the* $1000y$ *scenario. Difference in standard deviation of maximum inundation depth* $[m]$ *between (a)* 1000 *and* 500*, (b)* 1500 *and* 1000*, (c)* 2000 *and* 1500*, (d)* 2500 *and* 2000*, (e)* 3000 *and* 2500 *runs. The frequency of* 5 *hydrograph clusters was retained in the assembled simulation subsets.*

by up to $0.3\ m\ s^{-1}$, whereas locally it can achieve $2.1\ m\ s^{-1}$.

The product of maximum water depth and flow velocity, referred as impulse, is given for $100y$ in Figure 4.37. On average, with an impulse of about $1\ m^2\ s^{-1}$ the stability of a person in a flooded area becomes affected (see e.g. Merz, 2006). Such values are achieved seldom for the $100y$ scenario. However, with increasing flood magnitude, higher maximum impulse values are expected, which sometimes

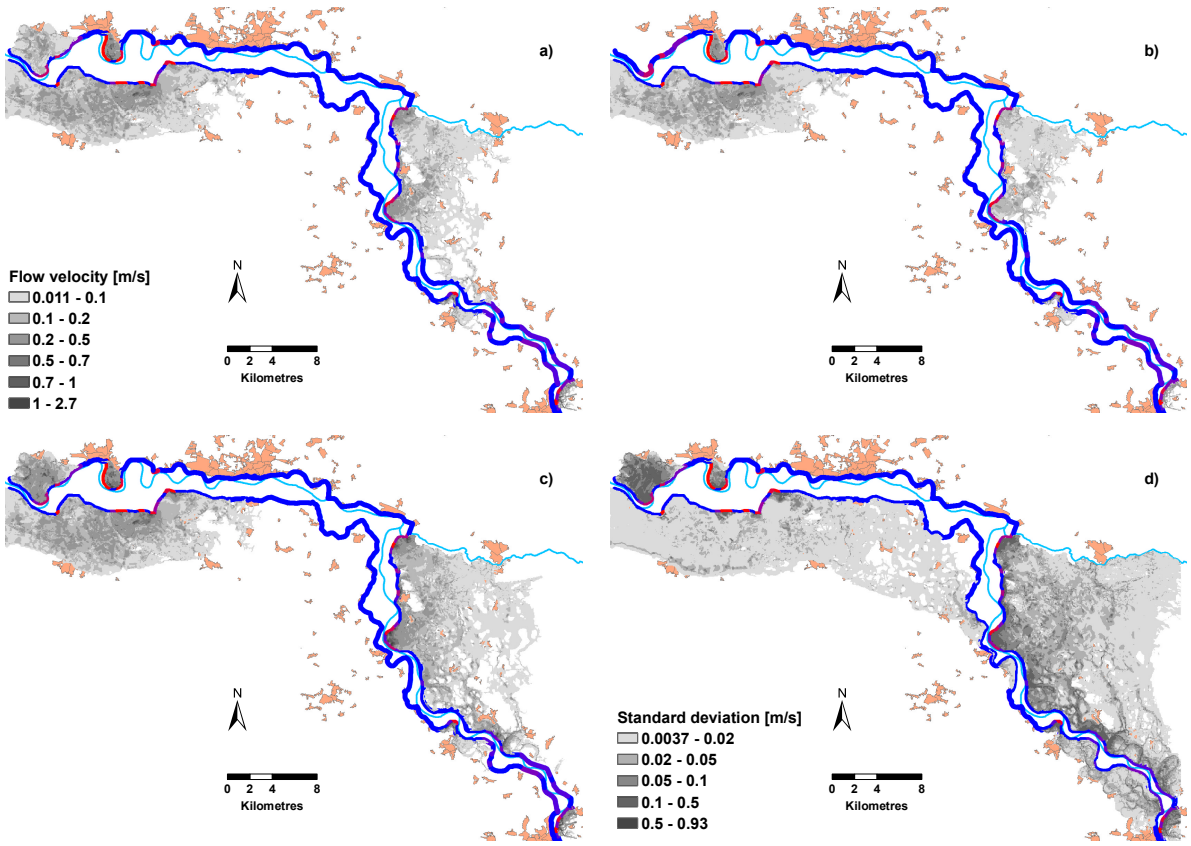


**Figure 4.36:** *Hazard maps for the* $100y$ *scenario. (a) Median, (b)* $10^{th}$ *and (c)* $90^{th}$ *percentiles and (d) standard deviation of the maximum flow velocity. Legend in (a) applies to (b) and (c).*

exceed $1\ m^2\ s^{-1}$. This was simulated for the median as well as for both percentiles of the impulse (Figures C.7-C.9).

The strongest variation of the impulse is modelled near the breach locations (Figure 4.37d) that emphasises the effect of breach stochasticity. At the majority of these locations, the standard deviation is increasing with greater flood magnitude (Figures C.7d-C.9d).

#### 4.7.2.4 Inundation duration

Inundation duration is considered to be an important flood intensity indicator. It becomes especially relevant for the calculation of direct losses in agriculture and indirect economic losses. For example, the agricultural damage model being developed in MEDIS (2007) considers losses to agricultural crops, depending on the inundation duration with water levels above $0.2$ and $0.5\ m$. These threshold depths were adopted for generation of the flood hazard maps with maximum inundation duration as intensity indicator. The maps for the $100y$ scenario are presented in Figures 4.38 and 4.39. The range of variation in inundation duration appears to be very large — from a few up to 700 hours. The total simulation duration was set to 30 days (720 hours). Hence, the model simulates the possibility of the first dike breaches already during the rising hydrograph limb for a 100-year event. The presented methodology admits the possibility of dike failures, before they may be overtopped, by accounting for piping and slope micro-instability. However, too early breaches could be a consequence of an overestimated breach

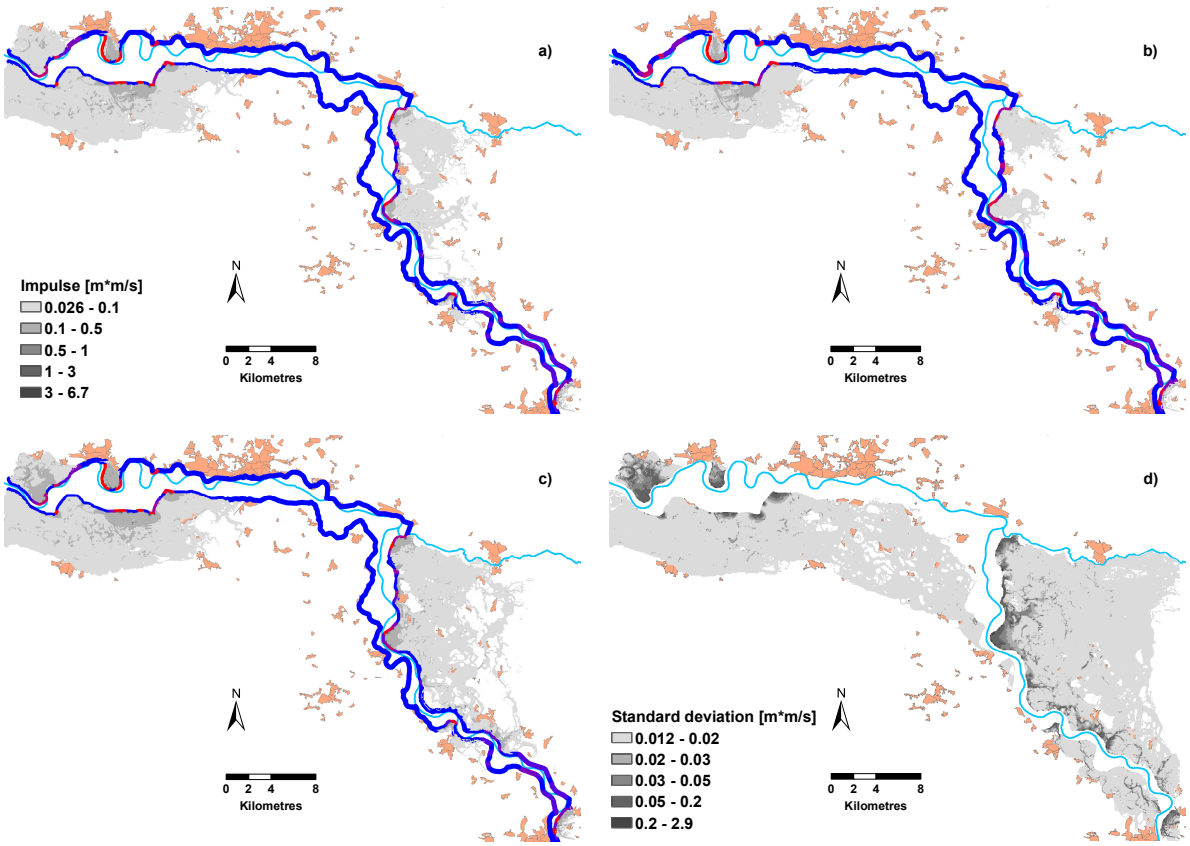


**Figure 4.37:** *Hazard maps for the* $100y$ *scenario. (a) Median, (b)* $10^{th}$ *and (c)* $90^{th}$ *percentiles and (d) standard deviation of the maximum impulse. Legend in (a) applies to (b) and (c).*

probability (Sect 4.7.1). Secondly, this could be an indication of too low protection standards of some dike stretches addressed in IKSE (2003).

Evidently, inundation duration with $0.5\ m$ threshold depth is less than that with $0.2\ m$, although the difference is masked in some parts of the domain by selected legend intervals. With increasing flood magnitude, inundation duration also shows an upward trend for most of the pixels (Figures C.10-C.15). Exceptionally, some cells downstream of Wittenberg exhibit decreasing inundation duration for the $90^{th}$ percentile maps (Figures C.10c, C.11c, C.12c, C.13c, C.11c, C.12c). Taking into account the longer maximum inundation duration for the $10^{th}$ percentile and median maps and decreasing standard deviation in these regions, it can be expected that longer inundation durations become more frequent for these cells.

#### 4.7.2.5 Rate of water rise

The maximum rate of water rise can be used in conjunction with water levels to determine the drowning probability. Corresponding approaches, developed on the basis of victim statistics from the storm surge in 1953 in the Netherlands, are reviewed by Merz (2006). However, the empirical background and scarce knowledge about the toll influencing factors are criticised as limitations for their applicability. Especially, the transferability to other regions and flood events are questioned (Merz, 2006). Despite the lacking universality of the mentioned approaches, the rate of water rise may be a significant loss

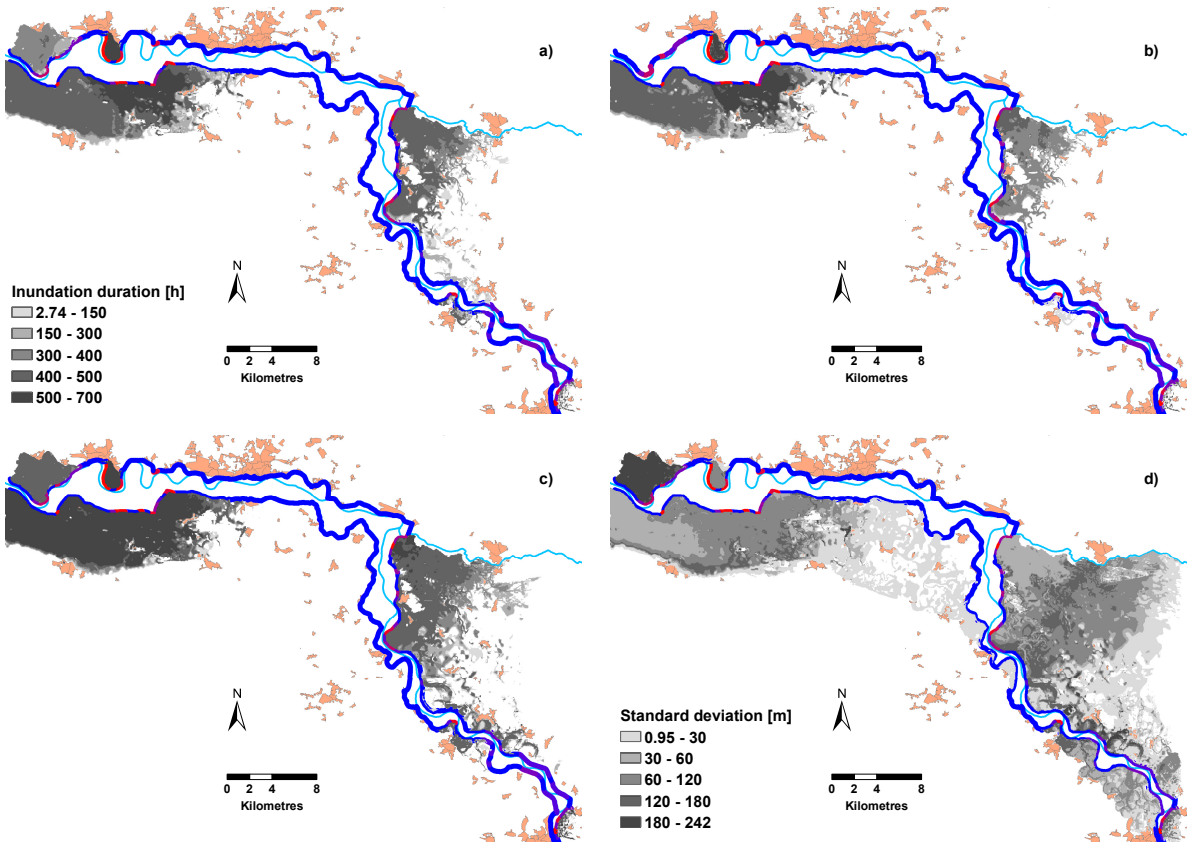


**Figure 4.38:** *Hazard maps for the* $100y$ *scenario. (a) Median, (b)* $10^{th}$ *and (c)* $90^{th}$ *percentiles and (d) standard deviation of the maximum inundation duration with water depth over* $0.2\ m$*. Legend in (a) applies to (b) and (c).*

influencing factor, although its impact is poorly quantified and not yet reflected in contemporary damage models.

The maximum rate of water rise averaged over 1 hour ranges in the $100y$ scenario between nearly $0$ and $3.5\ m/h$ for the $10-90$ interpercentile interval (Figure 4.40b, c). Maximum rates are expected near the breach locations as well as at local depressions, such as lakes and ponds. The latter trap the water flow from various directions that explains high simulated rates.

With increasing flood magnitude, the maximum rate of water rise increases modestly for the majority of the cells (Figures C.16-C.18). High increase rates with differences of more than $1\ m/h$ are mainly observed in areas, which become inundated only at higher flood magnitudes. For instance, the area downstream of Torgau becomes only inundated beginning from the $200y$ scenario with probability less than $50\%$ (Figure C.16c). There, large differences in maximum rate of water rise are expected compared to the $100y$ scenario.

A decrease of the rate of water rise with increasing flood magnitude is simulated only for small domain compartments, mainly in the downstream part of the reach. It can be explained partly by the slight redistribution of hydraulic load along the reach due to dike breaches. Furthermore, a shift in frequency of the rate of water rise values comparing two scenarios may result in negative differences between corresponding percentile maps.

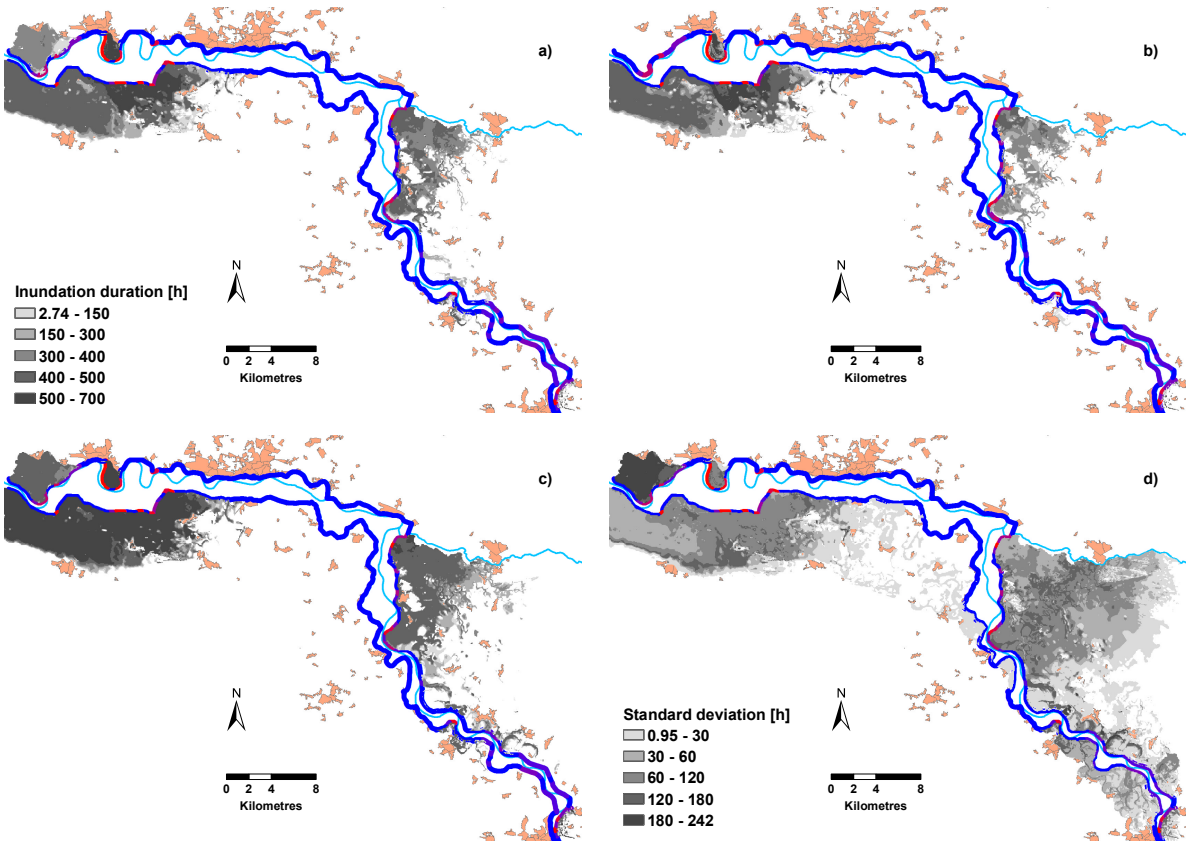


**Figure 4.39:** *Hazard maps for the* $100y$ *scenario. (a) Median, (b)* $10^{th}$ *and (c)* $90^{th}$ *percentiles and (d) standard deviation of the maximum inundation duration with water depth over* $0.5\ m$*. Legend in (a) applies to (b) and (c).*

### 4.7.3 Uncertainty of discharge hydrographs

Uncertainty of discharge hydrographs is analysed by plotting the uncertainty range at four selected locations along the study reach (Figure 4.41). The locations at Elbe-Km 184.5, 214.0, 236.5, 245.5 correspond to gauges Mauken-Pretzsch, Wittenberg, Coswig-Anhalt and Vockerode. Hence, the hydrograph transformation along the reach can be detected from comparison at those points. The dependency of the uncertainty bounds on the flood magnitude can further be analysed by comparison of computed scenarios in Figure 4.41.

Uncertainty of the hydrographs appears to be large, reaching up to 2000 $m^3\ s^{-1}$. It originates from two sources:

- uncertainty in the flood wave form represented by the mean discharge hydrographs of 5 hydrograph clusters (Figure 4.22). Here it should be noted that since the hydrographs represent the mean discharge for each cluster, the range of uncertainty given by the flood wave form is greater than reflected in the model.

- stochasticity of the dike breaches, which implies the stochasticity of breach locations, breach time during the simulation course and ultimate breach width.

Additionally, hydrograph attenuation may contribute to the transformation of the uncertainty bounds.

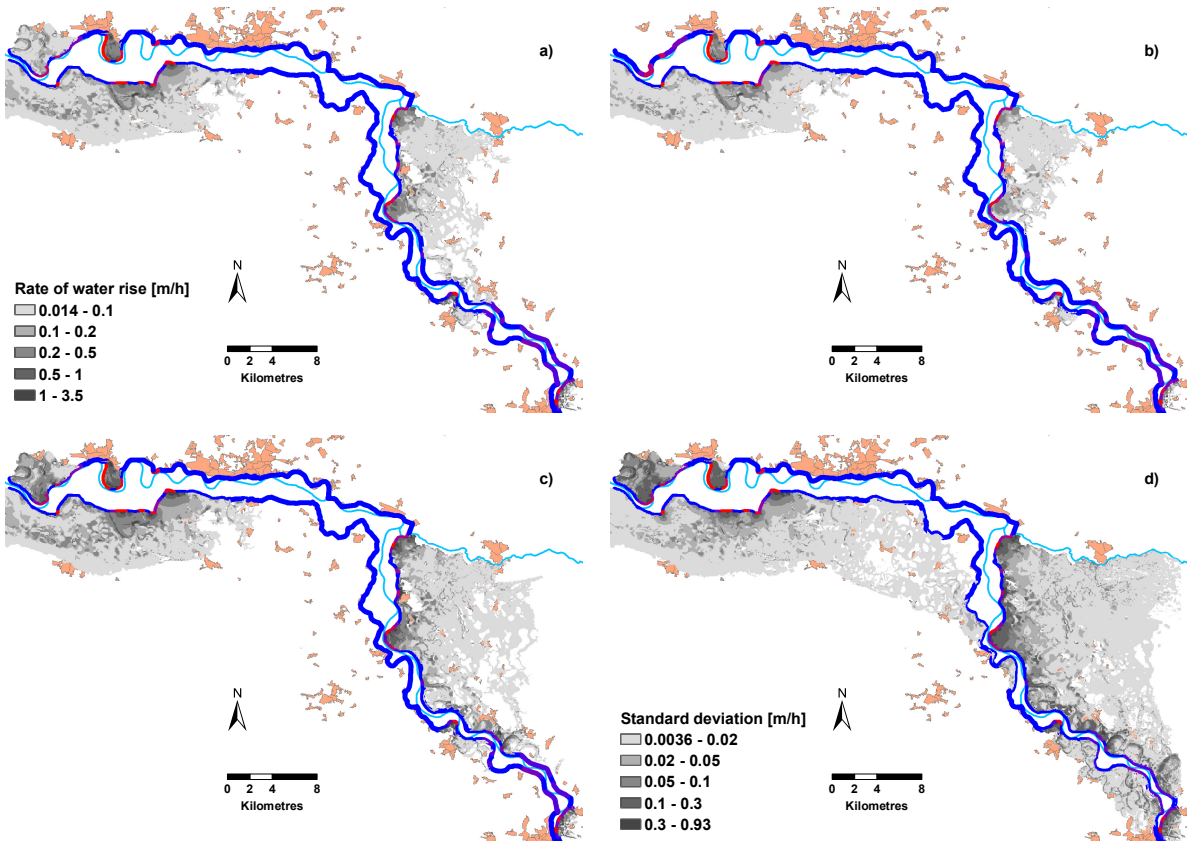


**Figure 4.40:** *Hazard maps for scenario* $100y$*. (a) Median, (b)* $10^{th}$ *and (c)* $90^{th}$ *percentiles and (d) standard deviation of the maximum rate of water rise. Legend in (a) applies to (b) and (c).*

Hydrographs with distinct peak discharges may attenuate differently. However, the difference is expected to be relatively small, since the storage capacity between dikes is limited, and the friction value along every cross-section is assumed to be uniform. Therefore, this storage capacity has only limited power to affect the discharge hydrograph.

Inspection of Figure 4.41 indicates a considerable transformation of uncertainty bounds, represented by the $10^{th}$ and $90^{th}$ discharge percentiles, along the reach. Especially, between Elbe-Km $214.0$ and $236.5$ the effect is strongly pronounced. While uncertainty of the rising and falling hydrograph limbs is reduced towards downstream, the bounds around the hydrograph peak are increased. Such a signature can be explained by the influence of dike breaches. The lower uncertainty bound of the rising limb remains almost unchanged, whereas the upper one reduces strongly. The hydrographs with higher discharge induce dike breaches already prior to the peak, and therefore experience reduction due to the outflow, contrary to the clusters with lower peak discharge values.

Peak discharge for a particular scenario is originally equal for all hydrograph clusters. The widening of uncertainty bounds around the peak, which is particularly emphasised at Elbe-Km $236.5$, is therefore an effect of the dike breach stochasticity between Elbe-Km $214.0$ and $236.5$ and the related considerable outflow. With increasing flood magnitude this impact on the flood peak uncertainty is already clearly pronounced between Elbe-Km $184.5$ and $214.0$. This indicates a stronger influence of breaches on this stretch, and is in concordance with Figures 4.24b, c, d. The latter indicate an increasing dike failure frequency in higher magnitude scenarios for the right-side dike sections in this part of the reach.

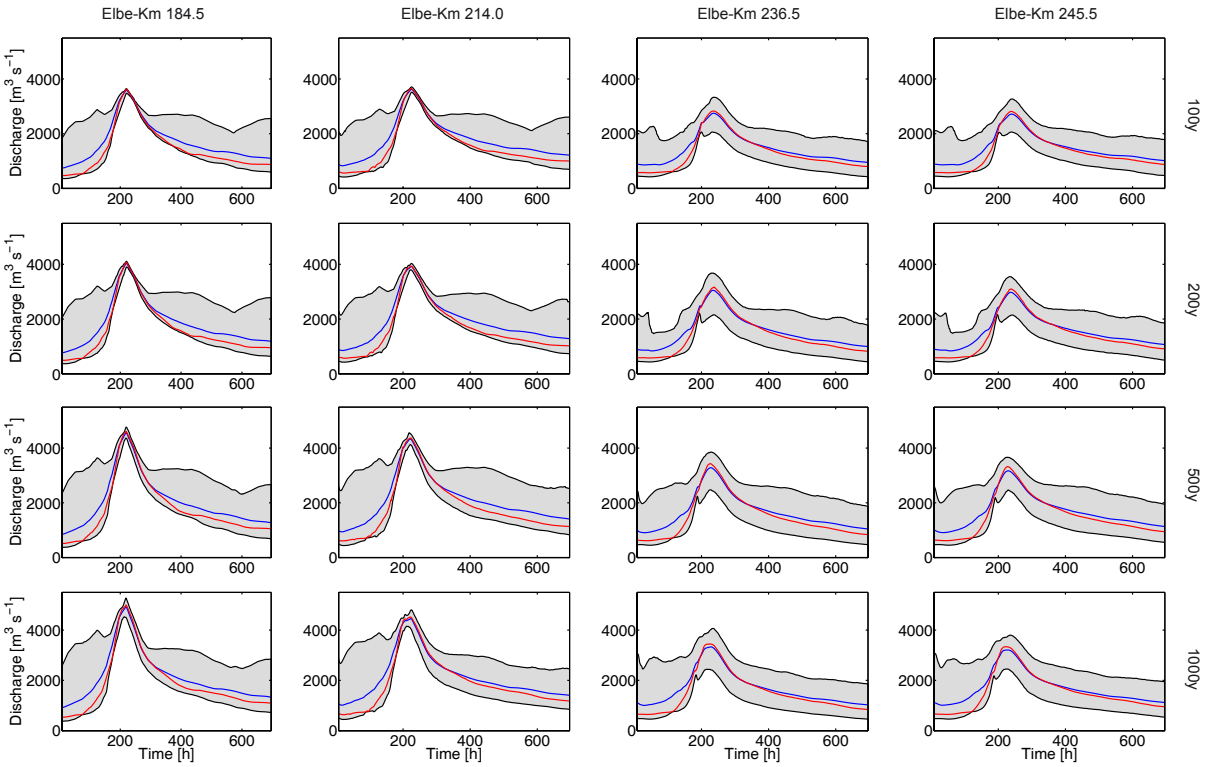


**Figure 4.41:** *Uncertainty of discharge hydrographs at four locations at Elbe-Km* 184.5*,* 214.0*,* 236.5*,* 245.5 *for the flood scenarios* $100y$*,* $200y$*,* $500y$ *and* $1000y$*. Blue and red lines represent mean and median discharge, respectively. Uncertainty bounds correspond to the* $10^{th}$ *and* $90^{th}$ *percentiles.*

Uncertainty bounds of the falling hydrograph limb narrow towards downstream. Simultaneously, the discharge, corresponding to the $10^{th}$ and $90^{th}$ percentiles, reduces slightly. The clusters with high discharges in the falling limb experience stronger discharge reduction. This is indicated by the course of the median hydrographs: whereas the distribution of the discharge is highly skewed at Elbe-Km 184.5 and 214.0, the skewness becomes weaker at Elbe-Km 236.5 and 245.5. This is affirmed by the tendency of the median hydrographs towards the middle of the uncertainty range.

In order to distinguish between the contribution of different sources to the uncertainty range, the total discharge hydrograph range was disaggregated into 5 hydrograph clusters, exemplarily for the $100y$ scenario (Figure 4.42). The total discharge uncertainty for the $100y$ scenario (Figure 4.41) is constituted by the flood wave form to much greater extent in the upper part of the reach till gauge Wittenberg (Elbe-Km 214.0). On this stretch the impact of dike failures results in a very narrow uncertainty range.

Contrary, the breaches downstream of Wittenberg contribute vastly to the uncertainty enlargement. The effect is clearly observed around the hydrograph peaks. The uncertainty bounds begin to enlarge at earliest for cluster 5, which is explained by the comparably higher load during the rising hydrograph limb. The lower the mean discharge is, the narrower the uncertainty bounds get, which is observed on the falling hydrograph limbs of the cluster 1 and 2. At lower discharges, the imapct of dike breaches and breach outflow diminishes.

Summarising the analysis shown in Figure 4.42, it becomes clear that dike breaches have a strong potential to frame the discharge uncertainty. Originally masked by the uncertainty range due to hydrograph form, the uncertainty due to breach stochasticity becomes particularly evident in the downstream part of the reach, when disaggregation of hydrographs according to hydrograph clusters is performed.

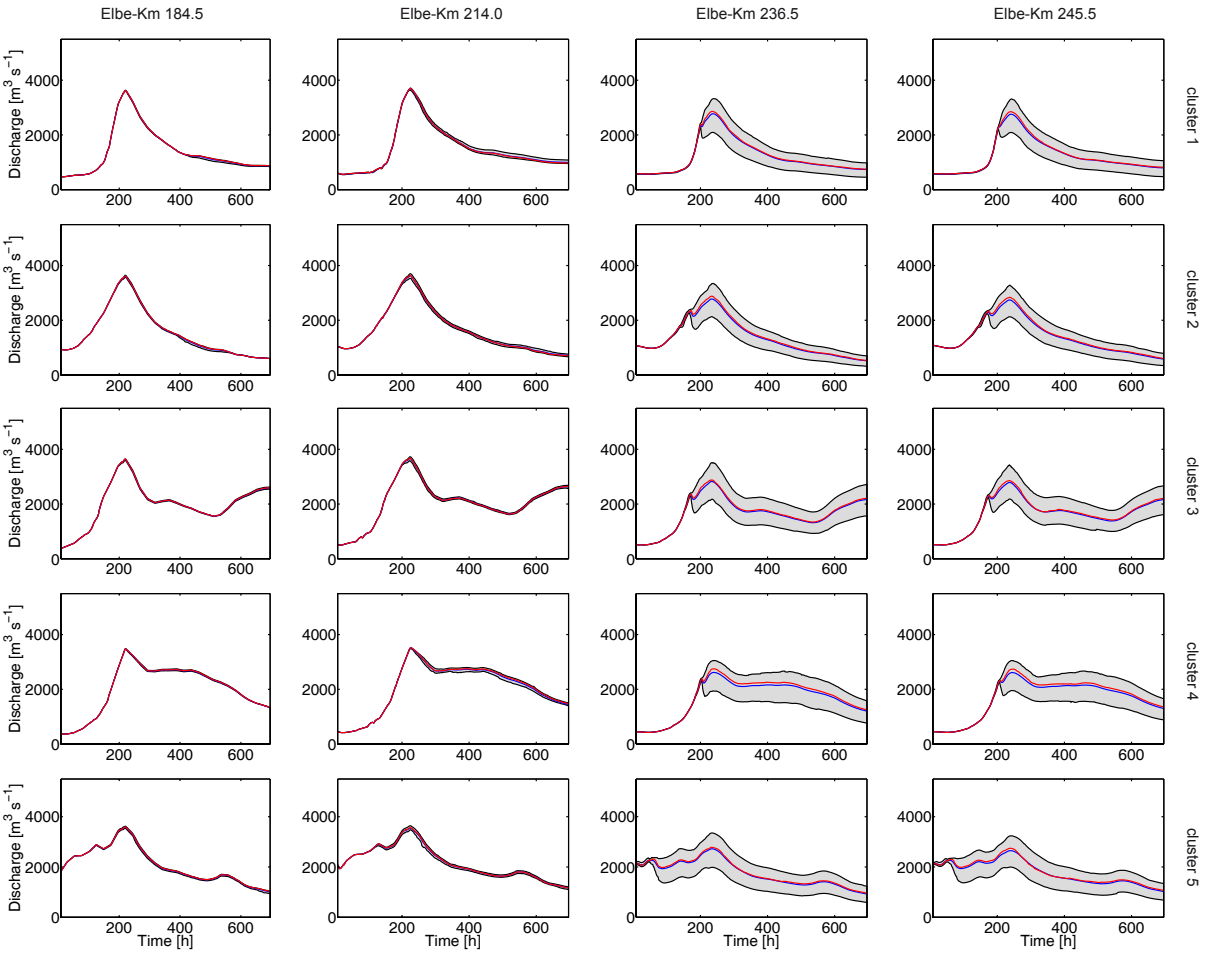


**Figure 4.42:** *Uncertainty of discharge disaggregated into* 5 *hydrograph clusters at four locations at Elbe-Km* 184.5, 214.0, 236.5, 245.5 *for the flood scenario* $100y$. *Blue and red lines represent mean and median discharge, respectively. Uncertainty bounds correspond to the* $10^{th}$ *and* $90^{th}$ *percentiles.*

## 4.8 Assessment of polder retention effect on flood hazard

### 4.8.1 Model setup and objectives

Polders represent retention areas, which are surrounded by dikes and become filled during flood events in order to reduce peak discharge and water level, aiming at hazard and risk reduction for downstream areas. Polder filling can be uncontrolled or activated by human intervention and has to follow a certain strategy in order to achieve an optimum capping effect. A recent example of polder deployment on the Elbe River can be given by the flooding of the Lower Havel polders during the August 2002 flood event (LUA, 2002), actually for the first time since their construction in 1930s. These areas, at the mouth of the Elbe tributary, were filled with backwater flow into the Havel River. Facing the experience during the August 2002 flood, an optimisation of the Lower Havel polder deployment was recently undertaken in several research projects (Bronstert, 2004; WASY, 2005), taking into account hydrological, hydrodynamic and ecological aspects. The August 2002 flood also manifested that besides an optimisation of control strategies for existing polders, additional retention capacities are required on the Elbe in order to alleviate adverse effects of extreme inundations. Potential retention areas on the Middle Elbe, considered prior to the

2002 flood event (Helms et al., 2002), further gained their actuality afterwards (IWK, 2004). Three of these proposed polders, upstream of the Schwarze Elster mouth, were recently analysed by Huang et al. (2007) with the aim to develop a polder control strategy for an efficient flood peak reduction. A polder control strategy typically includes:

- identification of a point in time for polder activation;
- estimation of optimal filling rates taking into account the expected flood wave, i.e. derivation of optimal polder inflow hydrographs;
- development of polder emptying schemes.

In this section, the impact of a polder proposed by IWK (2004) was analysed with the IHAM model. This modelling exercise was particularly focused on studying the changes in dike breach probability and inundation hazard. Furthermore, it should reveal the potential of the proposed probabilistic approach to assess the effectiveness of structural flood protection measures.

A polder, outlined in Figure 4.43a, was integrated into the IHAM model setup. Actually comprised of two hydraulically connected retention areas, it was represented by one aggregated entity for the purpose of simplicity. The proposed polder was integrated into the DEM and surrounded by hypothetical dikes of $3.5\ m$ height resulting in the total volume of ca. $105 \cdot 10^6\ m^3$ (Huang et al., 2007). Polder inflow location at Elbe-Km $179.5$ was selected, for which the optimal inflow hydrographs (Figure 4.43b) were provided by Lindenschmidt, K.-E. (GFZ, personal communication). The hydrographs were computed applying the polder control strategy developed by Huang et al. (2007) with a quasi-2D hydrodynamic model. The

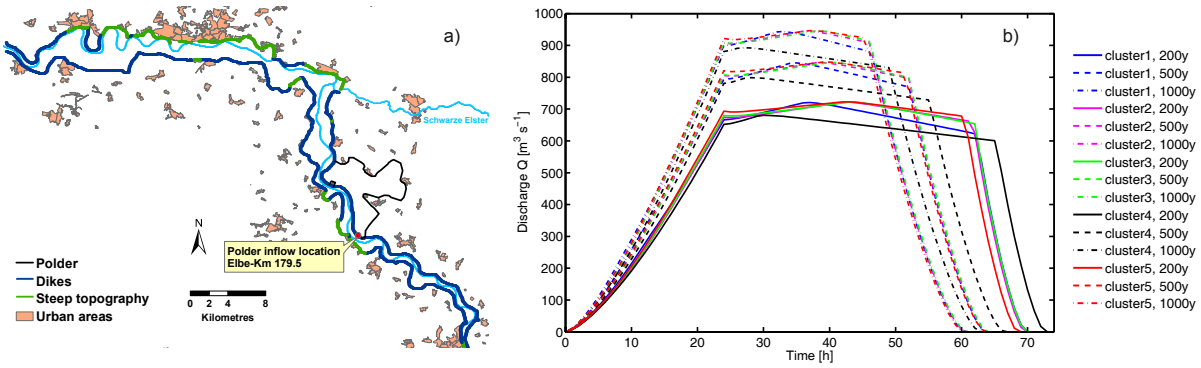


**Figure 4.43:** *(a) Location of a polder on the Middle Elbe reach as proposed by IWK (2004). (b) Inflow hydrographs into the polder at Elbe-Km* $179.5$*, computed by Lindenschmidt, K.-E. (GFZ, personal communication), applying the polder control strategy developed by Huang et al. (2007) with a quasi-2D hydrodynamic model. Each outflow hydrograph corresponds to a certain flood return period and input hydrograph cluster at gauge Torgau.*

outflow hydrographs were developed for each of five hydrograph clusters used as upstream boundary condition for the study reach (Sect. 4.6.1). Since the polders are aimed at peak reduction of severe floods with $T > 100$, filling scenarios for $T = 200, 500, 1000$ were developed. They are further referred as $200y\_pol$, $500y\_pol$ and $1000y\_pol$, respectively. The outflow hydrographs for higher magnitude scenarios are characterised by greater maximum discharge but the outflow duration is less (Figure 4.43b). The polder thus captures larger water volume in shorter time. This seems to be logical, in order to attain an efficient capping with fixed retention capacity.

For this modelling study, no controlled polder emptying was considered. However, backwater flow into the river can occur through dike breaches, which were allowed anytime on the interface between the Elbe channel and polder. The possibility of dike breaches at the landward polder barrier was not considered in this study. However, it may be overtopped if water depth inside the polder exceeds $3.5\ m$.

The polder is activated as soon as a certain discharge value at the polder opening location (Elbe-Km $179.5$) is reached. This triggering discharge was computed depending on the flood wave form and peak magnitude (Lindenschmidt, K.-E., GFZ, personal communication) and summarised in Figure 4.44. The

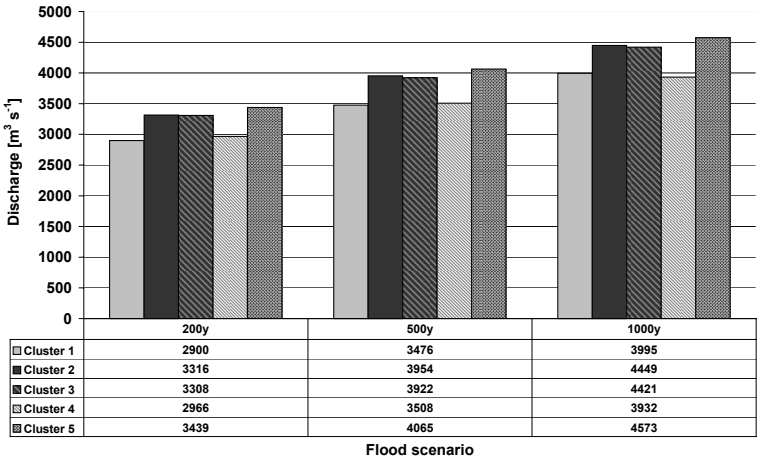


| | 200y | 500y | 1000y |
|---|---|---|---|
| Cluster 1 | 2900 | 3476 | 3995 |
| Cluster 2 | 3316 | 3954 | 4449 |
| Cluster 3 | 3308 | 3922 | 4421 |
| Cluster 4 | 2966 | 3508 | 3932 |
| Cluster 5 | 3439 | 4065 | 4573 |

**Figure 4.44:** *Discharge in the Elbe River at Elbe-Km* $179.5$ *when the polder is activated (Lindenschmidt, K.-E., GFZ, personal communication). Each triggering discharge corresponds to the flood return period and input hydrograph cluster at gauge Torgau.*

smallest triggering discharges resulted for the hydrograph clusters 1 and 4. They exhibit the narrowest peaks (Figure 4.22). Therefore, in order to achieve the maximum discharge capping, the inflow has to be initiated at lower discharges, compared to cluster hydrographs with less steeper rising and falling limbs.

A set of $3000$ IHAM simulation runs was carried out for every scenario deploying the projected polder. The dike section at Elbe-Km $179.5$ was not allowed to breach during the simulation but was opened for outflow upon achievement of the triggering discharge. Stability of other dike sections was modelled based on fragility functions as in previous scenarios without polder. The impact of polder utilisation is discussed in detail in the following sections.

### 4.8.2 Impact on river discharge hydrographs

Discharge hydrographs at four selected locations at various distances downstream of the polder opening were simulated for three investigated scenarios. The difference in the mean and median discharge between scenario sets with and without polder is expressed in terms of percental change with respect to the scenario without polder (Figure 4.45). For all scenario sets at Elbe-Km $184.5$, the difference in the median discharge is nearly zero in the first approx. $180$ hours. After approx. $180$ hours, the reduction of the mean and median discharge by a few percent points is attributed to the retention effect of the polder. The reduction of up to $5\%$ which corresponds to $200 - 250\ m^3\ s^{-1}$, appears to be much smaller than maximum outflow discharges into the polder (Figure 4.43b). This suggests that considerable water volume is diverted back into the river channel through dike breaches on the channel/polder interface, thus reducing the aspired retention effect. This character of the system dynamics merits, however, a further detailed investigation.

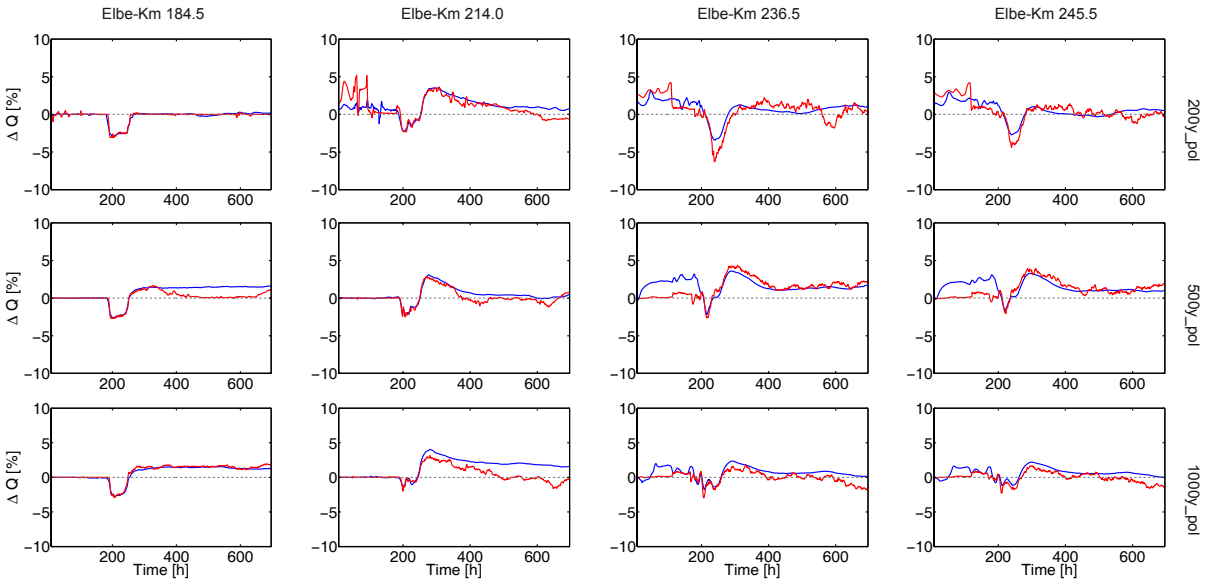


**Figure 4.45:** *Difference in mean (blue line) and median (red line) discharge between respective flood scenarios with and without polder. The difference is given in [%] compared to the discharge in scenarios without polder.*

The degree, to which the the mean and median discharges are reduced, propagates downstream differently for various magnitude scenarios. For instance, the discharge decline at Elbe-Km $184.5$ appears to be similar for all three scenarios, while at the downstream control points the reduction is more pronounced for lower magnitude scenarios, e.g. $200y\_pol$ vs. $1000y\_pol$. This indicates a declining potential of polder to achieve sustainable average discharge reduction with increasing flood magnitude. The discharge reduction effect of the polder dissipates downstream, presumably due to more frequent dike failures at higher severity events. In this case, less outflow discharge through the numerous breaches, compared to the non-polder scenarios, compensates for the polder retention effect and results in reduction of the difference in discharge towards downstream.

The increase of the mean and median discharge after ca. $250$ hours by up to $5\%$ above the initial value could be interpreted as an indication for enhancement of dike stability. Due to capping of the peak discharges, dike breach probability is slightly reduced downstream of the polder for all flood magnitudes (Figure 4.46a, b, c). Therefore, higher average discharges are modelled in the river channel at downstream locations after polder filling, since more water passes through the channel that otherwise would spill into the hinterland.

Mean and median discharges begin to fall slightly after approx. $300$ hours. The decline of the mean and median discharge is various for different scenarios and control locations. It is conjectured that such a behaviour results from different temporal redistribution of dike failures in this time window. Unfortunately, the breach frequency maps (Figures 4.46a, b, c) are insufficient for manifesting this suggestion, since they represent an overall static picture of average system state. Representation of breach frequencies as a function of time would provide an insight into the system dynamics.

### 4.8.3 Impact on dike breach probability

The deployment of the projected polder results mainly in a reduction of dike breach probabilities for all magnitude scenarios (Figures 4.46a, b, c). However, a few dike sections are exposed to more frequent

failures. Reduction in breach frequency appears to be spatially heterogeneous. In the upstream half of the reach the decline of up to $10\%$ $points$ is simulated for the majority of dikes. A stronger reduction, up to $68\%$ $points$, results for a series of left-side dike sections, which are closely clustered downstream of Seegrehna. The increase in breach probabilities appears to be rather modest, with up to $3\%$ $points$ for the majority of the sections. However, they are also clustered together downstream of Wittenberg. Such a clustered pattern deserves a closer look, which is provided by the disaggregation of probabilities according to breach mechanisms examplified for the $500\_pol$ scenario (Figures 4.46d, e, f).

It becomes evident that considerable reduction of dike failure probabilities due to overtopping (Figure 4.46d) is conjugated with the slight but spatially agglomerated increase of breach frequencies due to piping and slope micro-instability (Figures 4.46e, f). Those agglomerations are detected mainly for the dike sections, which experienced a relief from overtopping failures around Seegrehna or farther downstream. This pattern suggests that the overtopping failure probability of several dike sections reacted sensitively to the polder deployment. The latter leads to lower water level extremes. On the other hand, enhanced stability of non-overtopped dikes results in the greater average load in terms of water stage and duration. This impels dike failures due to piping and micro-instability that is manifested in their total increasing breach probability in this part of the reach (Figures 4.46e, f).

This logical result is further affirmed by the changes in relative frequency of mechanisms responsible for dike failures (Figure 4.47). The diagram indicates a slight decrease of overtopping failure frequency in favour of primarily piping but also micro-instability when scenarios of corresponding magnitudes with and without polder are compared.

The analysis indicated a slight decrease of breach frequencies for a number of dike sections in the upper half of the reach due to the deployment of the polder. The polder was shown capable to considerably reduce the breach probability due to overtopping, by up to $68\%$ $points$ for several dike sections downstream of Wittenberg. However, the breach frequency for one nearby section jumped up by $100\%$ $points$. Simultaneously, faint but consistently increased failure probabilities due to piping and slope micro-instability are detected downstream. The net effect of the breach frequency alteration on the flood hazard is explored in Sect. 4.8.4.

### 4.8.4 Impact on flood hazard indicators

The impact of polder deployment on the flood hazard is investigated for the example of inundation depth and duration intensity indicators. Inundation duration with water depth above $0.2\ m$ is considered. These flood intensity indicators are decisive for direct economic damages in residential and industrial areas and to agricultural crops, respectively.

The maximum inundation depth in the $200y\_pol$ scenario increased in the polder area mainly by up to $0.5 - 2\ m$, in local depressions by up to $4\ m$ (Figures 4.48a, b, c), compared to the $200y$ scenario without polder. The standard deviation in the area inside the polder mainly decreased (Figure 4.48d) that signifies a smaller degree of variability in water depth for the case of controlled polder filling. The eastern polder part exhibits, however, a slight increase of standard deviation. The comparison of the respective scenarios with and without polder indicates a hazard relief for downstream areas between $0$ and $1\ m$, locally up to $4.1\ m$. The vast majority of the inundated areas in the downstream half of the reach experiences a decline of maximum water depth of up to $0.5\ m$. This holds also for more severe event scenarios (Figures C.19a, b, c and Figures C.20a, b, c). At the downstream tail of the reach, slightly deeper flows, up to $0.5\ m$, are simulated and attributed to increased piping and micro-instability failure frequencies. The strongest hazard relief is attained directly downstream of the polder and closely to the dike sections with reduced overtopping probability near Seegrehna (Sect. 4.8.3).

On the other hand, the implementation of polder leads to remarkable increase of maximum inundation depth south-east of polder for all scenarios and percentiles except for the $10^{th}$ percentile in $200y\_pol$.

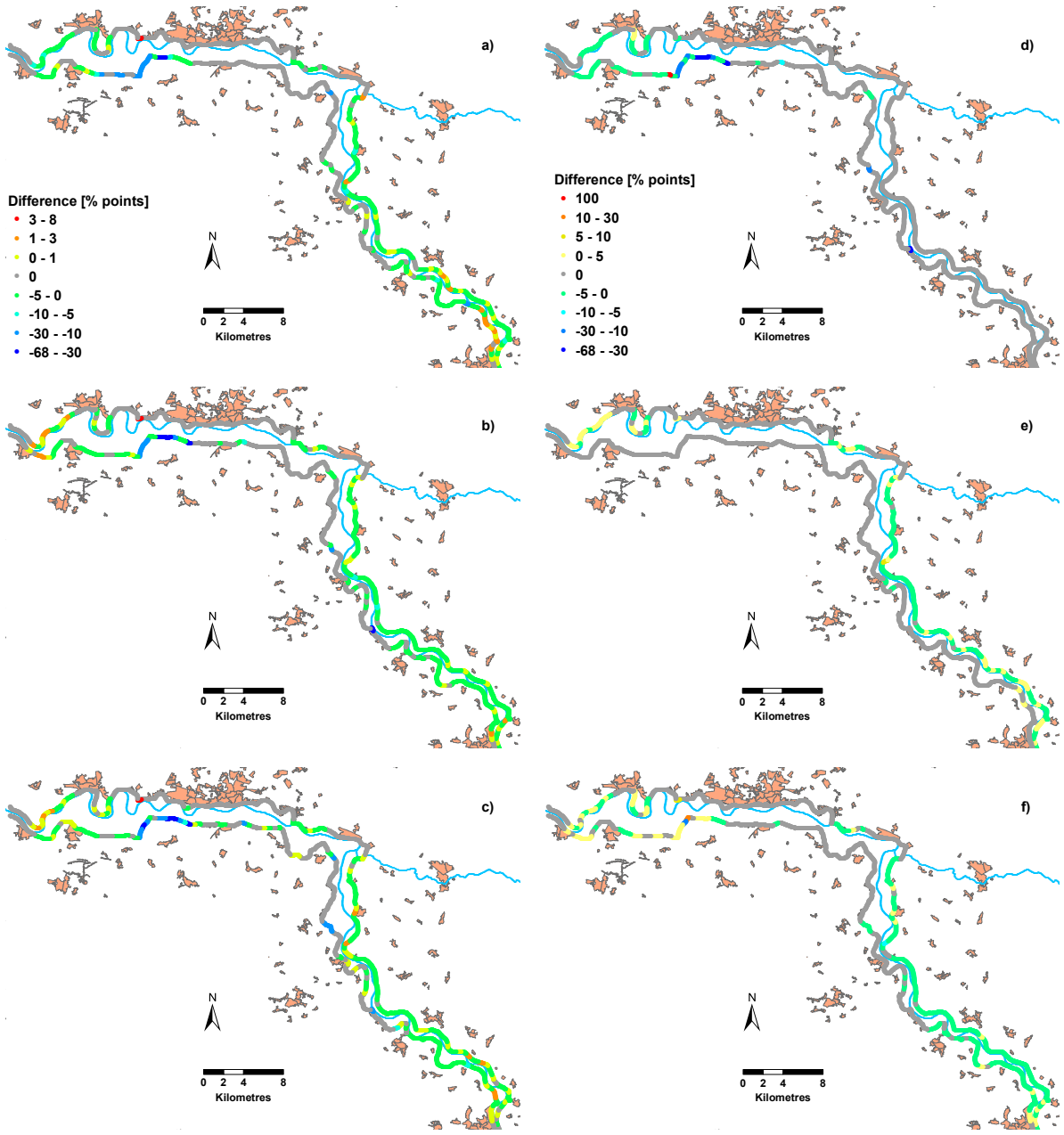


**Figure 4.46:** *Difference in dike failure probabilities between the flood scenarios (a)* $200y\_pol$ *and* $200y$*, (b)* $500y\_pol$ *and* $500y$*, (c)* $1000y\_pol$ *and* $1000y$*. Legend in (a) applies to (b) and (c). Difference in dike failure probabilities between the flood scenarios* $500y\_pol$ *and* $500y$ *disaggregated into* 3 *breach mechanisms (d) overtopping, (e) piping and (f) slope micro-instability. Legend in (d) applies to (e) and (f).*

A detailed inspection of the inundation patterns indicated no water spillover out of polder for median of $200y\_pol$ scenario and $10^{th}$ percentile of $500y\_pol$ scenario. This suggests that the increase in inundation depth results from the detention of flow in the hinterland by the polder surrounding dikes. This flow originates from the breaches upstream of the polder inflow location and would otherwise unhamperedly

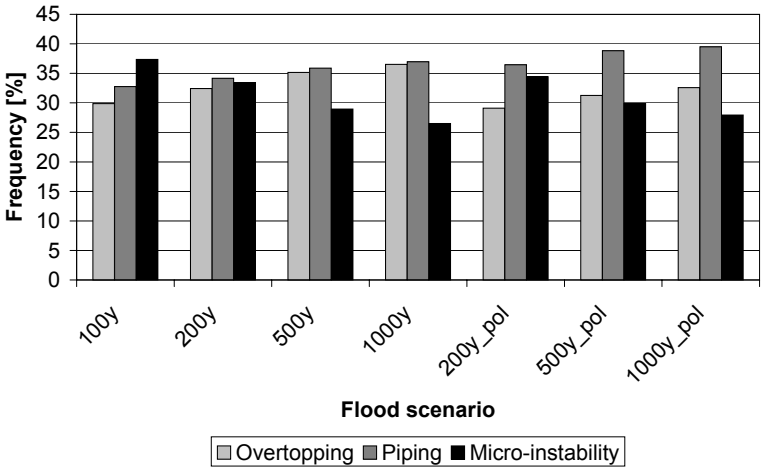


**Figure 4.47:** *Relative frequency of considered dike breach mechanisms responsible for dike failures in simulated scenarios with and without polder.*

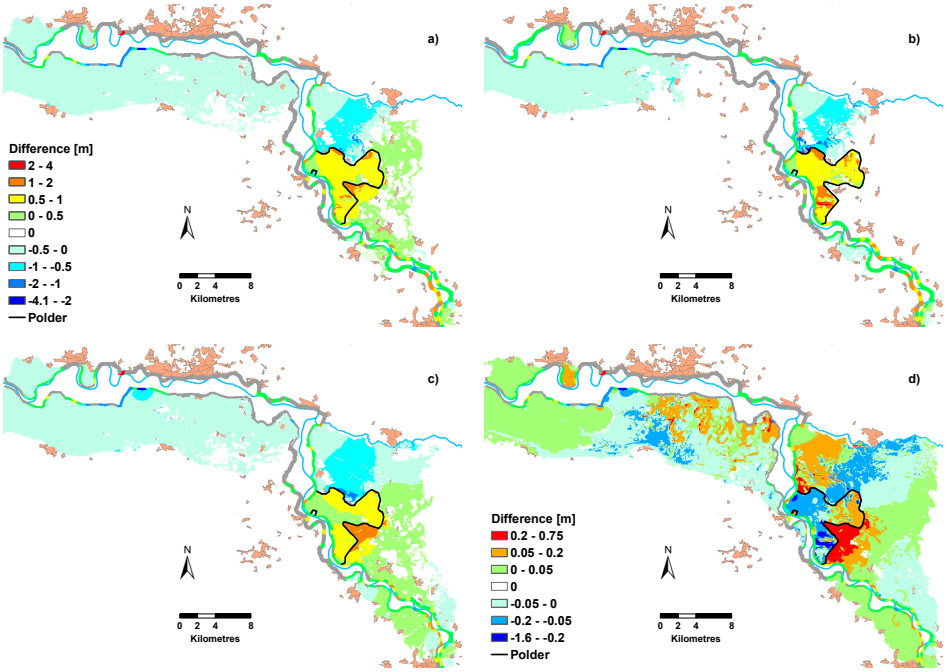


**Figure 4.48:** *Difference in maximum inundation depth between the scenarios* $200y\_pol$ *and* $200y$ *for (a) median, (b)* $10^{th}$*,* $90^{th}$ *percentiles. (d) Difference between corresponding standard deviations. Legend in (a) applies for (b) and (c).*

spread over the whole hinterland area.

In case of more extreme scenarios and higher percentiles, a polder spillover was detected over its south-eastern barrier. It additionally contributes to the hazard increase. The overtopping of the inner polder dike barrier at higher severity events is due to the additional water input through the dike breaches on the channel/polder interface. However, it has to be mentioned here that the situation is aggravated by the assumption of zero backwater flow through the polder opening that would otherwise provide a relief

and possibly prevent spillover in a real flood situation.

The maps for inundation duration with flow depth over $0.2\ m$ exhibit widely similar patterns as the maximum inundation depth (Figures 4.49a, b, c; Figures C.21a, b, c and Figures C.22a, b, c). Visual inconsistencies of respective patterns are partly attributed to the selected boundaries of legend classes. Generally, in the areas of increasing maximum water depth, inundation duration also increases. This particularly holds for the polder and adjoined upstream areas. Inundation duration, corresponding to the

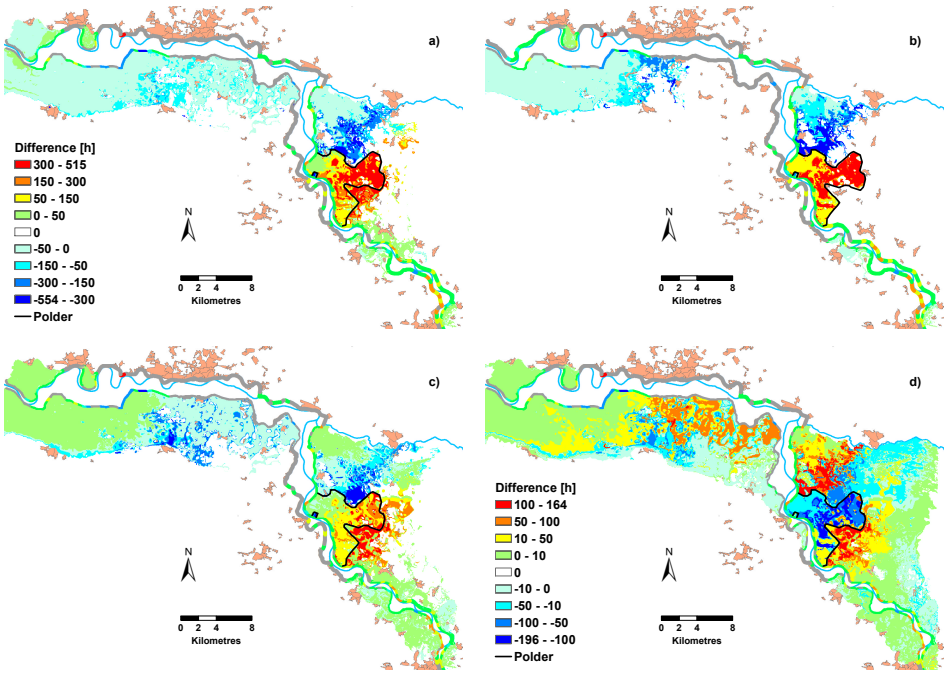


**Figure 4.49:** *Difference in maximum inundation duration with water depth above* $0.2\ m$ *between the scenarios* $200y\_pol$ *and* $200y$ *for (a) median, (b)* $10^{th}$*,* $90^{th}$ *percentiles. (d) Difference between corresponding standard deviations. Legend in (a) applies for (b) and (c).*

$90^{th}$ percentile (Figures 4.49c, C.21c and C.22c), tends to increase by more than $50\ h$ downstream of Wittenberg. This is surprising at a first glance, taking into account the significantly reduced overtopping probabilities of the nearby dikes and mainly decreasing maximum water depths (Figures 4.48c, C.19c and C.20c). However, the increased mean and median channel discharge in the phase of falling hydrograph limbs (Figure 4.45) is likely to preclude fast dewatering of the hinterland. This may cause a shift of the $90^{th}$ percentile towards more lengthy water stages above $0.2\ m$ threshold depth.

The analysis carried out in this section showed that the deployment of polder has a potential in reducing maximum inundation depth and duration for downstream parts of the reach. However, a more severe hazard is likely to be expected for areas upstream of polder due to flow detention and, at higher magnitude events, due to polder spillover, although the latter is conditioned by modelling assumption. Whether the redistribution of the hazard is economically and socially bearable can be determined by cost-benefit analysis. Such analysis would logically complement the presented work.

# Chapter 5

# Conclusions and perspectives

## 5.1 Summary of novel implementations and key findings

The main motivation behind the development of the IHAM methodology was the need for the improvement of presently available flood hazard assessment approaches by accounting for the dynamical nature of the fluvial inundation processes that may be significantly influenced by failures of flood defences. The presented methodology extends the works of Apel et al. (2004, 2006) by incorporating a more complex channel flow representation, extending the dike breach model with piping and slope micro-instability failure mechanisms, and implementing a more complex treatment of hinterland inundation process with a 2D storage cell hydrodynamic model for overland flow (Sect. 2.5). In IHAM, the modelling components for channel flow, dike breaching and hinterland inundation are dynamically coupled. It implies data exchange between the simulation domains in every time iteration. Therefore the methodology allows for interactions between dike breaches due to dynamic coupling of channel and overland flow models. Hence, the effect of load relief onto downstream flood defences as well as the hazard reduction could be considered in case of upstream breaches or flood peak capping by structural measures such as polders (Sect. 4.7 and 4.8). Thus the advantage over the widely used steady-state approximations of flood extent, combined with water level interpolation techniques or even subsequent hydraulic modelling of hinterland flow (Chapter 2), becomes evident. In view of the rapidly advancing research on hybrid models of fluvial inundation (Chapter 2), the IHAM approach, besides using the hybrid channel-floodplain concept, incorporates the dike breach model. Hence, attention is devoted to the reliability of flood defence systems, which are common attributes of the densely populated catchments with high asset accumulation.

The approach presented in this thesis allows, for the first time, computation of an extended spectrum of flood intensity indicators under consideration of dike failures due to three principal breach mechanisms in a modelling framework which combines dynamic deterministic models and probabilistic treatments. Although these implementations introduce a considerable increase of computational burden, they bring an advantage in terms of more detailed and comprehensive flood hazard assessment on the reach scale.

#### 1D hydrodynamic modelling

The dynamic nature of the flood wave propagation is captured by the utilisation of an unsteady 1D hydrodynamic model for a river channel. This approach represents a mature engineering practice for modelling of water stages and discharges along a discretised river channel. Contemporary 1D hydrodynamic codes employ fast and robust implicit numerical schemes that contribute insignificantly (in the order of several minutes) to the increase of computational time compared to the hydrological routing methods combined with simple transformation schemes, such as discharge-water stage look-up tables. The latter, by the way, require parameterisation and application of a steady hydrodynamic model for their

development. Available 1D hydrodynamic modelling techniques are suitable for a wider range of flow conditions including backwater flow, that may, for instance, occur in tributaries during severe floods, while the Muskingum-type routing or kinematic wave approach fail to simulate such situations. Considering the mentioned versatility, convenience in input and output data processing and modest increment of computational demand, the 1D hydrodynamic model was favoured for use in the framework of IHAM.

Since the model's capability to provide robust predictions of water stages along the river channel were in the focus, the 1D code was calibrated in steady-state against spatially distributed high water marks (Sect. 4.3.1). The use of lumped roughness values and calibration against gauge records rather ensure the model's routing capability. Correct predictions of local water stages can be achieved by spatially distributed calibration. The steady and unsteady model validation complemented the setup process. For the steady model, nearly $0\ BIAS$ and $RMSE$ of $0.169\ m$ was achieved for the reach between Dresden and Vockerode.

The results of the unsteady validation for the upstream part of the reach could be regarded as acceptable. Downstream of Wittenberg, the model exhibited strong weaknesses especially in the meandering part of the reach with extremely wide floodplains. Even very high roughness values, of up to $0.2\ m^{-1/3}\ s^{-1}$, could not compensate for the poor representation of primarily two-dimensional flow pattern by the 1D hydraulic model. The roughness values therefore do not correspond to solely the energy loss due to friction, but rather represent effective roughness, which compensates for the shortcomings of an imperfect model. This limitation is further discussed in Sect. 5.2.1 along with possible solutions.

#### Dike breach modelling

Contrary to the traditional investigations of dike breach induced inundations, reviewed in Sect. 2.5, the IHAM approach does not adopt hypothetical breach locations. It rather tries to predict possible breaches (location, time, breach width) by incorporating process knowledge and empirical evidence into probabilistic analysis. Differently from the analysis of Hall et al. (2003), who explicitly estimated the probability of all possible defence failure combinations resulting from combinatorial permutations and then disregarded combinations with low probability of occurrence, the presented analysis approaches the consideration of dike failure combinations by Monte Carlo simulation given a dynamically simulted load and feasible number of runs. It provides the finally achieved convergence level of the Monte Carlo results in terms of change in breach probability and intensity indicators.

The ultimate dike breach width was considered, for the first time, as a random variable in a dynamic modelling framework. Where records of breach widths are available, the proposed probabilistic treatment represents an alternative to still very uncertain deterministic modelling of breach development. Provision of further data on breach width may stipulate the development of differentiated probability distribution functions depending on e.g. dike age and/or type of construction material.

The dike stability analysis, due to three possible dike breach mechanisms: overtopping, piping and slope micro-instability, was based on prior computed fragility functions, which are grounded either on physically-based or empirical process formalisation. In the fragility functions, the uncertainty of parameters that influence the breaching process is accounted for by treating them as random variables in a Monte Carlo framework. The sensitivity analysis for piping and micro-instability identified a particularly strong dependance of the seepage fragility functions and fragility function for critical pipe development upon the mean hydraulic conductivity for dike core and foundation materials. Due to the extremely wide range of possible hydraulic conductivity values, the impact on failure probability can be dramatic. Therefore, the variation range should be constrained by obtaining further survey data of materials and composition of core and foundation. The mean thickness of the covering clay layer was shown to be the crucial determinant of the fragility curve for rupture.

Whereas overtopping is determined by only one critical process and can be described by one reliabil-

ity function, piping and micro-instability are characterised by a sequence of dependable events. Hence, the fragility functions for each of those determinative processes are combined in a probabilistic framework as required by the probability theory of dependable events. Some of the sub-processes leading to dike failure were neglected, e.g. dike core subsidence in case of piping, because of insufficient process knowledge and lacking formalisation. However, the probabilistic framework is open for integration of future process knowledge in form of fragility functions. Other breach mechanisms can also be incorporated into IHAM.

Consideration of various breach mechanisms in a dynamic analysis enables the differentiation of dike sections according to the primary threatening failure mode (Sect. 4.7.1). Such analysis produces dike hazard maps that facilitate an efficient allocation of resources for planing and implementation of dike reinforcement measures. Moreover, during the operational flood management, spatially distributed, failure mode-specific information may be useful for deciding on effective protection measures for each particular dike stretch. For the study reach, different dike stretches were identified being amendable to various failure modes.

The outcome of the Monte Carlo analysis was tested for convergence by assembling random subsets out of $3000$ performed runs. Dike breach probability converges to $\pm 3\%$ $points$ for the $100y$ scenario, whereas for the higher magnitude event set $1000y$ this level of convergence is attained after $1000$ runs. It is suggested that the different speed of convergence is explained by the less pronounced effect of dike breach stochasticity on changes in dike breach hazard for more extreme floods. In other words, the magnitude of load and larger water volume in the $1000y$ scenario lead to a more homogeneous spatial failure pattern. The load relief due to earlier breaches seems to have a weaker potential to prevent further dike failures.

The simulation results indicate primarily an increase of dike breach probabilities with increasing flood severity. Furthermore, the proportion of overtopping and piping failures increased slightly compared to the share of micro-instability. This indicates a higher sensitivity of these two failure modes to an increase in peak and load duration. A slight decrease in failure probability was modelled for several left-side dike sections upstream of Torgau, presumably because of the load relief due to more frequent breaches of the right-side dikes. The effect of considerable breach probability reduction for downstream dikes due to the load relief as a consequence of more frequent upstream failures for high severity floods could not be observed. Firstly, the increase of failure frequency upstream may not be sufficient to cause significant load reduction. Indeed, the impact of dike failures on the flow hydrographs in the upstream half of the reach is much smaller compared to the downstream part (Sect. 4.7.3). Secondly, the limited retention capacity at some places and water spread velocity at other hinterland compartments may limit the flood wave reduction to some extent. Finaly, the erroneous probability sampling (Sect. 4.7.1) is likely to overestimate failure probabilities and reduce the failure sensitivity to the load changes.

**Flood hazard assessment**

The 2D storage cell hydrodynamic model, employed in this study for overland flow, provides the estimations of an extended spectrum of flood intensity indicators, such as inundation depth, flow velocity, impulse, inundation duration with water level above a threshold, and rate of water rise (Sect. 4.7.2). Different intensity indicators are known to be relevant for damages at private households, agricultural sector and for human casualties. An application of more specialised damage functions can be facilitated with the provided methodology that possibly has a potential to reduce the immense uncertainty of flood risk estimates.

Flood extent during the August 2002 derived from a visible range satellite image was found to be insufficient to constrain uncertainty in roughness parameterisation of the raster-based inundation model (Sect. 4.5). The employed statistical performance measures indicated very weak sensitivity to changes in

roughness values, due to the constraining topography in some model subdomains and gross over- and underestimations of inundation extent in others. Contrary to the vastly explored calibration tasks for fluvial inundations without dike breaches, floods shaped by defence failures appear to be of limited value for calibration as long as breach outflow dynamics, overtopping discharge rates and tributary contributions are unknown. These circumstances forced an adoption of spatially distributed, literature based roughness values assigned to landuse classes.

The developed flood hazard maps for a range of intensity indicators provide a basis for reach-scale flood risk assessment when combined with the respective damage functions and values at risk. The probabilistic nature of the developed hazard maps embraces inherent uncertainty bounds expressed by the percentile maps. Moreover, first impressions about possible inundation extents and their likelihood can be gained from the binary pattern maps.

Convergence of inundation depth predictions was assessed by comparing mean and standard deviation of spatially distributed values (Sect. 4.7.2.2). As in the case of breach probability, a comparable convergence level for the $1000y$ scenario was achieved faster for both mean and standard deviation, compared to $100y$. This further signifies a declining potential of breach stochasticity to affect flood hazard pattern with increasing flood magnitude.

With higher flood severity, the increase of all intensity indicators was simulated for majority of the model domain. Small locally pronounced decreases in flood hazard were simulated mainly in the downstream part of the study reach.

#### Assessment of polder impact

The IHAM methodology was shown to be applicable for the assessment of the polder impact on flood wave, dike breach probability and inundation hazard (Sect. 4.8). The polder scenario simulations adopted, however, some assumptions that are outlined here. Firstly, the backwater flow through the dike opening was not explicitly simulated. Further, the optimal control strategy derived for polder scenarios with a quasi-2D hydrodynamic model was based on input hydrographs at gauge Torgau. However, it did not take into account possible dike failures upstream of the polder opening, that might change the optimal control rules. These breaches would have an influence onto both the triggering discharge and outflow hydrograph. The effect is, however, expected to be insignificant, since the hydrograph transformation due to breaches between Torgau and polder opening (Elbe-Km 179.5) appears to be small.

The effect of the polder was tested for extreme flood scenarios with $T = 200, 500, 1000$ return periods. The reduction of mean and median hydrographs in the main channel by maximum of $200 - 250\ m^3\ s^{-1}$ appeared to be smaller than expected compared to the peak polder outflow discharges between $700 - 950\ m^3\ s^{-1}$. The effect of the polder was thus shown to be rather weak. It is suggested that dike breaches on the polder/river channel interface resulted in a considerable water backflow that consequently caused an increase of mean and median channel flow discharge. The mean and median flow reduction effect diminishes with increasing flood magnitude and dissipates towards downstream.

Different flow hydrograph behaviour for the computed scenarios after polder deployment is presumably impacted by the redistribution of breach frequencies over event time period. The temporal patterns of dike failures merit therefore a detailed consideration in the future in order to gain knowledge about this feature of system dynamics.

With increasing flood magnitude, the deployment of the polder caused a drop of breach frequencies mainly by up to $5\%\ points$, locally up to $30\%\ points$ in the upstream half of the reach, and by mainly by up to $5-10\%\ points$, locally up to $68\%\ points$ in the downstream part of the reach. The strong reduction of breach frequencies downstream is chiefly due to the reduction of overtopping failures, however, with slight increase in piping and micro-instability failure probabilities. The majority of dike sections that experienced a decrease in breach probability in the upstream half of the reach are less prone to piping

and micro-instability.

The polder is expected to achieve its maximum utility for floods with return periods between 100 and 200 years. For the flood scenarios with high return periods, mainly a small positive hazard reduction effect in terms of water level and inundation duration was simulated downstream of polder. However, with increasing flood magnitudes an increase of inundation hazard is expected for the upstream hinterland areas. The flow originated from upstream breaches and detained by outer polder dikes as well as polder spillover are the reasons for the simulated hazard increase. The net benefit of the polder construction should be evaluated in a cost-benefit analysis which requires the computation of expected damage and its change due to polder deployment.

## 5.2 Recommendations for model improvement and future perspectives

### 5.2.1 Limitations of the IHAM approach

#### Inherent limitation

The inherent limitation of the modelling approach employed in IHAM is the practical impossibility to validate the results. Modelling of extremely infrequent processes, such as high return period events, and unrepeatable processes, such as dike failures, faces a problem of validation. Because of the absence of reliable system state records models of such processes cannot be validated in a strict sense by direct comparison with measured data ($1^{st}$ order validation) (Hall and Anderson, 2002; Merz, 2006). Furthermore, the probabilistic nature of IHAM, realised in a Monte Carlo framework, predicts the possible system states and their associated probability of occurrence. Hence, even if the next severe flood causes a certain dike breach pattern and inundation extent, these observations can merely be used to assess the model plausibility but not to validate the results. Modelling results can, however, be invalidated if the observed flood outcomes lie outside of the predicted uncertainty range.

In light of this limitation, Hall and Anderson (2002) and Merz (2006) advocate an alternative approach to quality assurance of such models. They claim a transparent presentation of the process parameterisation and assumptions, sensitivity analysis, representation of uncertainty bounds and their main sources, analysis of uncertainty propagation through the model structure, and finally model benchmarking. This approach can be regarded as validation of the $3^{rd}$ order (Merz, 2006). Moreover, any evidence of the system state variables and corresponding response in any form, ranging from precise records to verbal descriptions, must be collected and integrated into the evaluation process.

This work has done justice to some of the listed requirements, where it was made feasible by available data and computational resources. The formalisation and parameterisation of processes has been described in Chapters 2, 3 and 4. Sensitivity analysis of fragility functions was performed with regards to dike geotechnical parameters in case of piping and micro-instability (Sect. 4.4). However, high sensitivity of fragility functions does not necessarily mean high sensitivity of breach probability of the dike section. Uncertainty due to dike breach stochasticity and flood wave form were shown and separated in terms the of flow hydrographs along the reach. The separation revealed a considerable impact of dike failures on hydrograph uncertainty in the downstream part of the reach, whereas in the upstream half, the uncertainty due to the flood generation processes was found dominant.

#### Limitations of the IHAM structure

The IHAM model adopts a series of assumptions in the spatial representation of the fluvial inundation process. Firstly, the channel and floodplain flow between dikes is treated with a 1D hydrodynamic model. While for the channel flow this approximation is widely accepted, on wide floodplains with meandering channels and crossing flows, the treatment shows considerable weaknesses. This was highlighted by

the calibration and validation results in Sect. 4.3.1. Secondly, the hydraulic load computed by the 1D flow model is compared to the average height of discretised dike sections. The variation of the absolute dike height in a section was therefore not considered in the model. This source of uncertainty can be considered in future modelling studies, although it can adversely affect the convergence of Monte Carlo simulation. Thirdly, overtopping flow in case of non-breached dikes is neglected. This may cause an underestimation of inundated areas in some regions.

Finally, the discrepancy between the observed and simulated breach frequencies suggested an overestimation of breach probabilities due to piping and micro-instability compared to overtopping. Since there exist only a few evidences of dike breaches for the study reach the model cannot be directly validated using observations. As discussed in Sect. 5.2.1, the way to ensure the plausibility of modelling results is the correct representation of underlying processes assured by the verification of implemented algorithms. In the course of the IHAM revision, an error in dike failure probability sampling from fragility functions was located (Sect. 4.7.1). The error resided in the direct reading of the dike breach probability from fragility functions without considering the failure probabilities that were already sampled and used in the precedent Monte Carlo samplings. This is likely to cause an overestimation of breach frequencies. Especially, piping and micro-instability are expected to be overestimated, since their fragility functions are much less sensitive to water level changes than in case of overtopping. This error will be corrected in the next IHAM version.

#### Consideration of uncertainty

Previously, a great number of studies explored the uncertainty in inundation predictions for typical unprotected river reaches. It was stipulated by uncertainty in hydraulic model parameters, rating curve boundary condition and constraining observations (Chapter 2). Apel et al. (2004) and Apel et al. (2006) considered further uncertainty sources for diked river reaches, such as variability of the hydrograph form for the main river and tributaries, uncertainty in dike geometry, turf quality, breach width in form of scenarios, rating curves used for hydraulic transformation within a modelling domain, and uncertainty in depth damage curves. The authors thus could derive the uncertainty range for the risk curve.

In this work, the number of considered uncertainty sources is reduced to flood wave form, dike and foundation properties and ultimate breach width. However, complexity of process representation was increased to allow a more detailed analysis of dike failure modes and inundation dynamics. It appears that one continuously faces a trade-off between the degree of process representation, scale of model application and number of considered uncertainty sources in light of restricted computational power. Depending on the question under study, the degree of process complexity should be adjusted to approach predictions, uncertainty reduction and estimation on considered scale. From the stand-point of the presented methodology, two possible ways can be thought of for further model developments, which are discussed in the next sections.

### 5.2.2 Towards enhanced representation of fluvial inundation processes

Retaining the IHAM scale of application, river reaches of a couple of hundreds kilometres, one can further develop the modelling system to subsequently overcome the limitations addressed in Sect. 5.2.1. The weakness of the 1D hydraulic model in the areas of extended floodplains could be addressed by implementing a branched discretisation of these regions. Another more sound, but computationally demanding solution would be a 2D treatment of the floodplain flow between dikes. Further, significant tributaries and their defences may be integrated into the modelling setup to allow explicit treatment of possible backwater flows and resulting inundations due to dike failures. Among further breach mechanisms, slope macro-instability certainly should be considered for implementation in the modelling ap-

proach. With increasing computational power or optimisation of the computational algorithms, further uncertainty sources, such as, for example, uncertainty in roughness parameterisation of the river channel and floodplain, can be included into the presented methodology. To reduce the uncertainty in flood hazard statements, more detailed knowledge on flood defence properties and their behaviour upon loading ought to be integrated into fragility and breach development models. As far as the uncertainty due to the 2D hydraulic model parameterisation is concerned, further spatially distributed data, such as a series of inundation extent remote sensing images or distributed water level dynamics records, are believed to bear a potential to constrain friction parameters.

### 5.2.3 Towards a hazard assessment on regional scale

In view of the changing climate, there is a need for large-scale national flood hazard and risk assessment to support decision making on high political levels and sane allocation of resources. The methodologies used for this purpose attained considerable achievements, however, at costs of a number of assumptions and simplifications addressed in Chapters 1 and 2.

The further methodological improvement for the large-scale risk assessment relies, among others, on performing dynamical hydraulic simulations of possible load scenarios under consideration of dike failures — the key concept used in IHAM. However, current computational constraints would rigourously limit a direct transfer of the presented methodology to the national scale. Furthermore, the challenge in acquiring and integrating national datasets ought to be considered.

From experience gained during this work, the 2D hydraulic simulations can be seen as a bottleneck in terms of computational speed. However, the simplicity of the 2D raster-based approach to incorporate raster data sets makes it much more suitable for nation-wide applications compared to the detailed 1D hydrodynamic model of river channels combined with an overland flow model. Here not so much the computational time is of concern as the integration of input data in 1D model setup. Detailed topography description by cross-section profiles, setup and calibration of the 1D hydrodynamic mdoel on the large scale seems to be an overwhelming task. Contrary, the gridded topographic and landuse datasets are readily available at the national scale for integration with raster-based codes. Furthermore, dike height data, once available, can be integrated into the digital elevation model and used to explicitly model overtopping and other failure mechanisms.

However, a series of limitations has to be overcome in order to enable flood hazard assessment with raster cell codes on the national scale. Firstly, the national topographic raster datasets, with typical spatial resolution of $50 \times 50$ or $25 \times 25$ metres, often do not resolve river channels that may convey considerable amount of flow. Here the approach of estimation of the bankful discharge and subtracting it from the total flow prior to storage cell based computation deserves detailed consideration. Furthermore, computational constraints in performing large-scale hydraulic computations should be overcome. In this respect, the possibility of a sane increase of the model cell size, up to several hundred metres or more, should be taken into consideration, perhaps, including the parameterisation of the sub-scale effects. A step towards an implicit solution scheme to the governing diffusive wave equations bear a possibility to use larger time steps compared to the currently implemented explicit treatment. Simultaneously, the problem of using the flow limiter approach or adaptive time stepping to achieve solution stability would be omitted. Finally, approaches to efficient utilisation of high performance computational resources, such as code parallelisation schemes, can be considered for implementation with the raster-based model.

# Bibliography

AH, 2002. Hochwasser 2002 im Land Sachsen-Anhalt. Auswertung des Katastrophenschutzmanagements. Tech. rep., Arbeitsgruppe Hochwasser, 153 pp.

Alkema, D., Middelkoop, H., 2005. The influence of floodplain compartmentalization on flood risk within the Rhine-Meuse delta. Natural Hazards 36, 125–145.

Alsdorf, D. E., Melack, J. M., Dunne, T., Mertes, L. A. K., Hess, L. L., Smith, L. C., 2000. Interferometric radar measurements of water level changes on the Amazon flood plain. Nature 404 (6774), 174–177.

Alsdorf, D. E., Rodríguez, E., Lettenmaier, D. P., 2007. Measuring surface water from space. Reviews of Geophysics 45 (2), RG2002.

Andreadis, K. M., Clark, E. A., Lettenmaier, D. P., Alsdorf, D. E., 2007. Prospects for river discharge and depth estimation through assimilation of swath-altimetry into a raster-based hydrodynamics model. Geophysical Research Letters 34 (L10403), DOI 10.1029/2007GL029721.

Apel, H., Merz, B., Thieken, A. H., in press. Influence of dike breaches on flood frequency estimation. Computers & Geosciences.

Apel, H., Thieken, A., Merz, B., Blöschl, G., 2004. Flood risk assessment and associated uncertainty. Natural Hazards and Earth System Science 4, 295–308.

Apel, H., Thieken, A., Merz, B., Blöschl, G., 2006. A probabilistic modelling system for assessing flood risks. Natural Hazards 38 (1-2), 79–100, DOI 10.1007/s11069-005-8603-7.

Armbruster-Veneti, H., 1999. Über das Versagen von Erddämmen. Wasserwirtschaft 89 (10), 504–511.

Aronica, G., Bates, P. D., Horritt, M. S., 2002. Assessing the uncertainty in distributed model prediction using observed binary pattern information within GLUE. Hydrological Processes 16, 2001–2016.

Aronica, G., Hankin, B., Beven, K., 1998a. Uncertainty and equifinality in calibrating distributed roughness coefficients in a flood propagation model with limited data. Advances in Water Resources 22 (4), 349–365.

Aronica, G., Tuciarelli, T., Nasello, C., 1998b. 2D multilevel model for flood wave propagation in flood-affected areas. Journal of Water Resources Planning and Management 124, 210–217.

Assmann, A., 2005. Simulation von Überflutungsflächen und Deichbrüchen auf der Grundlage von Rasterdaten. In: Wittmann, J., Nguyen, X. T. (Eds.), Simulation in Umwelt- und Geowissenschaften. Umweltinformatik. Shaker Verlag, pp. 109–116.

Aureli, F., Maranzoni, A., Mignosa, P., Ziveri, C., 2005. Flood hazard mapping by means of fully-2D and quasi-2D numerical modelling: a case study. In: Alphen, V., van Beek, Taal (Eds.), Floods, from defence to management. Taylor & Francis Group, London, pp. 41–51.

Aureli, F., Mignosa, P., 2004. Flooding scenarious due to levee breaking in the Po river. Water Management 157 (WM1), 3–12.

Ballio, F., Guadagnini, A., 2004. Convergence assessment of numerical Monte Carlo simulations in groundwater hydrology. Water Resources Research 40 (W04603), DOI 10.1029/2003WR002876.

Bates, P. D., 2004. Remote sensing and flood inundation modelling. Hydrological Processes 18, 2593–2597, DOI 10.1002/hyp.5649.

Bates, P. D., De Roo, A. P. J., 2000. A simple raster-based model for flood inundation simulation. Journal of Hydrology 236, 54–77.

Bates, P. D., Horritt, M. S., Aronica, G., Beven, K., 2004. Bayesian updating of flood inundation likelihoods conditioned on flood extent data. Hydrological Processes 18, 3347–3370.

Bates, P. D., Horritt, M. S., Hervouet, J.-M., 1998a. Investigating two-dimensional, finite element predictions of floodplain inundation using fractal generated topography. Hydrological Processes 12, 1257–1277.

Bates, P. D., Horritt, M. S., Smith, C. N., Mason, D., 1997. Integrating remote sensing observations of flood hydrology and hydraulic modelling. Hydrological Processes 11, 1777–1795.

Bates, P. D., Stewart, M. D., Siggers, G. B., Smith, C. N., Hervouet, J.-M., Sellin, R. H. J., 1998b. Internal and external validation of a two-dimensional finite elements code for river flood simulations. Proceedings of the Institute of Civil Engineering, Water, Maritime & Energy 130, 127–141.

Bates, P. D., Wilson, M. D., Horritt, M. S., Mason, D. C., Holden, N., Currie, A., 2006. Reach scale floodplain inundation dynamics observed using airborne synthetic aperture radar imagery: Data analysis and modelling. Journal of Hydrology 328, 306–318, DOI 10.1016/j.jhydrol.2005.12.028.

Bechteler, W., Nujic, M., Otto, A. J., 1994. Calculation of 2D flood propagation using the program package FLOODSIM. In: Molinaro, P., Natale, L. (Eds.), Proceedings of the Speciality Conference on modelling of flood propagation over initially dry areas. American Society of Civil Engineers (ASCE), Miland, IT, pp. 257–267.

Beffa, C., Connel, R. J., 2001. Two-dimensional flood plain flow. I: Model description. Journal of Hydrologic Engineering 6 (5), 397–405.

Berry, P. L., Reid, D., 1987. An introduction to soil mechanics. McGraw-Hill.

Beven, K., 2001. How far can we go in distributed hydrological modelling? Hydrology and Earth System Sciences 5 (1), 1–12.

Beven, K., 2006. A manifesto for the equifinality thesis. Journal of Hydrology 320 (1-2), 18–36, DOI 10.1016/j.jhydrol.2005.07.007.

Beven, K., Binley, A., 1992. The future of distributed models: Model calibration and uncertainty prediction. Hydrologal Processes 6, 279–298.

BfG, 1998. Untersuchungen zum Abflussregime der Elbe. BfG-Bericht 1228, Bundesanstalt für Gewässerkunde, Berlin, 62 pp.

BfG, 2002. Das Augusthochwasser 2002 im Elbegebiet. Tech. rep., Bundesanstalt für Gewässerkunde, Koblenz, 49 pp.

Bhargava, K., Ghosch, A. K., Agrawal, M. K., Patnaik, R., Ramanujam, S., Kushwaha, H. S., 2002. Evaluation of seismic fragility of structures — a case study. Nuclear Engineering and Design 212, 253–272.

Birkett, C. M., 1998. Contribution of the TOPEX NASA radar altimeter to the global monitoring of large rivers and wetlands. Water Resources Research 34 (5), 1223–1239.

Bishop, A. W., 1955. The use the slip circle in the stability analysis of slopes. Geotechnique 5, 7–17.

BKG, 2007. Digitales Geländemodell für Deutschland DGM-D. Tech. rep., Bundesanstalt für Kartographie und Geodäsie, URL: http://www.geodatenzentrum.de/docpdf/dgm-d.pdf.

Bláde, E., Gómez, M., Dolz, J., 1994. Quasi-two dimensional modelling of flood routing in rivers and flood plains by means of storage cells. In: Molinaro, P., Natale, L. (Eds.), Proceedings of the Speciality Conference on modelling of flood propagation over initially dry areas. American Society of Civil Engineers (ASCE), Miland, IT, pp. 156–170.

Bligh, W. G., 1912. The practical design of irrigation works, 2nd Edition. Constable, London.

Bloß, S., 2005. Anwendungsbereich 1D-Modelle. In: Bloß, S., Kleeberg, H.-B. (Eds.), Numerische Simulationsmodelle für Fließgewässer. Vol. 03.05 of Forum für Hydrologie und Wasserbewirtschaftung. pp. 151–170.

Bollrich, G., 2000. Technische Hydromechanik. Verlag Bauwesen, Berlin.

Bradbrook, K., Waller, S., Morris, D., 2005. National floodplain mapping and methods — 160,000 km in 12 month. Natural Hazards 36, 103–123.

Bradbrook, K. F., Lane, S. N., Waller, S. G., Bates, P. D., 2004. Two dimensional diffusion wave modelling of flood inundation using a simplified channel representation. International Journal of River Basin Management 2 (3), 211–223.

Brakenridge, G. R., Tracy, B. T., Knox, J. C., 1998. Orbital SAR remote sensing of a river flood wave. International Journal of Remote Sensing 19 (7), 1439–1445.

Brauns, J., 1999. Verhalten zeitweise eingestauter Dämme und Überwachung ihres Verhaltens. 6. Erfahrungsaustausch — Betrieb überörtlicher Hochwasserrückhaltebecken, Schwäbisch-Gmünd.

Broich, K., 2003. Sediment transport in breach formation process. In: 3rd IMPACT Project Workshop. Louvian-la-Neuve, Belgium.

Bronstert, A. E., 2004. Möglichkeiten der Minderung des Hochwasserrisikos durch Nutzung von Flutpoldern an Havel und Oder. Schlussbericht zum BMBF-Projekt im Rahmen des Vorhabens "Bewirtschaftungsmöglichkeiten im Einzugsgebiet der Havel", Institut für Geoökologie, Universität Potsdam.

Calle, E. O. F., Weijers, J. B., 1995. Berechnugsvorschlag zum hydraulischen Grundbruch bei Flußdeichen in den Niederlanden. Wasserwirtschaft 85 (5), 254–258.

Casagrande, A., 1937. Seepage trough dams. Vol. 51(2). New England Water Works Association.

Cheng, S. T., 1993. Statistics on dam failures. In: Yen, B. C., Tung, Y. K. (Eds.), Relieability and uncertainty analyses in hydraulic design. ASCE, Reston, pp. 97–105.

Chow, V. T., 1959. Open Channel Hydraulics. McGraw-Hill, New York, USA.

Clayton Eng., 2003. EPDRiv1 — A dynamic one-dimensional model of hydrodynamics and water quality. URL: http://www.epdriv1.com.

Cunge, J. A., 1975. Two-dimensional modeling of flood plains. Water Resources Publications, Ch. 17, pp. 705–762.

CUR/TAW, 1990. Probabilistic design of flood defences. Report 141, Centre for civil engineering research and codes. Technical advisory committee on water defences, Gouda, The Netherlands, 154 pp.

Dawson, R. J., Hall, J. W., 2006. Adaptive importance sampling for risk analysis of complex infrastructure systems. Proceeding of the Royal Society A 462 (2075), 3213–3499, DOI 10.1098/rspa.2006.1720.

Dawson, R. J., Hall, J. W., Sayers, P. B., Bates, P. D., Rosu, C., 2005. Sampling-based flood risk analysis for fluvial dike systems. Stochastic Environmental Research and Risk Assessment 19, 388–402.

Decker, J., Ludwig, K., Meuser, A., 2002. Überlegungen zur Überflutung größerer Gebiete durch Deichbrüche. Wasserwirtschaft 11-12, 15–20.

DHI, 2007. MIKE FLOOD Software. URL: http://www.dhisoftware.com/mikeflood/index.htm.

Diersch, H.-J. G., 2000. Numerishe Modellierung ober- und unterirdischer Strömungs- und Transportprozesse. Vol. 4 of Technische Hydromechanik. Verlag Bauwesen, Ch. 3, pp. 111–168.

DKKV, 2003. Hochwasservorsorge in Deutschland. Lernen aus der Katastrophe 2002 im Elbegebiet. Vol. 29 of Schriftenreihe des DKKV. Deutsches Komitee für Katastrophenvorsorge e.V., 152 pp.

Dutta, D., Herath, S., Musiake, K., 2000. Flood inundation simulation in a river basin using a physically based distributed hydrologic model. Hydrological Processes 14, 497–519.

Estrela, T., Quintas, L., 1994. Use of GIS in the modelling of flows on floodplains. In: White, W. R., Watts, J. (Eds.), Proceedings of the 2nd International Conference on River Flood Hydraulics. Wiley, pp. 177–189.

EU, 2007. Directive 2007/60/EC of the European Parliament and of the Council of 23 October 2007 on the assessment and management of flood risks. Official Journal of the European Union L228, 27–34.

Fenton, G. A., Griffiths, D. V., 1996. Statistics of free surface flow through a stochastic earth dam. Journal of Geothechnical Engineering ASCE 122 (6), 427–436.

Frank, E., Ostan, A., Coccato, M., Stelling, G. S., 2001. Use of an integrated one dimensional modelling approach for flood hazard and risk mapping. In: Falconer, R. A., Blain, W. R. (Eds.), Proceedings of the 1st Conference on River Basin Management. WIT Press, Southhampton, UK, pp. 99–108.

Frappart, F., Do Minh, K., L'Hermitte, J., Cazenave, A., Ramillien, G., Le Toan, T., Mognard-Campbell, N., 2006. Water volume change in the lower Mekong from satellite altimetry and imagery data. Geophysical Journal International 167 (2), 570–584, DOI 10.1111/j.1365-246X.2006.03184.x.

Gocht, M., 2002. Deichbrüche und Deichüberströmungen an Elbe und Mulde im August 2002. Final report, Water & Finance, 56 pp.

Greenhill, R. K., Sellin, R. H. J., 1993. Development of a simple method to predict discharges in compound meandering channels. Proceedings of the Institute of Civil Engineering, Water, Maritime, Energy 101, 37–44.

Gregersen, J. B., Gijsbers, P. J. A., Westen, S. J. P., 2007. OpenMI : Open Modelling Interface. Journal of Hydroinformatics 9 (3), 175–191.

Gui, S., Zhang, R., Xue, X., 1998. Overtopping reliability models for river levee. Journal of Hydraulic Engineering 124 (12), 1227–1234.

Güntner, A., Bronstert, A., 2004. Representation of landscape variability and lateral redistribution processes for large-scale hydrological modelling in semi-arid areas. Journal of Hydrology 297, 131–161.

Hahn, W., Hanson, G. J., Cook, K. R., 2000. Breach morphology observations of embankment overtopping tests. In: Joint Conference on Water Resources Planning and Management. ASCE Conference Proceedings. Minneapolis, Minnesota, USA.

Hall, J. W., 2003. Handling uncertainty in the hydroinformatic process. Journal of Hydroinformatics 5 (4), 215–232.

Hall, J. W., Anderson, M., 2002. Handling uncertainty in extreme or unrepeatable hydrological processes — the need for an alternative paradigm. Hydrological Processes 16, 1867–1870.

Hall, J. W., Dawson, R. J., Sayers, P. B., Rosu, C., Chatterton, J. B., Deakin, R., 2003. A methodology for national-scale flood risk assessment. Proceedings of the Institution of Civil Engineers, Water & Maritime Engineering 156 (3), 235–247.

Hall, J. W., Sayers, P. B., Dawson, R. J., 2005a. National-scale assessment of current and future flood risk in England and Wales. Natural Hazards 36, 147–164.

Hall, J. W., Tarantola, S., Bates, P. D., Horritt, M. S., 2005b. Distributed sensitivity analysis of flood inundation model calibration. Journal of Hydraulic Engineering 131 (2), 117–126, DOI 10.1061/(ASCE)0733-9429(2005)131:2(117).

Han, K.-Y., Lee, J.-T., Park, J.-H., 1998. Flood inundation analysis resulting from levee-break. Journal of Hydraulic Research 36 (5), 747–759.

Hanses, U., Müller-Kirchenbauer, H., Savidis, S., 1985. Zur Mechanik der rückschreitenden Erosion unter Deichen und Dämmen. Bautechnik 5, 163–168.

Helms, M., Büchele, B., Merkel, U., Ihringer, J., 2002. Statistical analysis of the flood situation and assessment of the impact of diking measures along the Elbe (Labe) river. Journal of Hydrology 267, 94–114.

Herrmann, U., Thieken, A., Suhr, U., Lindenschmidt, K.-E., 2007. Hochwasserrisikoanalysen an der Elbe — Methodenvergleich und Datenauflösung. Österreichische Wasser- und Abfallwirtschaft 59 (11-12), 151–162.

Hervouet, J.-M., 2000. A high resolution 2-D dam-break model using parallelization. Hydrological Processes 14, 2211–2230.

Hesselink, A. W., Stelling, G. S., Kwadijk, J. C. J., Middelkoop, H., 2003. Inundation of a Dutch river polder, sensitivity analysis of a physically based inundation model using historic data. Water Resources Research 39 (9), 1234, DOI 10.1029/2002WR001334.

Hewlett, H. W. M., 1987. Design of reinforced grass waterways. Report, (CIRIA) Construction Industry Research and Information Association, London.

HORA, 2007. HORA: Hochwasser Risikozonierung Austria. URL: http://www.hochwasserrisiko.at.

Horlacher, H.-B., Bielagk, U., Heyer, T., 2005. Analyse der Deichbrüche an der Elbe und Mulde während des Hochwassers 2002 im Bereich Sachsen. Research report 2005/09, Institut für Wasserbau und Technische Hydromechanik, Technische Universität Dresden, 82 pp.

Horritt, M. S., 1999. A statistical active contour model for SAR image segmentation. Image and Vision Computing 17, 213–224.

Horritt, M. S., 2000. Calibration of a two-dimensional finite element flood flow model using satellite radar imagery. Water Resources Research 36 (1), 3279–3291, DOI 2000WR900206.

Horritt, M. S., Bates, P. D., 2001a. Effects of spatial resolution on a raster based model of floodplain flow. Journal of Hydrology 253, 239–249.

Horritt, M. S., Bates, P. D., 2001b. Predicting floodplain inundation: raster-based modelling versus finite element approach. Hydrological Processes 15, 825–842.

Horritt, M. S., Bates, P. D., 2002. Evaluation of 1D and 2D numerical models for predicting river flood inundation. Journal of Hydrology 268, 87–99.

Horritt, M. S., Mason, D. C., Cobby, D. M., Davenport, I. J., Bates, P. D., 2003. Waterline mappping in flooded vegetation from airborne SAR imagery. Remote Sensing of Environment 85, 271–281.

Horritt, M. S., Mason, D. C., Luckman, A. J., 2001. Flood boundary delineation from synthetic aperture radar imagery using a statistical active contour model. International Journal of Remote Sensing 22 (13), 2489–2507.

Huang, S., Rauberg, J., Apel, H., Disse, M., Lindenschmidt, K.-E., 2007. The effectiveness of polder systems on peak discharge capping of floods along the middle reaches of the Elbe River in Germany. Hydrology and Earth System Sciences 11, 1391–1401.

Hunter, N. M., 2005. Development and assessment of dynamic storage cell codes for flood inundation modelling. Ph.D. thesis, School of Geographical Sciences, University of Bristol, UK, 359 pp.

Hunter, N. M., Bates, P. D., Horritt, M. S., De Roo, P. J., Werner, M. G. F., 2005a. Utility of different data types for calibrating flood inundation models within a GLUE framework. Hydrology and Earth System Sciences 9 (4), 412–430.

Hunter, N. M., Bates, P. D., Horritt, M. S., Wilson, M. D., 2005b. Comparison of classical and adaptive time-step storage cell codes for flood inundation modelling. In: Alphen, V., van Beek, Taal (Eds.), Floods, from defence to management. Taylor & Francis Group, London, pp. 231–240.

Hunter, N. M., Horritt, M. S., Bates, P. D., Wilson, M. D., Werner, M. G. F., 2005c. An adaptive time step solution for raster-based storage cell modelling of floodplain inundation. Advances in Water Resources 28, 975–991, DOI 10.1016/j.advwatres.2005.03.007.

IKSE, 2001. Bestandsaufnahme des vorhandenen Hochwasserschutzniveaus im Einzugsgebiet der Elbe. Tech. rep., Internationale Kommission zum Schutz der Elbe, Magdeburg, 74 pp.

IKSE, 2003. Aktionsplan Hochwasserschutz Elbe. Tech. rep., Internationale Kommission zum Schutz der Elbe, 79 pp.

IKSE, 2004. Dokumentation des Hochwassers vom August 2002 im Einzugsgebiet der Elbe. Tech. rep., Internationale Kommission zum Schutz der Elbe, 207 pp.

IKSE, 2006. Erster Bericht über die Erfüllung des "Aktionsplans Hochwasserschutz Elbe" im Zeitraum von 2003 bis 2005. Tech. rep., Internationale Kommission zum Schutz der Elbe, 52 pp.

IKSR, 2001. Atlas der Überschwemmungsgefährdung und möglichen Schäden bei Extremhochwasser am Rhein. URL: http://www.iksr.org, Internationale Kommission zum Schutz des Rheins.

IMPACT, 2001. IMPACT – Investigation of extreme flood processes and uncertainty. URL: http://www.samui.co.uk/impact-project/, Project Reference No. EVG1-CT2001-00037.

IWK, 2004. Untersuchung von Hochwasserretentionsmaßnahmen entlang der Elbe im Bereich der Landkreis Wittenberg und Anhalt-Zerbst (Kurzfassung). Tech. rep., Institut für Wasserwirtschaft und Kulturtechnik, Universität Karlsruhe.

Jain, M. K., Singh, V. P., 2005. DEM-based modelling of surface runoff using diffusion wave equation. Journal of Hydrology 302, 107–126, DOI 10.1016/j.hydrol.2004.06.042.

Jankiewicz, P., Kofalk, S., Spierling, C., Scholten, M., 2005. Digitale Erfassung von Informationen zur Höhe und Lage der Deichkronen an der Elbe (deutscher Teil) und Aufbereitung für hydro-dynamische Modellierungen. Mitteilung 9, Bundesanstalt für Gewässerkunde, URL: http://elise.bafg.de/?1817.

Kanowski, H., 1977. Ein Beitrag zur zerstörungsfreien Untersuchung von Flussdeichen. Ph.D. thesis, Technische Universität Dresden.

Khilar, K. C., Fogler, H. S., Gray, D. H., 1985. Model for piping-plugging in earthen structures. Journal of Geotechnical Engineering 111 (7), 833–846.

Kim, S.-H., Shinozuka, M., 2004. Development of fragility curves of bridges retrofitted by column jacketing. Probabilistic Engineering Mechanics 19, 105–112, DOI 10.1016/j.probengmech.2003.11.009.

Koblinsky, C. J., Clarke, R. T., Brenner, A. C., Frey, H., 1993. Measurement of river level variations with satellite altimetry. Water Resources Research 29 (6), 1839–1848.

Koenders, M. A., Sellmeijer, J. B., 1992. Mathematical model for piping. Journal of Geotechnical Engineering 118 (6), 943–946.

Kortenhaus, A., Oumeraci, H., 2002. Probabilistische Bemessungsmethoden für Seedeiche (ProDeich). Bericht Nr. 877, Leichtweiss-Institut für Wasserbau, Technische Universität Braunschweig, 205 pp.

Kron, W., 2006. Extremes Wetter — von Rekorden zur Risikovorsorge. In: Disse, M., Guckenberger, K., Pakosch, S., Yörük, A., Zimmermann, A. (Eds.), Forum für Hydrologie und Wasserbewirtschaftung. Vol. 15.06. DWA, pp. 191–204.

Lane, E. W., 1935. Security from under-seepage. Masonry dams on earth foundations. Transactions of the ASCE 100, 1235–1351.

Lane, S. N., 2005. Roughness — time for a re-evaluation? Earth Surface Processes and Landforms 30, 251–253, DOI 10.1002/esp.1208.

Lane, S. N., James, T. D., Pritchard, H., Saunders, M., 2003. Photogrammetric and laser altimetric reconstruction of water levels for extreme flood event analysis. Photogrammetric Record 18 (104), 293–307.

Lassing, B. L., Vrouwenvelder, A. C. W. M., 2003. Reliability analysis of flood defence systems in the Netherlands. In: Bedford, van Gelder (Eds.), Proceedings of ESREL 2003: Safety and Reliability. Swets & Zeitlinger, Lisse, pp. 1005–1014.

Leopold, L. B., Wolman, M. G., Miller, J. P., 1964. Fluvial processes in geomorphology. W. H. Freeman, New York.

LfUG, 2005. Hochwasser in Sachsen. Gefahrenhinweiskarten. Tech. rep., Sächsisches Landesamt für Umwelt und Geologie.

Linstead, C., 2005. TDT — A Library for Typed Data Transfer. In: Geophysical Research Abstracts. Vol. 7. SRef-ID: 1607-7962/gra/EGU05-A-04391.

LTV, 2006. HWSK-Arbeitsdaten. unpublished, Landestalsperrenverwaltung Sachsen.

LUA, 2002. Das Elbehochwasser im Sommer 2002. Tech. Rep. Heft 73, Landesumweltamt Brandenburg.

Ludwig, K., 2005. Erfolgsgeschichten der Hochwasservorsorge. Wasserwirtschaft 10, 3.

Macke, E., 2001. Bewertung von Zustand und Hochwasserschutzgrad der Elbedeiche. Technical report, Ingenieurgesellschaft Prof. Dr.-Ing. E. Macke mbH, 118 pp.

Mai, S., von Liebermann, N., 2001. RisK — Risikoinformationssystem Küste. Jahrbuch der Hafenbautechnischen Gesellschaft 53, Hamburg.

Maidment, D., 2002. Arc Hydro. GIS for water resources. ESRI Press.

MEDIS, 2007. MEDIS — Methods for the evaluation of direct and indirect losses. In: RIMAX — Risk management of extreme flood events. GeoForschungsZentrum Potsdam, p. 12.

Merz, B., 1996. Modellierung des Niederschlag-Abfluß-Vorgangs in kleinen Einzugsgebieten unter Berücksichtigung der natürlichen Variabilität. In: Mitteilungen des Instituts für Hydrologie und Wasserwirtschaft. Vol. 56. Universität Karlsruhe, 215 pp.

Merz, B., 2006. Abschätzung von Hochwasserrisiken. Methoden, Grenzen und Möglichkeiten. E. Schweizerbart'sche Verlagsbuchhandlung (Nägele und Obermiller), Stuttgart, Habilitationsschrift.

Merz, B., Gocht, M., 2003. Karten zur Hochwasservorsorge und zum Risikomanagement auf der lokalen Skala. Hydrologie und Wasserbewirtschaftung 47 (5), 186–194.

Merz, B., Thieken, A. H., 2004. Flood Risk Analysis: Concepts and Challenges. Österreichische Wasser- und Abfallwirtschaft 56 (3-4), 27–34.

Merz, B., Thieken, A. H., 2005. Separating natural and epistemic uncertainty in flood frequency analysis. Journal of Hydrology 309, 114–132.

Merz, B., Thieken, A. H., Gocht, M., 2007. Flood risk mapping at the local scale: Concepts and challenges. In: Begum, S., Stive, M. J. F., Hall, J. W. (Eds.), Flood Risk Management in Europe. Innovation in Policy and Practice. Vol. 25 of Advances in Natural and Technological Hazards Research. Springer.

MpCCI, 2007. MpCCI — Mesh-based parallel code coupling interface. URL: http://www.mpcci.de, Fraunhofer SCAI.

Müller-Kirchenbauer, H., Rankl, M., Schlötzer, 1993. Mechanism for regressive erosion beneath dams and barrages. In: Brauns, J., Heilbaum, M., Schuler, U. (Eds.), Proceedings of the First International Conference: Filters in Geotechnical and Hydraulic Engineering. Balkema, Rotterdam, pp. 369–376.

Nagy, L., Tóth, S., 2005. Detailed Technical Report on the collation and analysis of dike breach data with regards to formation process and location factors. Tech. rep., H-EURAqua Ltd., URL: http://www.samui.co.uk/impact-project/AnnexII_DetailedTechnicalReports/AnnexII_PartE2_WP6/IMPACT_DTReport_EURAQ_2005-01-15.pdf.

Nash, J., Sutcliffe, J., 1970. River flow forecasting through conceptual models, part I — a discussion of principles. Journal of Hydrology 10, 282–290.

Neelz, S., Pender, G., 2007. Sub-grid scale parameterisation of 2D hydrodynamic models of inundation in the urban area. Acta Geophysica 55 (1), 65–72.

Nestmann, F., Büchele, B., 2002. Morphodynamik der Elbe. Final report, Institut für Wassewirtschaft und Kulturtechnik, Universität Karlsruhe, ISBN 3-00-008977-2.

Niemeyer, M., van Linn, A., Köngeter, J., 2005. Partitioning of vulanerable areas into compartments — a risk mitigation measure. In: Alphen, V., van Beek, Taal (Eds.), Floods, from defence to management. Taylor & Francis Group, London, pp. 889–895.

Oberstadtler, R., Hönsch, H., Huth, D., 1997. Assessment of the mapping capabilities of ERS-1 SAR data for flood mapping: A case study in Germany. Hydrological Processes 11, 1415–1425.

Pappenberger, F., Beven, K., Horritt, M., Blazkova, S., 2005. Uncertainty in the calibration of effective roughness parameters in HEC-RAS using inundation and downstream level observations. Journal of Hydrology 302, 46–69, DOI 10.1016/j.jhydrol.2004.06.036.

Pappenberger, F., Frodsham, K., Beven, K., Romanowicz, R., Matgen, P., 2007. Fuzzy set approach to calibrating distributed flood inundation models using remote sensing observations. Hydrology and Earth System Sciences 11, 739–752.

Petrow, T., Merz, B., Lindenschmidt, K.-E., Thieken, A. H., 2007. Aspects of seasonality and flood generating circulation patterns in a mountainous catchment in south-eastern Germany. Hydrology and Earth System Sciences 11 (4), 1455–1468.

Pohl, R., 1999. Probabilistic aspects of the seepage flow in dikes. In: Proceedings of the XXVIII IAHR Congress. Vol. Theme A: 28. Graz, Austria.

Pohl, R., 2000a. Aspekte der Sicherheit von Deichen mit inhomogenem Aufbau. Wasser und Abfall 11, 52–57.

Pohl, R., 2000b. Probabilistische Aspekte der hydraulischen Bemessung. Vol. 4 of Technische Hydromechanik. Verlag Bauwesen, Ch. 5, pp. 237–285.

Press, W. H., Vetterling, W. T., Teukolski, S. A., Flannery, B. P., 1992. Numerical recipes in C: the art of scientific computing, 2nd Edition. Cambridge University Press.

Raclot, D., 2006. Remote sensing of water levels on floodplains: a spatial approach guided by hydraulic functioning. International Journal of Remote Sensing 27 (12), 2553–2574, DOI 10.1080/01431160600554397.

Robson, A., Reed, D., 1999. Flood estimation handbook. Statistical procedures for flood frequency estimation. Vol. 3. Institute of Hydrology, Crowmarsch Gifford, Wallingford, UK.

Rodda, H. J. E., 2005. The development an application of a flood risk model for the Czech Republic. Natural Hazards 36, 207–220.

Romanowicz, R. J., Beven, K. J., 2003. Estimation of flood inundation probabilities as conditioned on event inundation maps. Water Resources Research 39, 1061–1073, DOI 10.1029/2001WR001056.

Saucke, U., 2006. Nachweis der Sicherheit gegen innere Erosion für körnige Erdstoffe. Geotechnik 29 (1), 43–54.

Sayers, P. B., Hall, J. W., Rosu, C., Chatterton, J. B., Deakin, R., 2002. Risk assessment of flood and coastal defences for strategic planning (RASP) — A high level methodology. In: DEFRA Conference of Coastal and River Engineers. Keel University, UK.

Scawthorn, C., Blais, N., Seligson, H., Tate, E., Mifflin, E., Thomas, W., Murphy, J., Jones, C., 2006a. HAZUS-MH flood loss estimation methodology. I: Overview and flood hazard characterization. Natural Hazards Review 7 (2), 60–71, DOI 10.1061/(ASCE)1527-6988(2006)7:2(60).

Scawthorn, C., Flores, P., Blais, N., Seligson, H., Tate, E., Chang, S., Mifflin, E., Thomas, W., Murphy, J., Jones, C., Lawrence, M., 2006b. HAZUS-MH flood estimation methodology. II. Damage and loss assessment. Natural Hazards Review 7 (2), 72–81, DOI 10.1061/(ASCE)1527-6988(2006)7:2(72).

Scheuermann, A., 2005. Instationäre Durchfeuchtung quasi-homogener Erddeiche. Ph.D. thesis, Institut für Bodenmechanik und Felsmechanik, Universität Karlsruhe.

Schumann, G., Hostache, R., Puech, C., Hoffmann, L., Matgen, P., Pappenberger, F., Pfister, L., 2007a. High-resolution 3-D flood information from radar imagery for flood hazard management. IEEE Transactions on Geosciences and Remote Sensing 45 (6), 1715–1725, DOI 10.1109/TGRS.2006.888103.

Schumann, G., Matgen, P., Hoffmann, L., Hostache, R., Pappenberger, F., Pfister, L., 2007b. Deriving distributed roughness values from satellite radar data for flood inundation modelling. Journal of Hydrology 344 (1-2), 96–111, DOI 10.1016/j.jhydrol.2007.06.024.

Sellmeijer, J. B., 1989. On the mechanism of piping under impervious structures. Ph.D. thesis, Delft University of Technology, The Netherlands.

Sellmeijer, J. B., Koenders, M. A., 1991. A mathematical model for piping. Applied Mathematical Modelling 15 (11-12), 646–651.

Shinozuka, M., Feng, M. Q., Lee, J., Naganuma, T., 2000. Statistical analysis of fragility curves. Journal of Engineering Mechanics 126 (12), 1224–1231.

Singh, V. P., 1996. Dam breach modeling technology. Vol. 17 of Water Science and Technology Library. Kluwer.

Smith, L. C., 1997. Satellite remote sensing of river inundation area, stage, and discharge: A review. Hydrologcial Processes 11, 1427–1439.

SOBEK, 2007. WL | Delft Hydraulics, SOBEK Software. URL: http://www.sobek.nl.

Stedinger, J. R., Vogel, R. M., Foufoula-Georgiou, E., 1992. Frequency analysis of extreme events. Handbook of hydrology. McGraw-Hill, Ch. 18.

Steenbergen, H. M. G. M., Vrouwenvelder, A. C. W. M., 2003. Theoriehandleidung PC-RING, Versie 4.0, Deel A: Mechanismenbeschrijvingen. TNO-Report 2003-CI-R0020, TNO Civiele Infrastructuur, Delft, The Netherlands, in Dutsch.

Stelling, G. S., Kernkamp, H. W. J., Laguzzi, M. M., 1998. Delft Flooding System: A powerful tool for inundation assessment based upon a positive flow simulation. In: Babovic, V., Larsen, L. C. (Eds.), Hydroinformatics'98. Balkema, Brookfield, Vt., pp. 231–238.

Szidarovszky, F., Duckstein, L., Bogardi, I., 1975. Levee system reliability along a confluence reach. Journal of the Engineering Mechanics Division EM5, 609–621.

TAW, 2004. Floris: flood risk and safety in the Netherlands. URL: http://www.tawinfo.nl/engels/downloads/FloodRisksandSafety.pdf, Technical Advisory Committee on Flood Defence.

Terzaghi, K., Peck, R., Mesri, G., 1996. Soil mechanics in engineering practice, 3rd Edition. John Wiley & Sons.

UniBwM, 2004. Breach location. Work package 2.4. Identification of possible breach locations. Technical report EU Impact Project, Universität der Bundeswehr München.

Uno, T., Sugii, T., Hayashi, M., 1994. Logit model for river levee stability evaluation considering the flood return period. Structural Safety 14, 81–102.

USACE, 1995. CE-QUAL-RIV1: A Dynamic, One-Dimensional (Longitudinal) Water Quality Model for Streams. Tech. rep., Environmental Laboratory, U.S. Army Corps of Engineers, Vicksburg, MS, user's Manual. Final Report.

USACE, 1999. Risk-based analysis in geotechnical engineering for support of planning studies. Engineer Technical Letter 1110-2-556, U.S. Army Corps of Engineers.

Van, M. A., Koelewijn, A. R., Barends, F. B. J., 2005. Uplift phenomenon: model, validation and design. International Journal of Geomechanics 5 (2), 98–106.

van Loon, L., 2001. Proven strength for piping. In: Proceedings of the 15th International Conference on Soil Mechanics and Geotechnical Engineering. Vol. 3. Balkema, Istanbul, Turkey, pp. 2283–2284.

van Noortwijk, J. M., Vrouwenvelder, A. C. W. M., Calle, E. O. F., Slijkhuis, K. A. H., 1999. Probability of dike failure due to uplifting and piping. In: Proceedings of ESREL: The 10th European Conference on Safety and Reliability. Balkema, Rotterdam, pp. 1187–1192.

Vaskinn, K. A., Løvoll, A., Höeg, K., 2004. Wp2.1 Breach formation — large scale embankment failure. Tech. Rep. IMPACT Project Reference No. EVG1-CT2001-00037, Sweco Gröner Norway, Norconsult AS Norway, Norwegian Geotechnical Institute, http://www.samui.co.uk/impact-project/AnnexII_DetailedTechnicalReports/AnnexII_PartA_WP2/Impact_kav.pdf.

Vrijling, J. K., 2001. Probabilistic design of water defence systems in the Netherlands. Reliability Engineering and System Safety 74, 337–344.

Vrijling, J. K., van Gelder, P. H. A. J. M., 1998. The effect of inherent uncertainty in time and space on the reliability of flood protection. In: Lydersen, S., Hansen, G. K., Sandtorv, H. (Eds.), Safety and Reliability. Proceedings ESREL98 Conference. Balkema, Rotterdam, The Netherlands, pp. 451–456.

Vrijling, J. K., van Gelder, P. H. A. J. M., 2000. Probabilistic design. IHE-Delft Lecture notes, Delft University of Technology.

Vrouwenvelder, A. C. W. M., Wubs, A. J., 1985. Een probabilistisch dijkontwerp (A probabilistic dyke design). Technical Report B-85-64/64.3.0873, TNO-IBBC, Delft, The Netherlands, (in Dutch).

Wahl, T. L., 1998. Prediction of embankment dam breach parameters. A literature review and needs assessment. Research report DSO-98-004, U.S. Department of Interior. Bureau of Reclamation. Dam Safety Office, http://www.usbr.gov/pmts/hydraulics_lab/pubs/pap/PAP-0735_DSO-98-004.pdf.

Wahl, T. L., 2001. The uncertainty of embankment dam breach paramter predictions based on dam failure case studies. In: USDA/FEMA Workshop on issues, resolutions, and research needs related to dam failure analysis. Oklahoma City, OK, http://www.usbr.gov/pmts/hydraulics_lab/pubs/pap/PAP-0876.pdf.

Wang, M., Hjelmfelt, A. T., 1998. DEM based overland flow routing model. Journal of Hydrologic Engineering ASCE 3 (1), 1–8.

WASY, 2005. Untersuchungen zur Optimierung der Flutung der Havelpolder bei Extremhochwässern. Gutachten im Auftrag des Landesumweltamtes Brandenburg, WASY Gesellschaft für Wasserwirtschaftliche Planung und Systemforschung mbH, unpublished.

Weijers, J. B. A., Sellmeijer, J. B., 1993. A new model to deal with the piping mechanism. In: Brauns, J., Heilbaum, M., Schuler, U. (Eds.), Proceedings of the First International Conference: Filters in Geotechnical and Hydraulic Engineering. Balkema, Rotterdam, pp. 349–355.

Werner, M. G. F., 2001. Impact of grid size on GIS based flood extent mapping using 1D flow model. Physics and Chemistry of the Earth (B): Hydrology, Oceans, Atmosphere 26 (7-8), 517–522.

Werner, M. G. F., 2004. A comparison of flood extent modelling approaches through constraining uncertainties on gauge data. Hydrology and Earth System Sciences 8 (6), 1141–1152.

Werner, M. G. F., Blazkova, S., Petr, J., 2005a. Spatially distributed observations in constraining inundation modelling uncertainties. Hydrological Processes 19, 3081–3096, DOI 10.1002/hyp.5833.

Werner, M. G. F., Hunter, N. M., Bates, P. D., 2005b. Identifiability of distributed floodplain roughness values in flood extent estimation. Journal of Hydrology 314 (1-4), 139–157, DOI 10.1016/j.jhydrol.2005.03.012.

Werner, M. G. F., Lambert, M. F., 2007. Comparison of modelling approaches used in practical flood extent modelling. Journal of Hydraulic Research 45 (2), 202–215.

Wilson, C. A. M. E., Bates, P. D., Hervouet, J.-M., 2002. Comparison of turbulence models for stage-discharge rating curve predictions in reach-scale compound channel flows using two-dimensional finite elemen methods. Journal of Hydrology 257, 42–58.

Wood, E., 1977. An analysis of flood levee reliability. Water Resources Research 13 (3), 665–671.

Yu, D., Lane, S. N., 2006a. Urban fluvial flood modelling using a two-dimensional diffusion-wave treatment, part 1: mesh resolution effects. Hydrological Processes 20, 1541–1565, DOI 10.1002/hyp.5935.

Yu, D., Lane, S. N., 2006b. Urban fluvial flood modelling using a two-dimensional diffusion-wave treatment, part 2: development of a sub-grid-scale treatment. Hydrological Processes 20, 1567–1583, DOI 10.1002/hyp.5936.

Zesch, R., Saucke, U., Kast, K., Biberstein, A., 2007. Versagenswahrscheinlichkeit von Flussdeichen unter Berücksichtigung geotechnischer Aspekte — Anwendung auf Deichstrecken mit Schwachstellen. In: Köngeter, J. (Ed.), 37. Internationales Wasserbau-Symposium Aachen (IWASA). Sicherheit und Risiko wasserbaulicher Anlagen. Vol. 148 of Mitteilungen. pp. F/1 –F/21.

# Appendix A

## A.1 Derivation of a slide height for micro-instability

Based on Vrouwenvelder and Wubs (1985) and Calle, E. O. F. (GeoDelft, personal communication), the slide height $h_a$ can be derived from the geometrical relationships shown in Figure A.1.

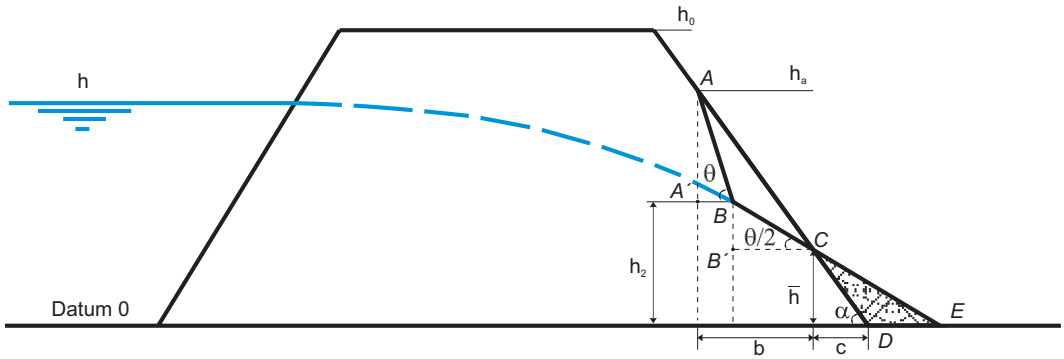


**Figure A.1:** *Schematic representation of slope failure due to micro-instability. Adopted from Vrouwenvelder and Wubs (1985) for the special case of a dike without ditch.*

Related to the dike foot, $h_a$ is given by:

$$h_a = \frac{b+c}{\cot\alpha}, \tag{A.1}$$

where

$$b = \frac{h_2 - \overline{h}}{\tan\frac{1}{2}\theta} + \frac{h_a - h_2}{\tan\theta}, \tag{A.2}$$

and

$$c = \frac{\overline{h}}{\tan\alpha} \tag{A.3}$$

Substituiting $b$ and $c$ in Eq. A.1 with Eq. A.2 and Eq. A.3 yields:

$$h_a \frac{1}{\tan\alpha} = \frac{\overline{h}}{\tan\alpha} + \frac{h_2 - \overline{h}}{\tan\frac{1}{2}\theta} + \frac{h_a - h_2}{\tan\theta} \iff \tag{A.4}$$

$$h_a\left(\frac{1}{\tan\alpha} - \frac{1}{\tan\theta}\right) = h_2\left(\frac{1}{\tan\frac{1}{2}\theta} - \frac{1}{\tan\theta}\right) + \overline{h}\left(\frac{1}{\tan\alpha} - \frac{1}{\tan\frac{1}{2}\theta}\right) \tag{A.5}$$

Using trigonometrical relationships:

$$\left(\frac{1}{\tan\alpha} - \frac{1}{\tan\theta}\right) = \frac{\cos\alpha\sin\theta - \sin\alpha\cos\theta}{\sin\alpha\sin\theta} = \frac{\sin(\theta-\alpha)}{\sin\alpha\sin\theta} \tag{A.6}$$

and

$$\frac{1}{\tan\frac{1}{2}\theta} = \frac{1+\cos\theta}{\sin\theta} \tag{A.7}$$

yields:

$$\left(\frac{1}{\tan\frac{1}{2}\theta} - \frac{1}{\tan\theta}\right) = \frac{1+\cos\theta}{\sin\theta} - \frac{\cos\theta}{\sin\theta} = \frac{1}{\sin\theta} \tag{A.8}$$

and

$$\left(\frac{1}{\tan\alpha} - \frac{1}{\tan\frac{1}{2}\theta}\right) = \frac{\cos\alpha}{\sin\alpha} - \frac{1+\cos\theta}{\sin\theta} = \frac{\cos\alpha\sin\theta - \sin\theta - \sin\alpha\cos\theta}{\sin\alpha\sin\theta} \tag{A.9}$$

$$= \frac{\sin(\theta-\alpha) - \sin\alpha}{\sin\alpha\sin\theta} \tag{A.10}$$

Introducing Eq. A.6, Eq. A.8 and Eq. A.10 into Eq. A.5 leads to Eq. 3.48 presented in Sect. 3.3.3:

$$h_a\frac{\sin(\theta-\alpha)}{\sin\alpha\sin\theta} = h_2\,\frac{1}{\sin\theta} + \overline{h}\,\frac{\sin(\theta-\alpha)-\sin\alpha}{\sin\alpha\sin\theta} \iff$$

$$h_a = h_2\,\frac{\sin\alpha}{\sin(\theta-\alpha)} + \overline{h}\left(1 - \frac{\sin\alpha}{\sin(\theta-\alpha)}\right)$$

## A.2 Derivation of slide bend height $h_2$

Vrouwenvelder and Wubs (1985) make use of the Casagrande method (Casagrande, 1937) for the determination of the exit point of the phreatic line (point $P$ in Figure A.2) and apply empirical adjustment to derive $h_2$ as a function of water level $h$.

The slide bend height $h_2$ can be derived as follows:

$$h_2 = S_2\left(\cot\alpha + \frac{1}{\sin\frac{\theta}{2}}\right)(0.58 + 0.0015\,\frac{\theta}{2}) \tag{A.11}$$

where

$$S_2 = \sqrt{d_2^2 + h^2} - d_2 \tag{A.12}$$

with

$$d_2 = d_1 + \frac{1}{2}h_1(\cot\frac{\theta}{2} - \cot\alpha) \tag{A.13}$$

$h_1$ is given by:

$$h_1 = S_1\left(\cot\alpha + \frac{1}{\sin\alpha}\right)(0.58 + 0.0015\alpha) \tag{A.14}$$

where

$$S_1 = \sqrt{d_1^2 + h^2} - d1 \tag{A.15}$$

with

$$d_1 = (2h_0 - \frac{2}{3}h)\cot\alpha + b_k \tag{A.16}$$

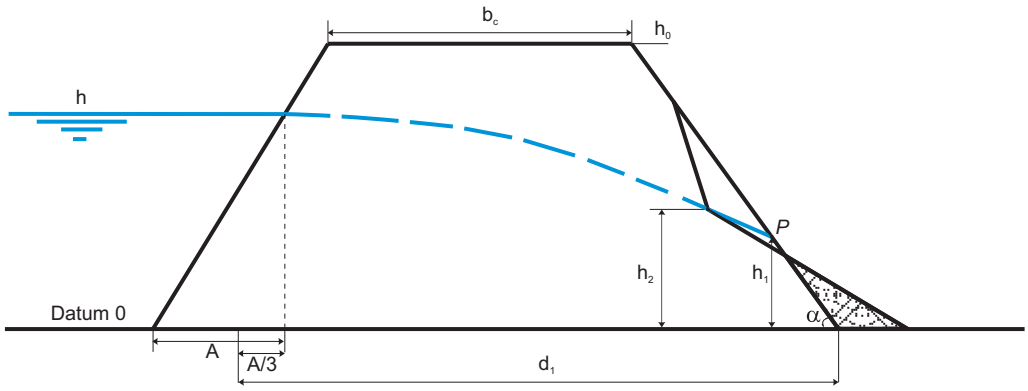


**Figure A.2:** *Schematic representation of slope failure due to micro-instability. Adopted from Vrouwenvelder and Wubs (1985) for the special case of a dike without ditch.*

**Table A.1:** *Summary of random variables used in the dike breach component of the IHAM to derive the fragility curves in a Monte Carlo simulation: mean, standard deviation, range of variation and probability distribution functions ($norm$ -normal distribution, $logn$ - log-normal distribution). Range of variation represents assumed possible parameter interval and used to truncate probability distribution function. Observed parameter values ($obs$) were used where available, otherwise values based on the literature review were employed. The presented parameter values are used in the reference model version.*

| Description | Variable | Unit | Mean | Std. dev. | Range | | PDF | Reference |
|---|---|---|---|---|---|---|---|---|
| | | | $\mu$ | $\sigma$ | min | max | | |
| Air-filled porosity | $n_a$ | $[-]$ | 0.188 | $0.15\mu(n_a)$ | 0.095 | 0.288 | $norm$ | Kanowski (1977) |
| Crest height | $h_0$ | $[m]$ | $obs$ | $obs$ | $obs$ | $obs$ | $norm$ | |
| Crest height | $h_0$ | $[m]$ | 3.25 | 0.2236 | 1 | 5 | $norm$ | Vrijling and van Gelder (2000) |
| Crest rounding | $R_c$ | $[-]$ | 5 | 0 | – | – | – | Vrijling and van Gelder (2000) |
| Crest width | $b_c$ | $[m]$ | $obs$ | $obs$ | $obs$ | $obs$ | $norm$ | |
| Crest width | $b_c$ | $[m]$ | 3 | 0.15 | 1 | 15 | $norm$ | Vrijling and van Gelder (2000) |
| Friction angle | $\theta$ | $[deg]$ | 29.249 | 0.3 | 20.807 | 37.596 | $logn$ | Kanowski (1977)<br>Vrijling and van Gelder (2000) |
| Hyadraulic conductivity of dike material | $K_f$ | $[m\ s^{-1}]$ | $10^{-5}$ | $25\mu(K_f)$ | $10^{-6}$ | $10^{-4}$ | $logn$ | Pohl (2000a)<br>USACE (1999) |
| Hydraulic conductivity of dike foundation | $K_f$ | $[m\ s^{-1}]$ | $3 \cdot 10^{-5}$ | $25\mu(K_f)$ | $3 \cdot 10^{-6}$ | $3 \cdot 10^{-4}$ | $logn$ | Berry and Reid (1987)<br>USACE (1999) |
| Inner slope | $m$ | $[-]$ | $obs$ | $obs$ | $obs$ | $obs$ | $norm$ | |
| Inner slope | $m$ | $[-]$ | 2.5 | $0.05\mu(m)$ | 1 | 5 | $norm$ | Vrijling and van Gelder (2000) |
| Inner slope angle | $\alpha$ | $[rad]$ | $obs$ | $obs$ | $obs$ | $obs$ | $norm$ | |
| Inner slope angle | $\alpha$ | $[rad]$ | 0.4914 | $\frac{0.05\mu(m)^5}{\mu(m)^2+1}$ | 0.1974 | 0.7854 | $norm$ | Vrijling and van Gelder (2000) |
| Outer slope | $n$ | $[-]$ | $obs$ | $obs$ | $obs$ | $obs$ | $norm$ | |
| Outer slope | $n$ | $[-]$ | 3 | $0.05\mu(n)$ | 1 | 10 | $norm$ | Vrijling and van Gelder (2000) |
| Particle diameter | $d_{70}$ | $[-]$ | 0.0004 | $0.15\mu(d_{70})$ | 0.00006 | 0.0008 | $logn$ | Bollrich (2000)<br>Vrijling and van Gelder (2000)<br>Saucke (2006)<br>Müller-Kirchenbauer et al. (1993) |

**Table A.2:** *Table A.1 continued*

| Description | Variable | Unit | Mean | Std. dev. | Range | | PDF | Reference |
|---|---|---|---|---|---|---|---|---|
| | | | $\mu$ | $\sigma$ | min | max | | |
| Roughness of inner slope | $k$ | $[m]$ | 0.015 | $0.25\mu(k)$ | 0.0003 | 244 | $logn$ | Vrijling and van Gelder (2000) |
| Thickness of clay layer | $d$ | $[m]$ | 1 | $0.3\mu(d)$ | 0 | 3 | $logn$ | Vrijling and van Gelder (2000) |
| Thickness of sand layer | $D_s$ | $[m]$ | 5 | $0.1\mu(D_s)$ | 0 | 15 | $logn$ | Vrijling and van Gelder (2000) |
| Turf quality | $f_g$ | $[-]$ | $obs$ | $obs$ | 0.5 | 1.5 | $norm$ | Apel et al. (2006) |
| Weight per volume of sand | $\gamma_p$ | $[kN\ m^{-3}]$ | 18 | 1.0 | 13 | 21 | $norm$ | Kortenhaus and Oumeraci (2002)<br>Gocht (2002) |
| Weight per volume of clay | $\gamma_k$ | $[kN\ m^{-3}]$ | 19 | 0.05 | 17 | 21 | $norm$ | Kortenhaus and Oumeraci (2002)<br>Gocht (2002) |
| White's coefficient | $\eta$ | $[-]$ | 0.25 | $0.15\mu(\eta)$ | $-$ | $-$ | $logn$ | van Loon (2001)<br>Vrijling and van Gelder (2000) |

# Appendix B

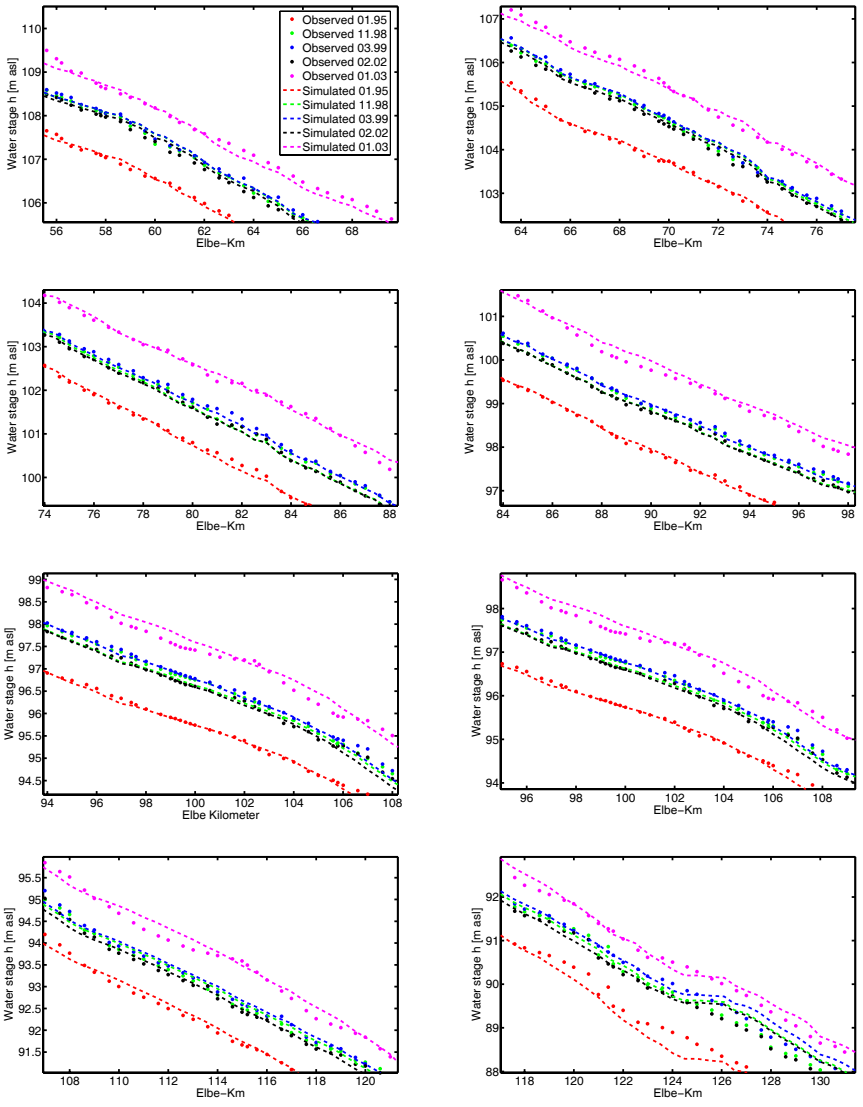


**Figure B.1:** *Comparison between simulated water stages and recorded high water marks along the Elbe River. Flood events in 1995, 1998, 1999 and 2000 were used for calibration. The steady-state model was validated on the 2003 flood event data.*

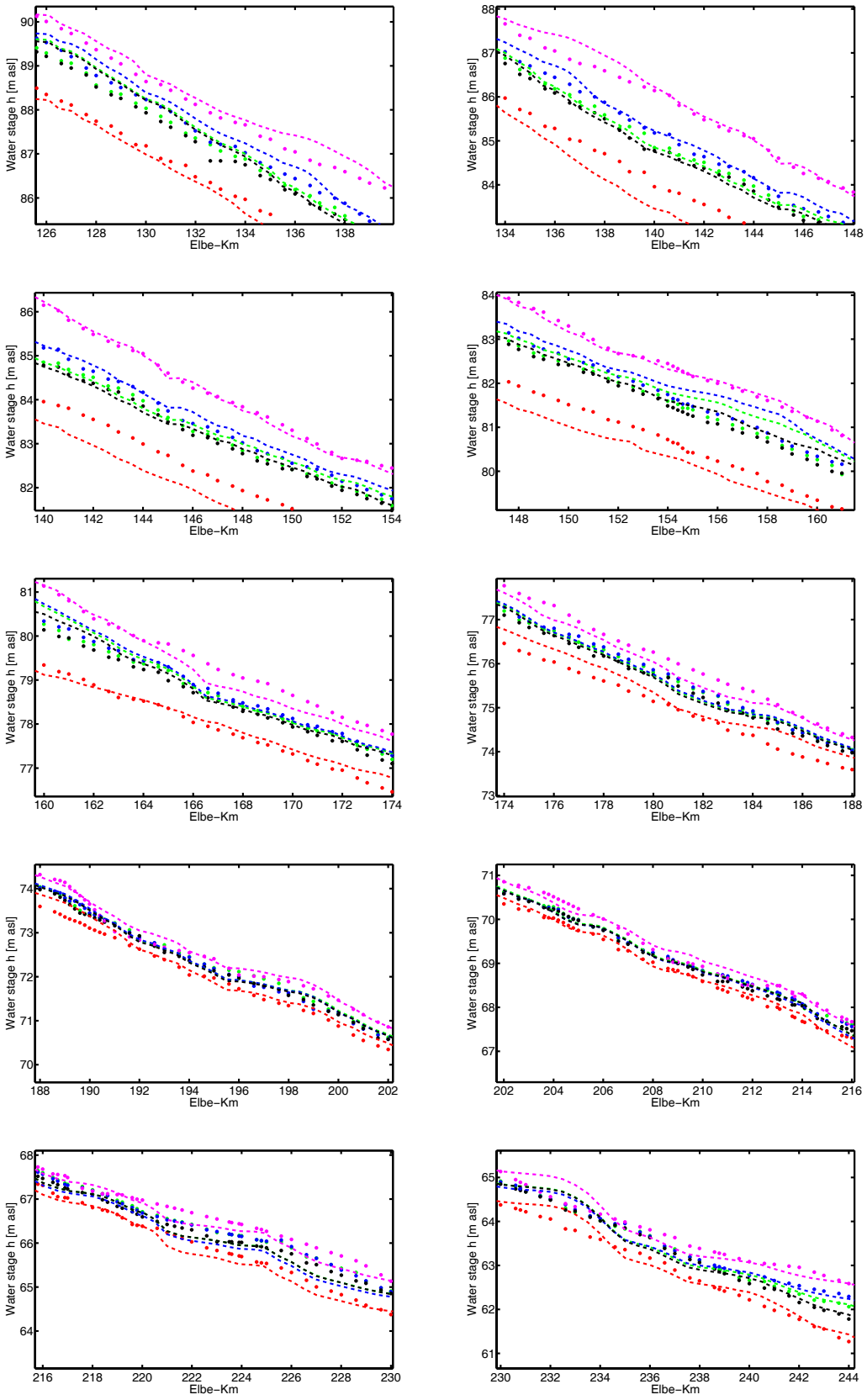


**Figure B.2:** *Figure B.1 continued.*

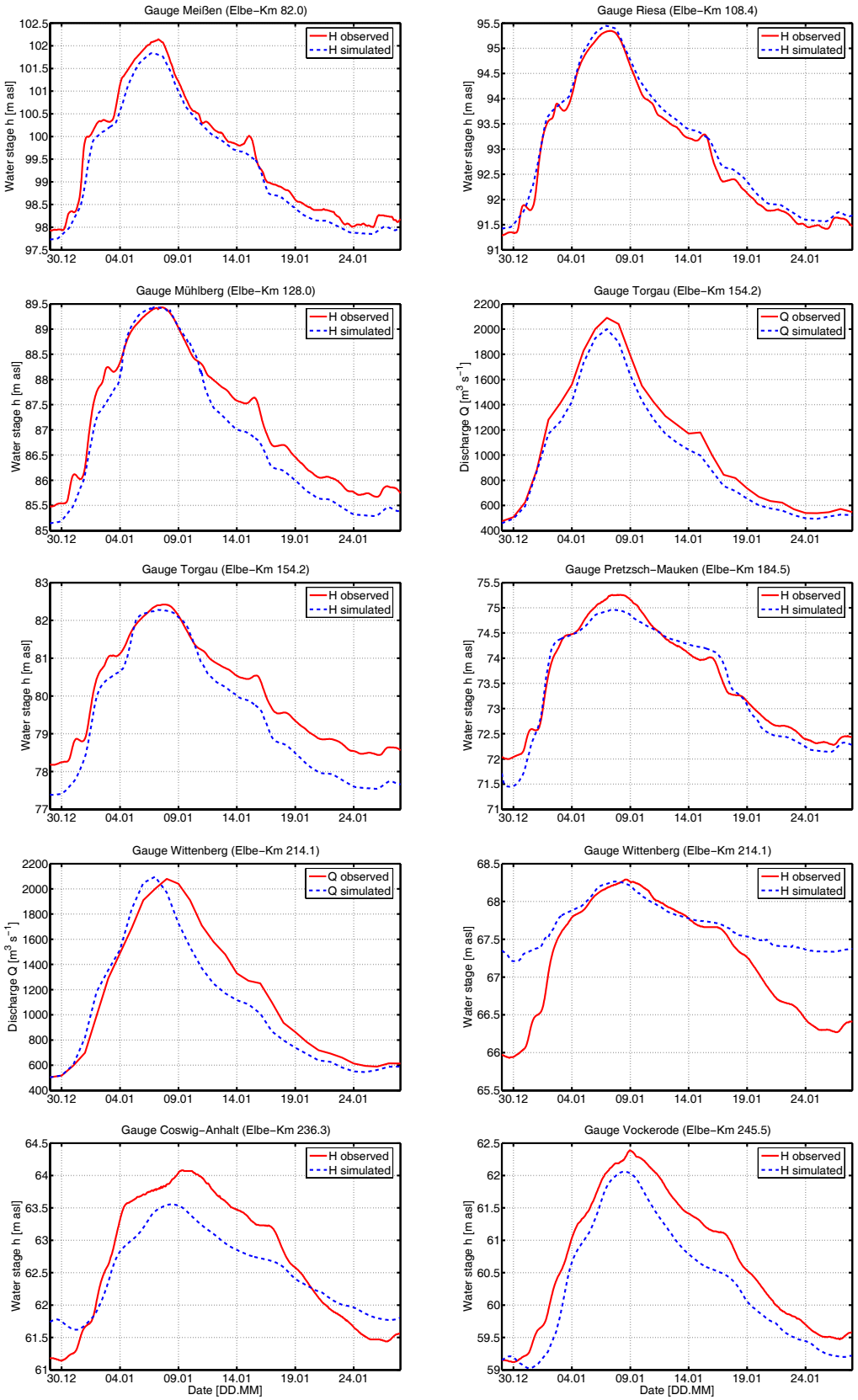


**Figure B.3:** *Observed vs. simulated discharge and water stage hydrographs for the January flood event in 2003 at Elbe gauges between Dresden and Vockerode.*

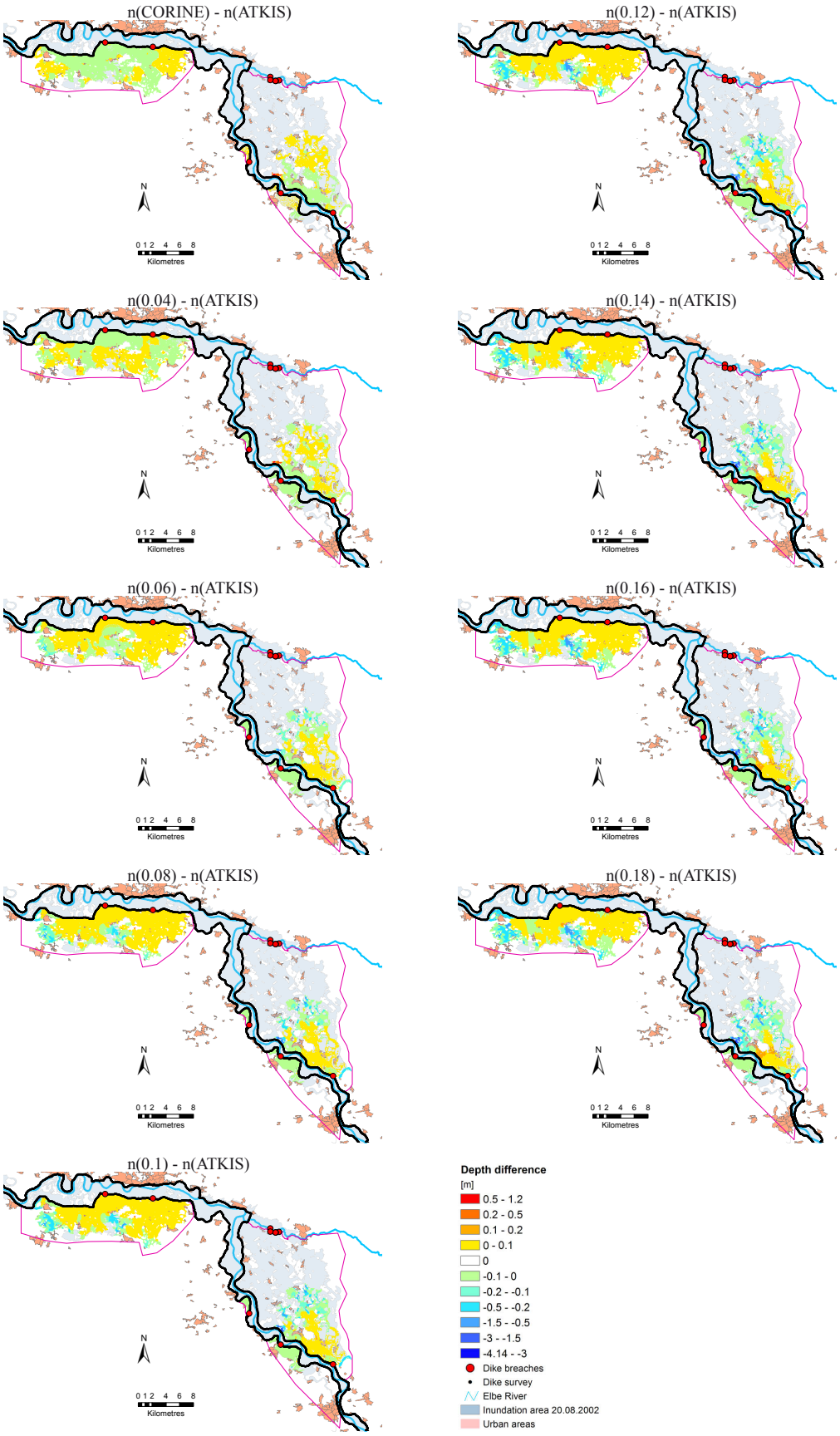


**Figure B.4:** *Difference in maximum inundation depth, simulated with CORINE- and ATKIS-based roughness, as well as between uniform and ATKIS-based roughness parameterisation.*

# Appendix C

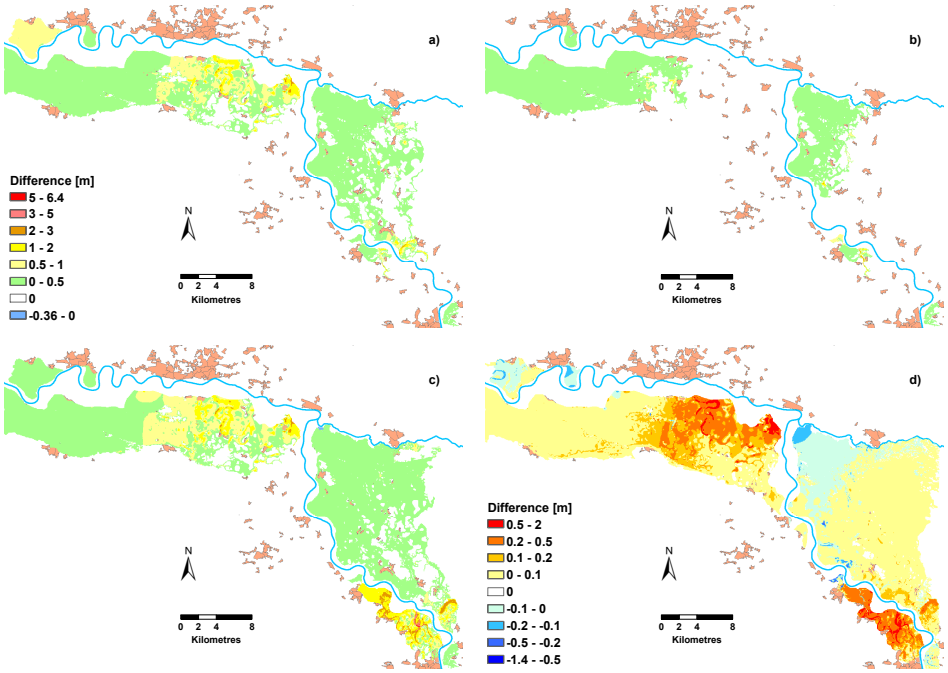


**Figure C.1:** *Difference in maximum inundation depth between the scenarios* $200y$ *and* $100y$ *for (a) median, (b)* $10^{th}$ *and (c)* $90^{th}$ *percentiles. (d) Difference between the corresponding standard deviations. Legend in (a) applies to (b) and (c).*

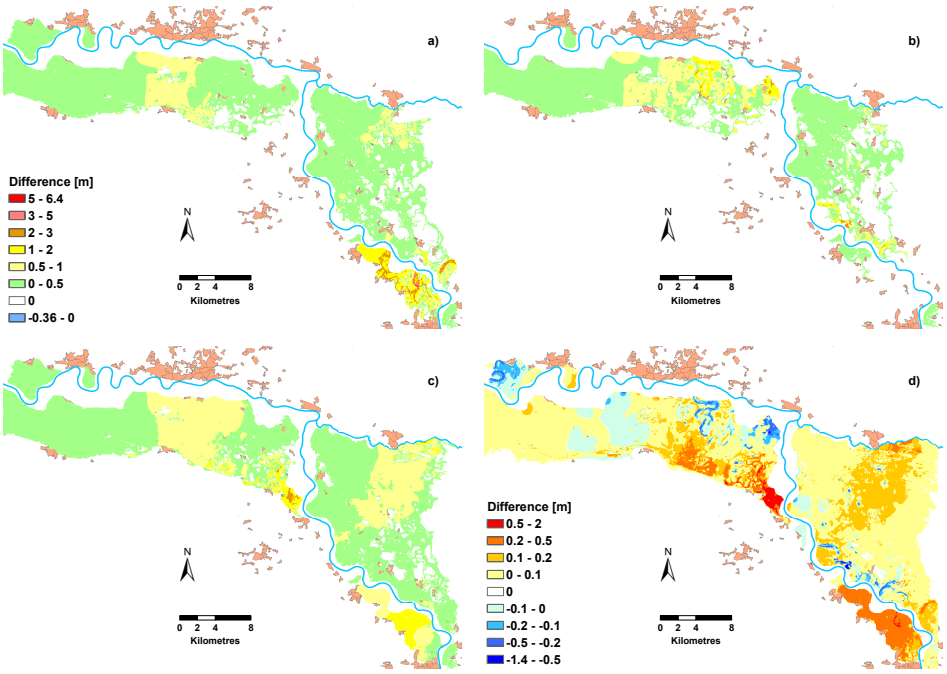


**Figure C.2:** *Difference in maximum inundation depth between the scenarios* $500y$ *and* $200y$ *for (a) median, (b)* $10^{th}$ *and (c)* $90^{th}$ *percentiles. (d) Difference between the corresponding standard deviations. Legend in (a) applies to (b) and (c).*

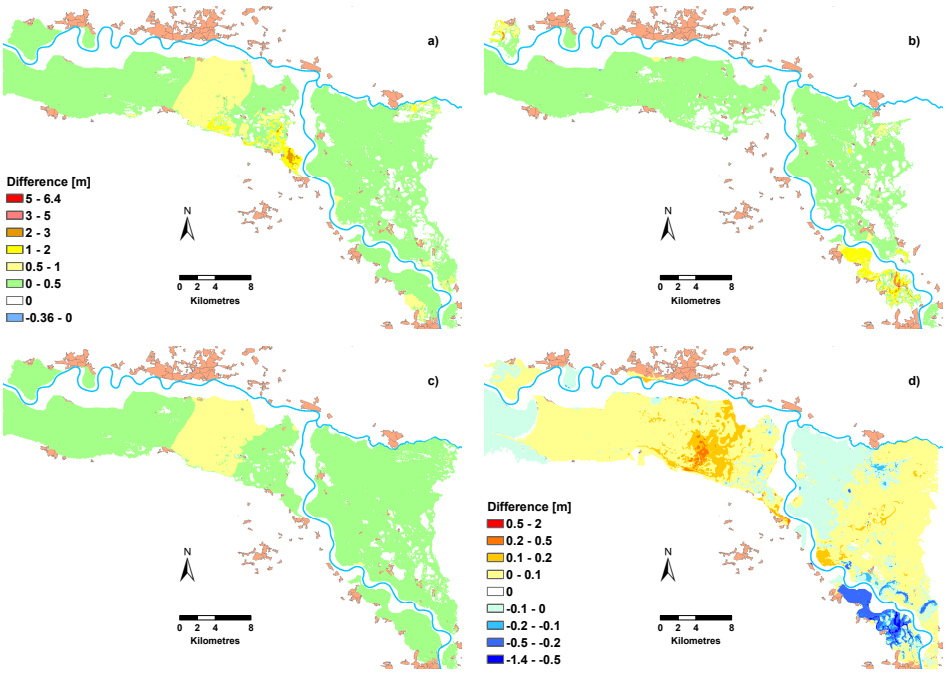


**Figure C.3:** *Difference in maximum inundation depth between the scenarios* $1000y$ *and* $500y$ *for (a) median, (b)* $10^{th}$ *and (c)* $90^{th}$ *percentiles. (d) Difference between the corresponding standard deviations. Legend in (a) applies to (b) and (c).*

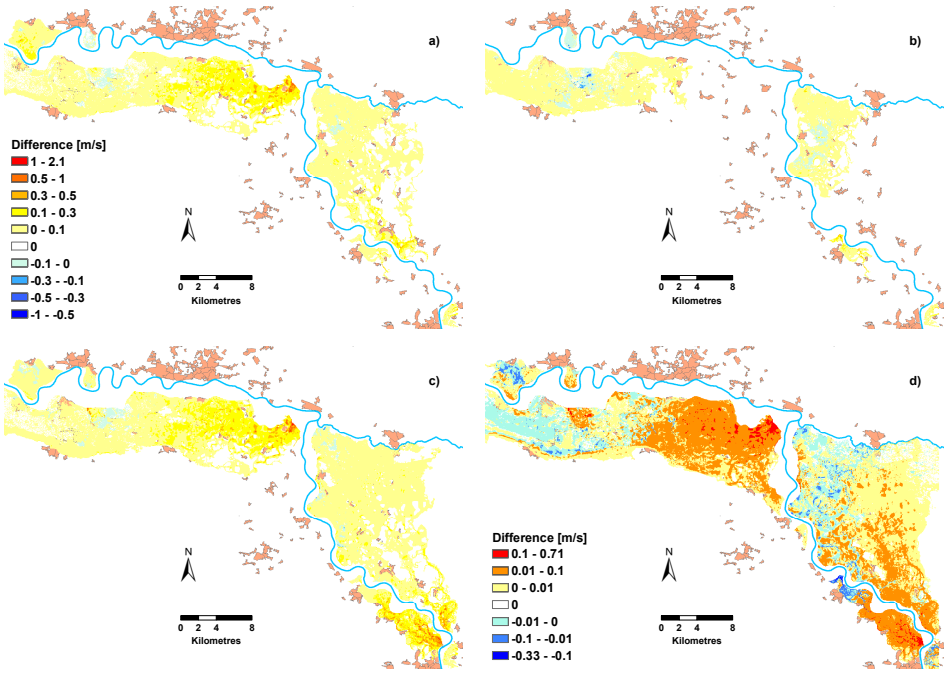


**Figure C.4:** *Difference in maximum flow velocity between the scenarios* $200y$ *and* $100y$ *for (a) median, (b)* $10^{th}$ *and (c)* $90^{th}$ *percentiles. (d) Difference between the corresponding standard deviations. Legend in (a) applies to (b) and (c).*

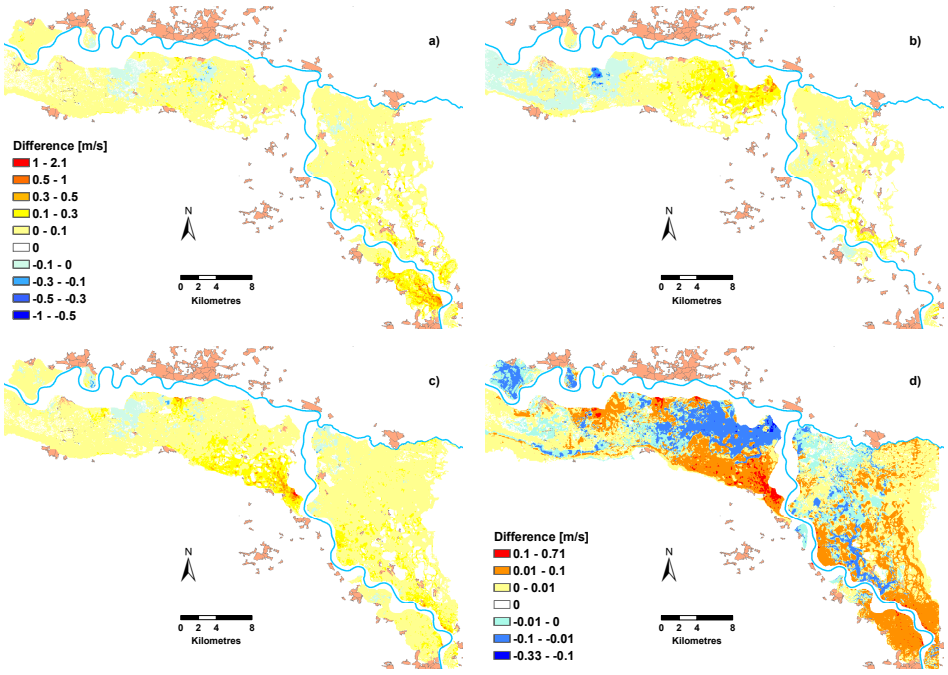


**Figure C.5:** *Difference in maximum flow velocity between the scenarios* $500y$ *and* $200y$ *for (a) median, (b)* $10^{th}$ *and (c)* $90^{th}$ *percentiles. (d) Difference between the corresponding standard deviations. Legend in (a) applies to (b) and (c).*

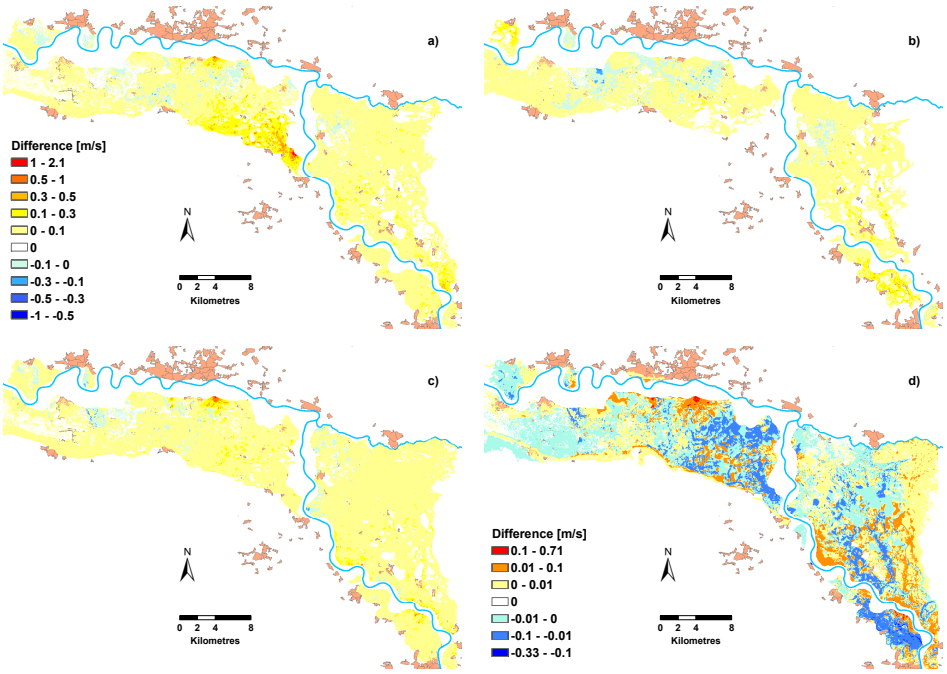


**Figure C.6:** *Difference in maximum flow velocity between the scenarios* $1000y$ *and* $500y$ *for (a) median, (b)* $10^{th}$ *and (c)* $90^{th}$ *percentiles. (d) Difference between the corresponding standard deviations. Legend in (a) applies to (b) and (c).*

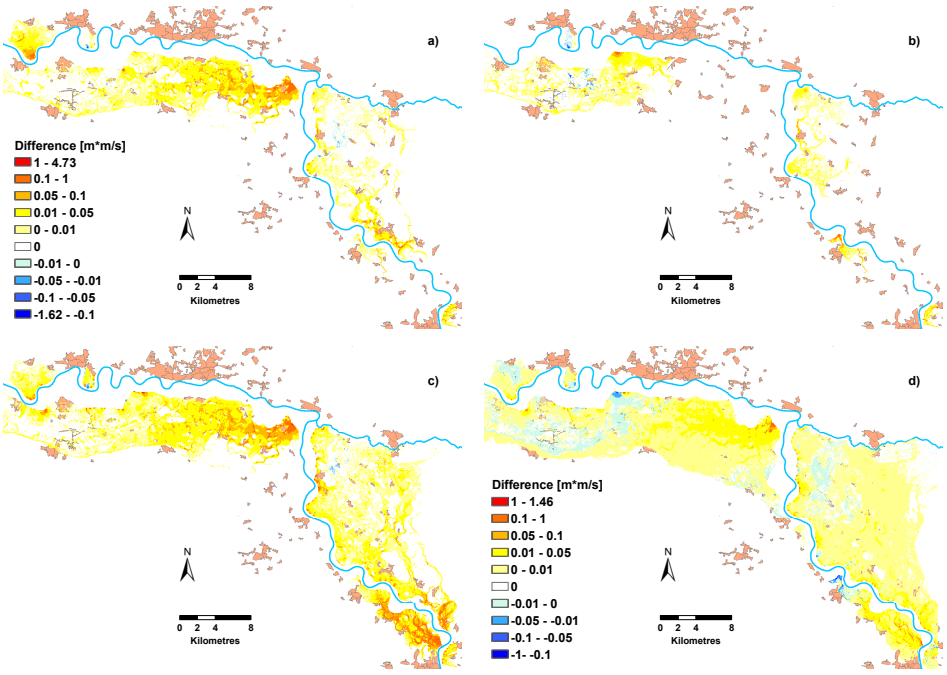


**Figure C.7:** *Difference in maximum impulse between the scenarios* $200y$ *and* $100y$ *for (a) median, (b)* $10^{th}$ *and (c)* $90^{th}$ *percentiles. (d) Difference between the corresponding standard deviations. Legend in (a) applies to (b) and (c).*

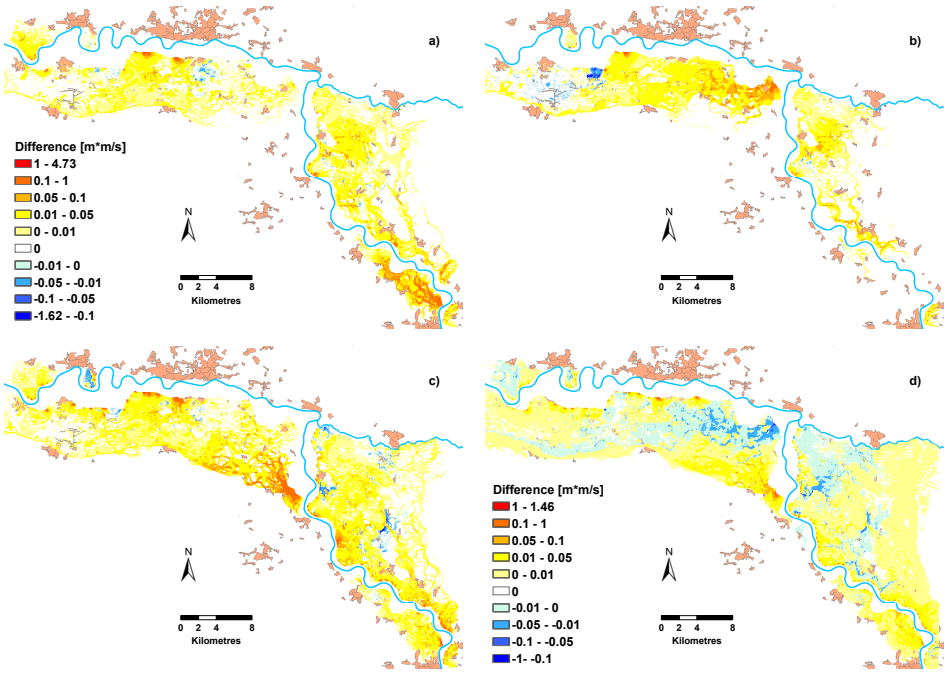


**Figure C.8:** *Difference in maximum impulse between the scenarios* $500y$ *and* $200y$ *for (a) median, (b)* $10^{th}$ *and (c)* $90^{th}$ *percentiles. (d) Difference between the corresponding standard deviations. Legend in (a) applies to (b) and (c).*

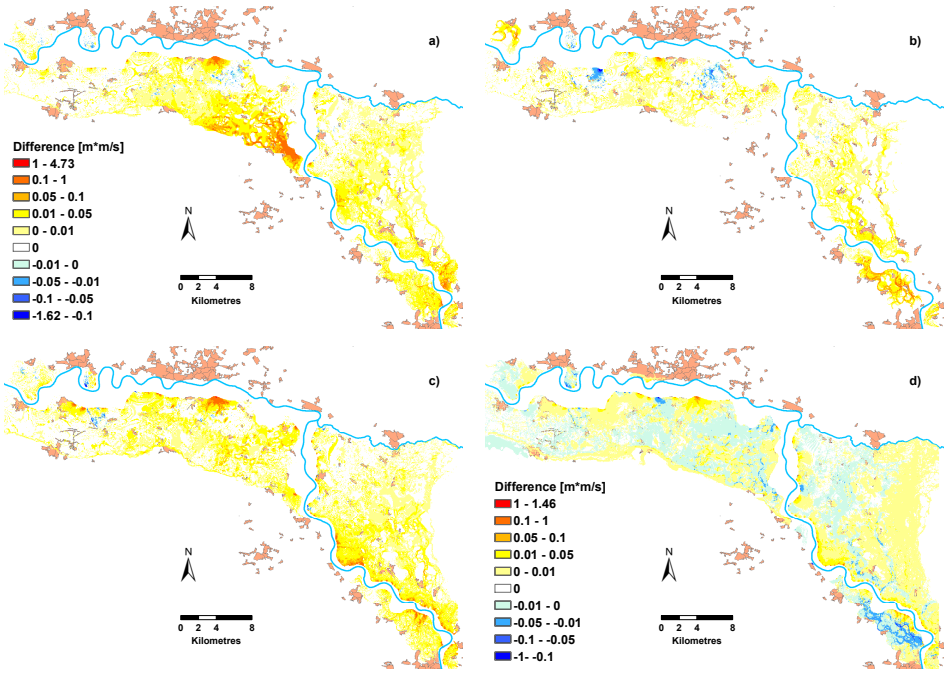


**Figure C.9:** *Difference in maximum impulse between the scenarios* $1000y$ *and* $500y$ *for (a) median, (b)* $10^{th}$ *and (c)* $90^{th}$ *percentiles. (d) Difference between the corresponding standard deviations. Legend in (a) applies to (b) and (c).*

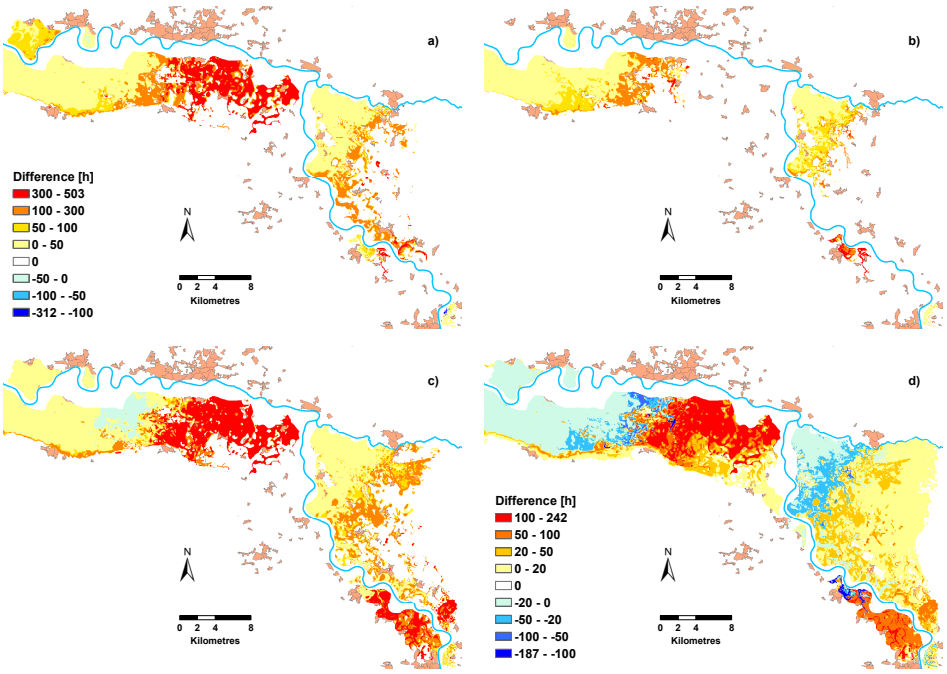


**Figure C.10:** *Difference in inundation duration with water depth above* $0.2\ m$ *between the scenarios* $200y$ *and* $100y$ *for (a) median, (b)* $10^{th}$ *and (c)* $90^{th}$ *percentiles. (d) Difference between the corresponding standard deviations. Legend in (a) applies to (b) and (c).*

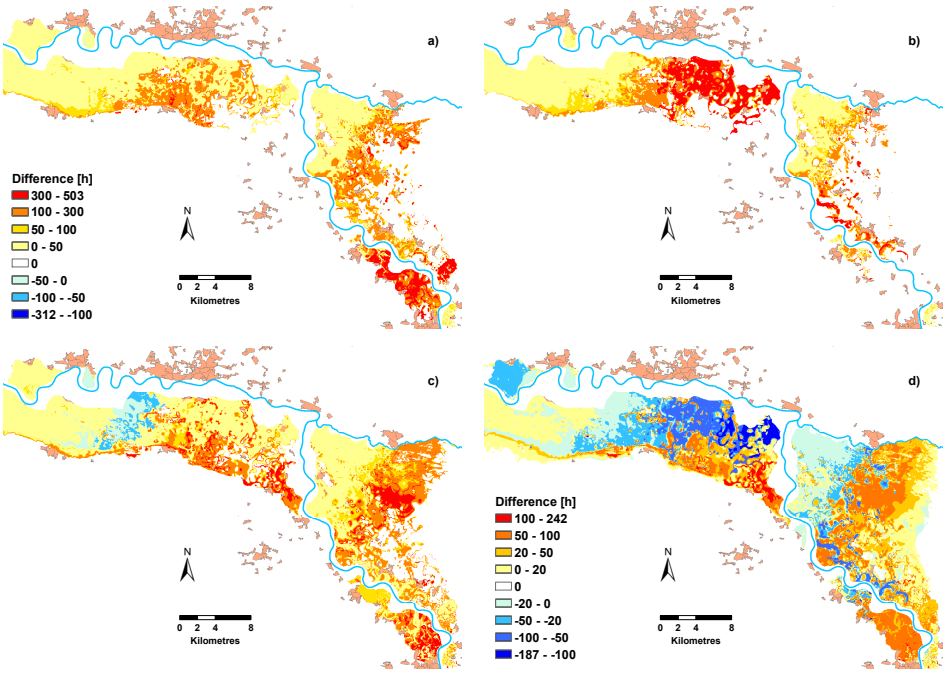


**Figure C.11:** *Difference in inundation duration with water depth above* $0.2\ m$ *between the scenarios* $500y$ *and* $200y$ *for (a) median, (b)* $10^{th}$ *and (c)* $90^{th}$ *percentiles. (d) Difference between the corresponding standard deviations. Legend in (a) applies to (b) and (c).*

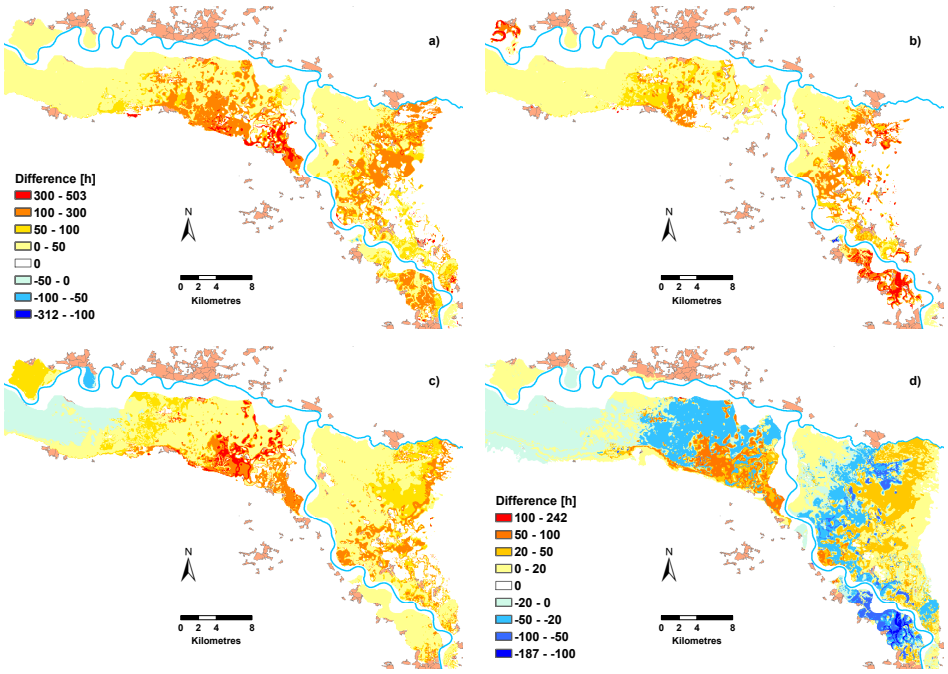


**Figure C.12:** *Difference in inundation duration with water depth above* $0.2\ m$ *between the scenarios* $1000y$ *and* $500y$ *for (a) median, (b)* $10^{th}$ *and (c)* $90^{th}$ *percentiles. (d) Difference between the corresponding standard deviations. Legend in (a) applies to (b) and (c).*

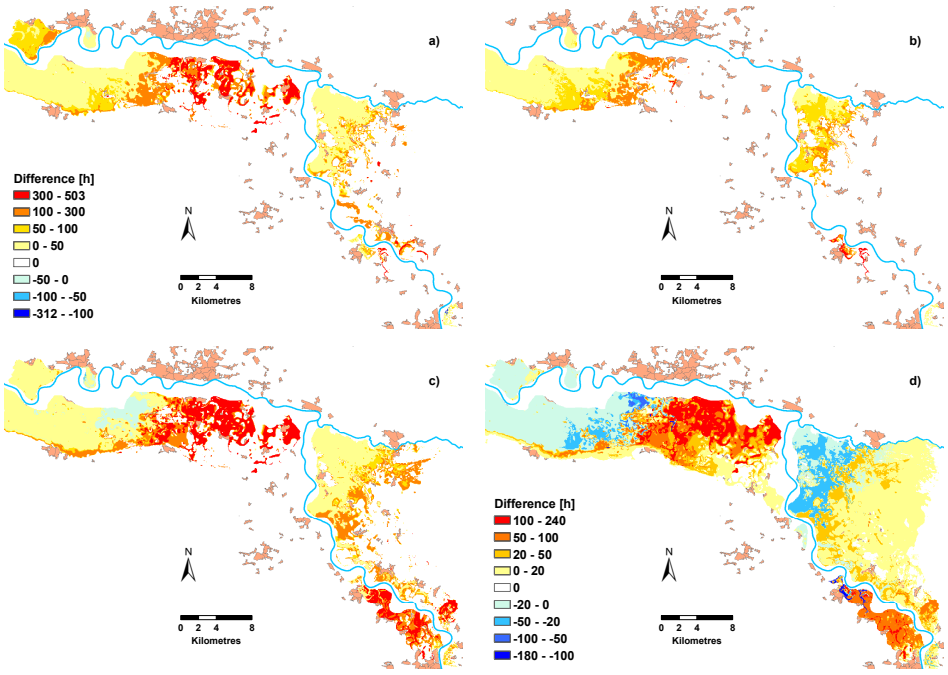


**Figure C.13:** *Difference in inundation duration with water depth above* $0.5\ m$ *between the scenarios* $200y$ *and* $100y$ *for (a) median, (b)* $10^{th}$ *and (c)* $90^{th}$ *percentiles. (d) Difference between the corresponding standard deviations. Legend in (a) applies to (b) and (c).*

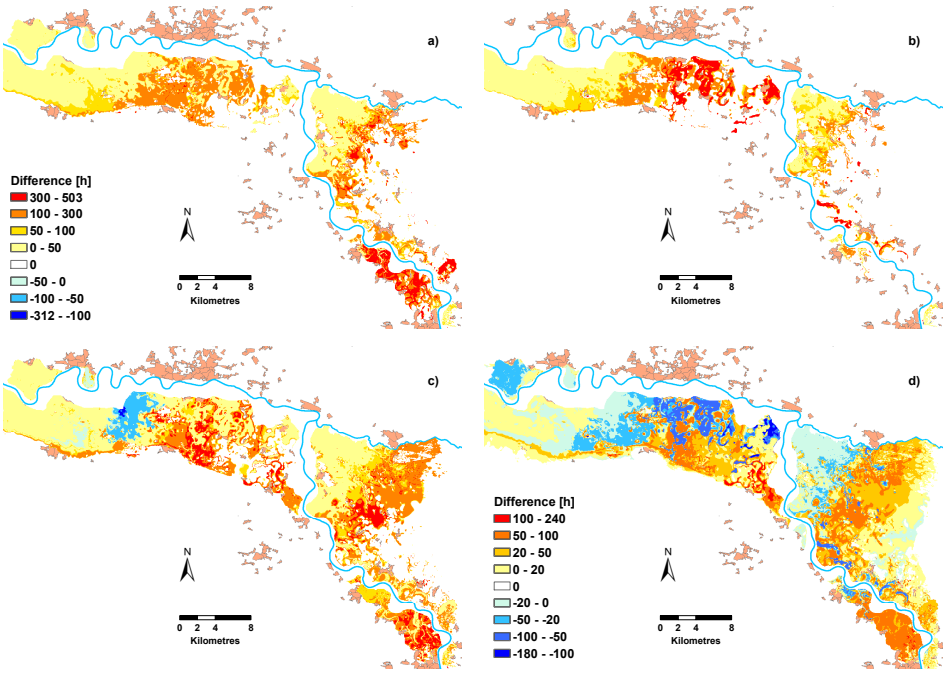


**Figure C.14:** *Difference in inundation duration with water depth above* $0.5\ m$ *between the scenarios* $500y$ *and* $200y$ *for (a) median, (b)* $10^{th}$ *and (c)* $90^{th}$ *percentiles. (d) Difference between the corresponding standard deviations. Legend in (a) applies to (b) and (c).*

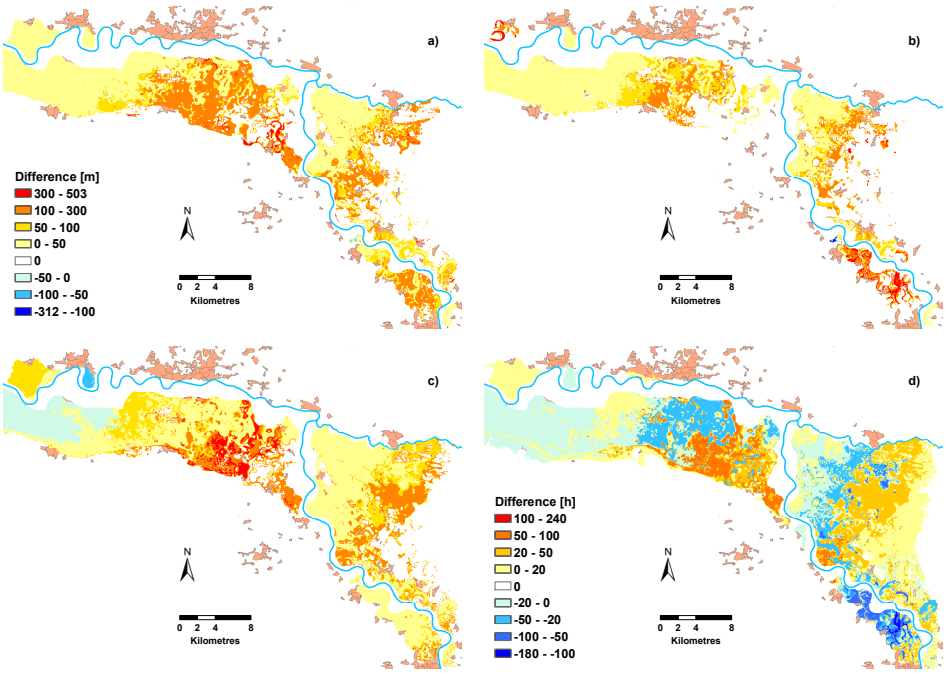


**Figure C.15:** *Difference in inundation duration with water depth above* $0.5\ m$ *between the scenarios* $1000y$ *and* $500y$ *for (a) median, (b)* $10^{th}$ *and (c)* $90^{th}$ *percentiles. (d) Difference between the corresponding standard deviations. Legend in (a) applies to (b) and (c).*

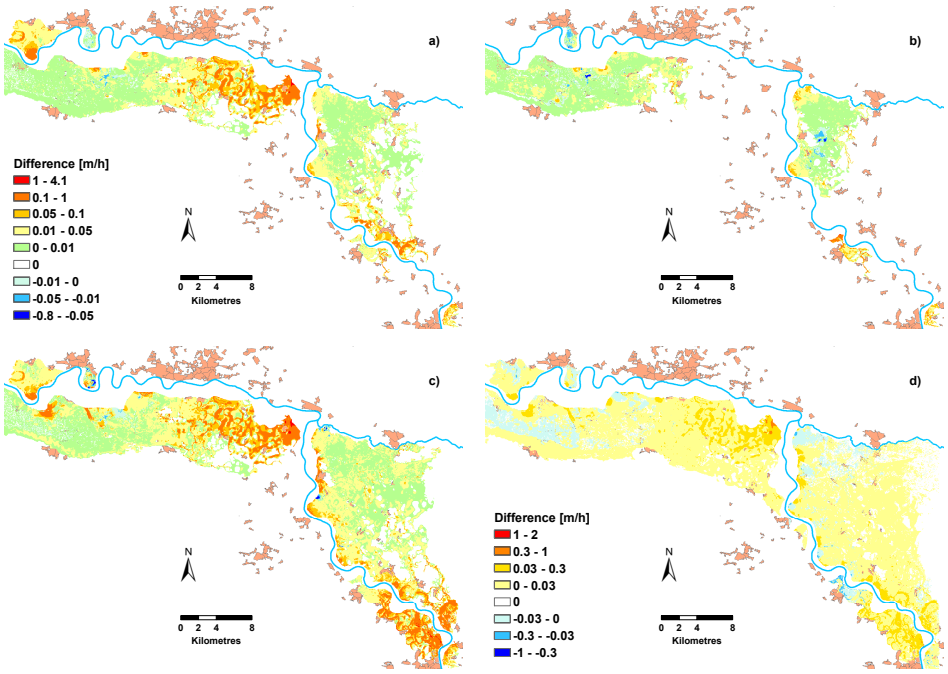


**Figure C.16:** *Difference in maximum rate of water rise within* 1 *hour between the scenarios* $200y$ *and* $100y$ *for (a) median, (b)* $10^{th}$ *and (c)* $90^{th}$ *percentiles. (d) Difference between the corresponding standard deviations. Legend in (a) applies to (b) and (c).*

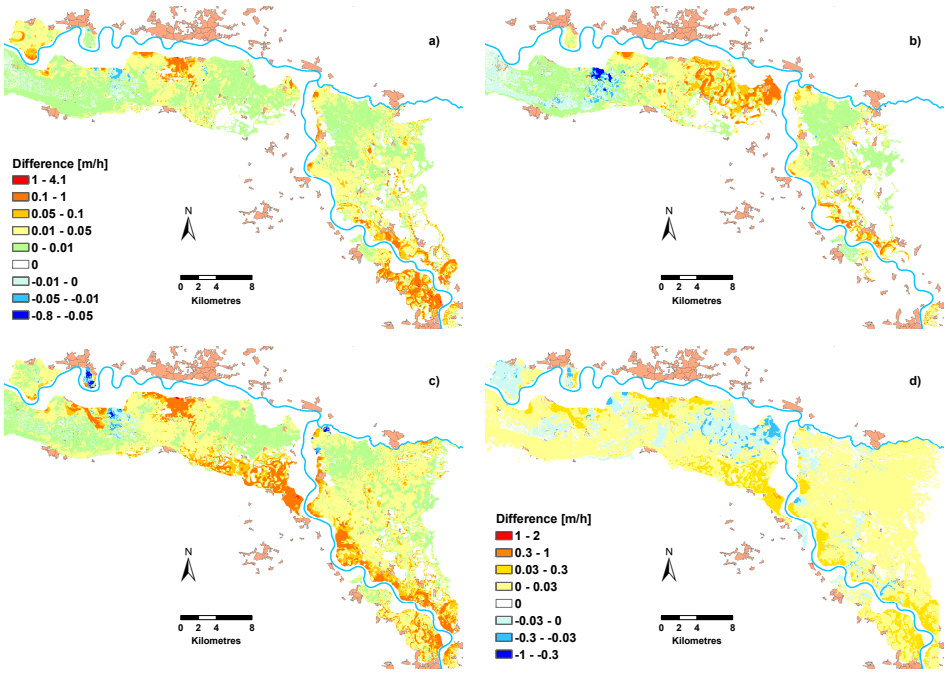


**Figure C.17:** *Difference in maximum rate of water rise within* 1 *hour between the scenarios* $500y$ *and* $200y$ *for (a) median, (b)* $10^{th}$ *and (c)* $90^{th}$ *percentiles. (d) Difference between the corresponding standard deviations. Legend in (a) applies to (b) and (c).*

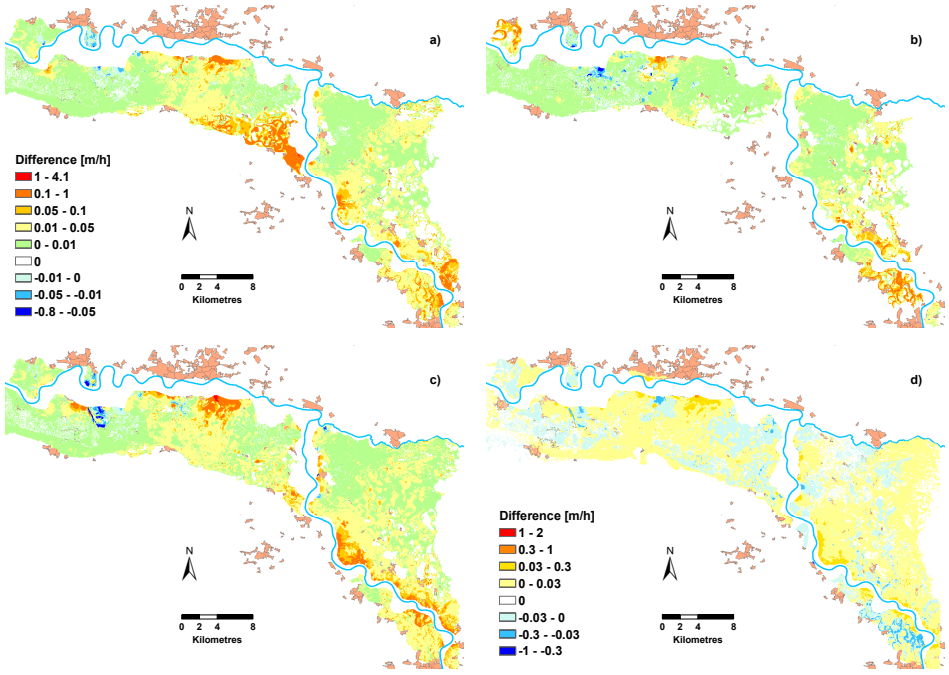


**Figure C.18:** *Difference in maximum rate of water rise within* $1$ *hour between the scenarios* $1000y$ *and* $500y$ *for (a) median, (b)* $10^{th}$ *and (c)* $90^{th}$ *percentiles. (d) Difference between the corresponding standard deviations. Legend in (a) applies to (b) and (c).*

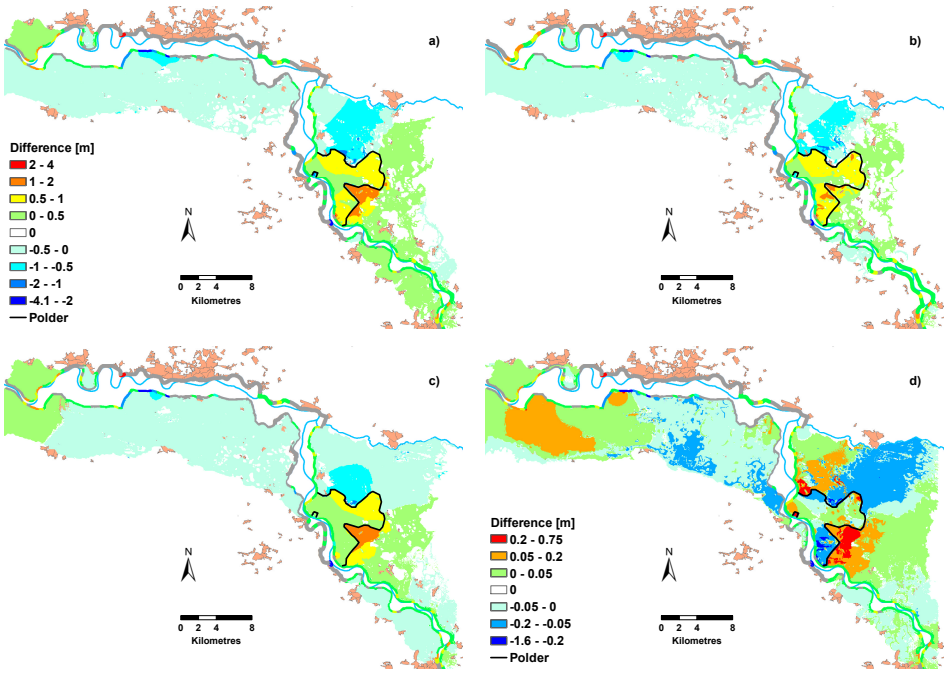


**Figure C.19:** *Difference in maximum inundation depth between the scenarios* $500y\_pol$ *and* $500y$ *for (a) median, (b)* $10^{th}$*,* $90^{th}$ *percentiles. (d) Difference between the corresponding standard deviations. Legend in (a) applies for (b) and (c).*

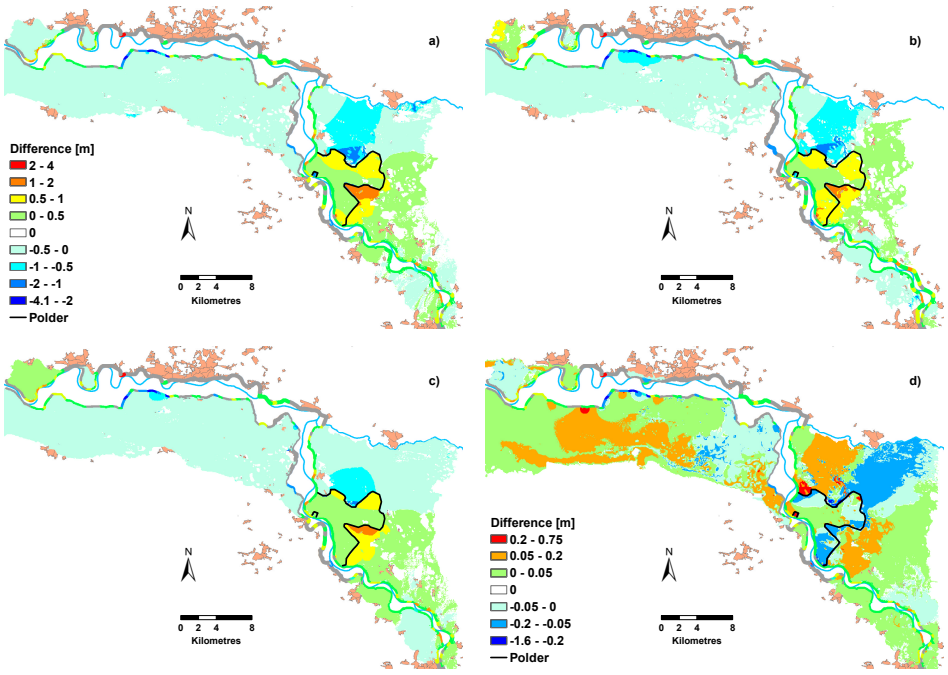


**Figure C.20:** *Difference in maximum inundation depth between the scenarios* $1000y\_pol$ *and* $1000y$ *for (a) median, (b)* $10^{th}$*,* $90^{th}$ *percentiles. (d) Difference between the corresponding standard deviations. Legend in (a) applies for (b) and (c).*

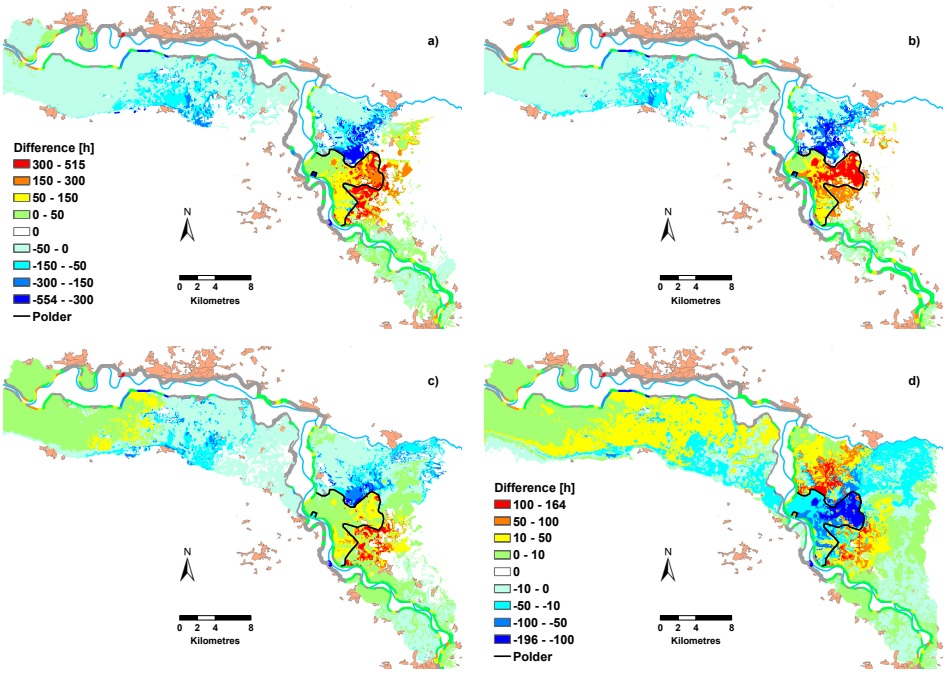


**Figure C.21:** *Difference in maximum inundation duration with water depth above* $0.2\ m$ *between the scenarios* $500y\_pol$ *and* $500y$ *for (a) median, (b)* $10^{th}$*,* $90^{th}$ *percentiles. (d) Difference between the corresponding standard deviations. Legend in (a) applies for (b) and (c).*

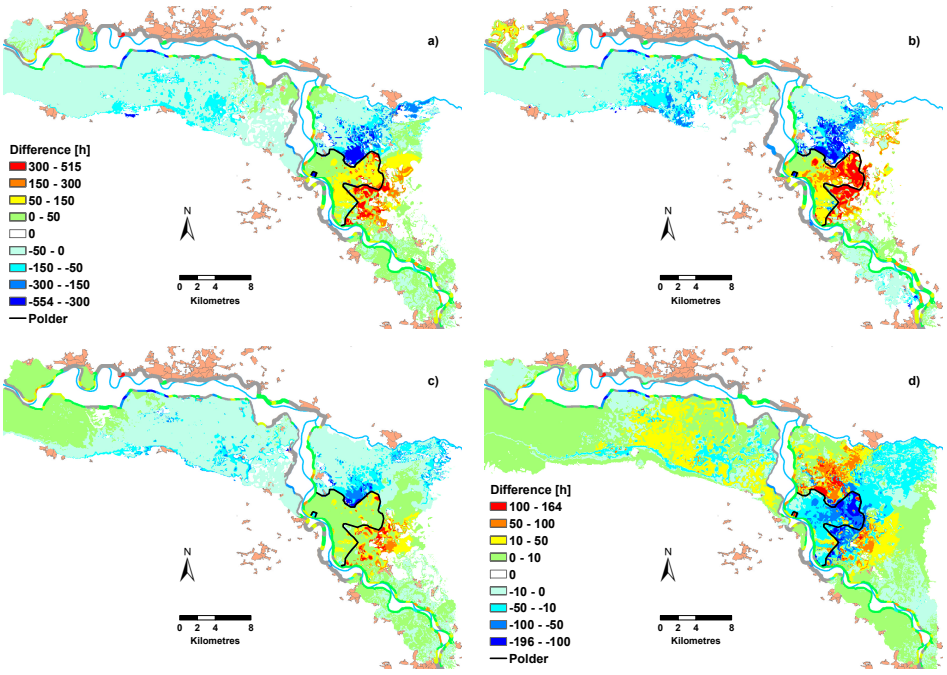


**Figure C.22:** *Difference in maximum inundation duration with water depth above* $0.2\ m$ *between the scenarios* $1000y\_pol$ *and* $1000y$ *for (a) median, (b)* $10^{th}$*,* $90^{th}$ *percentiles. (d) Difference between the corresponding standard deviations. Legend in (a) applies for (b) and (c).*

# List of Symbols

**Table C.1:** *Variables, description, units*

| | | |
|---|---|---|
| $A$ | flow cross-sectional area | $[m^2]$ |
| $\alpha$ | inner slope angle | $[deg]$ |
| $B_w$ | dike breach width | $[m]$ |
| $b_c$ | dike crest width | $[m]$ |
| $b_f$ | dike foundation width | $[m]$ |
| $C_{B,creep}$ | Bligh creep coefficient | $[-]$ |
| $C_{L,creep}$ | Lane creep coefficient | $[-]$ |
| $D(h)$ | duration of hydraulic load as function of water level | $[d]$ |
| $D_s$ | thickness of sandy layer | $[m]$ |
| $d$ | thickness of clay layer | $[m]$ |
| $d$ | water depth | $[m]$ |
| $d_{70}$ | sand particle diameter of $70\%$-weight grain size distribution | $[m]$ |
| $\eta$ | White's drag coefficient | $[-]$ |
| $f_g$ | turf quality parameter | $[-]$ |
| $g$ | gravitational acceleration | $[m\ s^{-2}]$ |
| $\gamma_k$ | weight per volume of clay soil | $[kN\ m^{-3}]$ |
| $\gamma_p$ | weight per unit of volume of sand particles | $[kN\ m^{-3}]$ |
| $\gamma_w$ | weight per volume of water | $[kN\ m^{-3}]$ |
| $H$, $h$ | water level | $[m]$ |
| $H_{crit}$ | critical water level for piping | $[m]$ |
| $h_a$ | height of slide for slope micro-instability | $[m]$ |
| $h_e$ | dike overtopping height | $[m]$ |
| $h_{flow}$ | difference between the maximum water surface elevation and maximum ground elevation of two adjacent cells | $[m]$ |
| $h^{i,j}$ | water surface elevation at cell $(i, j)$ | $[m]$ |
| $h_T$ | height of the phreatic line starting point | $[m]$ |
| $h_0$ | dike crest height | $[m]$ |
| $i$ | hydraulic gradient | $[-]$ |
| $K$ | conveyance | $[m^3\ s^{-1}]$ |
| $K_f$ | saturated hydraulic conductivity | $[m\ s^{-1}]$ |
| $k$ | absolute roughness of the inner slope | $[m]$ |
| $k$ | permeability coefficient of sand | $[m\ s^{-1}]$ |
| $\kappa$ | intrinsic permeability | $[m^2]$ |

**Table C.2:** *Variables, description, units*

| | | |
|---|---|---|
| $L$ | load | $[-]$ |
| $L$ | seepage length | $[m]$ |
| $L_d$ | length of defence structure/section | $[m]$ |
| $L_h$ | horizontal component of seepage length | $[m]$ |
| $L_p$ | pipe length during piping | $[m]$ |
| $L_v$ | vertical component of seepage length | $[m]$ |
| $1/m$ | dike inner slope | $[-]$ |
| $m$ | parameter multiplicator | $[-]$ |
| $N_{ic}$ | number of interface cells | $[-]$ |
| $n$ | Manning's roughness coefficient | $[m^{1/3}\ s^{-1}]$ |
| $1/n$ | dike outer slope | $[-]$ |
| $n_a$ | air-filled porosity | $[-]$ |
| $\nu$ | kinematic viscosity | $[m^2\ s^{-1}]$ |
| $P_{failure}$ | probability of failure | $[-]$ |
| $\psi$ | specific matric potential | $[-]$ |
| $Q$ | discharge | $[m^3\ s^{-1}]$ |
| $Q_a(t)$ | overtopping discharge | $[m^3\ s^{-1}]$ |
| $Q_{crit}(t)$ | critical discharge | $[m^3\ s^{-1}]$ |
| $QD$ | direct runoff | $[m^3\ s^{-1}]$ |
| $QD_{max}$ | maximum direct runoff | $[m^3\ s^{-1}]$ |
| $QD_{norm}$ | normalised direct runoff | $[m^3\ s^{-1}]$ |
| $Q_x$ | volumetric flow rates between cells in $x$ direction | $[m^3\ s^{-1}]$ |
| $Q_y$ | volumetric flow rates between cells in $y$ direction | $[m^3\ s^{-1}]$ |
| $Q_{0.1}$ | quantile of hazard indicator | $[-]$ |
| $q$ | net lateral inflow per unit length | $[m^2\ s^{-1}]$ |
| $R$ | wetted perimeter | $[m]$ |
| $R$ | resistance | $[-]$ |
| $R_c$ | crest rounding | $[-]$ |
| $r_i$ | uncertain dike state variable | $[-]$ |
| $S_f$ | friction slope | $[-]$ |
| $S_o$ | bottom slope | $[-]$ |
| $S_\triangle$ | area of triangle | $[m^2]$ |
| $T$ | return period | $[a]$ |
| $T$ | total dike impoundment duration | $[s]$ |
| $t$ | time | $[s]$ |
| $t_d$ | duration of piping | $[d]$ |
| $t_{db}$ | time step for checking dike stability | $[s]$ |
| $t_e$ | dike overtopping duration | $[h]$ |
| $t_s$ | time step for probability sampling | $[h]$ |
| $\tau$ | shear stress | $[N\ m^{-2}]$ |
| $\theta$ | friction angle of soil particles | $[deg]$ |

**Table C.3:** *Variables, description, units*

| | | |
|---|---|---|
| $v_{crit}$ | critical flow velocity | $[m\ s^{-1}]$ |
| $v_p$ | pore water velocity | $[m\ s^{-1}]$ |
| $v^{i,j}$ | flow velocity for $i, j$ cell | $[m\ s^{-1}]$ |
| $x$ | longitudinal distance along the channel | $[m]$ |
| $x$ | dimensionless load | $[-]$ |
| $x(t)$ | time-dependent seepage length through dike foundation | $[m]$ |
| $x(t)$ | time-dependent seepage length along dike foot | $[m]$ |
| $x^*$ | average seepage length | $[m]$ |
| $\Delta x$ | cell dimension, width | $[m]$ |
| $\Delta y$ | cell dimension, height | $[m]$ |
| $Z$ | fragility function | $[-]$ |
| $Z_{cl}$ | fragility function for critical length of pipes | $[-]$ |
| $Z_{mi}$ | fragility unction for slope micro-instability | $[-]$ |
| $Z_o$ | fragility function for overtopping | $[-]$ |
| $Z_p$ | fragility function for piping | $[-]$ |
| $Z_r$ | fragility function for rupture | $[-]$ |
| $Z_s$ | fragility function for seepage through dike foundation | $[-]$ |
| $Z_{sm}$ | fragility function for seepage through dike core | $[-]$ |
| $z$ | datum or bottom elevation | $[m]$ |

# List of Figures

# List of Tables

# Acknowledgments

First of all, I would like to cordially thank my principal supervisor, Prof. Dr. Bruno Merz, for all kinds of support he provided during this research. I highly appreciate his keen interest in my work expressed in numerous fruitful discussions. He kept balance between constructive devising suggestions and granting me freedom to realise my own ideas. I highly appreciate his continuous encouragement for striving an added value and seeking novelty and uniqueness in research, which I hopefully could realise in this work to a certain extent.

I would like to thank Dr. Heiko Apel, who provided through his research a solid starting point for this thesis. He was superb technically and always had an idea to seemingly dead-end problems. He kindly provided some MATLAB routines and supported me through fruitful discussions that strongly shaped my way of proceeding.

I am grateful to Dr. Karl-Erich Lindenschmidt for supervising the project of the Young Investigators Group and supplying polder control data, which were used in the modelling study. I thank him and also Prof. Dr. Axel Bronstert for useful comments and suggestions on various aspects of the thesis.

Saxonian Dam Authority (Landestalsperrenverwaltung (LTV) Sachsen), particularly Dr. Uwe Müller and Ivo Heiland are gratefully acknowledged for provision of dike data for the State of Saxony and having a continuous interest to the project of the Young Investigators Group. I thank to Dr. Sebastian Kofalk (BfG) and Martin Gocht (Water&Finance) for providing various dike data, Ciaron Linstead and Dan Beli (PIK) for support on the TDT Library and Bob Olson for assistance with the EPDRiv1 model.

Many thanks to all the colleagues at the Section "Engineering Hydrology" of GeoForschungsZentrum Potsdam who have influenced the presented study in any way and created a great working atmosphere. Particularly, I thank Theresia Petrow and Uli Herrmann for interesting, deep, espresso-enhanced discussions on various project-related, GIS-concerned and life-relevant topics that pleasantly adorned my daily work.

Finally, I would like to thank my whole family for their encouragement, concern and understanding that strongly supported me at various phases of the dissertation. Especially, I am deeply grateful to my wife, Svitlana, who helped me in every respect during those years and shared with me frustration about memory leaks and oscillating numerical solutions, sometimes encountered during simulations, and all the fascination about fancy pictures resulting from Monte Carlo runs.

# Author's declaration

I declare that this dissertation has been submitted neither as a whole nor in part at any other university for any other academic award. The work is original, except where indicated by special reference in the text.

Sergiy Vorogushyn
Potsdam, June 2008